



HAL
open science

Damage mechanisms under tensile stress of amorphous and low semi-crystalline polymers

Stéphanie Djukic

► **To cite this version:**

Stéphanie Djukic. Damage mechanisms under tensile stress of amorphous and low semi-crystalline polymers. Material chemistry. Université de Lyon, 2020. English. NNT: 2020LYSE1041 . tel-02797014

HAL Id: tel-02797014

<https://theses.hal.science/tel-02797014>

Submitted on 5 Jun 2020

HAL is a multi-disciplinary open access archive for the deposit and dissemination of scientific research documents, whether they are published or not. The documents may come from teaching and research institutions in France or abroad, or from public or private research centers.

L'archive ouverte pluridisciplinaire **HAL**, est destinée au dépôt et à la diffusion de documents scientifiques de niveau recherche, publiés ou non, émanant des établissements d'enseignement et de recherche français ou étrangers, des laboratoires publics ou privés.

N°d'ordre NNT :
2020LYSE1041



THESE de DOCTORAT DE L'UNIVERSITE DE LYON

opérée au sein de
l'Université Claude Bernard Lyon 1

Ecole Doctorale N° 34

École Doctorale Matériaux de Lyon

Spécialité de doctorat : Science des Matériaux

Soutenue publiquement le 05/03/2020, par :

Stéphanie DJUKIC

Damage mechanisms under tensile stress of amorphous and low semi-crystalline polymers

Devant le jury composé de :

Jérôme BIKARD	Ingénieur de Recherche	Solvay	Encadrant industriel
Noëlle BILLON	Professeure	CEMEF – MINES ParisTech	Rapporteur
Anthony BOCAHUT	Ingénieur de Recherche	Solvay	Encadrant industriel
Eliane ESPUCHE	Professeure	Université Lyon 1	Examineur
Valérie GAUCHER	Professeure	Université de Lille 1	Examineur
Lucien LAIARINANDRASANA	Professeur	MINES ParisTech	Rapporteur
Didier LONG	Chercheur CNRS	LPMA	Directeur de thèse

Je suis de ceux qui pensent que la science est d'une grande beauté. Un scientifique dans son laboratoire est non seulement un technicien : il est aussi un enfant placé devant des phénomènes naturels qui l'impressionnent comme des contes de fées.

Marie Curie

Remerciements

Le doctorat ... 3 ans de travail, l'aboutissement de 8 années d'études. En étant passionnée de course à pied, je pourrai comparer la thèse à un marathon. Le plus beau et le plus dur des marathons, avec des hauts mais également des bas ... Être parfois découragée face au travail qu'il reste à fournir. Un marathon pas si simple, avec beaucoup de dénivelé, de la peur (vais-je arriver à franchir la ligne d'arrivée ?) et enfin apercevoir et franchir cette ligne d'arrivée qui fait tant rêver. Ce manuscrit est l'aboutissement de cette course, une médaille en quelque sorte, qui n'aurait jamais été possible seule. Je tiens à remercier sincèrement plusieurs personnes sans qui ce travail n'aurait pas vu le jour.

Je remercie tout d'abord Florence Clément et Didier Long, directrice et directeur adjoint du Laboratoire des Polymères et Matériaux Avancés (LPMA) pour m'avoir donné l'opportunité de réaliser cette thèse au sein du laboratoire. Ce fut une expérience enrichissante, et m'a permis de découvrir le monde de la recherche en industrie. Florence, merci pour les nombreux échanges tout au long de ces trois années. Didier, je te remercie d'avoir été mon directeur de thèse. Nos discussions au cours de ces trois années m'ont beaucoup appris, et ont permis de rendre ce travail de qualité.

Je souhaite remercier mes encadrants Solvay Anthony Bocahut et Jérôme Bikard. Anthony, merci pour les discussions que nous avons eues au cours de ces trois années, pour tes conseils notamment en DMA. Jérôme, merci d'avoir rejoint le coche. J'ai beaucoup appris grâce à nos nombreuses discussions et tes conseils sur la mécanique des polymères. Je te remercie également d'avoir pris le temps de relire les articles et ce manuscrit.

Je tiens à exprimer mes remerciements à Noëlle Billon et à Lucien Lairinandrasana qui ont accepté de rapporter ce travail. Merci d'avoir pris un temps considérable à éplucher, commenter et évaluer ce manuscrit de manière constructive et instructive. Je remercie également Valérie Gaucher et Eliane Espuche pour l'intérêt porté à ma thèse et pour leur lecture du manuscrit. Merci Eliane Espuche d'avoir accepté de présider le jury lors de ma soutenance de thèse.

Je tiens également à remercier les différentes équipes du RICL de Solvay qui m'ont accueillie et formée sur les différentes techniques de caractérisation : merci Olivier Bronchart pour ta patience au labo méca, je suis désolée de t'avoir (surement) embêté avec mes questions et mon manque de force pour démonter les mords de la Z050 ; merci Sonia Perosino pour m'avoir appris les secrets de la DMA et de la DSC ; merci Fabrice Millet pour m'avoir appris tant de choses concernant l'injection des polymères ; merci à Léo Georges, Violaine Ducru et Robert Stutz au laboratoire Physique ; merci à Sandrine Rossi, Sylvie Ghiringhelli, Christiane Prebet (pour ton temps à me former rapidement), Vincent Curtil, Michel Sorin, Olivier Andres, pour votre gentillesse et votre accueil. Je remercie l'équipe de microscopie : Pauline Grau, Baptiste Gros et Clémence Abadie, pour leur formation, leur aide et leur bonne humeur. Merci également à Alexandre Corbin pour toutes les discussions que l'on a pu avoir pendant ces trois ans et plus.

Mes remerciements vont à l'ensemble des ingénieurs du LPMA et de PM2D, que ce soit pour leur accueil ou pour les différents échanges que j'ai pu avoir durant ma thèse. Je remercie Paul Sotta pour ses explications concernant les fits et les RX. Mathieu Tauban, Rabih Al Rahal Al Orabi, Alexandra Argoud, Pierre-Yves Lahary, Olivier Sanseau, Lise Trouillet-Fonti et Carroll Vergelati.

Je remercie à présent les non permanents stagiaires et/ou thésards qui sont devenus des amis et ont égayé mes journées : Éléonore, merci pour avoir débuté cette aventure en même temps que moi. Tu as apporté ta bonne humeur quotidienne au labo, ou même en conf. Je suis contente de t'avoir rencontrée ! C'est très bientôt ton tour ! Agathe C, merci pour tous les moments passés au labo, pour m'avoir appris tant de choses. Merci également pour les à côté, d'avoir partagé des cours de Yoga, notamment avant que j'entame la rédaction de ce manuscrit. Je remercie les meilleurs collègues de bureau qu'il peut y avoir : Rita, merci pour toutes les discussions qu'on a pu avoir, ta bonne humeur au sein du bureau 103-c, le partage des musiques de Noël, tes conseils et ton aide quand je me posais des questions, les macarons lors de mon pot de thèse ; Nicolas, merci pour ta bonne humeur et tes propositions d'afterwork ; Julien, bien que très peu présent au LPMA, tu as mis une bonne ambiance au labo ! Je vais bientôt te rejoindre dans le monde des câbles (une fois que le confinement sera terminé !). Merci Thomas pour ta gentillesse, tes explications quand je galérais avec des équations. Désolée de ne pas avoir parlé des « cônes » avec ta petite animation lors de ma soutenance ! Grazie Francesco, ta bonne humeur constante va me manquer. Je viendrai te voir à Gorgonzola (et pas que pour le fromage promis !). Je remercie également Jessica et Agathe V., avec qui j'ai partagé une bonne partie de ma thèse. Merci pour nos discussions, notamment le midi. Merci Ludo, pour ta bonne humeur, nos discussions running et quelques sorties « on va courir à midi ». Je n'ai pas été autant disciplinée que toi, et parfois il faisait vraiment trop chaud pour aller courir ! Je n'aurai plus cette excuse lors de mon entraînement marathon ! Merci Héléoise, pour les discussions lors des trajets Navette et ta gentillesse. Je remercie les derniers stagiaires que j'ai eu la chance de connaître : Emmanuelle, Mini-Pauline, Léa, Océane et Alexandre : bon courage à ceux qui ont décidé de poursuivre par une thèse. C'est un long travail, mais une très belle expérience. Merci également à Tiffany, Ilan, Aurélien, Thibaut et Anne-Cha. Pour terminer, je souhaite remercier Mélissa, la petite dernière arrivée au bureau 103-c. Bon courage pour ce début de thèse, je te souhaite plein de réussite. Merci à vous tous pour cette unité entre les thésards et stagiaires, la bonne ambiance au sein du labo, les bons moments partagés que ce soit au travail ou en dehors, autour d'un chocolat chaud, ou autour d'un verre (ou plus) à découvrir de nouveaux lieux sympas, le choix et l'élaboration des traditionnelles galettes des rois ... Je vous souhaite à tous une très bonne continuation et espère vous revoir encore et encore.

Je voudrais remercier mes parents, mes sœurs et mon frère, pour leur soutien, même à distance.

Le meilleur pour la fin. Corentin. Merci énormément pour ton soutien infailible durant ces trois années, durant les moments les plus difficiles et stressant. Merci pour tes relectures, pour l'installation du pot de thèse. Merci d'avoir cru en moi. Un chapitre important de ma vie se clôt, et un nouveau débute, avec toi.

Summary in English

In the last few years, a new class of polyamides has been developed for specific applications requiring better mechanical and thermal properties, such as electronics or automotive industry. Polyphthalamides (PPA) are semi-aromatic polyamides containing aromatic rings in their main chain. The resulting PPA can be amorphous or semi-crystalline depending on the monomer combination used and can be used in composites for high temperature applications.

Recently, the damage mechanisms have been studied in the case of semi-crystalline (PA66) and amorphous (cellulose acetate) polymers. The aim of the PhD thesis was to study the damage mechanisms of amorphous and semi-crystalline polymers. In addition, few studies have been conducted to characterize the properties of pure PPA. More detailed data regarding their mechanical properties are needed. The study of the properties of this class of polymers is important, especially since their applications are different from aliphatic polyamides. We first characterized these polymers (^1H NMR, SEC, DMTA) and then studied their mechanical behavior in traction, compression and Charpy impact strength.

We have thus been able to highlight the appearance of a necking phenomenon and a strain hardening regime from 20% deformation for three PPA studied. Strain hardening has also been observed in other amorphous ductile polymers such as polycarbonate (PC) or poly(methyl methacrylate) (PMMA). The strain hardening stabilizes the deformation by avoiding the localization of the damage.

In order to describe the microscopic mechanisms associated with the initiation and propagation of damage under tensile deformation of our polymers, we have carried out observations by scanning transmission electron microscopy (STEM) and optical microscopy as well as by Ultra-small angle X-ray scattering (USAXS).

The analysis of these different polymers (amorphous and semi-crystalline PPA, PC, PMMA) by USAXS highlights different modes of damage. The simultaneous nucleation of nanometric crazes around the pre-existing defects (defects related to the injection process), then the limited growth of these crazes are observed for the amorphous PPA, the PC and the PMMA studied, in a mechanism similar to that studied in the case of cellulose acetate. The damage is blocked in the first place by the strain hardening. However, in the case of polycarbonate and PMMA, when the stress applied becomes sufficiently high, a small fraction of these crazes grows faster to cause the rupture of the sample, which allows to observe the evolution of a second family of larger crazes. We also observe the growth of a second family of crazes for one of the amorphous PPA, but their growth stops at the appearance of necking. No failure of the sample

is observed. The second amorphous PPA is damaged by cavitation up to about 5% deformation. The cavities stop to grow at the appearance of shear bands. When the shear bands propagated on either side of the sample, the failure is observed. The two semi-crystalline PPA deform by necking without failure. No cavitation was observed by USAXS.

The damage of the polymers studied can be classified into three categories. The first category concerns polymers that behave similarly to cellulose acetate. Crazing nucleation is observed, which growth is initially blocked by strain hardening. When the stress applied becomes sufficiently high, a fraction of these crazes increases more rapidly until the sample is broken, which makes it possible to observe the evolution of a second family of larger crazes. This category concerns polycarbonate and PMMA. The second category concerns one of the amorphous PPA with crazes whose growth is initially blocked also by strain hardening. The growth of a second family of crazes stops at the appearance of necking, and no failure of the specimen is observed. The last category concerns polymers that do not show any damage. These are the two semi-crystalline PPA.

We propose in this thesis an interpretation of these different mechanisms of damage.

Keywords: Polyphthalamide, polyamide, mechanical properties, strain hardening, necking, damage mechanisms, USAXS

Résumé en français

Ces dernières années, une nouvelle classe de polyamides a été développée pour des applications spécifiques nécessitant de meilleures propriétés mécaniques et thermiques, telles que l'électronique ou l'industrie automobile. Les polyphthalamides (PPA) sont des polyamides semi-aromatiques, contenant des cycles aromatiques dans leur chaîne principale. Le PPA résultant peut être amorphe ou semi-cristallin en fonction de la combinaison de monomères utilisée et peut être utilisé dans des composites pour des applications à haute température.

Récemment, les mécanismes d'endommagement ont été étudiés dans le cas de polymères semi-cristallins (PA66) et amorphes (acétate de cellulose). Le but de la thèse a été d'étudier les mécanismes d'endommagement de polymères amorphes et semi-cristallins. Par ailleurs, peu d'études ont été réalisées pour caractériser les propriétés des PPA purs. Des données plus détaillées concernant leurs propriétés mécaniques sont nécessaires. L'étude des propriétés de cette classe de polymères est importante, d'autant plus que leurs applications sont différentes des polyamides aliphatiques. Nous avons dans un premier temps caractérisé ces polymères (RMN, SEC, DMTA) puis étudié leur comportement mécanique en traction, compression et choc.

Nous avons ainsi pu mettre en évidence l'apparition d'un phénomène de striction et d'un régime de durcissement plastique (*strain hardening*) dès 20% de déformation pour trois PPA étudiés. Le durcissement plastique a également été observé dans d'autres polymères amorphes ductiles tels que le polycarbonate (PC) ou le poly(méthyle methacrylate) (PMMA). Le durcissement plastique stabilise la déformation en évitant la localisation de l'endommagement.

Afin de décrire les mécanismes microscopiques liés à l'initiation et la propagation de l'endommagement sous traction de nos polymères, nous avons réalisé des observations par microscopie électronique à balayage en transmission (STEM) et microscopie optique ainsi que par diffusion des rayons X aux très petits angles (USAXS).

L'analyse de ces différents polymères (PPA amorphes et semi-cristallins, PC, PMMA) par USAXS met en évidence différents modes d'endommagement. La nucléation simultanée de craquelures nanométriques autour des défauts préexistants (défauts liés au processus d'injection), puis la croissance limitée de ces craquelures sont observées pour les PPA amorphes, le PC et le PMMA étudiés, dans un mécanisme similaire à celui étudié dans le cas de l'acétate de cellulose. L'endommagement est bloqué dans un premier temps par le durcissement plastique. Cependant, dans le cas du polycarbonate et du PMMA, lorsque la contrainte appliquée devient suffisamment élevée, une petite fraction de ces craquelures croît

plus rapidement jusqu'à entrainer la rupture de l'échantillon, ce qui permet d'observer l'évolution d'une deuxième famille de craquelures de plus grandes tailles. On observe également la croissance d'une deuxième famille de craquelures pour l'un des PPA amorphe, mais leur croissance s'arrête à l'apparition de la striction. Aucune rupture n'est observée. Le deuxième PPA amorphe s'endommage par cavitation jusqu'à environ 5% de déformation. Les cavités cessent de croître à l'apparition de bandes de cisaillement. Lorsque les bandes de cisaillement se sont propagées de part et d'autre de l'échantillon, la rupture est observée. Les deux PPA semi-cristallins se déforment par striction sans rupture. Aucune cavitation n'a été observée par USAXS.

L'endommagement des polymères étudiés se classe ainsi en trois catégories. La première catégorie concerne les polymères qui ont un comportement similaire à l'acétate de cellulose. On observe la nucléation de craquelures dont la croissance est dans un premier temps bloquée par le durcissement plastique. Lorsque la contrainte appliquée devient suffisamment élevée une fraction de ces craquelures croît plus rapidement jusqu'à entrainer la rupture de l'échantillon, ce qui permet d'observer l'évolution d'une deuxième famille de craquelures de plus grandes tailles. Cette catégorie concerne le polycarbonate et le PMMA. La deuxième catégorie concerne l'un des PPA amorphe ayant des craquelures dont la croissance est dans un premier temps bloquée par le durcissement plastique. La croissance d'une deuxième famille de craquelures s'arrête à l'apparition de la striction, et aucune rupture n'est observée. La dernière catégorie concerne les polymères ne présentant pas d'endommagement. Il s'agit des deux PPA semi-cristallins.

Nous proposons dans cette thèse une interprétation de ces différents mécanismes d'endommagement.

Mots-clés : Polyphthalamide, polyamide, propriétés mécaniques, durcissement plastique, striction, mécanismes d'endommagement, USAXS

Table of Contents

REMERCIEMENTS	III
SUMMARY IN ENGLISH	I
RESUME EN FRANÇAIS	III
TABLE OF CONTENTS	V
LIST OF SYMBOLS AND ABBREVIATIONS	IX
GENERAL INTRODUCTION	1
CHAPTER 1 – STATE OF THE ART	5
1.1 Polyamides	5
1.1.1 Generalities	5
1.1.2 Polyphthalamides.....	6
1.1.2.1 Presentation, synthesis and applications.....	6
1.1.2.2 Water absorption	9
1.1.2.3 Processing	9
1.1.2.4 Properties of PPA	10
1.2 Mechanical properties of amorphous polymers	11
1.2.1 Stress-Strain curve and plastic instability	11
1.2.2 True stress - true strain curve	13
1.2.3 Plastic instability: necking.....	15
1.2.4 The brittle-ductile transition temperature T_{bd}	19
1.2.5 Law of elastic behavior	20
1.3 Molecular relaxations	21
1.4 Deformation mechanisms of semi-crystalline and amorphous polymers	24
1.4.1 Deformation of the interlamellar amorphous phase.....	24
1.4.2 Deformation of the crystalline phase	25
1.4.2.1 Crystalline slips.....	25
1.4.2.2 Cavitation	25
1.4.3 Micro-mechanisms of deformation in glassy polymers.....	27
1.4.3.1 Shear bands.....	27
1.4.3.2 Crazes	29
1.5 Objectives of the research	35
CHAPTER 2 – MATERIALS AND METHODS	36

2.1	Materials	36
2.2	Injection molding process.....	38
	2.2.1. Skin-core effect	40
2.3	Experimental techniques	43
2.3.1	Thermal and structural characterizations	43
2.3.1.1	Differential scanning calorimetry (DSC).....	43
2.3.1.2	Wide Angle X-Ray Scattering (WAXS).....	44
2.3.1.3	Determination of the surface tension.....	48
2.3.2	Chemical structure characterization	51
2.3.2.1	Molecular weight distribution	51
2.3.2.2	Secondary reaction: branching quantification.....	52
2.3.2.3	¹ H NMR.....	53
2.3.3	Macroscopic mechanical properties	55
2.3.3.1	DMTA	55
2.3.3.2	Impact test	58
2.3.3.3	Video-controlled tensile test.....	59
2.3.3.4	Compression test	61
2.3.4	Study of damages morphologies.....	62
2.3.4.1	Microscopic study	62
2.3.4.2	Ultra Small Angle X-ray Scattering (USAXS)	66
CHAPTER 3 – THERMAL AND STRUCTURAL CHARACTERIZATION.....		71
3.1	Thermal properties	71
3.2	Thermo-mechanical properties.....	74
3.2.1	Time/temperature dependence of relaxations	75
3.2.2	Secondary relaxations	77
3.2.3	Main relaxation	78
3.2.4	Time-Temperature Superposition (tTS)	78
3.2.5	Thermo-mechanical properties of Polycarbonate and PMMA	80
3.3	Proton Nuclear Magnetic Resonance	81
3.4	Chemical structure	83
3.5	Conclusion	87
CHAPTER 4 – MACROSCOPIC STUDY OF THE MECHANICAL PROPERTIES		88
4.1	Characterization of the brittle-ductile transition T_{bd}.....	88
4.1.1	Charpy impact strength.....	88
4.1.2	Influence of frequency on T_{bd}	91

4.2	Tensile behavior	93
4.2.1	Temperature dependence of the Young modulus E and the yield stress σ_y	94
4.2.2	Evolution of the Poisson's ratio ν	95
4.2.3	Volume variation.....	99
4.2.4	Necking: Considère's construction.....	101
4.2.5	Influence of the injection process and the polymer chains orientation.....	102
4.3	Compression behavior	105
4.4	Surface tension	107
4.5	Conclusion.....	110
CHAPTER 5 – DAMAGE MECHANISMS UNDER TENSILE DEFORMATION.....		112
5.1	Microscopic study	112
5.2	Characterization of damage by Ultra-small Angle X-ray Scattering (USAXS).....	125
5.2.1	Fitting equations	125
5.2.2	Experimental results	130
5.2.2.1	Before tensile experiments.....	130
5.2.2.2	Evolution of damage under tensile deformation.....	132
5.2.2.3	Absence of strain induced crystallization	149
5.2.3	Interpretation and discussion	151
5.2.3.1	Introduction	151
5.2.3.2	Damage mechanisms of polycarbonate and PMMA.....	156
5.2.3.3	Damage mechanisms of polyphthalamides	158
5.2.3.4	Summary of damage mechanisms observed	160
5.2.4	Conclusion.....	162
GENERAL CONCLUSION.....		166
BIBLIOGRAPHY		169

List of Symbols and Abbreviations

Symbols

a_T	Horizontal shift factors in time-temperature superposition
C_1, C_2	Constants in the WLF equation (referred to T_{ref})
E	Young modulus
E^*	Elastic modulus in nano-indentation
E'	Storage modulus in DMTA
E''	Loss modulus in DMTA
E_A	Activation energy
E_{SH}	Strain hardening modulus
h	Sample thickness
I_p	Polydispersity ($I_p = M_w/M_n$)
M_n	Number-average molecular weight obtained by EGT or SEC
M_w	Weight-average molecular weight obtained by EGT or SEC
N_A	Avogadro number
q	Scattering vector
R	Ideal gas constant
t	Time
T	Temperature
T_c	Crystallization temperature
T_{bd}	Brittle-ductile transition temperature
T_g	Glass transition temperature
T_m	Melting temperature
T_{ref}	Reference temperature used in time-temperature superposition

Greek Symbols

α	Main relaxation process associated to the glass transition
β	Secondary relaxation process associated to the rotation of amide groups
ε	Strain
γ	Secondary relaxation process associated to the aliphatic chain rotation
δ	Phase angle ($\tan \delta = E''/E'$)
ΔG	Free energy
ΔS	Entropy
θ	Scattering angle
λ	Wavelength
ρ	Density

σ	Stress
τ	Relaxation time
ν	Poisson's ratio

Abbreviations

AEG	Amine End Group
BDS	Broadband Dielectric Spectroscopy
BEG	Blocked End Group
BF	Bright-Field
BHT	Bis-(Hexamethylene)Triamine
BPA-PC	Bisphenol A Polycarbonate
CDA	Cellulose Diacetate
CEG	Acid End Group
d.a.m.	Dried as molded
DF	Dark-Field
DMSO	Dimethylsulfoxide
DMTA	Dynamic Mechanical Thermal Analysis
DSC	Differential Scanning Calorimetry
EGT	End Group Titration
ESRF	European Synchrotron Radiation Facility
HFIP	Hexafluoroisopropanol
HMDA	Hexamethylenediamine
HVTEM	High Voltage Transmission Electron Microscope
IPA	Isophthalic acid
MALLS	Multi Angle Laser Light Scattering
MXDA	Meta-xylenediamine
NMR	Nuclear Magnetic Resonance
OM	Optical Microscopy
PA	Polyamide (or nylon)
PA 6	Polyamide 6
PA 6,6	Polyamide 66 (hexamethylene diamine + adipic acid)
PA 6I	Polyamide 6I (hexamethylene diamine + isophthalic acid)
PA 6T	Polyamide 6T (hexamethylene diamine + terephthalic acid)
PE	Polyethylene
PP	Polypropylene
PPA	Polyphthalamide
p.p.m	parts-per-million
PPO	Poly(p-phenylene oxide)

PS	Polystyrene
PVC	Polyvinyl chloride
PVDF	Polyvinylidene fluoride
RCS	Rapid Cooling System (DSC)
RH	Relative Humidity
RI	Refractive Index
RT-PMMA	Rubber Toughened Poly(methyl methacrylate)
SAXS	Small Angle X-ray Scattering
SEC	Size Exclusion Chromatography
SEM	Scanning Electron Microscopy
STEM	Scanning Transmission Electron Microscopy
TEM	Transmission Electron Microscopy
TPA	Terephthalic acid
tTS	Time-Temperature Superposition
USAXS	Ultra Small Angle X-ray Scattering
UV	Ultraviolet
WAXS	Wide Angle X-ray Scattering
WLF	William-Landel-Ferry

General introduction

This PhD thesis was carried out in the Laboratoire des Polymères et Matériaux Avancés UMR 5268, a joint research unit between the CNRS and Solvay.

Polyamides are engineering thermoplastics which are useful for their mechanical and high barrier properties. They are widely used in textile and automotive industries, where they compete with metals in a context of weight's reduction [1]–[3]. Polyamides are generally aliphatic and semi-crystalline such as PA 6 or PA 66. However, other structures have been developed in the last years for specific applications such as semi-aromatic or aromatic polyamides (MXDA, PA 6T/X, PA 10T/X, PA 10T [4]), as well as amorphous polyamides [1] especially in order to improve the mechanical and thermal properties [5]. Polyphthalamides (PPA) are polyamides containing aromatic rings in their backbones, giving them high mechanical strength and thermal resistance. The resulting PPA may be amorphous or semi-crystalline depending on the combination of monomers used [1]. These new PPA are used in several industries such as electronic devices, packaging or automotive industries, in composites for high temperature applications. Mechanical properties are keys for these applications. The ductile behavior of polymers is controlled strain hardening [6]. Strain hardening corresponds to an increase of the stress with deformation in the plastic regime, after the stress softening regime which follows the yield stress. Though its microscopic origin is still under debate [7]–[19], it is interpreted as a result of a stress contribution of the orienting molecular network [6], [7], [20]–[22]. Strain hardening is a phenomenon observed in the case of amorphous polymers such as polycarbonate (PC), poly(methyl) methacrylate (PMMA), polyvinyl chloride (PVC), and cellulose diacetate (CDA) [23]–[26]. Strain hardening can be characterized by the slope of the stress versus strain at large deformations (strain hardening modulus E_{SH}) [9], [11], [24], [27]–[29]. Polymers with no or low strain hardening have a fragile behavior characterized by rupture at small deformation, while polymers with a high strain hardening such as polycarbonate [30] exhibit better mechanical properties, display a ductile deformation behavior and break – if they do – at large deformation amplitudes. This ductile behavior associated to strain hardening has been explained by Govaert and Meijer [29] by the fact that strain hardening prevents strain localization and thus suppresses defects propagation or the appearance of shear bands. As mentioned, even polymers which display strain hardening may eventually break. The issue is: what are the corresponding damage mechanisms? How do they appear? What is the more precise role of strain hardening for stabilizing these damages?

Damaging in polymers under strain has been the subject of research for many years [31]–[39]. Michler [31] has shown that polymers with a 'brittle' behavior such as polystyrene (PS) deform by crazing, whereas polymers considered as 'ductile' deform by shear banding or by homogeneous deformation bands

[32], [33], [35]. These homogeneous deformation bands are craze-like zones, filled with the stretched polymer. This is the case of polycarbonate (PC). The crazing process takes place in three stages: initiation step, growth and rupture, and is an active research field [37], [39], [40]. For describing the growth of crazes, Argon and Salama [41] introduced in the context of polymers the concept of “meniscus-instability model” [37], [39], [42]. This hydrodynamic instability had been described by Taylor [43]. In this model, the plastic deformation is initiated by a local effect of stress concentration around the defect, as suggested by Monnerie et al [44]. Indeed, the local stress concentration generates a plastic deformation in a thin polymer layer which is surrounded by glassy polymer because this thin polymer layer has not reached its yield point yet. Recently, Michler [35] supposed that the initiation of a craze is preceded by the formation of a localized plastic deformation zone. As this plastic deformation zone develops, the hydrostatic stress increases until it becomes higher than a critical stress level. Cavitation can occur, leading to the local development of microvoids. According to Michler [35], this localized plastic deformation zone is related to the entanglement network. The second step of the crazing process, the craze growth, is described in literature by a two-step process: the craze tip propagation (‘meniscus-instability model’) and the craze opening, related to the chain entanglements [39], [42], [44]. Failure in polymers is assimilated to this last process (craze opening). Recently, experimental studies concerning deformation mechanisms in amorphous polymers and in particular the crazes morphology, generated during tensile experiments, have been done [45]–[49]. These studies are performed after the failure of the samples by microscopy (optical microscopy or transmission electron microscopy (TEM)) or X-ray scattering (Ultra-Small Angle X-ray Scattering USAXS/SAXS) [45]–[48]. Damage during the strain hardening regime has not been studied with the aim of clarifying its role in the stabilizing mechanism of damaged as described macroscopically by Govaert and Meijer [29]. Most of these studies have also been performed during the last stages of damaged and not at the very beginning of damaging.

Stoclet et al [49] performed in-situ USAXS analysis in order to follow the damage under tensile deformation of poly(lactic acid). More recently, the damage mechanisms have been studied in the case of semi-crystalline (PA66 [50]) and amorphous polymers (cellulose acetate [26]). Mourglia-Seignobos et al studied the fatigue damage mechanisms of neat PA66 [50]. They proposed a quantitative mechanism of damage in this polymer: cavities of the order of 50 nm nucleate in the amorphous phase, in the equator of spherulites. Breaking of the sample is the consequence of the accumulation of these defects and is not due to the propagation of a single crack. Charvet et al [26] studied the microscopic mechanisms of damaging in plasticized cellulose diacetate (CDA) under tensile deformation. The authors observed a heterogeneous nucleation of cavities in the vicinity of pre-existing impurities, which growth is initially blocked by strain

hardening. When the applied stress becomes sufficiently high, a fraction of these cavities grow faster until the failure of the sample.

The objective of this work is to study the damage mechanisms from the initiation until breaking of other amorphous and weakly semi-crystalline polymers: three different polyphthalamides (PPA), as well as polycarbonate (PC) and poly(methyl) methacrylate (PMMA). PC and PMMA are highly studied polymers known for their strain hardening behavior, especially in compression in the case of PMMA. PC presents a strong strain hardening regime, while PMMA presents a weaker strain hardening. The three polyamides of our study display also strain hardening. Our approach is similar to the approach used by Stoclet et al [49], Mourglia-Seignobos et al [50] and Charvet et al [26]. We analyze damage by USAXS at different elongations during a uniaxial tensile test for all our samples. Measurements performed by USAXS allow to determine the evolution of the number density, volume fraction and size of damages during the tensile deformation. All this information allows us to describe the damage mechanism in the studied polymers until breaking when it takes place.

This manuscript is divided into five chapters. The first chapter consists in a review of basic properties of polyamides and more specifically semi-aromatic polyamides, followed by a review of the mechanical properties of amorphous polymers, as well as the deformation mechanisms of semi-crystalline and amorphous polymers. The second chapter presents the studied polymers (polyphthalamides, polycarbonate and PMMA) as well as the description of the experimental techniques used to characterize the mechanical, thermal and structural properties of the different polymers considered. The techniques used to characterize the damages morphologies are also exposed. The third chapter deals with the results obtained for the thermal and structural characterization of the polymers studied. Then, the mechanical properties including the brittle-to-ductile transition temperature and the strain hardening regime observed under tensile and compressive measurements in PPA, PC and PMMA will be presented in fourth chapter. The tensile test at different temperatures permits to show different behaviors at low and high temperatures. At low temperatures, a fragile regime is highlighted, while at high temperatures a ductile regime can be observed. Finally, the fifth chapter deals with the damage mechanisms observed in PPA, PC and PMMA in their ductile regime. Our study of damage deals with polymers in their ductile regime. We discuss also the volume variations (sections 4.2.2 and 4.2.3) of our samples under applied strain, which allows calculating the Poisson ratio of our polymers in the linear regime and its extension in the large amplitude deformation. We measure the surface tension of our samples both before applied strain and far in the strain hardening regime (section 4.4). These two quantities are of interest for discussing qualitatively the

cavitation processes or why they are inhibited in some cases and not in other cases. Then the scattered intensities obtained by USAXS measurements at different strain values are modeled quantitatively and different parameters are presented (section 5.2.2) in order to describe the damage in the samples at different deformations. We describe in this chapter the initiation and growth of damage and the mechanisms of failure when the failure is reachable.

Finally, the main results of this work will be summarized in a concluding part, along with the perspectives.

Chapter 1 – State of the art

Polyamides are engineering thermoplastics which are useful for their high barrier properties. They are widely used in textile and automotive industries, where they compete with metals in a context of weight's reduction. Polyamides are generally aliphatic and semi-crystalline such as PA 6 or PA 66. However, other structures have been developed in the last years for specific applications such as semi-aromatic or aromatic polyamides, and amorphous polyamides in order to improve the mechanical and thermal properties. Polyphthalamides are polyamides containing aromatic rings in their backbones, giving them high mechanical strength and thermal resistance. The resulting polymer may be amorphous or semi-crystalline depending on the combination of monomers used.

This chapter consists in a review of basic properties of polyamides and more specifically semi-aromatic polyamides, followed by a review of the mechanical properties of amorphous polymers, since the study of the mechanical properties of this recent class of polyamides is not very extensive in literature.

The molecular relaxations, as well as the deformation mechanisms of semi-crystalline and amorphous polymers will be described in a third and a fourth part.

1.1 Polyamides

1.1.1 Generalities

In 1936, the work of Carothers led to the discovery of a molecule of high molar mass: the polyamide 66 (PA66). Since their industrial production by DuPont in 1938, these thermoplastic polymers have been widely used as technical plastics due to their excellent thermal stability (high temperature of use) and their good mechanical properties [1]. Polyamides (PA, also known as Nylon) are historically aliphatic and semi-crystalline (for example PA6 or PA66). Due to certain specific applications, there is now a very wide variety of polyamides: copolymers, semi-crystalline or amorphous (with different chemical structures, such as aromatic rings).

A PA is a polymer having at least one amide group, $-NHCO-$, and may be derived either from a chain polymerization of a lactam (polyaddition, eg PA6), or from a polycondensation reaction between a dicarboxylic acid (adipic acid for example) and a diamine (hexamethylenediamine for example) (case of PA66). According to the composition of their skeletal chain, the polyamides are classified into aliphatic, semiaromatic and aromatic [1]:

- Aliphatic polyamides: these polyamides, synthesized from two different monomers (a diamine and a diacid), are designated by PA x or PA x-y depending on the number of carbon atoms contained in their repeating unit: x denotes the carbon number of the skeletal chain of the diamine, and y denotes the carbon number of the skeletal chain of the diacid. They generally have a semi-crystalline structure. These polyamides have a good compromise between mechanical properties and chemical properties. However, they are sensitive to moisture due to the presence of polar groups, which can affect their mechanical and dimensional properties. The melting temperature (T_m) increases with the amide function concentration.
- Aromatic polyamides: also called aramids, are heat resistant polymers.
- Semi-aromatic polyamides: these are polyphthalamides (PPA) and are high-performance polymers. Compared to aliphatic polyamides, the difference stems from the presence of an aromatic ring on the diacid segments. These aromatic rings provide a certain rigidity, which allows a better conservation of the properties at high temperatures as well as a good dimensional stability. Usually, glass transition and melting temperatures are higher for a PPA than for an aliphatic polyamide. PPA may be semi-crystalline or amorphous [51].

Depending on the type of the repeating units, polyamides may be homopolymers (polymers derived from a single monomer) or copolymers (polymers resulting from the copolymerization of at least two different monomers) [1].

1.1.2 Polyphthalamides

1.1.2.1 Presentation, synthesis and applications

Polyphthalamides (PPA) are between aliphatic polyamides (such as PA66) and totally aromatic polyamides (aramids, such as Kevlar). They result from the reaction between an aliphatic diamine and an aromatic diacid. The term polyphthalamide only applies when at least 55% of the acid part is composed of terephthalic acid (TPA) or isophthalic acid (IPA) [52] (see Figure 1).

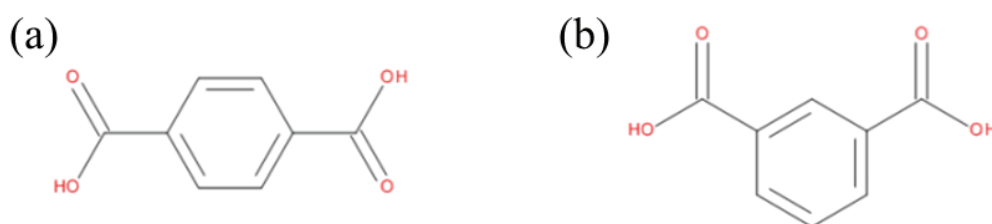


Figure 1 – Terephthalic acid (a) and Isophthalic acid (b) structures

PPA results from the copolymerization between polyamide 6T and polyamide 6I in different proportions (see Figure 2):

- Polyamide 6T is obtained by reaction of condensation between hexamethylenediamine (HMDA) and terephthalic acid. This polymer does not exist pure, but gives the crystalline part of the copolymer,
- Polyamide 6I is obtained by reaction between hexamethylenediamine (HMDA) and isophthalic acid. This polymer is amorphous.

Polyphthalamides contain aromatic rings in their backbones, thereby conferring a high mechanical and thermal resistance. These polymer materials have a high commercial potential and compete with metals, particularly in the automotive industry where weight reduction is an issue [52], [53]. Indeed, PPA have a lower density than metals for equivalent properties.

The resulting PPA can be amorphous or semi-crystalline depending on the combination of the monomers [1].

Semi-crystalline PPA are mainly based on PA6T. These polyamides are generally characterized by higher melting and glass transition temperatures, better chemical resistance, lower moisture absorption and better thermal stability compared to common aliphatic polyamides such as PA6 and PA66 [1]. When more than 55% of the acid portion of the PPA is composed of isophthalic acid, the resulting copolymer is amorphous [54].

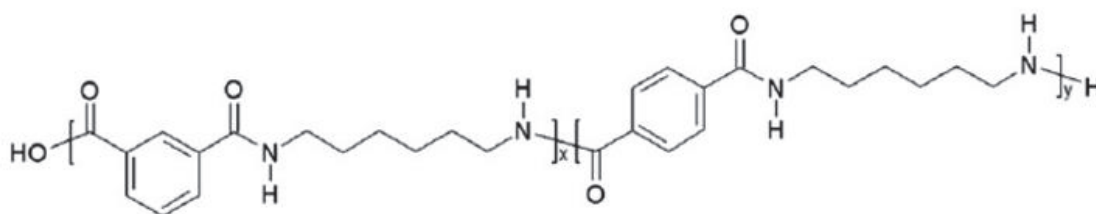


Figure 2 – PA6I(x)/6T(y) copolymer

PPA are synthesized in the same way as polyamide. Stoichiometric amounts of isophthalic and terephthalic acids, aliphatic diamines, additional comonomers, endcapping agents are mixed with a catalyst if necessary in water in a reactor [55]. The mixture is heated, leading to a removal of the water produced during reaction up to the desired viscosity and molar mass [55]. The first PPA synthesized was the PA6T. PA6T has a high melting temperature (about 370°C), making it difficult to process (indeed, the degradation of the polymer occurs before reaching the melting point) and leading to secondary reactions.

In industry, a two-step process is often used to synthesize PPA. During the first step, a low molar mass polymer with the desired composition is synthesized, it is a prepolymer. In a second step, the prepolymer is polymerized using Solid-State Polymerization. The Solid-State Polymerization used low temperature (between 200 to 300°C, which is below the melting point of the PPA) and is carried out under vacuum or inert atmosphere [56].

Several PPA are based on PA6T with other co-monomers (such as PA66, PA6, PA10). The use of these co-monomers decreases the melting point of the final PPA, at about 300°C, making the polymer suitable for injection molding process [57] (see Figure 3).

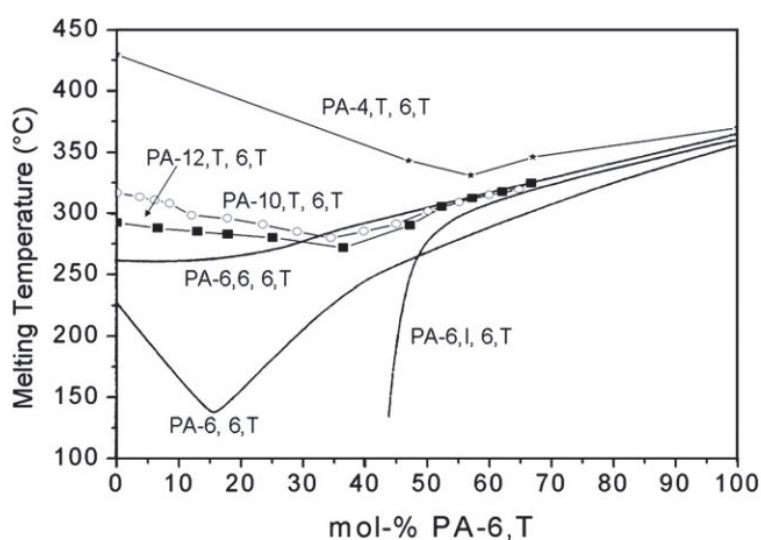


Figure 3 – Melting temperature of several PA6T based copolyphthalamides (from [54])

Figure 3 shows the melting temperature of several copolyphthalamides based on PA6T. An eutectic behavior can be observed [54].

This new class of polymers have been developed in the last years for specific applications such as semi-aromatic or aromatic polyamides (MXDA, PA 6T/X, PA 10T/X, PA 10T [57]), as well as amorphous polyamides [1], especially in order to improve the mechanical and thermal properties [4]. By incorporating aromatic rings into the backbone, Polyphthalamides have high mechanical strength, thermal and heat resistances, with a high melting point but they are still processable, which gives them a great industrial interest.

During the polyamide's synthesis, secondary reactions can occur. At high temperature (above 250°C), a thermal degradation can happen without oxygen, and lead to the thermal decomposition of the polymer

and/or the monomers [55]. Indeed the diacids could suffer a decarboxylation, while the diamines could suffer from a deamination [55], [58].

1.1.2.2 Water absorption

Polyamides are very sensitive to moisture. Indeed, the amide groups in their chemical structure tend to form high hydrogen bonding with water molecules. The water absorbed by the polymer will act as a plasticizer, and thereby changes their mechanical properties [59]. The water absorption in different polyamide structures, with two hygroscopic conditions (relative humidity of 50% and 100%) is shown in Table 1.

Table 1 – Absorption of water in different polyamide structures, with two hygroscopic conditions (relative humidity of 50% and 100%) [1]

Polyamide	Water absorbed at 23°C	
	50% RH	100% RH
66	2.5%	8.5%
6	2.8%	9.5%
6/6T	1.9%	6.0%
6I	2.0%	6.0%
MXD6	1.9%	5.8%

As shown in Table 1, at room temperature and with an atmosphere with a relative humidity of 50 %, a PA66 will absorb 2.5% of water in weight, whereas for a semi-aromatic polyamide in the same conditions such as PA6/6T, only 1.9% of water (in weight) will be absorbed. This absorption of water will be more important as the relative humidity will be high.

The amount of water absorbed by the polymer depends on the methylene/amide ratio (CH_2/CONH) [55]. Indeed, by increasing the number of amide groups in the polymer chain, the number of possible hydrogen bonding between the polyamide and water increases. However, this water absorption is reversible. The polyamide has to be dried before processing, in order to avoid its hydrolysis.

1.1.2.3 Processing

Pellets have to be dried before processing in order to avoid hydrolysis. Polyamides can be processed by extrusion or injection molding.

Injection-molding process and mold temperatures for different polyamides structures are shown in Table 2.

Table 2 – Injection-molding process temperatures for different polyamides structures [60].

Polyamide	Process temperature (°C)	Mold temperature (°C)
PA6	250-290	80
PA66	290-300	80-100
PA11	210-260	80
MXD6	250-280	130
PPA	327-332	135-150

The process temperature of PPA is much higher than that required for the PA6, as well as the mold temperature.

1.1.2.4 Properties of PPA

As said in the previous part, PPA are used in several industries such as electronic devices, packaging or automotive industries. They can be used in composites for high temperature applications. PPA used in composites are mostly semi-crystalline because they maintain their properties at T_g , which is not the case of amorphous PPA.

A table summarizing the main thermal and mechanical properties of PPA, compared to conventional aliphatic polyamides is presented below [1], [20], [52]:

Table 3 – Properties of PPA compared to aliphatic polyamides [1], [20], [52]

Properties	Aliphatic PA			Semi-crystalline PPA			Amorphous PPA
	PA 6	PA 66	PA 11	PA 6/6T	PA 6T/6I	MXD6	PA 6I
Density (g/cm ³)	1.13	1.14	1.04	1.18	1.18	1.22	1.18
T_m (°C)	215	265	187	295	320	243	-
T_g (°C)	50	57	46	110	125	90	125
Stress at break (MPa)	80	85	60	100	105	101	110
Elongation at break (%)	50	45	300	10	10	2	50

According to Table 3, PPA have a higher density than aliphatic PA (from 1.18 to 1.22 against 1.04 to 1.13). This difference comes from the stacking of aromatic cycles, which densifies the material. Compared to metals, PPA are still light (density of metals: between 5 and 10). PPA have also higher melting and glass transition temperatures than those of aliphatic PA. They can therefore be used for high temperature applications.

1.2 Mechanical properties of amorphous polymers

Amorphous polymers, such as PC, PMMA, PS and PVC will have a similar behavior to small deformations while their behavior at large deformations will be different.

1.2.1 Stress-Strain curve and plastic instability

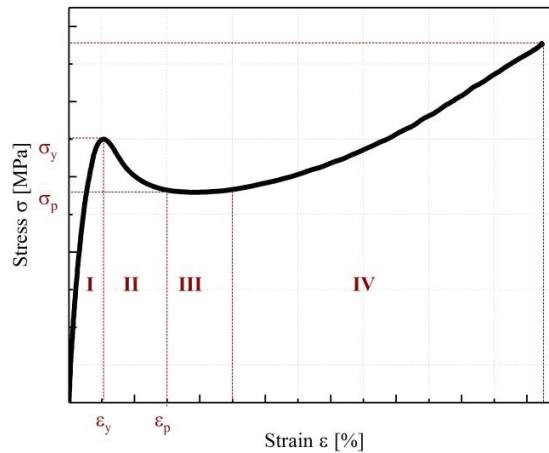


Figure 4 – Stress-strain curve for a ductile polymer

It is generally possible to define four behaviors from the nominal stress (σ) – nominal deformation (ϵ) curve for a ductile material (Figure 4):

(I): At low strains, the deformation is generally proportional to the stress, and the deformation is reversible. The Hooke's law can be applied:

$$\sigma = E \cdot \epsilon_e \quad (1)$$

With ε_e is the elastic strain. The slope of the straight-line E is called Young's modulus or elastic modulus. We talk of viscoelasticity when the deformation is reversible and that the return to a zero deformation depends on the time. This law applies in the case of a uniaxial tensile test.

(II): The end of the linear relationship between stress and strain marks the beginning of plasticity. The local nominal stress maximum after appearance of the plasticity is called plasticity threshold (yield point), σ_y . It may be followed by a stress decrease with strain, known as strain softening [61]. This phenomenon can be related to the emergence of damage, occurring in the form of shear bands or necking [62].

Beyond the yield point, amorphous and semi-crystalline polymers such as BPA-PC, PVC, PE, PP or PA may undergo a plastic instability, called necking [44]. Necking is associated with a local stress concentration that makes the strain field non-uniform within the sample [44]. Three behaviors can be observed beyond the yield point: a homogeneous deformation without necking, a stable necking, and an unstable necking. When the neck is stable, no sample failure occurs in the necking region. The sample section S_0 is uniform at the yield point. When a part of the sample has a section S_1 smaller than the sample section S_0 , necking will develop in this part. The local strain is larger in this part than in other parts of the sample: the deformation is localized in this region. The section of the necked region will decrease until reach a section S_2 . When the neck will have spread to the sample, a uniform deformation occurs, leading to the failure of the sample [44].

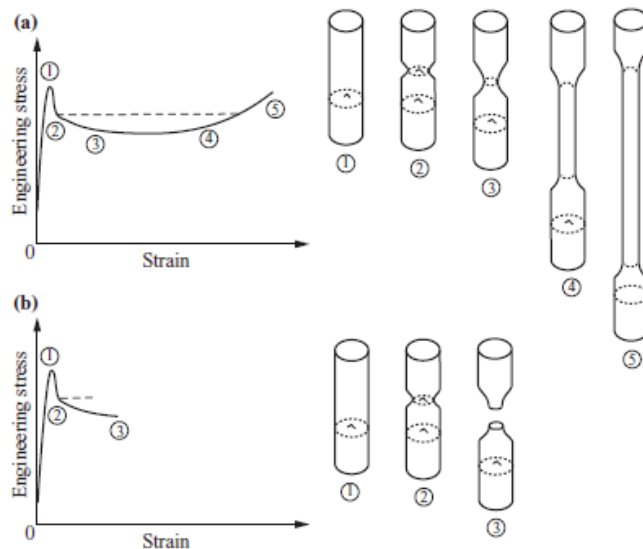


Figure 5 – Schematic representation of the necking phenomenon: (a) Stable necking; (b) Unstable necking leading to the sample fracture. From [44].

Figure 5 represents the different steps of the necking phenomenon. Figure 5-a shows the propagation of a stable necking whereas Figure 5-b shows an unstable necking, leading to the failure of the tensile specimen in the necking region.

(III): This domain is called the plastic flow regime and is characterized by a constant plateau stress, which is indicative of irreversible activated motion on a local segmental scale [61]. The effects of the thermal history and physical aging of the material are erased, which corresponds to a non-equilibrium steady state. This regime is strongly dependent on the temperature, the strain rate and the structure of the polymer [61].

(IV): At large deformation, the stress increases due to chain orientation in the loading direction. This orientation causes hardening of the material, called strain hardening [9], [13], [23], [24], [28], [63], [64].

The strain hardening regime is observed in glassy amorphous polymers such as PC or PMMA [24] (see Figure 6).

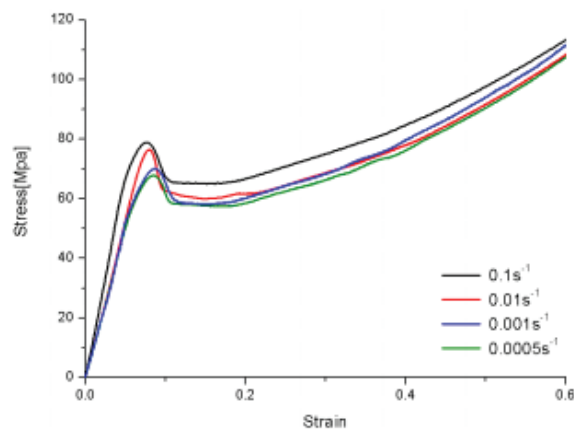


Figure 6 – Tensile true stress-strain curves for Polycarbonate at different strain rate. From [65].

1.2.2 True stress - true strain curve

At large deformations, amorphous polymers may have a high ductility. During the tensile test, the sample section is not constant. There are significant differences between the nominal stress σ_n and the true stress σ_v . The true stress differs from nominal stress after the yield point, especially for amorphous polymers which have high ductility at large deformations. Indeed, the nominal stress σ_n is based on the initial cross-

sectional area, S_0 , while true stress σ_v takes into account the section change and is based on the instantaneous cross-sectional area $S(t)$, as shown below by Equations 2 and 3.

$$\sigma_n = \frac{F}{S_0} \quad (2)$$

with F the force acting on the specimen and S_0 , the initial cross-sectional area.

$$\sigma_v = \frac{F}{S(t)} \quad (3)$$

The true strain ε_v also differs from ε_n . ε_n and ε_v are defined by Equations 4 and 5, respectively.

$$\varepsilon_n = \frac{\Delta l}{l_0} = \frac{l - l_0}{l_0} \quad (4)$$

with l the length at each time t and l_0 the initial length of the specimen.

$$\begin{aligned} \varepsilon_v &= \int_{l_0}^l \frac{dl}{l} = \ln\left(\frac{l}{l_0}\right) = \ln\left(\frac{l_0 + \Delta l}{l_0}\right) = \ln\left(\frac{l_0}{l_0} + \frac{\Delta l}{l_0}\right) = \ln\left(1 + \frac{l - l_0}{l_0}\right) \\ &= \ln(1 + \varepsilon_n) = \ln(\lambda) \end{aligned} \quad (5)$$

Figure 7 shows the deviation of the true stress strain curve from the nominal stress strain curve.

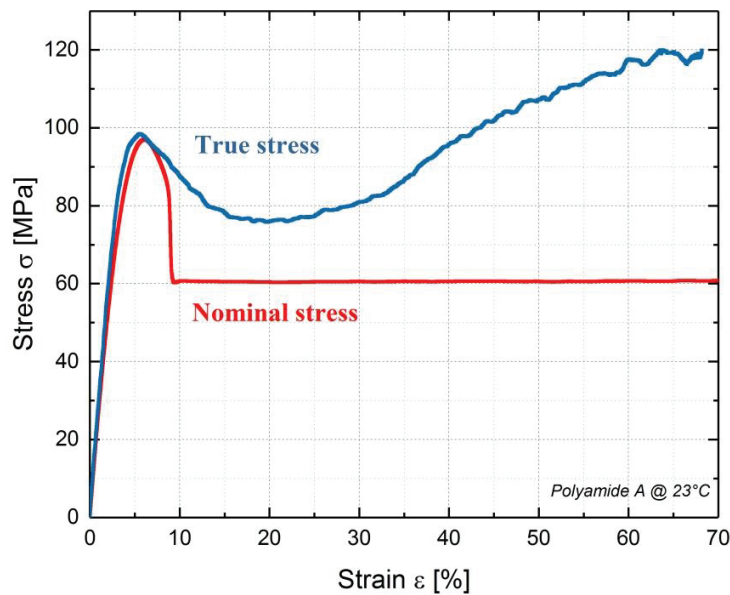


Figure 7 – Comparison between nominal stress-strain curve and true stress-strain curve for polyamide A at room temperature.

1.2.3 Plastic instability: necking

The equations mentioned so far apply when a polymer exhibits uniform deformation (see Equations 1 to 5). Beyond the plasticity threshold, several polymers (such as PC, PE, PVC, PP or PA) [66]–[69] show deformation heterogeneities called necking. This phenomenon is related to a local stress concentration (due to a variation of section or a defect) which makes the deformation field non-uniform within the sample.

The purpose of this section is to describe simply whether there is a link between the stability of the plasticized zone and the existence of a strain hardening regime. In our demonstration, the stress is considered to be the true stress. For reasons of simplicity, we use nominal strain. Indeed, with true strain, the equations would be more complex but the demonstration would remain the same.

Consider an isotropic material without strain hardening. Its behavior can be likened to a perfect elastoplastic behavior.

N section elements S_0 in series representing a specimen are considered, as schematized in Figure 8.

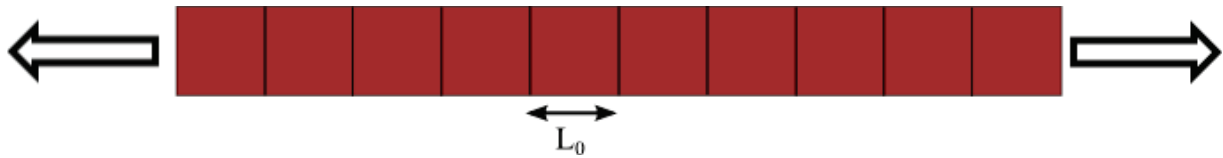


Figure 8 – Schematic representation of a specimen under tensile deformation.

The length of each element is L_0 . The observed behavior can be either elastic or perfect plastic, with a transition when the stress reaches a limit, σ_y , as schematized in Figure 9.

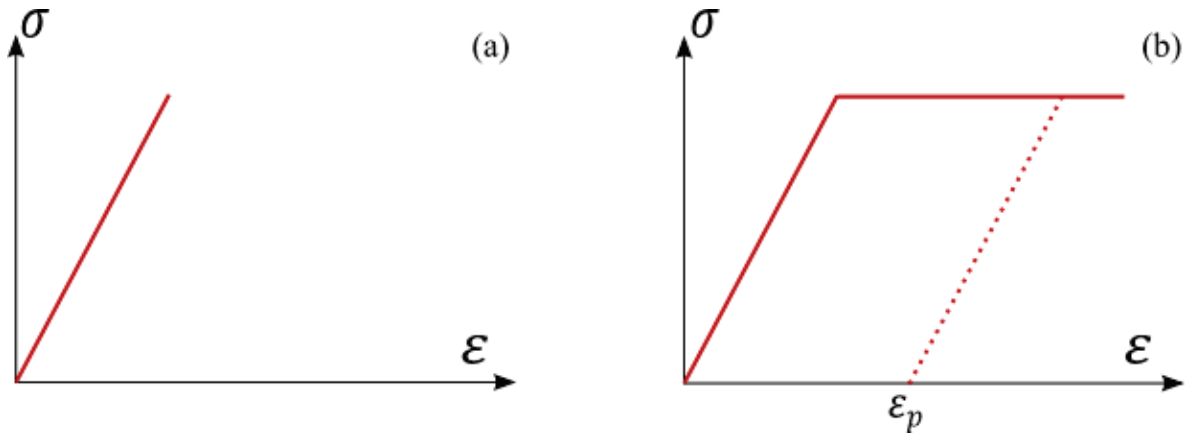


Figure 9 – Schematic representation of an elastic behavior (a) and a perfect plastic behavior (b).

The deformation in each element of the specimen follows Hooke's law:

$$\sigma = E(\varepsilon_v - \varepsilon^p) \quad (6)$$

With $\varepsilon_p = 0$ if $\sigma < \sigma_y$ and $\varepsilon_p = \varepsilon$ if $\sigma = \sigma_y$.

At the plasticity threshold (initial moment), the sample is subjected to an effort F . It is assumed that the field of deformation and stress are homogeneous. The uniform section S_1 is identical to the initial cross section S_0 , and $L_0 = L_1$. The stress in any part of the sample can be defined as follows:

$$\sigma_1(t) = \frac{F(t)}{S_1(t)} = E \cdot \varepsilon_1(t) \quad (7)$$

and the length L_1 is given by:

$$L_1(t) = L_0 \left(1 + \frac{F(t)}{E \cdot S_1(t)} \right) \quad (8)$$

Near a defect or a damage, the local Young modulus E is weaker. Thus, at the instant $t+dt$, when one element of the material reaches $\sigma_1(t) = \sigma_y$, there will be locally a decrease of the section S_1 (there is a new section in this area, called S_2): it is the start of the necking. In this area, the local stress σ_2 will be higher than the stress of the rest of the specimen σ_1 . The plasticity develops and there is a strain localization in the neck area. The section S_2 of the neck will decrease.

During the plastic deformation, there is volume conservation. The product of the section S_2 at $t+dt$ by the length L_2 at $t+dt$ is given by:

$$S_2(t + dt) \times L_2(t + dt) = S_1(t) \times L_1(t) \quad (9)$$

The stress at the instant $t+dt$ is given by:

$$\sigma_2(t + dt) = \frac{F(t + dt)}{S_2(t + dt)} = \frac{F(t + dt) L_2(t + dt)}{S_1(t) L_1(t)} \quad (10)$$

The deformation in this element is a plastic deformation then $\varepsilon_p = \dot{\varepsilon}$, and:

$$\varepsilon(t + dt) - \varepsilon_p(t + dt) = \varepsilon(t) - \varepsilon_p(t) \quad (11)$$

$$\sigma_2(t + dt) = \sigma_1(t) \quad (12)$$

Thus:

$$F_2(t + dt) = \sigma_1(t) S_1(t) \frac{L_1(t)}{L_2(t + dt)} = F_1(t) \frac{L_1(t)}{L_2(t + dt)} \quad (13)$$

Hence in the elements adjacent to the plasticized element for which the deformation is still elastic, we will have Equation 8 for the length variation. The section S_2 gradually increases. It is an elastic discharge in the areas adjacent to the plasticized zone. The stress in the plasticized element remains constant because the section of this element decreases. There are then two cases: if the necking does not spread to the entire material, there will be no strain hardening. This is a perfectly plastic behavior. On the contrary, if the necking propagates to the rest of the material, there will be a strain hardening. In our case, a necking propagation to the entire sample is observed, which is in agreement with the strain hardening behavior observed.

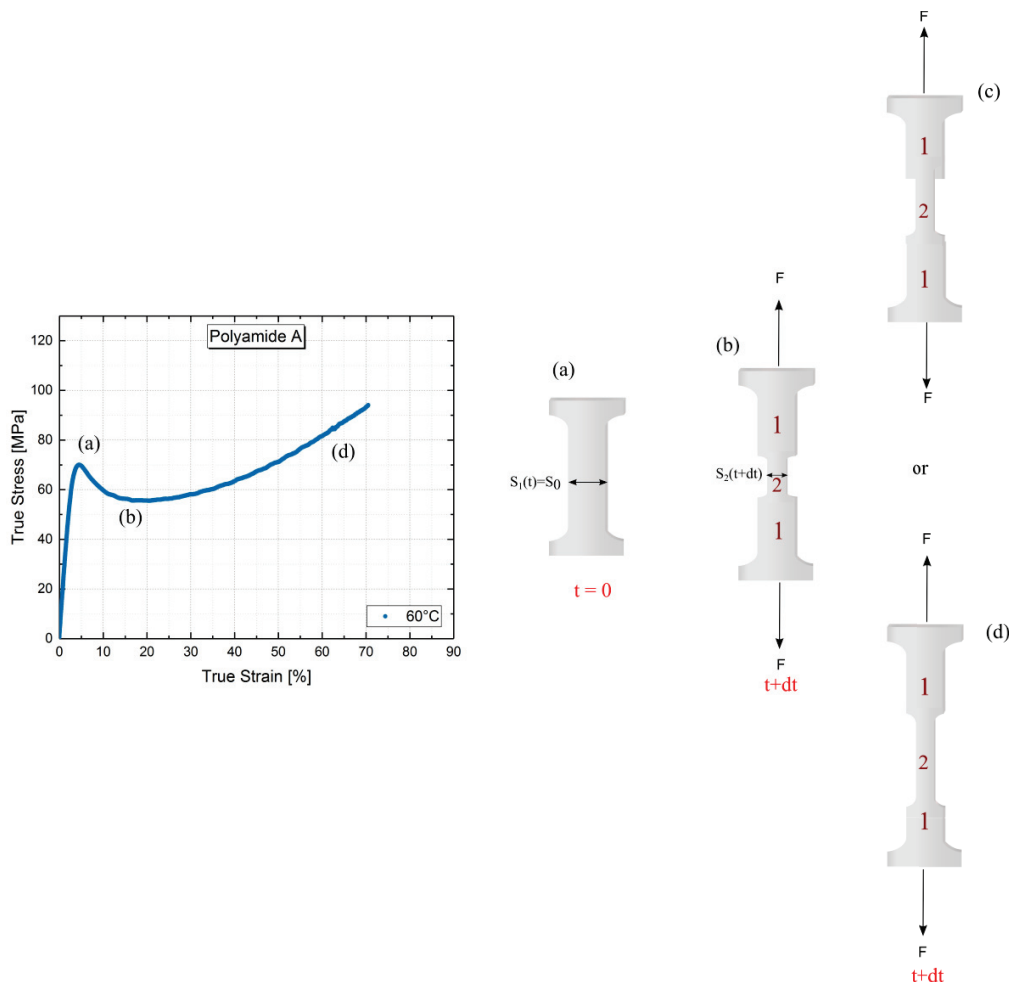


Figure 10 – Schematic representation of the necking phenomenon

The Considère's construction consists of plotting the true stress against the extension ratio. A possible tangent passing through the origin ($\lambda = 0$) can be drawn, as shown in Figure 11. This representation allows us to see if our polymers are in the case where there is a plastic flow without damage, or if on the contrary a damage occurs before reaching the yield stress σ_y .

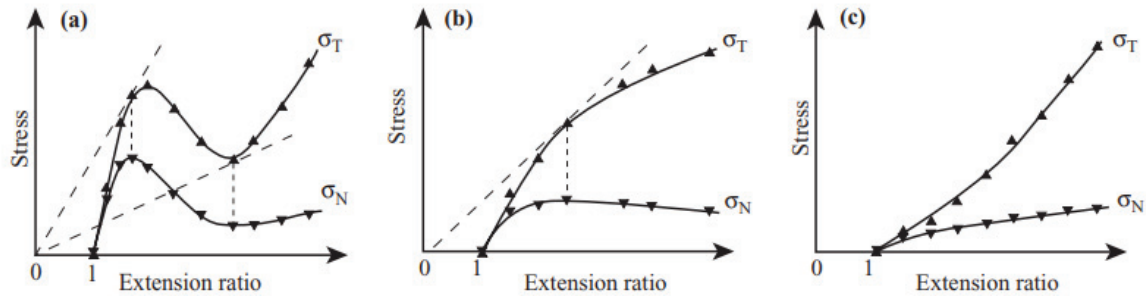


Figure 11 – Considère's construction: (a) Two tangents to true stress-strain curve: stable necking. (b) A single tangent: unstable necking. (c) No tangent: no necking, uniform deformation. From Halary et al.[44].

1.2.4 The brittle-ductile transition temperature T_{bd}

The brittle-ductile transition temperature T_{bd} is the temperature at which the material goes from a brittle behavior to a ductile behavior. The brittle behavior is characterized by a break for a very small deformation, before reaching the plastic regime while a ductile behavior is characterized by a rupture after a very important deformation.

There are mainly two methods to determine the T_{bd} temperature:

- The first method consists of plotting the stress-strain curve $\sigma(t) = f(\epsilon)$ (tensile test) according to the test temperature. The T_{bd} corresponds to the temperature for which there is a transition from the fragile behavior to the ductile behavior.
- The second method is to perform a Charpy impact test. The resilience graphs of the samples are plotted as a function of the test temperature. The greater the resilience, the more ductile the material is, and the weaker it is, the more fragile it is.

Tensile test is a quasi-static test at a frequency of 10^{-3} Hz. The Charpy impact test is a dynamic test at a frequency of 10^3 Hz.

Figure 12 shows a schematic evolution of the resilience with the temperature and the brittle-ductile transition (a), and the determination of the T_{bd} temperature in tensile test (b).

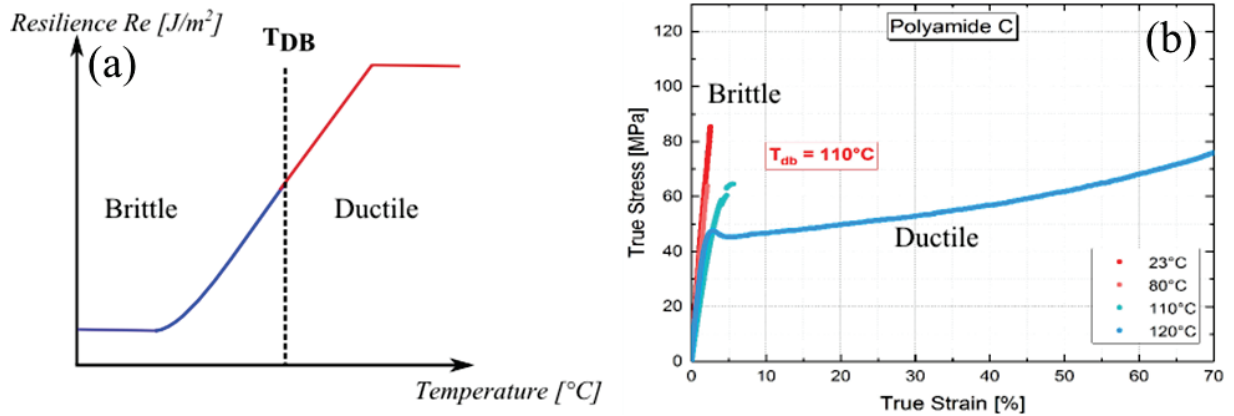


Figure 12 – Schematic evolution of the resilience with the temperature and the brittle-ductile transition (a), and the determination of the T_{bd} temperature in tensile test (b).

1.2.5 Law of elastic behavior

If we consider a small element of matter undergoing small deformations, its deformation law will be linear and reversible, regardless of the solicitation. Hooke's law can be generalized and expressed in tensor form, as expressed in Equation 14.

$$\bar{\sigma} = \frac{E}{1 + \nu} \left(\bar{\varepsilon} + \frac{\nu}{1 - 2\nu} Tr(\bar{\varepsilon}) \bar{I} \right) \quad (14)$$

With ν the Poisson's ratio.

This law can be applied in the case of an isotropic material. In the case of a uniaxial tensile test, Hooke's law applies (see Equation 1). Equation 14 explicitly accounts for local contractions of material subjected to uniaxial deformation.

The Poisson's ratio ν can be defined as the ratio between the transverse strain ε_z and the longitudinal strain ε_x in the elastic loading direction (Figure 13) [70] as expressed in Equation 15:

$$\nu = \frac{-\varepsilon_y}{\varepsilon_x} = \frac{-\varepsilon_z}{\varepsilon_x} \quad (15)$$

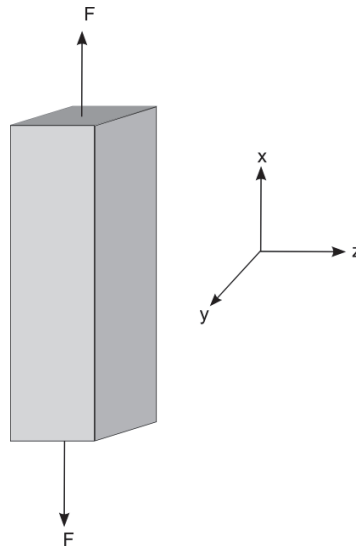


Figure 13 – Schematic representation of a sample during tensile test.

For isotropic materials, ν is comprised in the range $-1 \leq \nu \leq 0.5$. For polymers, the Poisson's ratio is generally comprised in the range $0.25 \leq \nu \leq 0.35$. For most polymer materials, Poisson's ratio increases with time and tends to 0.5. When ν is equal to 0.5, the material becomes non-compressible: there is volume conservation. This can be viewed as a shift from elasticity (with a volume change) to viscoelastic or viscoplastic flow (with a volume conservation) as time passes [71].

Generally, Poisson's ratio is determined in the linear elastic regime. It can be extended into the nonlinear regime to describe elastomers or ductile polymers. For time dependent materials (viscoelastic material), the Poisson's ratio is apparently variable.

The viscoelastic Poisson's ratio can be experimentally evaluated by a direct measurement, which involves the measurement of the transverse and axial deformations of the tested specimen. An accurate measurement of the transverse strain is of crucial importance and various techniques have been employed, such as optical methods (video extensometer [72]).

1.3 Molecular relaxations

There are two types of molecular relaxations: the main relaxation (α) and the secondary relaxations (β , γ , δ ...). The main relaxation process is associated to the glass transition T_g (the temperature of the α -relaxation, T_{α} , measured at 1 Hz is considered equivalent to the T_g of the polymer). At the glass transition,

the polymer changes from a glassy state to a rubbery state. This relaxation process corresponds to segmental movements, involving several monomers.

Secondary relaxations (β , γ , δ ... from the higher to the lowest temperatures) are associated to local motions of molecular groups. These relaxations have an influence on the mechanical properties, more specifically the β -relaxation [73], [74].

Each molecular relaxation is characterized by its characteristic relaxation time. It corresponds to the time describing the motions of molecular segments involved in the relaxation [75]. All the relaxation times depend on the temperature, and a time/temperature relaxation map ($\log \tau = f(1/T)$) can be established (see Figure 15).

In the case of secondary γ and β relaxations, the relaxation times can be described by an Arrhenius law [76], defined in Equation 16:

$$\tau(T) = \tau_0 \exp \frac{E_A}{RT} \quad (16)$$

where E_A is the activation energy, τ_0 is the relaxation time at infinite temperature, R is the ideal gas constant ($R=8.314 \text{ J/mol.K}$) and T is the temperature.

The main relaxation α does not follow an Arrhenius law. The α -relaxation follows the Williams-Landel-Ferry (WLF) equation defined as follow [77]:

$$\log(a_T) = \frac{-C_1(T - T_{ref})}{C_2(T - T_{ref})} \quad (17)$$

where C_1 and C_2 are the WLF constants, and T_{ref} is the arbitrary chosen reference temperature.

All the molecular relaxations described above can be measured by both DMTA (Dynamic Mechanical Thermal Analysis) and BDS (Broadband Dielectric Spectroscopy).

In semi-aromatic and aliphatic polyamides, three relaxations processes have been identified [78]–[81] by DMTA and by BDS [82], [83], as schematized in Figure 14.

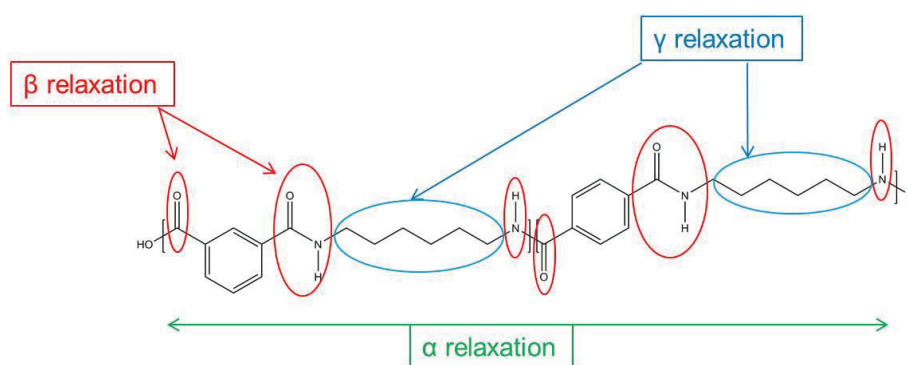


Figure 14 – Structure of the copolymer PA6I/6T and the associated relaxations α , β and γ .

At the lowest temperature, the γ -relaxation is generally assigned to local motions of short methylene sequences $-(CH_2)_n-$ internal to the monomer for aliphatic polyamides [78], [84]. The β -relaxation is associated to the rotation of amide groups $(-NHCO-)$ along the polyamide chain. The α -relaxation corresponds to large scale movements (several monomers) and is associated with the glass transition at 1 Hz. This main relaxation is observed at high temperature and is close to the glass transition temperature measured by DSC. This relaxation depends on the length of the methylene backbone, the orientation in space of the polymer chains, the presence of rigid chemical functions such as aromatic rings, and the strength of possible interactions between chains.

In Figure 15, the relaxation map for PA6,6 and PA6,6 formulations obtained by additivation or chemical modification of the polyamide chains is shown.

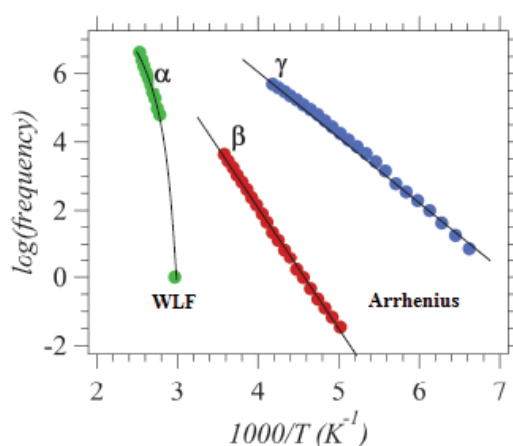


Figure 15 – Molecular relaxation map for PA6,6. From left to right: α -relaxation, fitted by a WLF law; β and γ relaxations following an Arrhenius law. Adapted from [75], [85].

1.4 Deformation mechanisms of semi-crystalline and amorphous polymers

1.4.1 Deformation of the interlamellar amorphous phase

Beyond the glass transition temperature T_g of the polymer, the amorphous phase becomes rubbery. Based on the work of Bowden and Young [86], the elastic and viscoelastic behaviors are associated with the deformation of the interlamellar amorphous phase. Bowden and Young characterized the crystalline structure by X-ray scattering at large and small angles (WAXS, SAXS). These experiments show the different mechanisms of deformation of the amorphous phase (see Figure 16).

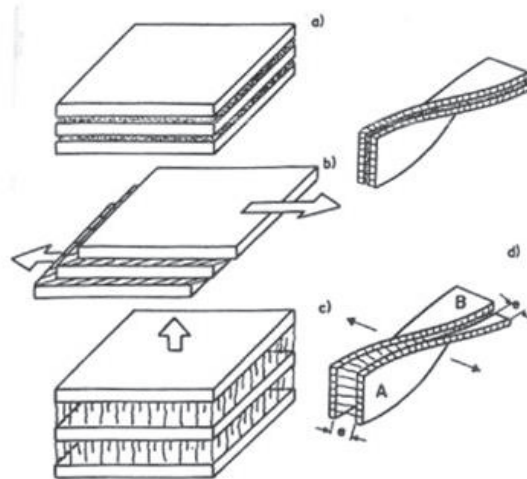


Figure 16 – Interlamellar deformation mechanisms: (a) Normal state, (b) Interlamellar shear, (c) Interlamellar separation and (d) Case of lamellae twisted: interlamellar separation in A and interlamellar shear in B. From [87].

The deformation of the amorphous phase mainly involves two types of deformation [86], [87]: interlamellar shear and interlamellar separation.

Interlamellar shear is characterized by a movement of the crystalline lamellae, which causes shearing of the amorphous phase (Figure 16-b). The reversibility of this shear is related to the presence of macromolecules bridging the crystalline phases which are put under tension during the shearing and which will relax during unloading of the material.

Interlamellar separation results from a variation of the distance between two lamellae when a stress is applied perpendicularly to these lamellae [87], [88] (Figure 16-c). This variation of local volume

(decrease of the density of the amorphous phase) can lead to the cavitation of the material as well as to the creation of microcavities [37], [40], [89].

These two mechanisms only cause the deformation of the interlamellar amorphous phase. Both mechanisms can coexist within the same lamella [87] if the lamellae are twisted (Figure 16-d).

1.4.2 Deformation of the crystalline phase

Plastic behavior involves the deformation of the crystalline phase through two types of deformation: crystalline slips and cavitation.

1.4.2.1 Crystalline slips

When the stresses become large and exceed the threshold stress of plastic flow, irreversible deformations take place. Bowden and Young did some work to attribute the plastic flow to the crystalline phase [86]. In their work, they explain the phenomenon of plasticity by shearing and fragmentation mechanisms of lamellae. There are two slip directions: in the direction of the chains (chain slip) and perpendicular to the chains (transverse slip) (see Figure 17).

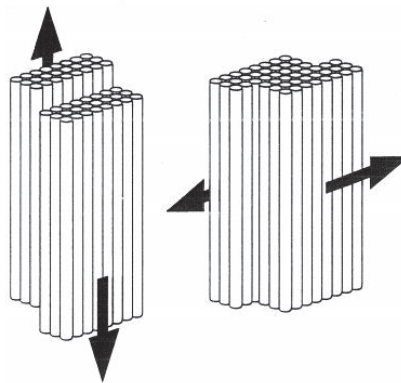


Figure 17 – Chain slip and transverse slip. From [87].

1.4.2.2 Cavitation

At the submicron scale, there are few studies on the characterization of damage in semi-crystalline polymers.

Cavitation is one of the micro-mechanisms of plastic deformation of semi-crystalline polymers during tensile loading such as polyethylene [21], [90], polypropylene [90] or PVDF [91], [92]. This phenomenon is also considered as a damaging process because it affects the plastic yield and the failure of the material [93].

The work done by Kuksenko and Tamusz [94] deals with characterizations of semi-crystalline polymers by X-ray experiments at small angles (SAXS). When the polymer is deformed, there is formation of microvoids, whose size remains constant and their number increases with the deformation. The final rupture is due to a critical density of microvoids. In the case of non-oriented polymers, the size of the cavities is of the order of a few hundred nanometers.

Castagnet et al [91] characterized the polyvinylidene fluoride (PVDF) by several methods: mechanical tests, volumetric measurements, analyzes by X-ray diffraction and diffusion. These methods allowed seeing the formation of cavities between the crystalline lamellae under deformation at the equator of the spherulites. Pawlak and Galeski [93] have compared the influence of crystalline shear and cavitation in the amorphous phase on the rupture of semi-crystalline polymers. The cavitation appears in polymers whose crystals have a high plastic resistance while those whose crystals have a low plastic resistance are deformed by crystalline shears.

The diameter of the cavities is about 4-5 nm, measured by X-ray scattering, which is close to the interlamellar distance [93]. Electron microscopic observations have allowed Galeski to locate these cavities within the interlamellar and interspherulitic amorphous phase (see Figure 18) [95].

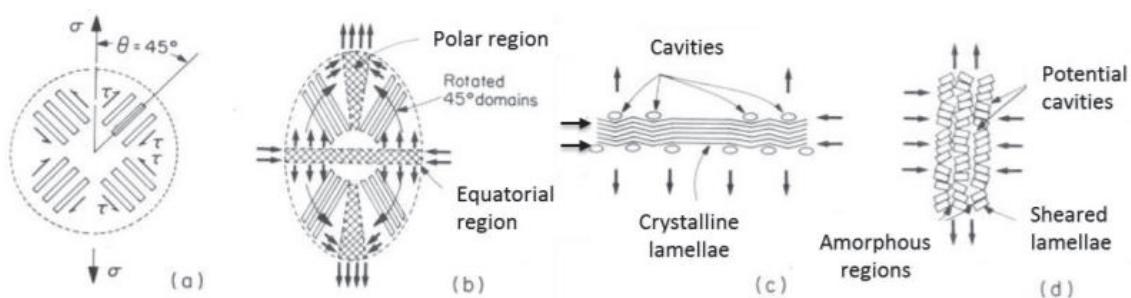


Figure 18 – Steps of cavities formation into equatorial regions of spherulites [95]: (a) Normal state; (b) Rotations due to simple shear; (c) Kink of underformed lamellae in equatorial regions; (d) Instabilities due to chain slip for lamellae in polar regions.

Cavitation occurs in three steps: nucleation, growth and coalescence. Cavitation can occur during crystallization of polymers. The negative pressure generated during crystallization leads to the cavitation nucleation. Below T_g , cavitation in PP or PE requires a negative pressure of the order of -5 to -20 MPa [96]. The nucleation of cavities can also appear when there is a chain splitting through the amorphous phase [97]. When a sample is subjected to a tensile test, cavitation begins in the amorphous phase, between the crystalline lamellae perpendicular to the stress axis [50].

1.4.3 Micro-mechanisms of deformation in glassy polymers

If the polymer is stressed below its glass transition, the plasticity is often localized, the rest of the material having an elastic or viscoelastic behavior. There are mainly two micro-mechanisms of deformation: shear bands or crazes [35].

1.4.3.1 Shear bands

The formation of localized deformations zones such as shear bands is often observed in metals and semi-crystalline polymers, but also in some amorphous polymers such as Polycarbonate or PVC [35], [98]. Shear bands appears at an angle of 45° to the maximum shear stress direction, which results in a high degree of chain orientation. Indeed, the polymer within the shear band is more highly oriented than in the adjacent regions [99]. They are based on a slip phenomenon. No void is created in the material by the formation of shear bands, unlike the cavities.

Shear bands can be observed by cross-polarized optical microscopy, in transmission[99], [100]. With no specimen or with an isotropic specimen, the field of view will be dark in cross-polarized optical microscopy. On the contrary, an anisotropic polymer will be birefringent. The birefringence is due to the orientation of optically anisotropic elements, such as the amorphous polymer chains, aligned during the tensile test for example or crystals aligned by deformation in the case of semi-crystalline polymer.

In amorphous polymers, shear bands can be observed as numerous localized micro-shear bands or as a larger diffuse shear deformation zone (see Figure 19) [98], [101]. According to Bowden and Young [86] and Quinson et al [102], the shear band morphology depends on the microstructural state of the polymer, and consequently on its thermomechanical history and chemical structure. The morphology depends also on the testing conditions (temperature, strain rate).

Shear bands are often observed under compressive experiment [102] (see Figure 19). Indeed, very few studies have been done under tensile deformation. In tensile deformation, the propagation of the shear

bands can lead to failure or necking. Shear bands can also coexist with crazes. Figure 20 shows the coexistence of crossed shear bands and crazes in PVC, observed by HVTEM. The initiation of localized deformations zones such as shear bands is not fully understood [38], [40], [103].

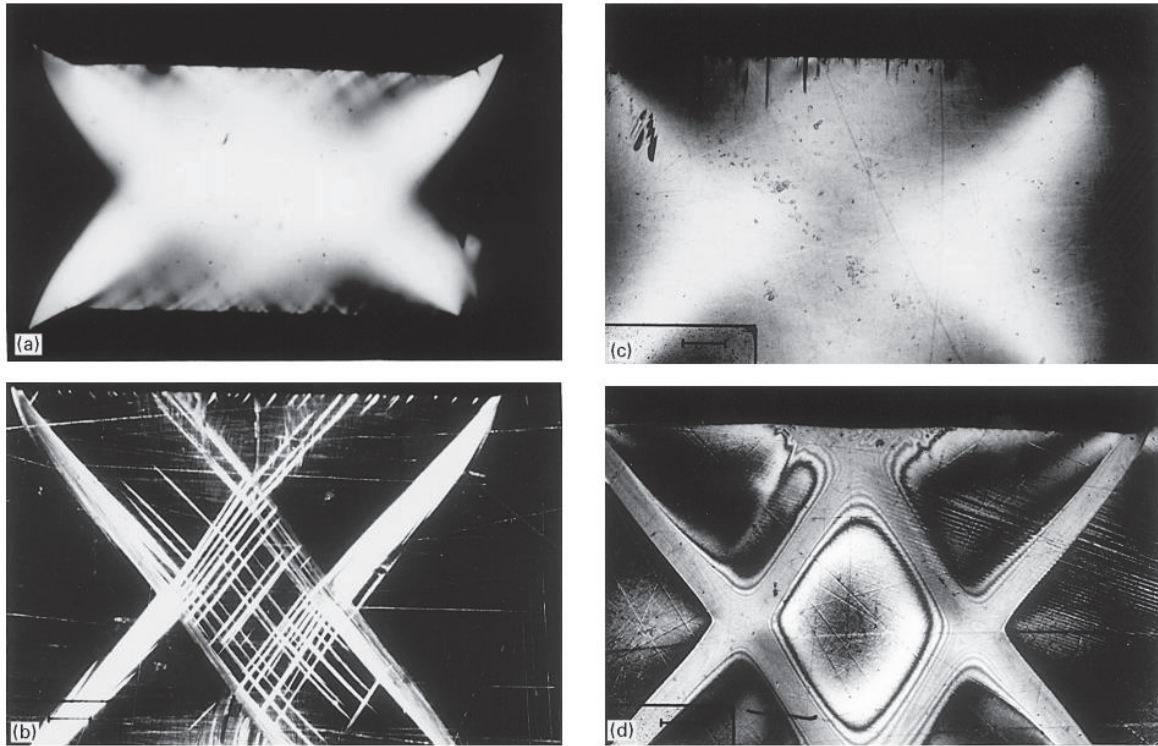


Figure 19 – Observations of shear bands in various amorphous polymers deformed under plane strain compression, by transmission optical microscopy between crossed polarizers: (a) PMMA deformed at 20°C (b) PS deformed at 20°C (c) PS deformed at 90°C and (d) PC slow cooled and deformed at 20°C. From [102].



Figure 20 – Coexistence of crossed shear bands and crazes in PVC, deformed semi-thin section, deformation direction horizontal, observed by HVTEM. From [35].

1.4.3.2 Crazes

Generalities

It can be found in literature some studies devoted to the analysis of the structure of the crazes in order to identify the physical micro-mechanisms involved [26], [37], [39], [50], [104], [105]. Most of the studies combine X-ray diffraction and microscopy techniques (SAXS, transmission electron microscopy TEM) in order to observe the evolution of the crazing phenomenon post-mortem [36], [37], [39], [42], [105]–[107].

Crazes appear perpendicular to the direction of the principal stress and are formed of two decohesion surfaces. These surfaces are interconnected by fibrils between which microvoids develop (Figure 24). There are two types of fibrils: i) primary fibrils crossing the craze from one surface to another and ii) secondary fibrils laterally connecting two microvoids [39]. Crazes are ellipsoidal heterogeneities with a diameter between 10 nm and 10 μm and a thickness ranging from 5 nm to 10 μm [32], [37], [104]. They contain between 30 and 50% by volume of fibrils having a diameter of the order of 10 nm. All these characteristics depend on the macromolecular network of the material (the nature of the entanglements) and the local stress at the level of crazing. Electron microscopy (scanning or transmission electron microscopy, SEM or TEM) permits the observation of craze architecture [26], [108].

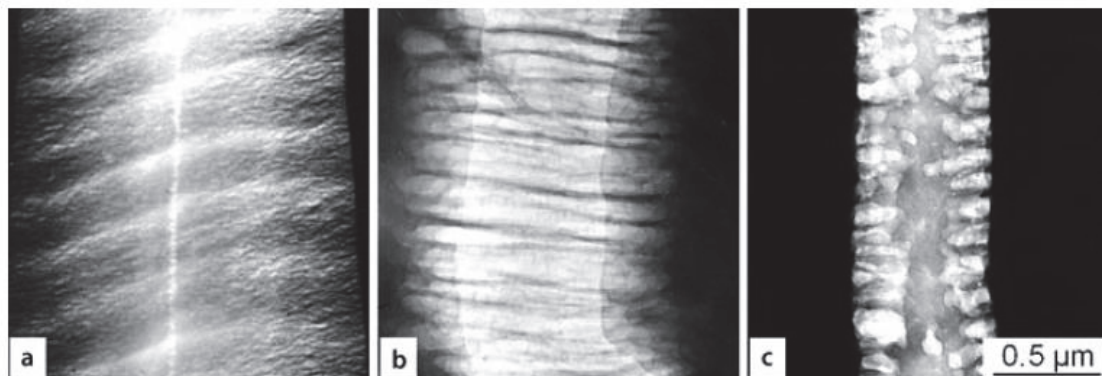


Figure 21 – Crazes with different inside structures, in PS. Observation of deformed thin sections of PS in HVTEM: (a) fine structure; (b) coarse fibrils; (c) microvoid concentration at the craze boundaries. From [35].

Figure 21 shows different interior crazes morphologies observed in PS. A fine or a coarse fibrillary structure can be observed, as well as homogeneous crazes [35].

The experiments performed in order to understand the craze microstructure in unreinforced polymers are based on direct observation of crazes that have been created on samples by Transmission Electron Microscopy (TEM). The process used for creation of crazes is to solvent cast the samples into thin films,

fixed on a copper grid and then crazed through the distortion of this grid. It permits the observation of microscopic and macroscopic crazes. However, the precision of the tools enables to watch distinctly the initiation of crazes only when those are bigger than 50 nm. Also, it must be noted that the thickness of the sample and the plastic constraint might have some impact on the observation of crazes and on the process of creation and evolution of these crazes. Indeed, as it is a voiding process, it is not clearly defined if the mechanisms will be identical for thin films and bulk samples. This is the reason why it is not possible to get quantitative data on volume fraction and size distributions when crazes are too small.

To detect and observe smaller crazes, another technique is generally used: the X-Ray scattering. This more sensitive technique enables to view crazes whose size is lower than 50 nm. The transmission of the X-ray scattering from the orthogonal craze walls and fibrils results in highly anisotropic patterns, which have the form of two elongated streaks approximately perpendicular to each other [45]–[47], [109], as shown in Figure 22.

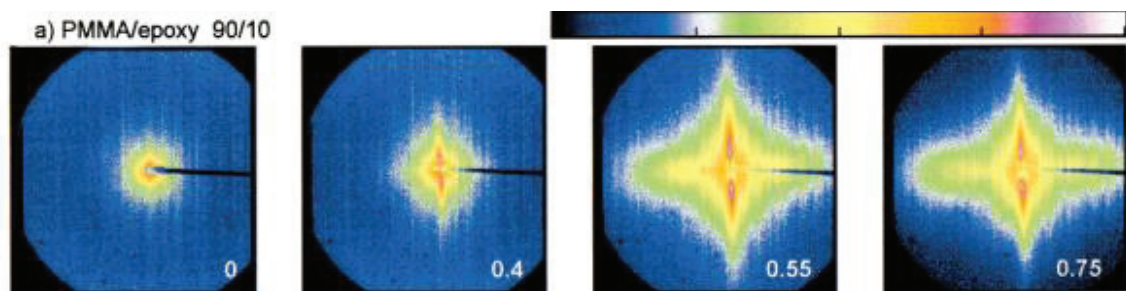


Figure 22 – Deformation SAXS patterns of PMMA/epoxy blend 90/10 measured at different clamp displacements (x , in mm), performed at the ESRF ID2-BL4. Tensile direction is vertical. From [110].

Figure 22 shows the deformation SAXS patterns for a PMMA/epoxy blend (90/10) at different clamp displacements. The patterns become highly anisotropic with deformation and have the form of two elongated streaks approximately perpendicular to each other.

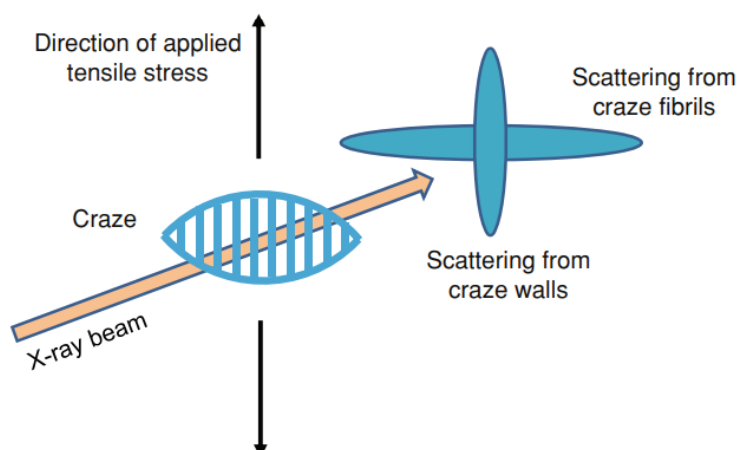


Figure 23 – Schematic representation of the structure of crazes and their SAXS patterns. From [111] and adapted from [46].

A schematic representation of the structure of crazes and their SAXS patterns is shown in Figure 23. Their SAXS patterns are anisotropic with deformation.

It is important to understand the structure of crazes, especially during their creation as it allows us to better represent the processes in the evolution of crazes in amorphous polymers and in the molecular deformation of the sample.

In literature, the circumstances and the exact point of the outbreak of the fibrillar and homogeneous crazes are still unclear. According to Donth and Michler [112], the initiation of crazes might be linked to the distance between entanglements and to the stress level applied on the object at a local scale. Kramer and Berger [39] suggest however that other aspects might act on the crazing process. According to their studies, the energy of bond dissociation along the polymer backbone, the density of chain entanglements and the van der Waals intermolecular separation energy could be the main players in the process of crazing. The importance of the density of the chain of entanglements in this process has been confirmed by different studies [113]–[115].

The crazing process takes place in three stages: i) initiation, ii) growth and iii) internal rupture.

Mechanisms of craze initiation

Crazes are cracks that remain bridged by fibrils of polymer and are perpendicular to stress [40], [86].

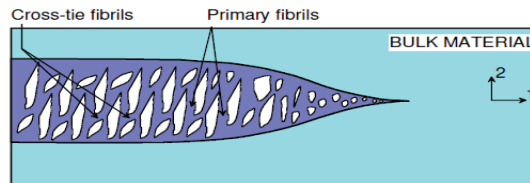


Figure 24 – Structure of a craze. From [39].

The formation of craze takes place in two steps according to Kramer and Berger [39]. First, microvoids appear under the action of a stress field. A strong plastic deformation located around these microvoids leads to a fibrillar structure (Figure 24). Crazes are connected to one another by fibrils between which microvoids develop (Figure 25).

According to Kausch [116], the heterogeneity of distribution of entanglements and their interactions is at the origin of cavitation. Defects are formed in areas of low entanglement density.

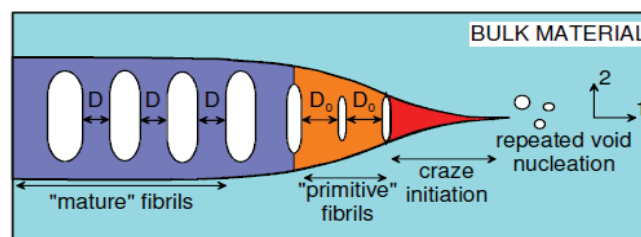


Figure 25 – Formation of a craze. From [39].

The stress concentration allowing the creation of a microcavity can take place on a heterogeneity, such as an impurity. This heterogeneity will generate a strong hydrostatic depression necessary for the formation and development of microcavities [117]. According to Friedrich [40], the creation of a microcavity may be due to the distortion generated by the intersection of two shear bands oriented perpendicular to one another.

Generally, the microcavity formation occurs at fairly high stresses, ranging from 0.4 to 0.5 times the yield stress [118].

Taylor [43] has described a hydrodynamic instability for a liquid film between two almost parallel hard sheets when they are pulled apart. This concept has been used for polymers by Argon and Salama [41], and is called ‘meniscus-instability model’ [37], [39], [42]. In this model, the plastic deformation is initiated by a local effect of stress concentration around the defect, as suggested by Monnerie et al [44]. Indeed, the local stress concentration generates a plastic deformation in a thin polymer layer which is surrounded by glassy polymer because this thin polymer layer has not reached its yield point yet. The model of meniscus-instability mentioned above induces the craze growth by coalescence of voids [37], [39], [44] and the behavior of the thin polymer layer under deformation can be assimilated to this model.

Recently, Michler [35] supposed that the initiation of a craze is preceded by the formation of a localized plastic deformation zone. As this plastic deformation zone develops, the hydrostatic stress increases until it becomes higher than a critical stress level. The cavitation can occur, leading to the local development of microvoids. According to Michler [35], this localized plastic deformation zone is related to the entanglement network. Figure 26 shows the so-called “pre-crazes” observed by Michler in PS by HVTEM in-situ tensile test.

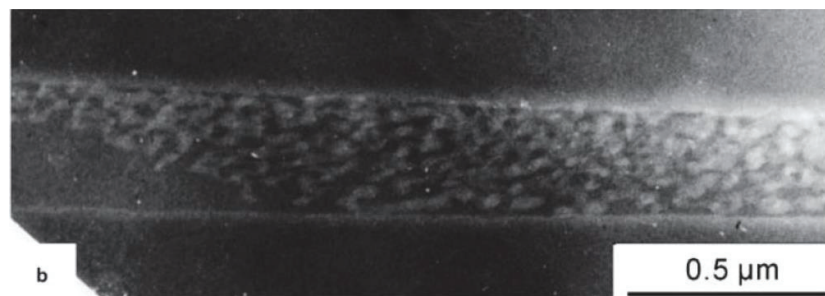


Figure 26 – Semi-thin section of deformed PS observed by HVTEM. Crazes and so-called “pre-crazes” are visible. From [35].

Mechanism of craze growth

The second step of the crazing process, the craze growth, is described in literature by a two-step process: the craze tip propagation (“meniscus-instability model”) and the craze opening, related to the chain entanglements [39], [42], [44]. Crazes growth occurs by fibril formation and elongation between microvoids. The lengthening of fibrils occurs by i) a creep process resulting in a decrease in the diameter of the fibrils and by ii) extraction of material from the polymer mass leading to a constant maintenance of the diameter of the fibrils ([37], [39]). Indeed, a local stretching process leads to the formation of a new

structure in an active area near the craze-solid material boundary. A disengagement of the chains then occurs in this active zone. The polymer at the junction point of the two plates behaves like a liquid forming "fingers" which gradually thin until they separate to form new fibrils ([37], [104]) (see Figure 27).

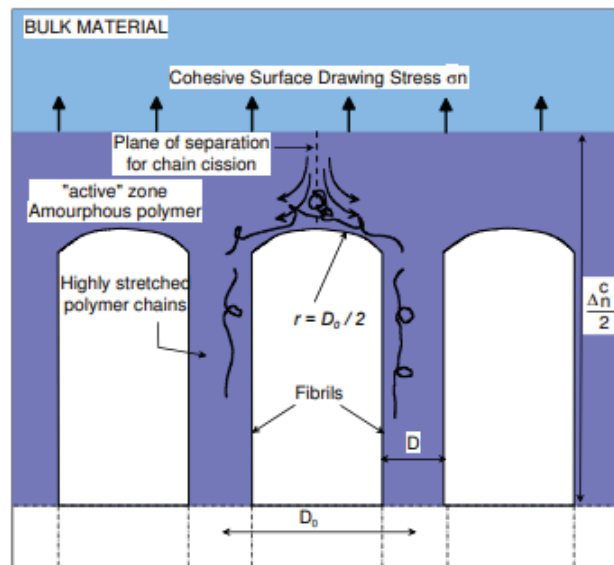


Figure 27 – Representation of craze growth. From [37], [106].

Craze breakdown

The ruin of a damaged polymer begins when the fibrils of the crazes start to break. There are two modes of failure of these fibrils depending on the loading rate, the temperature and the structure of the polymer ([39], [104]) (see Figure 28). The first mode leads to a breakdown of the fibrils in their environment which is favored at high temperatures because the molecular motions allow easy disentanglement of the chains. The second process is a random mode of failure along the fibrils, which usually occurs at low temperatures because the chains do not have enough degrees of freedom at short distances.

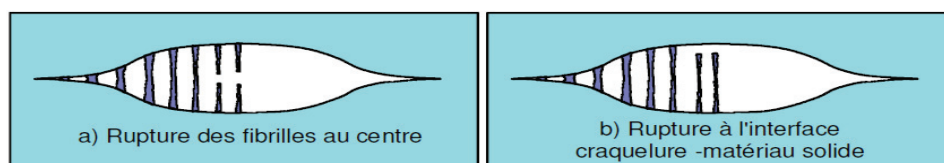


Figure 28 – Rupture of craze fibrils: (a) in the center and (b) at the interface (from [39], [119], [120]).

1.5 Objectives of the research

The aim of this study is to understand the mechanical properties and the micro-mechanisms of deformation of semi-crystalline and amorphous semi-aromatic polyamides.

Indeed, the mechanical properties of amorphous polymers such as PC, PVC, PS, PMMA are often described in literature. These polymers can be classified into two categories: ductile polymers and brittle polymers. PC can be classified as a ductile polymer because of its elongation at break and its high resilience at room temperature, whereas PS can be classified as a brittle material. Many current studies are dealing with ductility in amorphous polymers [121]. In semi-crystalline polymers, the ductility has been explained by the presence of second phase which constitute a “disorder” [122], allowing the stabilization of the damage growing [50]. However, the stabilization of the damage growing cannot be explained by this second phase in amorphous polymers. Ductility has also been observed in few amorphous polymers [23], [26]. Recently, Charvet et al [26] studied the microscopic mechanisms of damaging in plasticized cellulose acetate (CDA) under tensile deformation. The authors observed a heterogeneous nucleation of cavities in the vicinity of pre-existing impurities, whose growth is initially blocked by strain hardening. When the applied stress becomes sufficiently high, a fraction of these cavities grows faster until the failure of the sample, allowing the evolution of a second family of larger cavities to be observed. It has been shown that the strain hardening regime has an important role in the development of damages. Strain hardening has been observed in few amorphous polymers such as PC or PMMA [13], [24], which are ductile polymers. This regime appears to stabilize the deformation by avoiding the localization of damage.

The study of the mechanical and ultimate properties of a recent class of polyamides, polyphthalamides (PPA), from amorphous to semi-crystalline seems to be interesting regarding their ductility. We have investigated the impact resistance by Charpy impact test over a wide temperature range in order to determine the ductile-brittle transition temperature. Tensile and compression experiments were done under a wide range of temperature, and with a videometric monitoring, in order to characterize the strain hardening regime of each PPA.

The damage mechanisms were monitoring by microscopic observations and ultra-small angle X-ray scattering (USAXS).

Chapter 2 – Materials and Methods

In this chapter, the different polyphthalamides studied in this work will be presented. The experimental techniques used to characterize the mechanical properties of the PPA, as well as the thermal and structural characterization techniques will be presented. The techniques used to characterize the damages morphologies will be exposed.

2.1 Materials

As explained in the previous part, polyphthalamides (PPA) are polyamides containing aromatic rings in their backbones, giving them high mechanical strength and thermal resistance. They are formed by the reaction of aromatic acids with aliphatic diamines. The resulting PPA may be amorphous or semi-crystalline depending on the combination of monomers used [1]. Semi-crystalline PPA are mainly based on PA6T, obtained through condensation of hexamethylenediamine (HMDA) and terephthalic acid. When more than 55% of the acid part of the PPA is composed of isophthalic acid, the resulting copolymer is amorphous [54].

In order to evaluate the influence of the crystallinity ratio, amorphous and semi-crystalline PPA of equivalent chemical structure were needed. Random copolymers of PA6I and PA6T satisfy this criterion. Isophthalic and terephthalic acid monomers differ only by the position of their substituents on the aromatic rings: for the isophthalic acid, the substituent is a *meta* directing group whereas for the terephthalic acid, the substituent is a *para* directing group (for the chemical structure please refer to Figure 29). The stereochemical configuration of the carboxyl functions in the isophthalic acid monomer bends the polyamide chains, preventing them from aligning and crystallizing [123]. It is the contrary for the terephthalic acid monomer: the linear configuration of its carboxyl functions does not prevent aligning and crystallization.

Four semi-aromatic polyamides were considered. Figure 29 shows the structure of the copolymer PA6I/6T. Polymers are formed by copolymerization of the PA6T and PA6I in different proportions. Monomers are obtained by the condensation reaction of hexamethylenediamine (HMDA) with a diacid: isophthalic (terephthalic) acid for the PA6I (PA6T) monomer. Each PPA corresponds to a different fraction in PA6I or PA6T, indicated in Table 4.

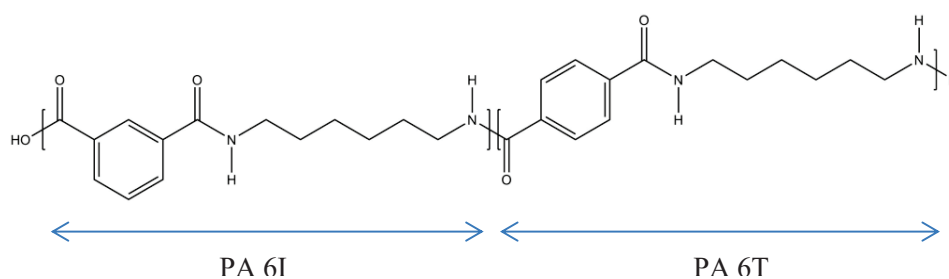


Figure 29 – Structure of the copolymer PA6I/6T.

The characteristics of these polymers can be found in Table 4. The number-average molecular weight M_n is around 10000 g/mol for polyamide A, B and D, and around 6000 g/mol for polyamide C whereas the weight-average molecular weight M_w is around 30000 g/mol for polyamide A, B and C, and around 40000 g/mol for polyamide D. M_n and M_w were used to calculate the polydispersity index I_p as $I_p = M_w/M_n$. Secondary reactions may take place during the polyamide synthesis, leading to a small fraction of branched chains.

Table 4 – List of studied semi-aromatic polyamides and corresponding molecular weight distribution (number-average M_n and weight-average M_w , polydispersity index $I_p = M_w/M_n$ in PMMA equivalent after relative calibration) determined by Size Exclusion Chromatography (SEC), glass transition T_g , melting temperatures T_m and crystallinity rate determined by Differential Scanning Calorimetry (DSC) (see 2.3.1). All the samples were dried as molded (d.a.m.).

		M_n (g/mol) ($\pm 5\%$)	M_w (g/mol) ($\pm 2.5\%$)	$I_p =$ M_w/M_n	Crystallinity (%) (d.a.m.)	T_g ($^{\circ}\text{C}$)	T_m ($^{\circ}\text{C}$)
Polyamide A	PA6I/6T 70/30	9356	27963	3.0	0	129	/
Polyamide B	PA6I/6T 50/50	10424	32917	3.2	4.3	129	265
Polyamide C	PA6I/6T 30/70	6450	32779	5.1	16.4	132	319
Polyamide D	PA6I/6T 70/30	11576 ($\pm 10\%$)	38337 ($\pm 5\%$)	3.3	0	127	/

The presence of branched chains may explain the variations in the polydispersity index from 3.0 to 5.1 [124]. As observed in Table 4, the values of polydispersity are larger than 2, which is the value expected by Flory's theory for linear polycondensation [124], [125].

The glass transition temperature T_g is similar and about 130°C. Polyamide A is amorphous, whereas polyamide B and C are both semi-crystalline, with a degree of crystallinity of 4.3 and 16.4, respectively. T_g increases with increasing molecular weight.

At large deformations, the PPA studied have a very ductile behavior. Beyond the brittle-ductile transition temperature T_{bd} , the failure takes place at a deformation larger than the deformation accessible within the testing machine, which is a limitation for the study of strain hardening and damage mechanisms. In order to compare the ductile amorphous and low semi-crystalline PPA which do not break with amorphous, ductile polymers and whose failure is reachable, a polycarbonate (PC) and a poly(methyl methacrylate) (PMMA) have also been studied. A polycarbonate Makrolon GP clear 099 (Bayer), and a PMMA plexiglas GS2458 were studied. The studied polymers are in the form of plate (dimensions $500 \times 500 \times 5 \text{ mm}^3$ for PC and dimensions $200 \times 300 \times 5 \text{ mm}^3$ for PMMA). 0.5 mm were removed on each side of the plate thickness, in order to remove a possible skin-core effect. Moreover, the specimens (tensile bars) with dimensions $92 \times 14 \times 4 \text{ mm}^3$ were cut in the plates, avoiding the edges of the plate.

2.2 Injection molding process

Two injection modes were defined. First, the process A: polymers were injection-molded into tensile and impact strength specimens with a Billion select 100T injection press. The principle of injection-molding is illustrated in Figure 30. The principle of the injection-molding process is the following: pellets of polymer are introduced in a hopper. A quantity of polymer gets into the screw, where the polymer melts and goes into the mold. With a counter-pressure applied, the polymer is maintained in the mold for a couple of seconds. The difference of temperature between the polymer melt and the mold allows the polymer to cool by taking the shape of the desired part. Some parameters have to be optimized to get suitable specimens for testing: the screw temperature, the dosing amount of polymer, the counter-pressure applied by the motor, the mold temperature and the piece retention time for example.

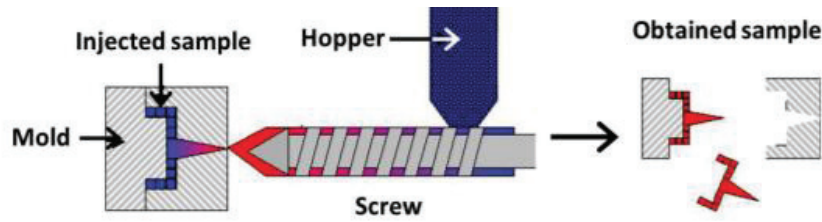


Figure 30 – Schematic representation of an injection-molding machine. From [75].

Prior to molding, water content has been controlled by Karl Fischer in order to avoid hydrolysis or post-condensation reaction. Higher water content leads to hydrolysis and the molecular weight decreases. If the moisture content is lower than that of the chemical equilibrium, a post-condensation reaction with water formation and an increase of the molecular weight of the resulting polyamide may occur. Pellets were dried 24 hours at 110°C under vacuum before processing. Mold temperature was kept at 30°C. After molding, the samples were stored in sealed bags to maintain them dry. Tensile and impact strength specimens dimensions were $150 \times 10 \times 4 \text{ mm}^3$ and $80 \times 10 \times 4 \text{ mm}^3$ respectively (ISO-527 and ISO-157 norms). The process A concerns only polyamide A, polyamide B and polyamide C.

The processing conditions are presented in Table 5.

Table 5 – Injection conditions for ISO-527 (Tensile) and ISO-157 (Choc) geometries (process A).

	Temperatures (°C)				Molding cycle time (s)	
	Screw		Mold		Choc specimens	Tensile specimens
	Choc specimens	Tensile specimens	Choc specimens	Tensile specimens		
Polyamide A	280	280	51	52	36.43	45.26
Polyamide B	290	290	52	50	41.32	47.24
Polyamide C	330	330	70	56	33.36	33.18

Second, the process B: plates with dimensions of $350 \times 100 \times 4 \text{ mm}^3$ were injected with a Billion 320T injection press. For the plate specimens, the mold included a v-shaped runner with a ramp. The flow in front of the polymer melt is uniform across the width of the plate. Based on observations on glass fibers reinforced semi-crystalline polymers, we assume that the injection molding process into plates leads to a homogeneous orientation of polymer chains in the thickness of the plates [126]. The mold temperature is kept at 130°C for the semi-crystalline polymer (polyamide C), in order to avoid the skin-core effect.

Tensile bars with dimensions $92 \times 14 \times 4 \text{ mm}^3$ and with a radius of curvature larger than ISO-527 tensile specimens were cut in the plates at different angles θ with respect to the main flow direction. This angle θ varies from 0° to 90° . The specimen's geometry is designed specifically in order to study the strain hardening behavior of our polymers. Polyamide C and polyamide D were injection-molded through this process and the injection conditions are presented in Table 6.

Table 6 – Injection conditions for the new tensile bar geometry (process B).

	Temperatures ($^\circ\text{C}$)		Molding cycle time (s)
	Screw	Mold	
Polyamide C	330	130	60
Polyamide D	260	80	54

The geometries of the tensile specimens obtained by both process A and process B are presented in Figure 31.

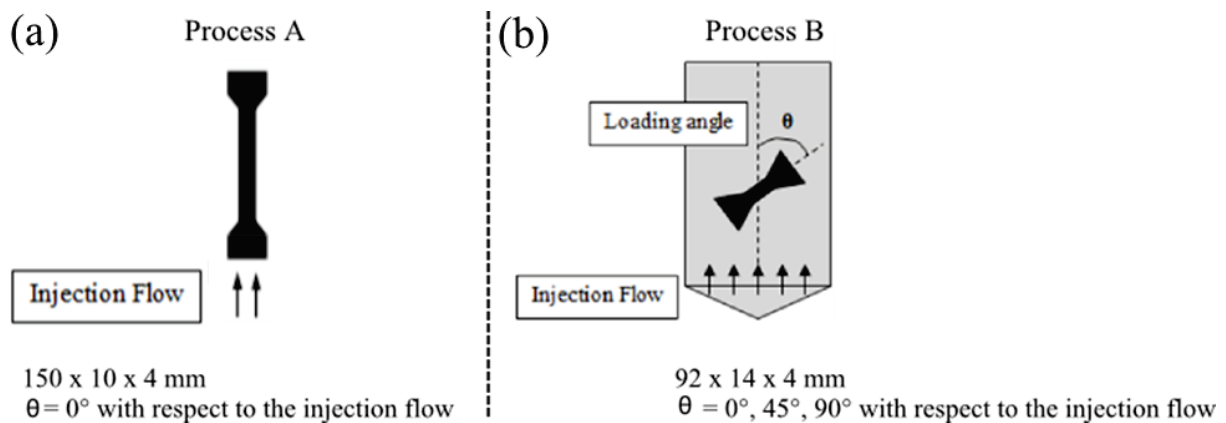


Figure 31 – Tensile geometries obtain by process A (a) and process B (b).

2.2.1. Skin-core effect

The injection process has an influence on mechanical properties of polymers, in particular on the skin-core effect due to flow during injection [121], [127]–[129]. This effect is often visible in the case of semi-crystalline polymers [129]. This effect is present in the industrial process, due to a temperature gradient between the mold and the polymer melt (at higher temperature) during the injection process. A skin-core effect was observed for polyamide C by cross-polarized optical microscopy (Figure 32-c-d). Indeed, a birefringent character was observed between the skin and the core of the polymer. Samples of polyamide

C were injection-molded with different mold temperatures (30, 60, 80 and 100°C). The storage modulus E' determined by DMTA at 1 Hz shows no difference regardless of the mold temperature ($E' = 3.1$ GPa at 25°C for the four mold temperatures). The temperature of the mold during the injection has no impact on the modulus E' . The degree of crystallinity remains low and is homogeneous over the thickness for the two semi-crystalline PPA (polyamide B and polyamide C) and was verified by DSC experiments. The skin-core effect observed for polyamide C is only related to shearing during the injection process and not to a difference in crystallinity within the material. The choice of setting the mold temperature at 30°C corresponds to an internal injection process and has no impact on our results. Amorphous and low-semi-crystalline PPA, polyamide A and polyamide B were also observed by cross-polarized optical microscopy. Figure 32 shows the skin-core effect observed on polyamide C by optical microscopy and the absence of this effect on polyamide A and B.

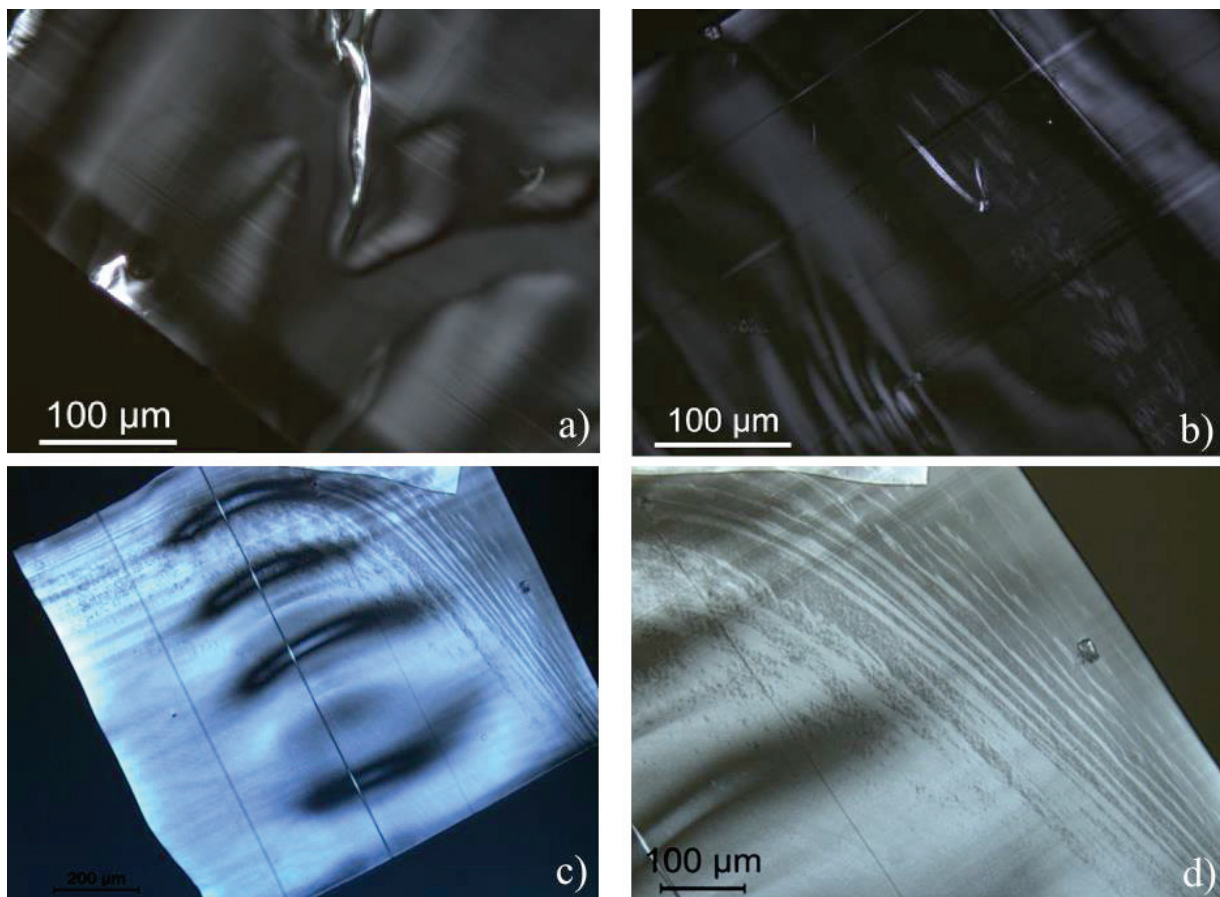


Figure 32 – Optical microscopy observations. No skin-core structure was observed for polyamide A (a) and polyamide B (b). Skin-core effect observed on polyamide C (c-d).

Nano-indentation analyses were performed on polyamide C in order to confirm the observations done by optical microscopy. A CPX-UNHT nanoindenter (Anton Paar) was used. The UNHT (Ultra nanoindentation Tester) module was equipped with a Berkovich diamond indenter tip and measurements were performed at 23°C and 50% RH (Solvay Research & Innovation Brussels, K. Didouche, N. Deligne). Measurements were performed on two sections of the sample: on the width and on the thickness of the sample (see Figure 33).



Figure 33 – Representation of the two sections analyzed by nano-indentation. 1) Measurements made on the width of the sample, 2) measurements made on the thickness of the sample.

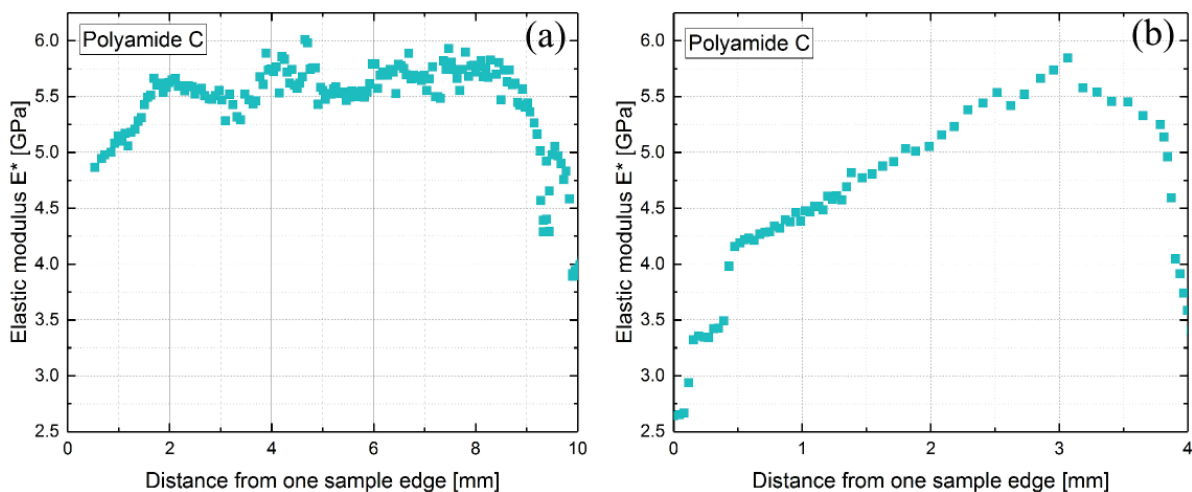


Figure 34 – Elastic modulus E^* obtained by nano-indentation measurements on section 1 (a) and section 2 (b) of polyamide C processed by process A.

The evolution of the elastic modulus E^* as a function of the position of the indenter with respect to its initial position is shown in Figure 34. The indentation modulus appears higher in the core than in the skin of the sample by a factor 2 for the two sections, as represented in Figure 34. This difference in modulus may be induced by a temperature gradient between the mold (at 30°C) and the polymer melt (at 320°C) during the injection process. Cooling is faster in a cold mold. Several studies have shown a dependence of

the skin thickness with the temperature of the mold [130]–[132]. The higher the temperature of the mold, the smaller the skin thickness.

The samples of polyamide C obtained with process B have a skin-core effect considered as negligible.

2.3 Experimental techniques

2.3.1 Thermal and structural characterizations

2.3.1.1 Differential scanning calorimetry (DSC)

The Differential Scanning Calorimetry (DSC) was used to determine the characteristic temperatures (glass transition, melting and crystallization temperatures) as well as the degree of crystallinity of the studied polymers. The principle of the calorimetry consists in applying a temperature ramp on two pans. One of the pans contains the polymer, whereas the second is empty and is considered as reference. The two pans are heated to the same temperature. The difference of energy provided to keep the reference pan and the pan with the sample at the same temperature is recorded. From this difference of energy, different temperatures can be determined (glass transition, melting, crystallization) and also the degree of crystallinity.

Data were acquired on a TA Instruments Q2000 calorimeter in the standard mode. For each measurement, non-hermetic aluminum pans were filled with 5-10 mg of polymer sample. Thermal measurements were performed at a heating/cooling rate of 10°C/min. A Rapid Cooling System (RCS) with a nitrogen gas flow of 50 mL/min was used. Samples were heated from 40 to 350°C, then cooled down to 40°C and finally heated again to 350°C. Glass transition, melting and crystallization temperatures were measured from the second heating cycle, the first one annealing the thermal history of the material. The glass transition temperature was determined at the onset. Two measurements were performed for each polymer to check the repeatability of the measurements. From the thermograms obtained, it is possible to calculate the crystalline fraction of the sample using the following formula:

$$\chi_c = \frac{\Delta H_f^{measured}}{\Delta H_f^{100\%}} \quad (18)$$

where $\Delta H_f^{100\%}$ is the enthalpy of melting of a 100% crystalline polymer. It can be found in literature for PA6,6 (188 J/g [6]) and PA6,10 (207 J/g [6]), but not for the crystalline PA6T part of polyamide C. As a

consequence, an average value of 200 ± 20 J/g is used [85]. To provide a better estimation of the crystalline fraction, $\Delta H_f^{100\%}$ value for the PA6T was determined by WAXS (Wide-Angle X-ray Scattering) experiments (see paragraph 2.3.1.2 below). The enthalpy of melting of a 100% crystalline PA6T is 196 J/g.

Figure 35 shows an example of two thermograms of an amorphous (a) and a semi-crystalline (b) PPA.

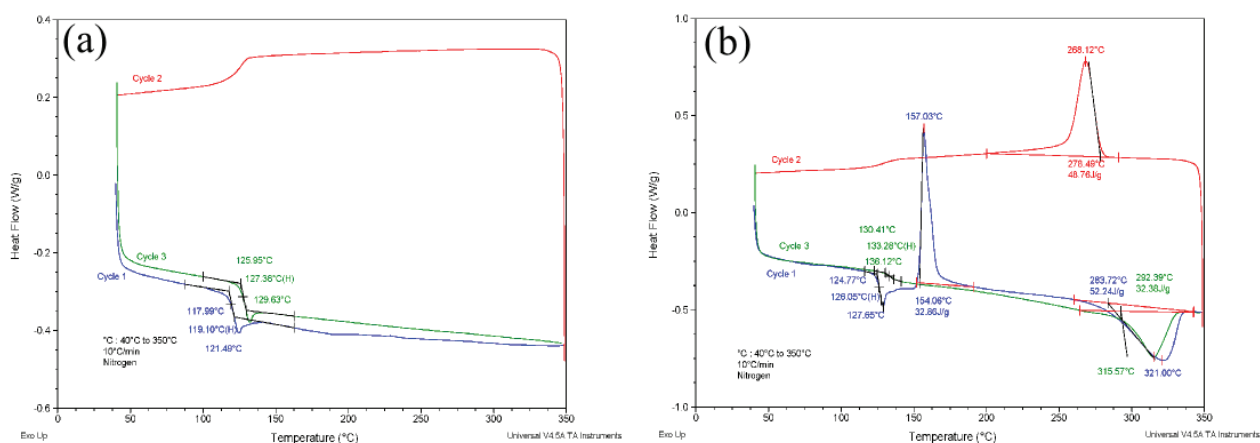


Figure 35 – Thermograms of an amorphous (a) and a semi-crystalline (b) PPA.

For the amorphous PPA, no melting or crystallization peak was observed. Only the glass transition temperature was observed around 127°C (Figure 35-a). This thermogram confirms that this PPA is amorphous. For the semi-crystalline PPA, a melting and a crystallization peak was observed, as well as a glass transition temperature (Figure 35-b).

2.3.1.2 Wide Angle X-Ray Scattering (WAXS)

X-ray scattering may be classified into Small Angle X-Ray Scattering (SAXS) and Wide Angle X-ray Scattering (WAXS), depending on the scattering angle. The distance from the sample to the detector is shorter in WAXS and the scattering reflects a larger structure. WAXS is a technique used for studying the crystalline structure of polymers and is a non-destructive method. It allows to identify the structural and crystalline phase, as well as to measure the crystalline index. The diffraction spectrum is analyzed according to the Bragg's law, which makes possible to obtain the spectra of the crystal lattice:

$$n\lambda = 2d\sin\theta \quad (19)$$

where n is an integer, λ is the wavelength of the incident X-ray beam, d is the distance between planes in the polymer structure and θ is the angle between the incident and the reflected X-ray beam with respect to the plane. The angle is equal to 2θ .

According to Bragg's formula (Equation 19), when the scattering angle 2θ decreases, the distance d between planes in the polymer structure (see Figure 36) increases. A representation of X-ray diffracting from crystal planes is shown in Figure 36. X-rays are generated by the impact of a high-energy electron beam on a metal target. The beam is sent to the sample at a fixed wavelength λ and is scattered. A detector is placed behind the sample and collects the scattered intensity as a function of the scattering angle 2θ .

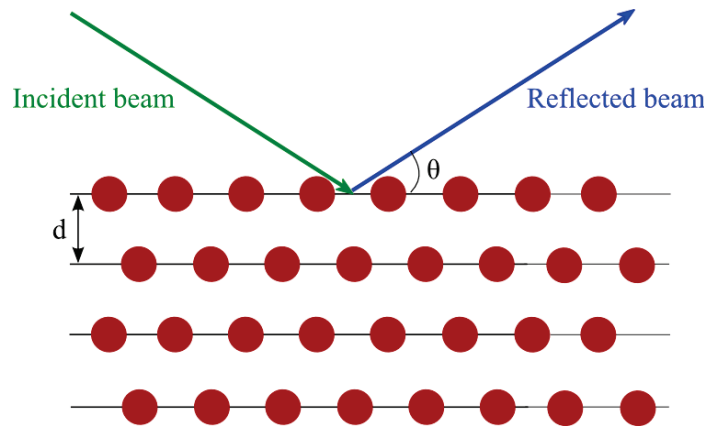


Figure 36 – Schematic representation of X-ray diffracting from crystal planes.

The scattering vector q can be expressed as:

$$q = \frac{4\pi \sin\theta}{\lambda} \quad (20)$$

where θ is the angle between the scattered beam and the incident beam, and λ the wavelength.

After an integration of the 2D pattern obtained over all the azimuth angles (if the sample is isotropic), the intensity as a function of the scattering angle 2θ is obtained. In the case of a semi-crystalline polyamide, the diffractogram obtained consists of the superposition of the amorphous halo with the crystalline peaks, as represented in Figure 37. Figure 37 represents the diffractograms obtained for polyamide A (amorphous) and polyamide B (semi-crystalline). The amorphous peak of polyamide A is located around $2\theta = 21.3^\circ$, which is in agreement with literature [133]. The semi-crystalline polyamide crystallizes in the

α form which has a triclinic unit cell (see Figure 38). The peak position is associated to different crystallographic planes [85]:

- First, around 6° the (001) plane perpendicular to the chain axis;
- Then, around 20° the (100) plane along the molecular chains and cutting through H-bonded sheets;
- Around 23° , a superposition of the (010) plane parallel to H-bonded sheets and the (110) diagonal plane.

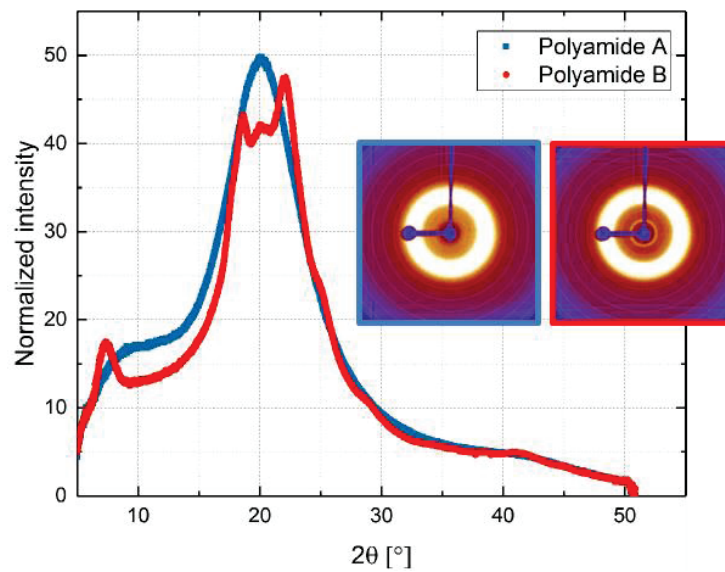


Figure 37 – WAXS patterns of polyamide A (blue) and polyamide B (red).

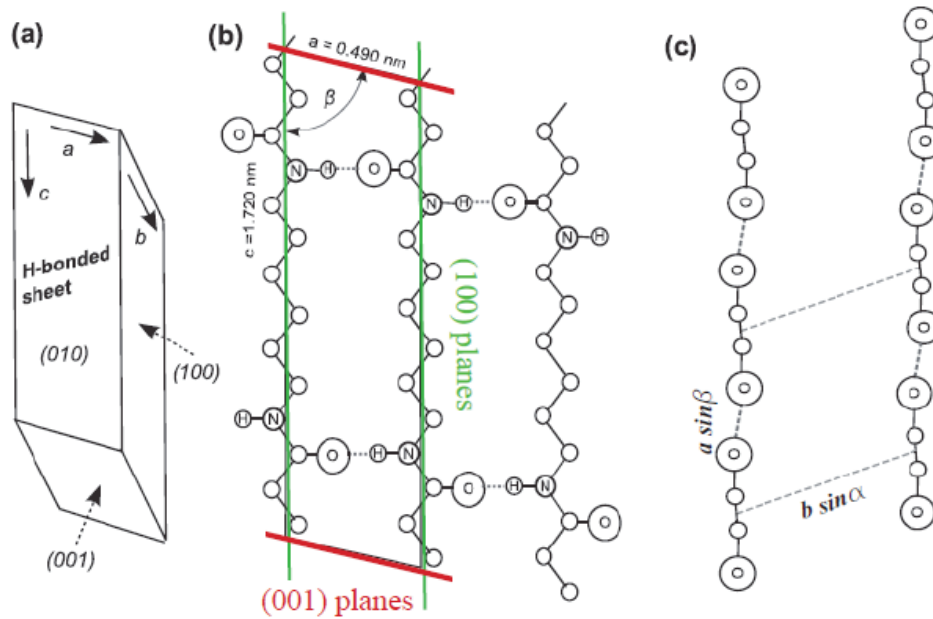


Figure 38 – Schematic representation of an α crystalline lattice in PA6,6 (a) triclinic unit cell with base vectors (chain axis is along \vec{c}), (b) chain arrangement in the a - c plane where H-bonds are formed (H-bonds are depicted by dashed line segments) and (c) chain arrangement in plane perpendicular to chain axis. Adapted from [1], [85].

WAXS patterns consist in plotting intensity as a function of 2θ . Measured values need to be adjusted, taking into account the absorption coefficient and the thickness of the sample. The intensity $I(h)$ of a monochromatic ray after having crossed a thickness h is defined by [134]:

$$\frac{I(h)}{I_0} = \exp \left[-\left(\frac{\mu}{\rho} \right) x \right] \quad (21)$$

where μ/ρ is the mass attenuation coefficient ($\text{cm}^2 \cdot \text{g}^{-1}$), x the mass thickness (equal to the product of the thickness and the density of the sample) and I_0 the intensity of the incident beam.

The value of the mass attenuation coefficient μ/ρ was calculated by the addition of the mass attenuation coefficients of each atomic element in the molecular structure of polyamides, taking into account its weight fraction. Our polymers have a mass attenuation factor of $5.52 \text{ cm}^2 \cdot \text{g}^{-1}$.

WAXS measurements were performed in order to verify the amorphous or semi-crystalline character of the studied PPA, also verified by DSC measurements. Moreover, to provide a better estimation of the crystalline fraction, $\Delta H_f^{100\%}$ value for the PA6T was determined by WAXS. The peaks obtained in WAXS were deconvolved using the Fityk software. This software permits the decomposition of the WAXS spectrum into crystalline and amorphous contributions. The amorphous halo was subtracted from

the crystalline peaks. The crystalline fraction χ_{RX} was calculated using the following formula: $\chi_{RX} = \frac{A_C}{A_C + A_A} \times 100$, with A_C and A_A the areas under the fitted crystalline peaks and amorphous halos, respectively. Then the enthalpy of melting of a 100% crystalline PA6T is calculated as follows: $\Delta H_f^{100\%} = \frac{\Delta H_{DSC}}{\chi_{RX}}$ and is 196 J/g.

WAXS measurements were conducted at the Henri Longchambon Diffractometry Center of (University of Lyon, R Vera, E. Jeanneau), using an Oxford Xcalibur Mova diffractometer in transmission mode. The samples were compression molded at a temperature of 20°C above T_g , with a 0.7 mm thick. Measurements were performed at room temperature, with a variation of the angle 2θ between 4 and 50°. A copper anode was used to generate X-rays with a wavelength of 1.54 Å (CuK α). The detector was set at a distance of 55.5 cm of the sample.

As it can be observed in Figure 37, the diffractogram of the amorphous PPA, polyamide A, contains two main peaks around $2\theta = 10^\circ$ and $2\theta = 20^\circ$. The first peak, at 10° , corresponds to the distance between monomers along one chain. The second peak at 20° corresponds to the average distance between locally parallel chains [135].

Additional measurements were performed in order to check if the polyamide A remains amorphous after tensile deformation. In that case, a Bruker D8 Advance θ - 2θ diffractometer in reflection mode (Bragg-Brentano geometry) was used. The scattering intensities were measured using an angular range (2θ) from 10° to 45° .

2.3.1.3 Determination of the surface tension

The surface energy of a solid (mJ.m⁻²), also called free surface enthalpy density, represents the excess of energy associated with the presence of a surface [136]. It is often assimilated to the surface tension described for liquids, γ_L . The molecules have an excess of energy at the interface, originating from the cohesive force between identical molecules. Young [137] describes a system in which a solid (S) is partially wetted by a liquid (L), the solid and the liquid being in equilibrium with a vapor phase (V) (see Figure 39).

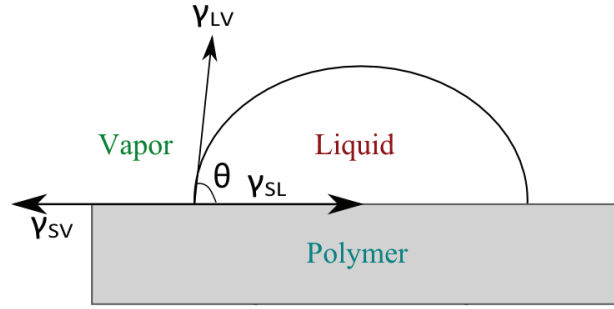


Figure 39 – Balance of forces at the intersection between the 3 phases: solid, liquid and vapor, according to Young [137].

The angle formed by the liquid on the surface of the solid is called θ . Along the V/L interface, the liquid surface tension (γ_L) acts. The surface tension of the solid (γ_S) acts along the V/S interface. At the L/S interface, the interfacial tension is γ_{SL} . In order to balance all the forces, the surface tension γ_S must be equal and opposite to the sum of the surface tensions γ_{SL} and $\gamma_L(\cos\theta)$. The Young equation can be described as:

$$\gamma_L \cos\theta = \gamma_S - \gamma_{SL} \quad (22)$$

The surface energy of a solid is difficult to measure directly. Owens and Wendt have proposed an extended model for interfaces for which polar intermolecular interactions are involved based on Fowkes' additive approach [138]–[142]. Surface tension is the sum of a dispersive component (γ_S^d , London forces) and a non-dispersive or polar component (γ_S^{nd} , hydrogen bonds, dipoles: Debye, Keesom):

$$\gamma_S = \gamma_S^d + \gamma_S^{nd} \quad (23)$$

The contact angle of a droplet deposited on the polymer sample is given by the relation:

$$\gamma_L(1 + \cos\theta) = 2\sqrt{\gamma_S^d \times \gamma_L^d} + 2\sqrt{\gamma_S^{nd} \times \gamma_L^{nd}} \quad (24)$$

Where θ is the angle of the drop of the liquid, γ_S^d and γ_L^d are respectively the dispersive components of the surface energy of the solid and the surface tension of the liquid, and γ_S^{nd} and γ_L^{nd} are the polar components of the surface energy of the solid and the surface tension of the liquid. γ_L^d and γ_L^{nd} of the surface tension of the liquid are known values. Using Equations 23 and 24, it is possible to calculate the

surface tension of the polymer. It is necessary to measure the contact angle of at least two different liquids [140], [143], [144].

The Owens-Wendt method makes it possible to have a good approximation of the surface energy of a material [140]. However, the model used is based on the condition that the surface of the solid is flat and smooth, which is not always the case.

The measurement of the contact angles consists of measuring the angle formed by a drop of a liquid at its point of contact with the surface of the sample and the air, as schematized in Figure 40.

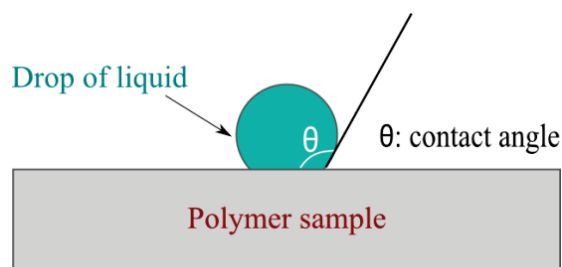


Figure 40 – Schematic representation of the contact angle

The method used to determine the surface energy of the sample is the Owens-Wendt method described previously (Equation 24). This method is sufficient to determine the dispersive component of the surface. The measurement of the contact angles of two liquid probes makes it possible to determine the surface energy of the various polymers studied before and after deformation.

Equation 24 allows to go back to the dispersive and polar components of the surface energy. The surface energy is calculated using Equation 23.

In order to determine the surface tension of our samples before deformation and during strain hardening, we measure the contact angle of droplets deposited on the polymer surfaces. A tensiometer (drop shape analyzer) DSA100 (Krüss) was used, at 23°C. This tensiometer makes it possible to measure the contact angles by optical methods (drop deposit). The values of the surface tensions of liquids are given in the literature. The two components of the surface energy of the polymer are the two unknowns, determined

by the two liquids. Two liquids probes were used: water, which is a polar liquid, and diiodomethane, which is a purely dispersive liquid. The surface tension γ_L of water and its dispersive component γ_L^d are respectively 72.8 mJ.m^{-2} and 21.8 mJ.m^{-2} [145], [146]. For diiodomethane, γ_L and its non-dispersive component γ_L^{nd} are respectively 50.8 mJ.m^{-2} and 2.3 mJ.m^{-2} [145].

2.3.2 Chemical structure characterization

The chemical structure of the studied polymers was studied by Size Exclusion Chromatography (SEC) and by End Group Titration (EGT). These two techniques allowed us to characterize the molar mass, the polydispersity, and the chemical structure of our PPA. It is important to characterize well the chemical structure because this has an influence on the macroscopic properties. The quantity of branching created during the synthesis of the PPA was estimated using a dosage (BHT quantification). The chemical structure was also studied by $^1\text{H NMR}$.

2.3.2.1 Molecular weight distribution

Size Exclusion Chromatography (SEC) is a liquid phase chromatographic method, which allows separating macromolecules as a function of their hydrodynamic volume. This method is used to evaluate the molecular mass distribution thanks to a calibration using standard samples.

From the molecular mass distribution, the number-average molecular mass M_n and the weight-average molecular mass M_w were calculated as follow:

$$M_n = \frac{\sum_i N_i M_i}{\sum_i N_i} \quad (25)$$

$$M_w = \frac{\sum_i N_i M_i^2}{\sum_i N_i M_i} \quad (26)$$

where N_i is the number of molecules of weight M_i .

From M_n and M_w , the polydispersity index (I_p) was determined by the following equation:

$$I_p = \frac{M_w}{M_n} \quad (27)$$

The polyamide sample is dissolved in an appropriate solvent and is passed through a porous column. The SEC analyses were performed on a GPC Agilent 1260 infinity II device with three detectors (UV, Refractive Index and Multiangle laser light scattering (MALLS) detectors), in the Solvay Analytical Laboratory (A. Siot, N. Delon-Anik). The average molecular weight are determined in PMMA equivalent, after relative calibration.

The End Group Titration (EGT) was performed by dissolution of the polyamide sample in a solvent and by a potentiometric back titration of the amine $-\text{NH}_2$ and acid $-\text{COOH}$ groups (Solvay Analytical Laboratory, K. Longé, N. Delon-Anik). The number of acid (CEG) and amine (AEG) end groups are expressed in mmol.kg^{-1} . From CEG and AEG, it is possible to calculate a number-average molecular weight, M_n (Equation 28):

$$M_n = \frac{2 \times 10^6}{[\text{CEG}] + [\text{AEG}] + [\text{BEG}]} \quad (28)$$

where [BEG] represents the blocked end groups known from the reaction recipe [135].

2.3.2.2 Secondary reaction: branching quantification

Secondary reactions may take place during the polyamide synthesis, leading to a small fraction of branched chains. It could be the reaction between two diamines or two amide chain ends. The amount of branching can be estimated by SEC. Bis-(hexamethylene) triamine (BHT) can be formed during the reaction (see Figure 41).

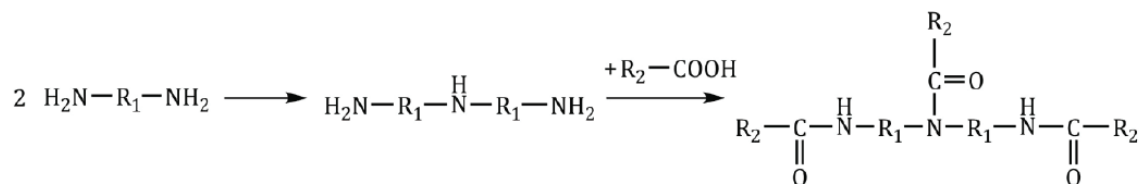


Figure 41 – Secondary reaction during polyamide synthesis leading to branching. From [135].

The concentration of BHT can be determined by dosage after hydrolyzation of polyamide (internal protocol, Solvay Analytical Laboratory, K. Longé, N. Delon-Anik). The BHT concentration is given in ppm (parts per million) referred to the initial polyamide weight.

2.3.2.3 ^1H NMR

Proton Nuclear Magnetic Resonance (^1H NMR) analysis was performed in order to confirm the composition of the different PPA (6I and 6T fractions), as well as to determine the number-average molecular weight, M_n of each polymer and the nature of the chain ends.

^1H NMR was performed using a Bruker Av500 (Solvay Analytical Laboratory, M. Lager, Y. Moskalenko). Polymers were analyzed in hexafluoroisopropanol (HFIP) with cap DMSO-d6 (dimethylsulfoxide-d6) solvent at room temperature.

^1H NMR spectra of the polyamide A is shown in Figure 42. The chemical shifts observed for all the PPA analyzed correspond to the structure of a PA6I/ 6T copolymer.

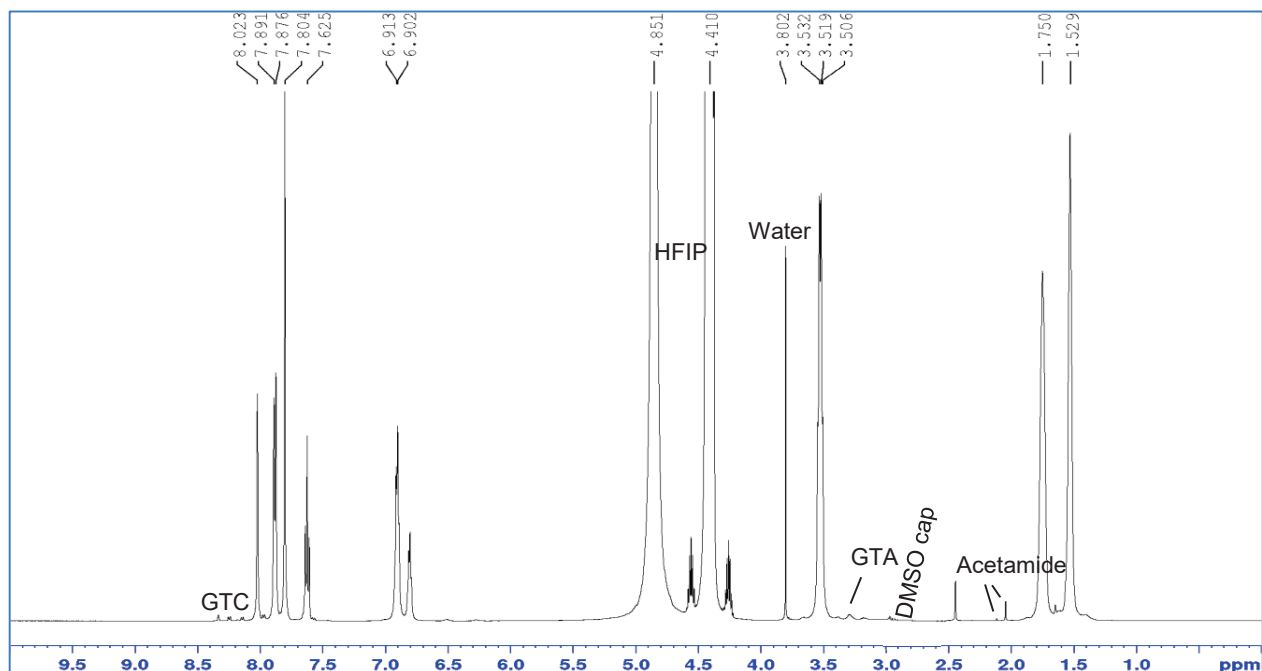


Figure 42 – ^1H NMR spectra of polyamide A obtained in HFIP with cap DMSO-d6 solvent.

The 6I/6T ratio can be calculated by integrating the signals corresponding to the aromatic protons of each motif (6I or 6T). Figure 43 shows the attribution of the aromatic protons to each peak.

The 6I/6T ratios were calculated with the following equation [55]:

$$\frac{\textit{Terephthalic}}{\textit{Isophthalic} + \textit{Terephthalic}} = \frac{I_d}{I_a + I_b + I_c + I_d} \quad (29)$$

where I_x is the integral of the corresponding x peak.

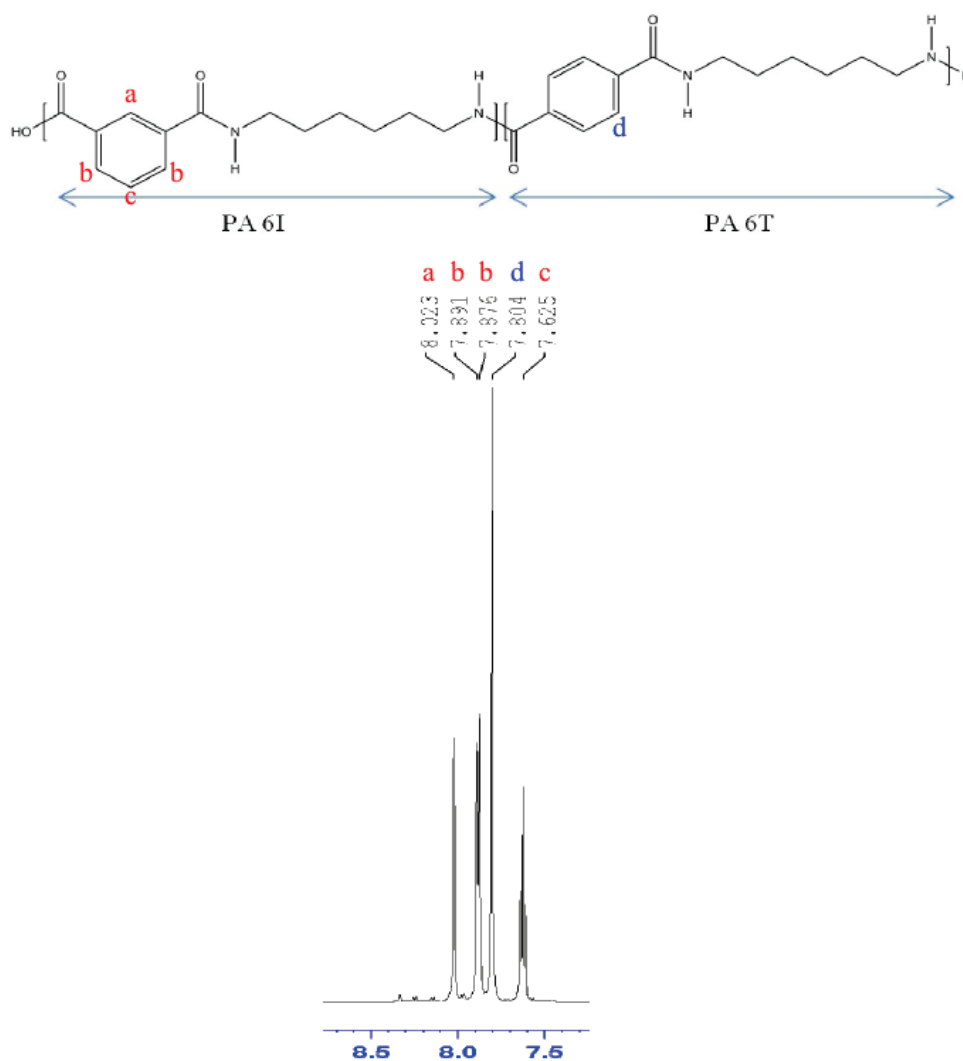


Figure 43 – Attribution of the aromatic protons to the corresponding peak.

2.3.3 Macroscopic mechanical properties

2.3.3.1 DMTA

Dynamic Mechanical Thermal Analysis (DMTA) allows studying the viscoelastic properties of a material by measuring its dynamical modulus at a given frequency as a function of temperature [20]. Polymers present a viscoelastic behavior: they have a viscoelastic response to oscillatory inputs (see Figure 44).

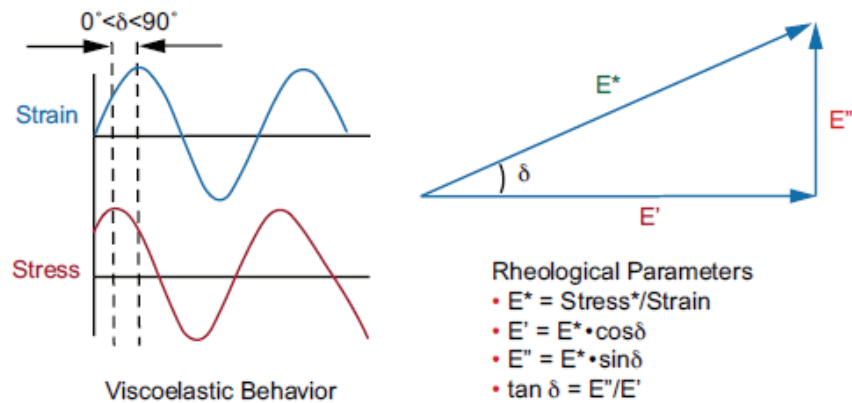


Figure 44 – Viscoelastic behavior from RSAG2 user guide [147]

During a DMTA test, a specimen is submitted to a sinusoidal oscillating deformation ε during a thermal cycle. The resulting stress σ is measured. The ratio between stress and strain is given by the dynamic complex modulus that can be decomposed in two parts: the storage modulus (E') and the loss modulus (E''), as described by Equations 30 to 32:

$$\frac{\sigma(t)}{\varepsilon_0} = E' \cos \omega t - E'' \sin \omega t \quad (30)$$

$$E' = \frac{\sigma_0 \cos \delta}{\varepsilon_0} \quad (31)$$

$$E'' = \frac{\sigma_0 \sin \delta}{\varepsilon_0} \quad (32)$$

A part of the applied energy is elastically restored by the polymer tested. This is associated to the storage modulus E' . The other part of the applied energy is absorbed by the polymer and dissipated as heat. This energy is associated to the loss modulus E'' . The ratio between E' and E'' is called the phase lag (or loss angle) $\tan \delta$ and is given by Equation 33:

$$\tan \delta = \frac{E''}{E'} \quad (33)$$

$\tan \delta$ represents the proportion of the energy dissipated as heat by the polymer sample.

With DMTA measurements, the polymer relaxations processes can be determined at different temperatures. When a polymer relaxation temperature is reached, at a given frequency, there is a decrease of the storage modulus E' . For secondary relaxations (β , γ), a small drop in E' can be observed while for the main relaxation α , a large drop in E' is observed (drop of about 1 or 2 decades). A peak is observed in E'' and $\tan \delta$ curves. A curve obtained by DMTA and the relaxations processes observed for polyamide A is shown in Figure 45.

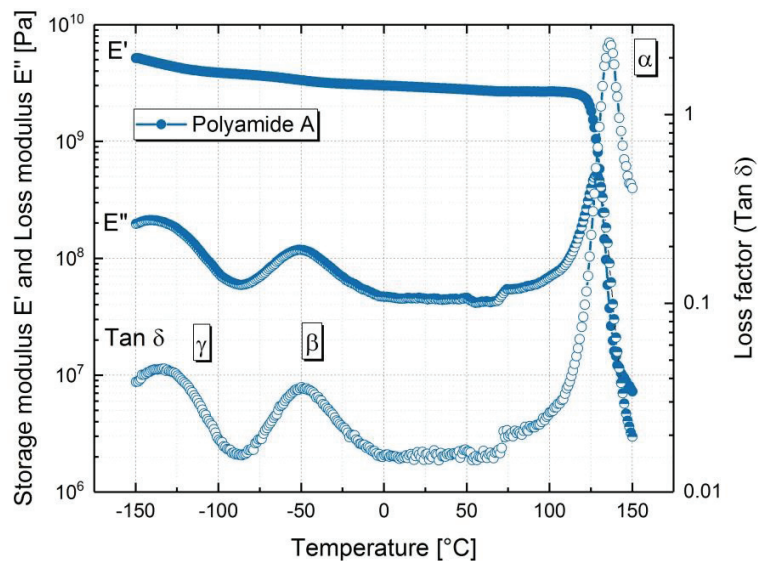


Figure 45 – Polyamide A (PPA) DMTA curves of E' , E'' and $\tan \delta$.

Viscoelasticity experiments were carried out in the field of linear behavior, with a deformation between $5 \times 10^{-3} \%$ and 0.01% . A TA Instruments RSA-G2 device, equipped with a three-point bending geometry was used. The samples were injected in the form of bars (Charpy impact specimens) then cut with a saw. Polymer samples dimensions were $40 \times 10 \times 4 \text{ mm}^3$. Measurements were performed at fixed

frequencies of 0.1Hz, 1Hz, 10Hz, 50Hz and 75Hz with a temperature sweep of -150°C to 150°C, at a rate of 2°C.min⁻¹. Each DMTA measurement was carried out twice for each frequency. The temperature corresponding to each relaxation was determined as the maximum of the relaxation peak observed in the loss modulus E'' plot, as described in the standard ASTM D5023.

Instead of performing a temperature sweep (i.e. varying the temperature at a fixed frequency), another testing mode for probing the viscoelastic behavior of a polymer can be used. It is known as a frequency sweep: at a given and fixed temperature, the frequency oscillates, and several temperatures can be tested. With a time-temperature superposition principle (tTS), a master curve can be established. Figure 46 represents schematically the time-temperature superposition principle, with the application of a horizontal shift factor, a_T .

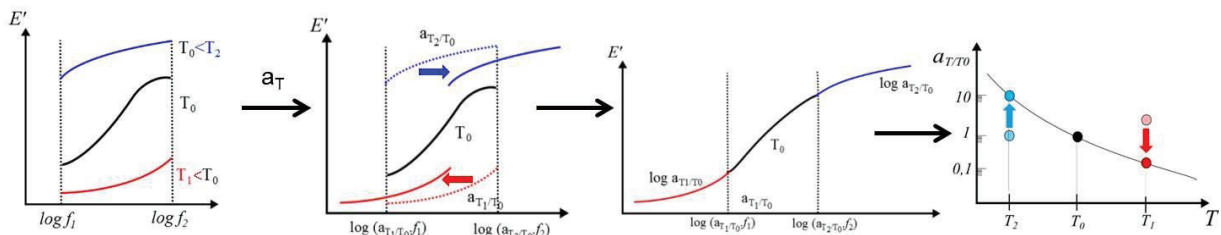


Figure 46 – Schematic representation of the time-temperature superposition principle (tTs).

In DMTA, datas are obtained over a small range of frequency (a few decades, in our case, less than 3), which does not allow us to obtain the totality of polymer relaxation. The master curve obtained with the tTS makes it possible to extend the frequency range. The time-temperature superposition is a combination of two shifts: a vertical shift and a horizontal shift. The horizontal shift factor a_T can be described by a WLF equation (see Equation 34) [77].

$$\text{Log } a_T(T) = \frac{C_1(T - T_{ref})}{C_2 + (T - T_{ref})} \quad (34)$$

where C_1 and C_2 are the WLF constants and T_{ref} is the arbitrary chosen reference temperature.

The values of C_1 and C_2 can be reported to T_g using Equations 35 and 36 [148].

$$C_1^g = \frac{C_1 C_2}{C_2 + T_g - T_{ref}} \quad (35)$$

$$C_2^g = C_2 + T_g - T_{ref} \quad (36)$$

The reference temperature T_{ref} can be chosen as the T_g of the polymer, in order to compare all the polymers.

2.3.3.2 Impact test

A Charpy impact setup was used in order to obtain the resilience of the studied polymers as well as to characterize their brittle-ductile transition temperature, T_{bd} . Three-point bend impact experiments are conducted on a CEAST 9050 Instron classic Charpy pendulum equipped with a 7.52 J-energy hammer. A schematic representation of the setup is given in Figure 47. The polymer samples, with a dimension of $80 \times 10 \times 4 \text{ mm}^3$ were notched with a notch radius of 0.25 mm and a notch depth fixed at 2 mm. Samples were hit at a speed $v_{impact} = 3.8 \text{ m/s}$, which corresponds to a deformation rate of $v_{impact}/r_{notch} = 1.5 \cdot 10^4 \text{ s}^{-1}$. In order to obtain the brittle-ductile transition temperature T_{bd} of the studied polymers, impact strength tests were conducted from -40°C to 230°C . Samples were kept in a thermally controlled chamber and were conditioned for 15 min at the set temperature for equilibrium prior to impact testing. The samples temperatures were estimated to remain roughly constant during the impact tests. The laboratory was at a controlled temperature (23°C) and hygrometry (RH 50). The studied PPA were dried as molded (d.a.m.), the temperature equilibration time was too small to induce significant water intake. For each temperature, ten specimens were tested. The resilience (J/m^2) was calculated by dividing the energy used to fracture the sample by the fracture surface area under the notch.

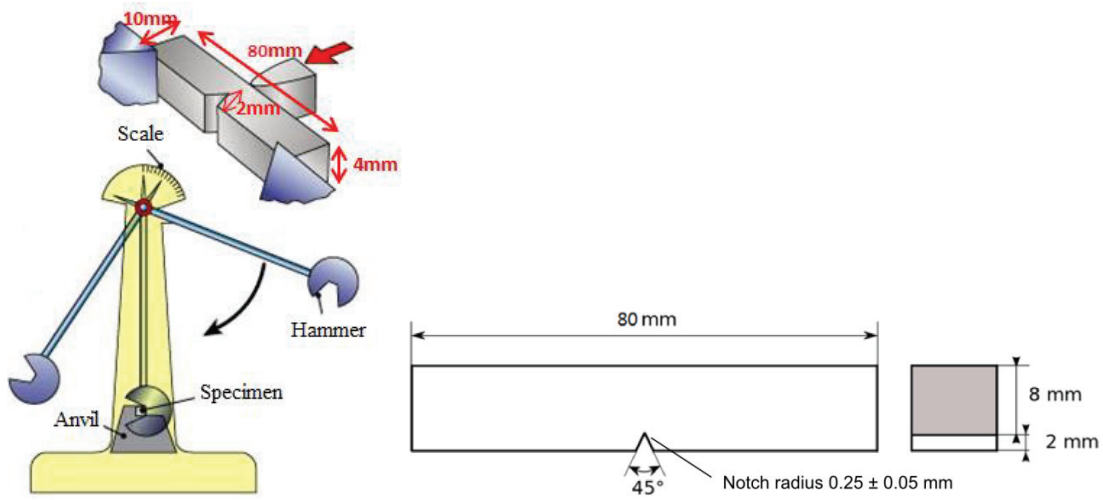


Figure 47 – Charpy impact setup and dimensions of the specimen.

2.3.3.3 Video-controlled tensile test

In order to characterize the Young modulus E , the yield stress σ_y and the brittle-ductile transition temperature T_{bd} of the studied polymers, tensile strength experiments were carried out on a Zwick/Roell Z050 universal testing machine equipped with a 50 kN load cell, a thermally controlled chamber and a non-contact extensometer (VidéoTraction®) [21]. The VidéoTraction® system is based on the measurement and regulation of the local deformation in a representative volume element (defined by several dot markers on the middle of the tensile specimen) and measures the true strain and the true stress during the test. Thanks to two cameras, we have access to both transverse strains (deformation in thickness and width) and also access to longitudinal strain. Figure 48 shows a schematic representation of the VidéoTraction system. The development of localization phenomena like necking is taken into account in the measured behavior [21], [22]. Samples were dried as molded (d.a.m.) and were strained at a constant strain rate $\dot{\epsilon} = 1.10^{-3} s^{-1}$ at different temperatures (between $-40^\circ C$ to $160^\circ C$). The temperature chamber is limited in minimum temperature: we cannot perform tensile tests below $-40^\circ C$. Each sample was conditioned 20 min in the temperature chamber before being tested. For each temperature, five samples were tested. Tensile tests were performed on ISO-527 standards.

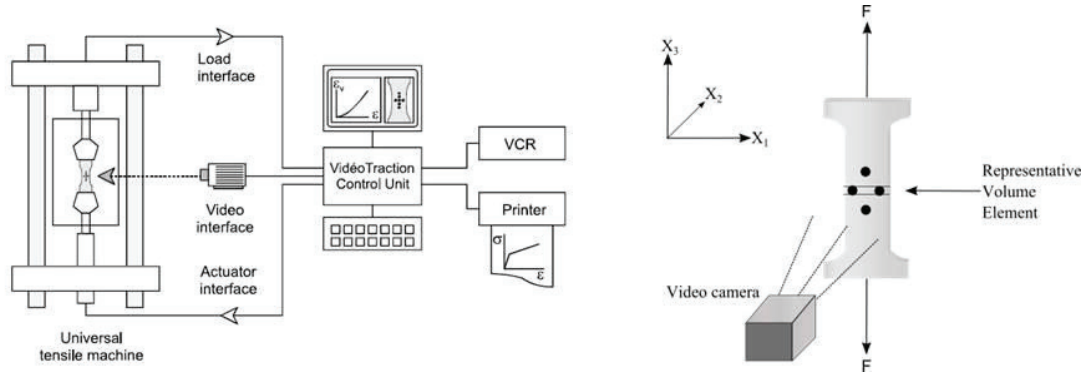


Figure 48 – Representation of the VideoTraction® system and the markers on the middle of the tensile specimen. From [21].

At large deformations, amorphous polymers have a high ductility. During the tensile test, the sample cross sectional area is not constant. The instantaneous cross-sectional area $S(t)$ should be used instead of S_0 . The videoextensometer gives access to the elastoviscoplastic response of polymers under uniaxial tension. Local measurements of true strains are performed at the center of the neck [21]. Four dot markers are printed on the front face of the sample prior to deformation, within a representative elementary frame. Local deformations are measured between the dots and the true strain ε_v is related to the nominal strain and the elongation ratio λ by the following equation [69]:

$$\varepsilon_v = \ln\left(\frac{l}{l_0}\right) = \ln\left(1 + \frac{l - l_0}{l_0}\right) = \ln(1 + \varepsilon_n) = \ln(\lambda) \quad (37)$$

The true strain rate $\dot{\varepsilon}_v$ is defined as:

$$\dot{\varepsilon}_v = \frac{\dot{l}}{l(t)} \quad (38)$$

with \dot{l} the velocity of elongation and $l(t)$ the length at each time t .

If there is no volumetric change in the material during the test and if the cross-sectional area remains consistent through the gauge length, the true stress σ_v can be defined as:

$$\sigma_v = \sigma_n(1 + \varepsilon_n) \quad (39)$$

From these measurements, a true stress – true strain curve is obtained. The Young modulus E is calculated from the tangent line in the elastic domain (between 0.05 and 0.25% of true strain) and the yield stress σ_y is defined as the observed maximum stress, as shown in Figure 49.

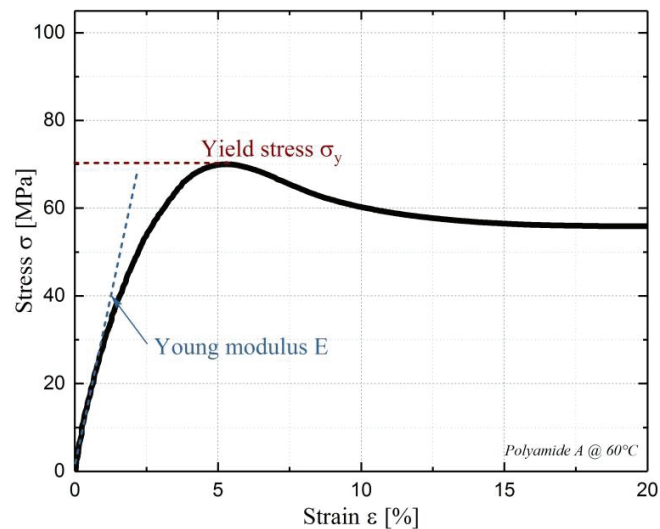


Figure 49 – Representation of the determination of the Young modulus E and the yield stress σ_y .

However, for some temperatures, no clear maximum can be observed. The stress corresponding to a strain of 0.6 was taken as the yield stress value.

2.3.3.4 Compression test

Compression tests were performed on a Zwick/Roell Z050 universal testing machine equipped with a 50 kN load cell, a thermally controlled chamber and a non-contact extensometer (VidéoTraction®) [21]. The geometry of the sample is an important limitation of this test. Cubes of dimensions $10 \times 10 \times 4 \text{ mm}^3$ were cut in the ISO-527 tensile specimens. It is necessary to avoid the barreling or buckling of the sample. The friction has been reduced by lubrication of the plate to prevent the buckling of the sample.

Specimens were compressed at a constant strain rate $\dot{\epsilon} = 1.10^{-3} \text{ s}^{-1}$ between two parallel flat steel plates. Tests were performed at different temperatures, from -20°C to 120°C . Each sample was conditioned 20 min in the temperature chamber before being tested. For each temperature, five samples were tested.

For the analysis of the strain hardening response, the compression curves were plotted versus the Green-Lagrange strain: $g(\lambda) = \lambda^2 - \lambda^{-1}$ [7]. The strain hardening modulus, E_{SH} , was determined from the slope of the curves in the strain range $1.75 \geq g(\lambda) \geq 1.25$.

2.3.4 Study of damages morphologies

2.3.4.1 Microscopic study

Depending on the polymer and on the size of the damage, two microscopy techniques were used: optical microscopy (OM) and Scanning Transmission Electron Microscopy (STEM).

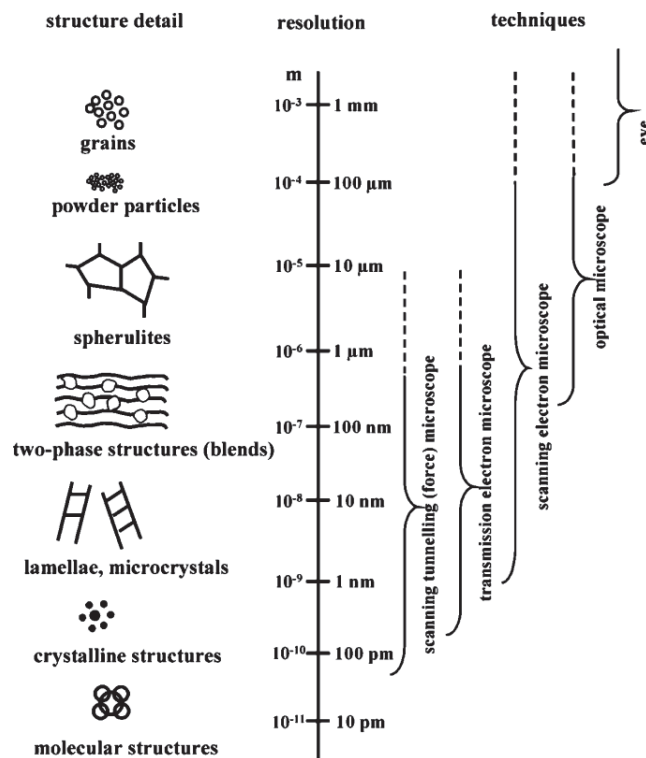


Figure 50 – Representation of different techniques adapted for different scales of observation. From [35] .

Figure 50 summarizes the different techniques adapted for different scales of observation. We can see that the optical microscope allows us to see objects larger than SEM, or even in TEM.

Scanning Transmission Electron Microscopy (STEM)

The scanning transmission electron microscopy (STEM) mode combines the principles of both transmission and scanning electron microscopy (TEM and SEM).

The similarity with SEM is that the STEM scans a focused beam of electrons across the sample in a rectangular pattern. One of the advantages over SEM imaging is the improvement of the spatial resolution in STEM. Like TEM, STEM analyzes a beam of electrons transmitted by the sample, which has to be very thin.

In STEM, the microscope lenses are adjusted to create a focused convergent electron beam or probe at the sample surface [35]. This focused probe is then scanned across the sample and various signals are collected point-by-point to form an image [35]. STEM analyses can be performed on SEM or TEM instrument. In STEM, the transmitted and scattered electrons can be directly observed. There are two detectors modes: bright-field and dark-field mode.

In STEM, the transmitted and scattered electrons can be directly observed. There are two detectors modes: bright-field and dark-field mode (see Figure 51).

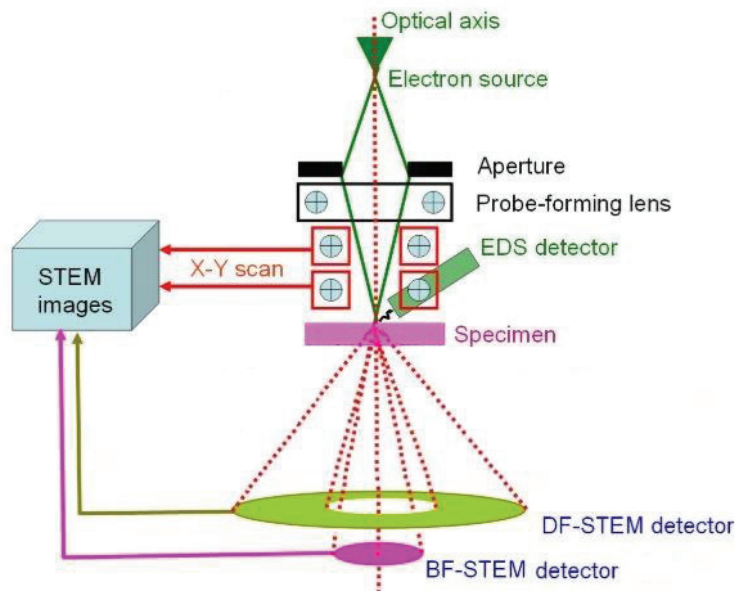


Figure 51 – Schematic representations of the different annular STEM detectors modes: bright-field and dark-field.

In the bright-field mode (BF), the unscattered (or transmitted) electron beam that leaves the sample at relatively low angles with respect to the optic axis is selected with the aperture and the scattered electrons are blocked. Since the unscattered beam is selected, objects which absorb electrons will appear dark, while objects which transmit electrons will appear white. On the contrary, in dark-field mode (DF), the unscattered electron beam is excluded from the aperture, and the scattered electrons are selected instead. Hence, the areas where there is no electron scattering will be black, while the objects which scattered electrons will appear bright. This mode can be used to enhance contrast when the bright field image is not clear enough.

All samples were ultramicrotomed to a specimen thickness of 150 nm using a Reichert Ultracut S microtome at room temperature with a diamond knife in order to obtain a mirror surface. The observation area is schematized in Figure 52. Sections are picked-up on a copper grid.

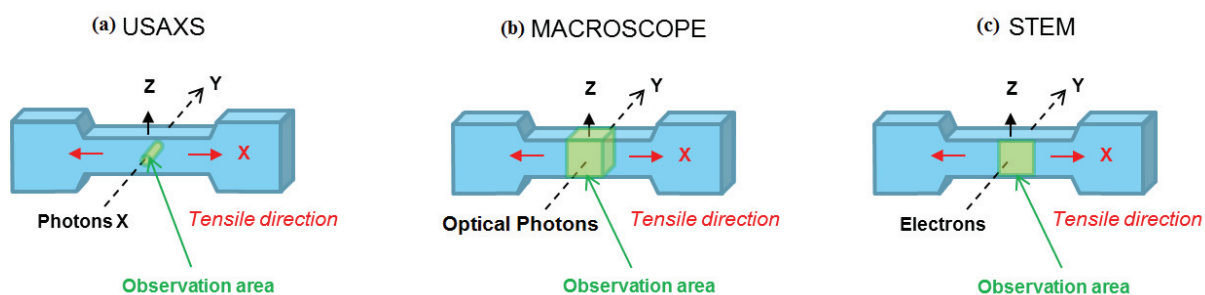


Figure 52 – USAXS (a), macroscopy (b) and STEM (c) observation zones of the tensile specimen.

Samples are imaged using a Zeiss Ultra 55 STEM, with an annular bright-field (or dark-field if necessary). Typical operating conditions for BF and DF STEM imaging include an accelerating tension of 20 kV, a diaphragm aperture size at 20 μ m and a working distance of about 6 mm.

Cross-polarized optical microscopy

Cross-polarized optical microscopy characterizations were performed on injection molding specimens after tensile deformation (see Figure 52). Section of 1500 nm was cut at room temperature by using a Reichert Ultracut S microtome equipped with a diamond knife. The sections are placed on a glass slide and then dispersed in paraffin and analyzed by using an optical microscope Leica DMRX in transmission

mode. Additional observations were made by microscope with a WILD M420 microscope on specimens after deformation in bright field and crossed-polarized light (Solvay Materials Analysis Department, Microscopy Laboratory, B. Gros, P. Grau).

Figure 53 shows the configuration of a polarized optical microscope composed of:

- an illumination system,
- a polarizer,
- a rotary stage,
- objectives,
- an analyzer,
- eyepieces.

The principle of measurement is simple and based on the interaction of microscopic objects with the polarized light, considered as transverse vibration with electric and magnetic field. With a birefringent material, the polarized light is split into two plane polarized-waves that vibrate in planes at right angles to one another.

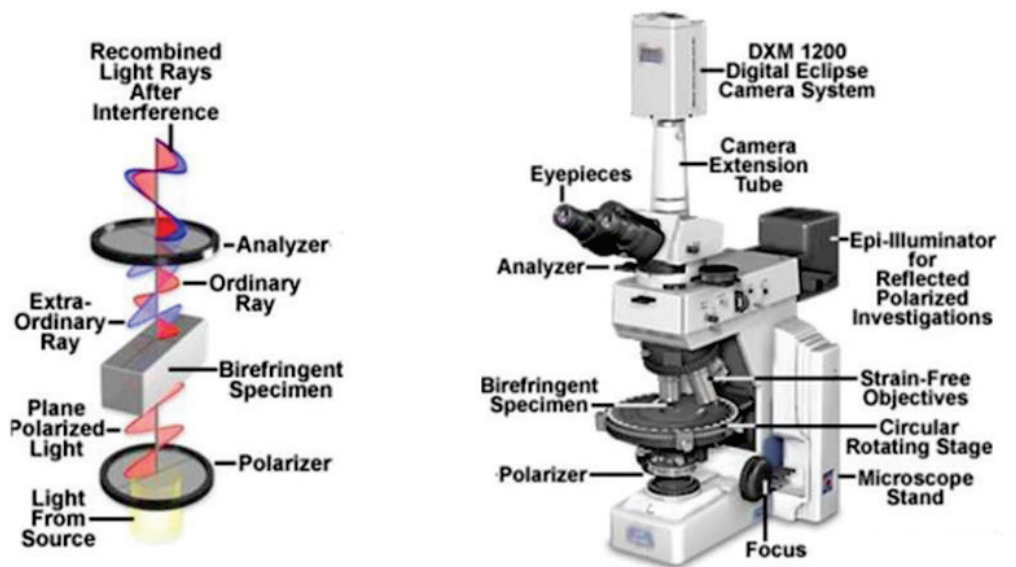


Figure 53 – Polarizer and microscope configurations. From [149]

This technique makes it possible to demonstrate the birefringent character of the materials (for example, the crystalline morphology in the case of semi-crystalline polymers will be visible, which will not be the

case of an amorphous polymer, which will appear extinguished). Shear bands can be observed by cross-polarized optical microscopy, in transmission [99], [100]. With no specimen or with an isotropic specimen, the field of view will be dark in cross-polarized optical microscopy. On the contrary, an anisotropic polymer will be birefringent. The birefringence is due to the orientation of optically anisotropic elements, such as the amorphous polymer chains, aligned during the tensile test for example or crystals aligned by deformation in the case of semi-crystalline polymer.

The phase contrast microscopy was also used. It is an optical microscopy technique that converts differences in refractive indices between two structures into contrast levels, which result in a phase difference for the light waves passing through them. It produces a halo around the observed structures.

2.3.4.2 Ultra Small Angle X-ray Scattering (USAXS)

SAXS experiment relies on the same technique used for WAXS experiment with a different range of scattering angle.

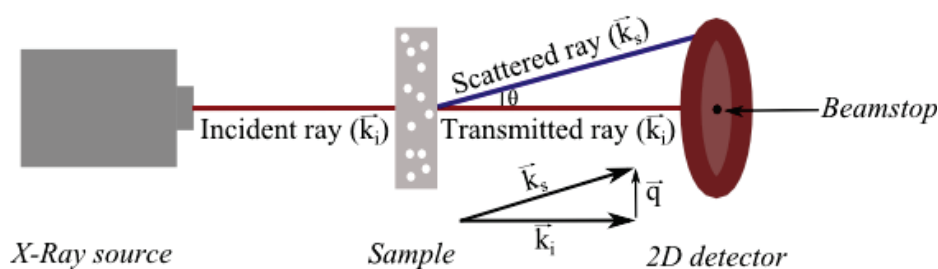


Figure 54 – Schematic representation of a X-ray scattering experiment.

X-ray beam is sent through the sample and can interact with the sample in three ways. First, a part of the beam is transmitted in the same direction as the incident beam. A small fraction of the beam is absorbed by the sample and transformed (for example in heat). The other part of the incident beam is scattered into another direction. The scattering signal is collected at different angles θ by a 2D-dectector (see Figure 54). In USAXS experiments, only the scattered intensity is measured. The higher the sample-to-detector distance, the smaller the scattering angle. The scattered intensity is normalized by the thickness of the sample (mm^{-1}) and is represented as a function of the scattering vector q (nm^{-1}) (see Figure 55), defined as:

$$\vec{q} = \vec{k}_s - \vec{k}_i \quad (40)$$

The scattering vector can also be related to the scattering angle by:

$$q = \frac{4\pi \sin\theta}{\lambda} \quad (41)$$

where λ is the X-ray wavelength, θ the angle between the incident and the scattered beam.

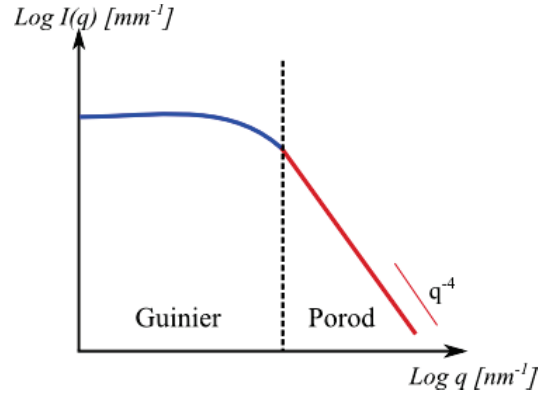


Figure 55 – Schematic representation of the scattering intensity of particles as a function of the scattering vector q . The Guinier and Porod regimes are visible.

The data are commonly represented on a log-log scale (see Figure 55). If we consider an homogeneous polymer matrix, with spherical objects (impurities, particles or cavities) of radius R randomly dispersed in the matrix, the resulting scattered intensity shows two characteristic regimes [150]. At low q values ($qR < 1$), the scattered intensity can be described by the so-called Guinier regime [151]:

$$I(q) \cong G \exp\left(\frac{-q^2 R^2}{5}\right) \quad (42)$$

where the prefactor G is equal to $G = \beta^2 \rho_e^2 N V^2$ with V the volume of the object defined by $V = 4\pi R^3/3$ and R , the radius of the scattering spherical object, linked to the radius of gyration of the particle by the following relation:

$$R_g^2 = \frac{3}{5} R^2 \quad (43)$$

At high q values ($qR > 1$), the scattered intensity can be described by the Porod regime [152]:

$$I(q) \cong Bq^{-4} \quad (44)$$

where the prefactor B of the power law can be related to the surface area of the particles and is equal to $B = 2\pi\beta^2\rho_e^2NS$, with $\beta^2 = 7.8 \times 10^{-24}\text{mm}^2$ is the electron cross section, ρ_e is the average electron density between the polymer matrix and the objects, N is the number density of the objects and $S = 4\pi R^2$ is the surface area.

The electron density of a polymer i can be expressed by:

$$\rho_i = \frac{n_i \times d_i \times N_A}{M_i} \quad (45)$$

with n_i the number of electrons per repeat unit in the polymer, d_i the density of the polymer, N_A the Avogadro's number ($N_A = 6.022 \times 10^{23}\text{mol}^{-1}$) and M_i the molar mass of the repeat unit of the polymer.

From Equation 45, the electron density of each polymer is determined and is available in Table 7.

Table 7 – Number of electrons per repeat unit n_i , density d_i , molar mass of the repeat unit M_i and electron densities of the different polymers studied.

	n_i	d_i ($\text{g}\cdot\text{mm}^{-3}$)	M_i ($\text{g}\cdot\text{mol}^{-1}$)	ρ_i (mm^{-3})
PPA	132	1.18×10^{-3}	246.3	3.81×10^{20}
PC	134	1.19×10^{-3}	254.3	3.78×10^{20}
PMMA	54	1.18×10^{-3}	100.0	3.84×10^{20}

Beaucage et al [152] have proposed a global unified scattering function. This function gives an approximation of the scattering of a spherical particle and contains Guinier and Porod regimes:

$$I(q) = G \exp\left(\frac{-q^2 R^2}{5}\right) + B \left(\frac{\left(\text{erf}\left(\frac{qR}{\sqrt{10}}\right)\right)^{12}}{q^4} \right) \quad (46)$$

where $\text{erf}(x)$ is the error function defined by [153]:

$$\text{erf}(x) = \frac{2}{\sqrt{\pi}} \int_0^x e^{-t^2} dt \quad (47)$$

The error function approaches zero when q approaches zero, and 1 when q tends to infinity.

The global unified scattering function is only valid for a single polydisperse level of spherical primary particle. If the material contains several polydisperse levels of different cavities or structures, the contributions of each should be integrated and added in the global scattering function [150]. As an example, if the structure is anisotropic (case of ellipsoids), the scattered intensities can be integrated along the directions perpendicular and parallel to the tensile direction. For ellipsoids elongated along the tensile direction, the scattered intensity gives access to the long radius d in the direction parallel to the tensile direction and to the small radius c in the direction perpendicular to the tensile direction:

$$I_{parallel}(q) = \beta^2 \rho_{pol}^2 V^2 N \left(\exp\left(\frac{-q^2 d^2}{5}\right) + 4.5 \left(\frac{\left(\text{erf}\left(\frac{qd}{\sqrt{10}}\right)^{12}\right)}{(qd)^4} \right) \right) \quad (48)$$

$$I_{perpendicular}(q) = \beta^2 \rho_{pol}^2 V^2 N \left(\exp\left(\frac{-q^2 c^2}{5}\right) + 4.5 \left(\frac{\left(\text{erf}\left(\frac{qc}{\sqrt{10}}\right)^{12}\right)}{(qc)^4} \right) \right) \quad (49)$$

The fitting of the scattered intensities was performed using Igor Pro Software.

SAXS/USAXS experiments were performed at two synchrotron facilities: the ESRF (ID02 beamline) and SOLEIL (SWING beamline). Configurations were chosen to achieve measurements at the largest possible q range. All the scattering data are expressed in terms of the modulus of the scattering vector $q = 4\pi \sin(\theta)/\lambda$, with λ the X-ray wavelength and 2θ the scattering angle.

USAXS experiments were carried out on the High brilliance Beamline (ID02) at the European Synchrotron Radiation Facility (ESRF, Grenoble, France). The X-ray wavelength was $\lambda = 0.995 \text{ \AA}$ and the X-ray energy was set to 12.46 keV. The region illuminated by the X-ray beam was about $100 \times 100 \mu\text{m}^2$. A 2D-detector Rayonix MX-170HS (X-ray area: $170 \times 170 \text{ mm}^2$) was used. Three sample-to-detector distances d from 1m to 31m were used. When $d = 31\text{m}$, the accessible q range is $10^{-3} \text{ nm}^{-1} < q < 10^{-2} \text{ nm}^{-1}$. For $d = 8\text{m}$, the q range is $10^{-2} \text{ nm}^{-1} < q < 10^{-1} \text{ nm}^{-1}$. For $d = 1\text{m}$, the q range is $10^{-1} \text{ nm}^{-1} < q < 10 \text{ nm}^{-1}$. For each sample, five measurements were made, with an acquisition time of 5 s. The X-ray scattering data were reduced (average of the 5 measures, integration, normalization,

subtraction of the empty frames) using SAXSutilities software, developed for the ID02 beamline by Sztucki et al [154].

Figure 56 shows an example of USAXS scattered intensities obtained on polyamide A at 60% of true strain during tensile test at 60°C for the five measurements performed on the same sample. The five curves overlap perfectly. The average of the 5 measurements can therefore be made.

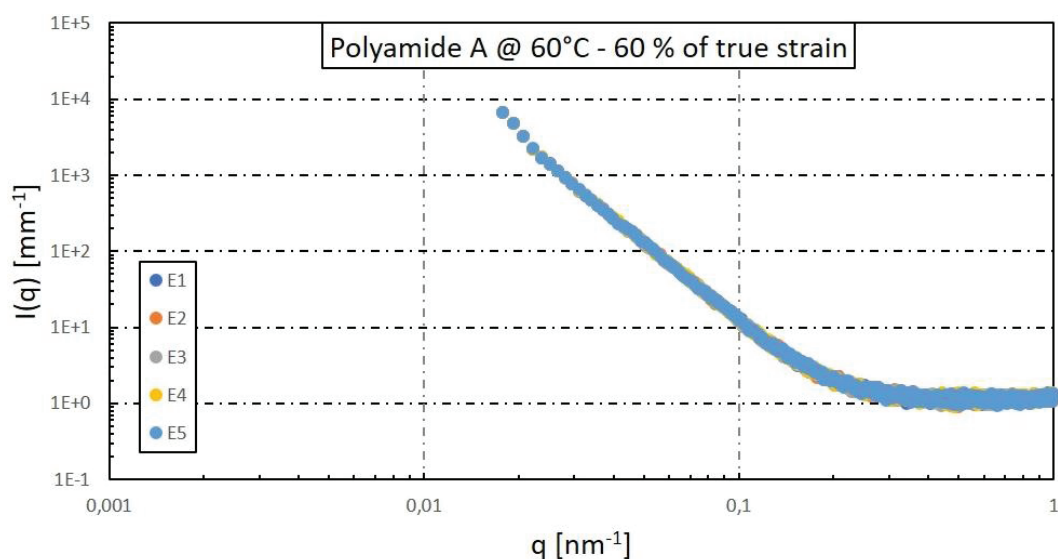


Figure 56 – USAXS scattered intensities obtained on polyamide A at 60% of true strain during tensile test at 60°C for the five measurements performed on the same sample.

Additional X-ray scattering data were collected on the SWING beamline at SOLEIL, the national French synchrotron facility (Saint-Aubin, France). The X-ray wavelength was $\lambda = 1.033 \text{ \AA}$ and the beam energy was set to 12 keV. A Dectris detector Eiger 4M was used (pixel size: $75 \times 75 \mu\text{m}^2$, dimension: 1035×1083). The q range was set to $0.00148 - 1.8844 \text{ nm}^{-1}$. The low q region was explored using a sample-to-detector distance of 6.18m. For each sample, five measurements were made, with an acquisition time of 600 ms.

The scattering patterns become anisotropic with the deformation. The scattering intensities have to be integrated along the parallel (in an interval of azimuth angle $[-10 - 10^\circ]$) and the perpendicular (in an interval of azimuth angle $[80 - 100^\circ]$) directions to the tensile deformation. All data were normalized by the thickness of the sample and plotted as a function of the scattering vector q.

Chapter 3 – Thermal and structural characterization

This chapter brings together the results obtained for the thermal and structural characterization of the polymers studied. Firstly, the thermal properties determined by DSC are described for the PPA, polycarbonate and PMMA studied. The study of the relaxations processes is then determined for the four PPA. The chemical structure of the studied PPA is studied by size exclusion chromatography (SEC) and by End Group Titration (EGT). These two techniques allowed us to characterize the molar mass, the polydispersity, and the chemical structure of our PPA. The quantity of branching created during the synthesis of the PPA is estimated using a dosage (BHT quantification). ^1H NMR analysis gives the composition of the different PPA.

3.1 Thermal properties

The different PPA were characterized by DSC, in order to study their thermophysical properties, as well as the influence of the terephthalic acid content. An example of a thermogram for polyamide A and C (amorphous and semi-crystalline, respectively) is presented in Figure 35.

For polyamide A and D, no melting or crystallization peak was observed between 40°C and 350°C. A glass transition temperature T_g was observed at 129°C for polyamide A and 127°C for polyamide D. The DSC analyses confirm that polyamide A and polyamide D are amorphous.

On the contrary, polyamide B and polyamide C show a typical semi-crystalline behavior. Indeed, as shown by Figure 35-b for polyamide C, a melting and crystallization peaks were observed, as well as a glass transition temperature T_g . All the temperatures determined for all the PPA are displayed on Table 8.

Table 8 – Glass transition temperatures T_g , melting temperatures T_m and crystallization temperatures T_c of the considered PPA.

Polymer	Terephthalic acid ratio	T_g (°C)	T_m (°C)	T_c (°C)
Polyamide A	29	129	/	/
Polyamide B	49	129	265	202
Polyamide C	67	132	319	279
Polyamide D	31	127	/	/

Polyamide B has a T_g of 129°C, whereas polyamide C has a T_g of 132°C.

The introduction of a fraction of terephthalic acid in the polymer mainly composed of isophthalic acid leads to a change in the glass transition T_g of the copolymer. Figure 57 represents the variation of the glass transition temperature T_g as a function of the terephthalic acid fraction.

In literature, the glass transition temperature of a PA6T is found equal to 140°C [1] whereas the T_g for PA6I is found equal to 126°C with the same M_n as our considered polymers (around 10 000 g.mol⁻¹) [124]. The T_g of the copolymers varies between 126°C and 140°C, from pure PA6I to pure PA6T respectively. When 6T fraction increases, up to 100%, the glass transition also increases.

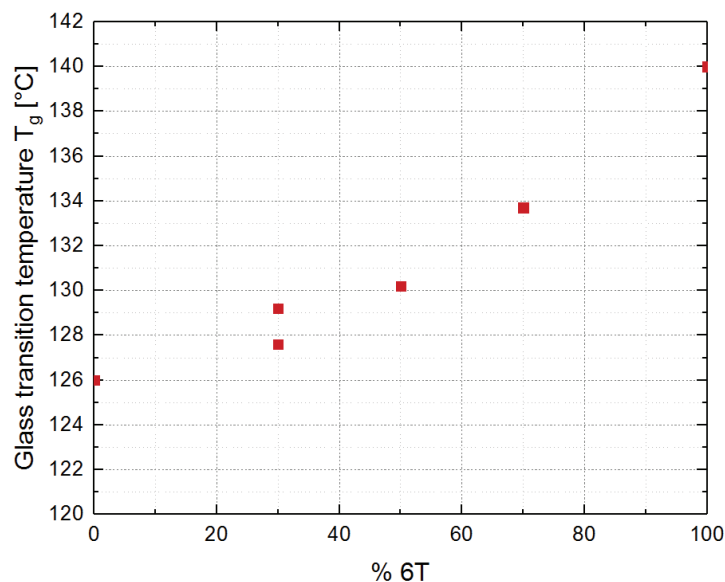


Figure 57 – Evolution of the glass transition temperature T_g as a function of the 6T fraction. T_g were determined by DSC. T_g value of 0% PA6T is from [124] and of 100% PA 6T is from [1].

The slight increase in T_g observed in Figure 57 is in agreement with literature for pure PA6I, PA6T and PA6I/6T copolymers [155], [156]. It can be related to the positions of the carboxylic acid functions on the aromatic ring on both terephthalic and isophthalic acids. Indeed, the 1,4 positions of the terephthalic acid give a symmetric monomer with an angle of 180° between the two functions, whereas the 1,3 positions of the isophthalic acid give a non-flat angle. The positions of the carboxylic acid functions on the aromatic ring lead to rigid and straight PA6T chains, with a reduced mobility and thereby a higher glass transition temperature T_g than PA6I is observed. Indeed, PA6I has more torsions between neighboring monomers and a higher flexibility, which decreases the glass transition temperature [156].

The more the PPA copolymer consists of PA6T (semi-crystalline polymer), the less the amorphous chains between the crystalline domains will have mobility and free volume compared to a totally amorphous PA6I, which leads to an increase in the glass transition temperature.

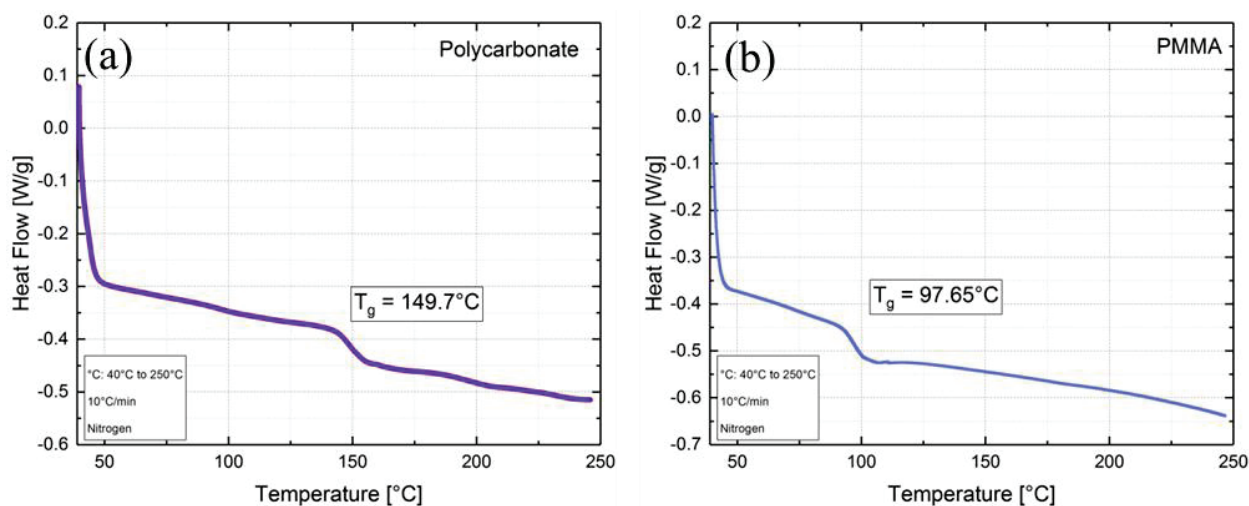


Figure 58 – Thermograms of Polycarbonate (a) and PMMA (b) obtained by DSC.

The polycarbonate and poly(methyl methacrylate) as comparison polymers for the study of damage mechanism were also studied by DSC. The thermograms obtained for these polymers are shown in Figure 58. The DSC analysis reveals the amorphous character of both polycarbonate and poly(methyl methacrylate), with a glass transition temperature of 150°C and 98°C , respectively. The T_g of polycarbonate is higher than the T_g of the PPA studied, in agreement with literature [157].

3.2 Thermo-mechanical properties

Temperature sweep measurements were performed at frequencies of 0.1, 1, 10, 50 and 75 Hz. The temperature of each relaxation was determined as the maximum of the relaxation peak observed in the loss modulus E'' plot. To determine correctly the characteristic temperature of each relaxation process, a Gaussian function was used to fit each peak, and therefore determined the peak maximum. The temperature dependences of the storage modulus E' , the loss modulus E'' and the damping factor $\tan\delta$, as determined at 1 Hz for the different PPA are shown in Figure 59.

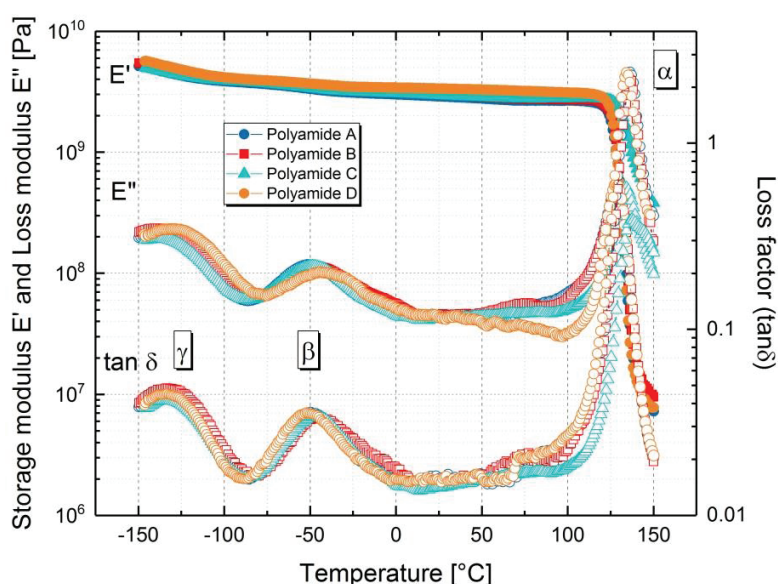


Figure 59 – Temperature dependences of the storage modulus E' and the damping factor $\tan\delta$, as determined at 1 Hz for the different PPA by DMTA measurements. The different relaxation processes are indicated on the $\tan\delta$ curves.

All the studied PPA exhibit a characteristic dynamic mechanical response for a thermoplastic material. At 23°C and 1Hz, the storage modulus E' is high and is about 3 GPa for the four PPA, which is comparable with literature for others polymers (2.5 GPa for PPO and 3 GPa for PS [24]). Starting from low temperature, the storage modulus E' reduces slowly and decreases strongly at the glass transition temperature T_g because the polymer chains obtain a full segmental mobility and their state changes from glassy to rubbery.

In addition to the final relaxation process (α) we observe two peaks on $\tan\delta$ for each polymer, denoted γ and β from the lower to the higher temperature. Indeed, three relaxations processes have been identified in other semi-aromatic and aliphatic polyamides [78]–[81] by DMTA and by broadband dielectric spectroscopy (BDS) [82], [83] as schematized in Figure 14.

At the lowest temperature, the γ -relaxation is generally assigned to local motions of short methylene sequences $-(CH_2)_n-$ internal to the monomer for aliphatic polyamides [78], [84]. This relaxation is observed around $-140^\circ\text{C}/-130^\circ\text{C}$ at 1 Hz, which is comparable to the γ -relaxation observed by Varlet et al. for PA 12 [84]. The β -relaxation is associated to the rotation of amide groups $(-NHCO-)$ along the polyamide chain and is observed around $-50^\circ\text{C}/-40^\circ\text{C}$ at 1 Hz. The α -relaxation corresponds to large segmental movements (several monomers). This main relaxation is observed at high temperature and is close to the glass transition temperature measured by DSC. The temperatures T_α , T_β and T_γ determined by DMTA at 1 Hz for the four PPA, are listed in Table 9. As shown by the data displayed in Table 9, the increase in PA6T content induces a slight increase of the α -relaxation temperature of 6°C , which is also observed in literature for other polyamides [78], [158]. A weak and wide shoulder is also observed in our measurements around 70°C and can be associated with departure of water [80], [81]. As measured by Karl Fischer, our polymers contain about 700 ppm of water. A departure of water contained in the polymer causes a shift of the relaxation towards high temperatures.

Table 9 – Temperatures of the different relaxations α , β , and γ for each polymer determined at 1 Hz.

Copolyamides	T_α ($^\circ\text{C}$)	T_β ($^\circ\text{C}$)	T_γ ($^\circ\text{C}$)
Polyamide A	128	-52	-141
Polyamide B	129	-47	-140
Polyamide C	134	-49	-138
Polyamide D	128	-42	-130

3.2.1 Time/temperature dependence of relaxations

From the DMTA curves obtained at different frequencies (0.1, 1, 10, 50 and 75 Hz), a time/temperature dependence of the γ , β and α relaxations processes $\log\tau = f(1000/T)$ for each polymer can be established and is shown in Figure 60.

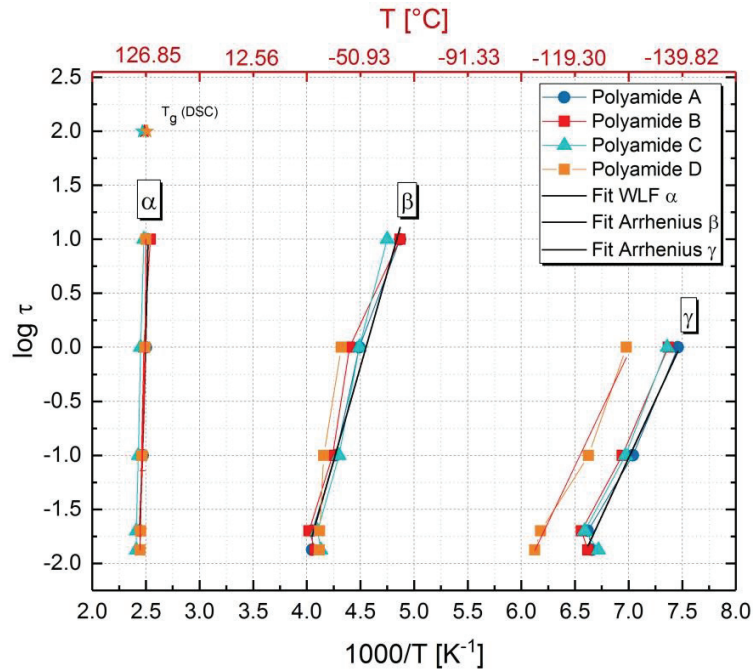


Figure 60 – Time/temperature relaxations map for the four PPA. From left to right, the different relaxations are shown: α , β and γ , as well as the T_g determined by DSC.

The main relaxation, α , follows the Williams-Landel-Ferry equation (WLF) [159] defined as follow [77]:

$$\log(a_T) = \frac{-C_1(T - T_{ref})}{C_2 + (T - T_{ref})} \quad (50)$$

where C_1 and C_2 are the WLF constants, and T_{ref} is the arbitrary chosen reference temperature defined as 300 K.

Secondary relaxations, γ and β , were fitted using an Arrhenius law:

$$\tau(T) = \tau_0 \exp \frac{E_A}{RT} \quad (51)$$

with E_A , the activation energy, τ_0 the characteristic time, R the ideal gas constant and T the temperature. Using the values obtained in the Arrhenius fit, the entropy related to each relaxation can be calculated (using this relation: $\tau_0 = \tau_{Debye} \exp \frac{\Delta S}{R}$). From this value, the free energy ΔG can be calculated for each relaxation at a reference temperature T_0 of 300K ($\Delta G = E_A - T_0 \Delta S$). Table 10 shows the activation energy

E_A , the characteristic time τ_0 , the entropy $-T\Delta S$ and the free energy ΔG of the γ and β relaxations for each PPA.

Table 10 – Activation energy E_A , characteristic time at infinite temperature τ_0 , entropy $-T\Delta S$ and free energy ΔG of the γ and β relaxations for each PPA.

Polymer	γ -relaxation				β -relaxation			
	E_A (kJ.mol ⁻¹)	τ_0 (s)	$-T_\gamma\Delta S$ (kJ.mol ⁻¹)	ΔG (kJ.mol ⁻¹)	E_A (kJ.mol ⁻¹)	τ_0 (s)	$-T_\beta\Delta S$ (kJ.mol ⁻¹)	ΔG (kJ.mol ⁻¹)
Polyamide A	41.16	10 ^{-16.1}	10.35	17.75	66.5	10 ^{-15.8}	15.62	45.4
Polyamide B	43.37	10 ^{-16.7}	12.05	16.3	66.04	10 ^{-15.6}	15.71	45.2
Polyamide C	46.66	10 ⁻¹⁸	15.48	12.4	85.06	10 ⁻²⁰	34.65	38.7
Polyamide D	40.06	10 ^{-14.7}	7.03	24.6	88.41	10 ⁻²⁰	37.64	39.6

3.2.2 Secondary relaxations

For the γ relaxation, the activation energy E_A is in the usual range of 40 kJ.mol⁻¹ (from 40 to 46 kJ.mol⁻¹) as reported in literature by Laurati et al for PA6,6/6I copolymers and Laredo et al for PA 6 [80], [81], [160]. The prefactor τ_0 is smaller than the expected value. Indeed, τ_0 should be equal to the Debye time ($\tau_{\text{Debye}} = 10^{-12}$ s [161]) if there is no contribution to the free energy barrier. Very small relaxations time values are an indication of an entropic contribution. Note that Laurati et al and Laredo et al have observed in the presence of water smaller values of τ_0 , close to the values determined for our polymers (see Table 10) [80], [81].

The value of ΔG (about 17 kJ.mol⁻¹) for polyamides A and B are similar to the rotational barrier for the C-C torsion motion [162], [163].

In the case of the β -relaxation, for the amorphous polyamide A, the free energy associated to this relaxation, ΔG , is 45.4 kJ mol⁻¹ which is in agreement with the value determined by Bocahut et al for the highest free energy barrier associated to amide rotation ($\Delta G = 40 \pm 5$ kJ mol⁻¹) [73]. Note that the entropy ΔS of polyamide C is twice the entropy of polyamides A and B. Small values of ΔS for polyamides A and B indicate that the motions responsible for the β -relaxation are very localized modes [78], [158]. On the contrary, the entropy ΔS is twice for polyamide C (based mainly on terephthalic acid) which is an indication that the motional cooperativity is higher [78]. The entropy ΔS is also twice for polyamide D

(based mainly on isophthalic acid). Polyamide D has a similar structure to polyamide A, so we should have the same entropy. This is not what is observed here.

3.2.3 Main relaxation

The α -relaxation can be fitted using the WLF equation mentioned above (Equation 50). The WLF constants C_1 and C_2 were respectively 7.54 and 32.33K, for the four PPA. C_1 and C_2 WLF constants can be reported to T_g using the following equations [148]:

$$C_1^g = \frac{C_1 C_2}{C_2 + T_g - T_{ref}} \quad (52)$$

$$C_2^g = C_2 + T_g - T_{ref} \quad (53)$$

where C_1 and C_2 are the WLF constants, T_g is the glass transition temperature determined by DSC for each polymer and T_{ref} is the arbitrary chosen reference temperature defined as 300 K.

The WLF constants C_1^g and C_2^g are reported in Table 11. No significant difference was observed in the WLF constants.

Table 11 – WLF fitting parameters for the α -relaxation.

Copolyamides	C_1^g	C_2^g (K)
Polyamide A	1.81	134.68
Polyamide B	1.81	134.78
Polyamide C	1.77	137.88
Polyamide D	1.83	132.98

3.2.4 Time-Temperature Superposition (tTS)

Figure 61 shows the evolution of the storage modulus E' as a function of the frequency, at several temperatures for polyamide A. The increase of the storage modulus E' with frequency is clearly shown, as well as a decrease of this modulus when increasing the temperature.

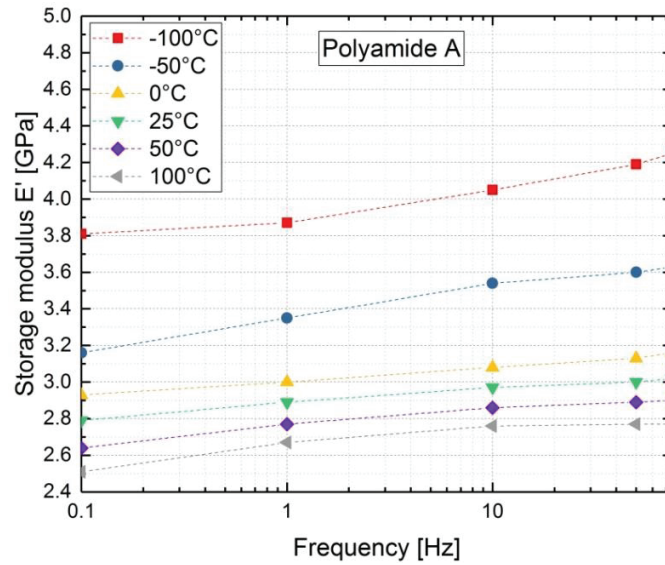


Figure 61 – Evolution of the storage modulus E' with the frequency, for several temperatures for polyamide A.

The storage modulus E' is equivalent for different experimental conditions. For example, as shown in Figure 61, at 50°C and 1 Hz, the storage modulus E' is equivalent to the storage modulus E' at 100°C and at a frequency of 10 Hz. The storage modulus E' has a strong dependency in frequency and temperature. The results obtained in frequency sweep experiments at several temperatures are shifted with a horizontal shift factor, a_T , along the frequency scale. This allowed us to establish a master curve at a reference temperature of 130°C. The master curve obtained is shown in Figure 62, as well as the corresponding horizontal shift factor as a function of the temperature.

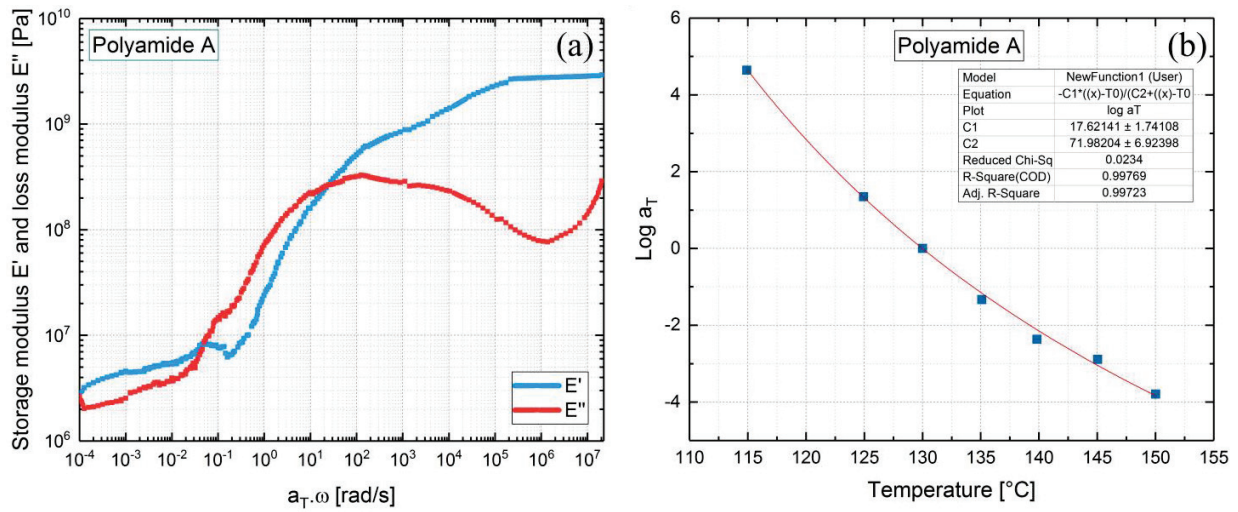


Figure 62 – Master curve of polyamide A. The reference temperature is the glass transition as determined by DSC (a). (b): Corresponding horizontal shift factor as a function of the temperature. Symbols are experimental data and the curve corresponds to WLF fit.

The horizontal shift factor a_T can be fitted with the WLF equation. C_1 and C_2 WLF constants are respectively 17.62 and 71.98K.

3.2.5 Thermo-mechanical properties of Polycarbonate and PMMA

The temperature dependence of the loss modulus E'' at 1Hz for polycarbonate and PMMA found in literature is shown in Figure 63.

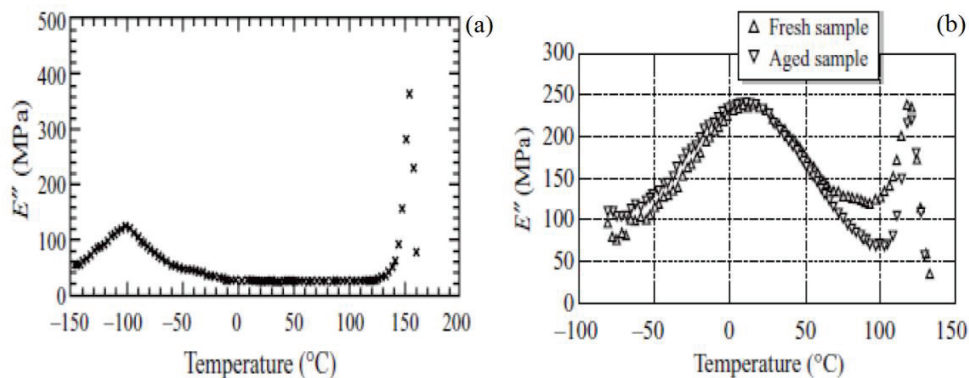


Figure 63 – Evolution of the loss modulus E'' with the temperature at 1Hz. (a) Neat BPA-PC (from [164]); (b) PMMA (quenched or physically aged) (from [165]).

For the polycarbonate, between the temperature range from -150°C to 170°C , two relaxations processes can also be observed. The α -relaxation is observed at high temperature, around 150°C at a frequency of 1 Hz. The β -relaxation is observed at low temperature, around -100°C at 1Hz. The temperature of the β -transition is very low, which reflects the very ductile behavior of this polymer. The activation energy of the β -relaxation is determined equal to $83 \pm 5 \text{ kJ}\cdot\text{mol}^{-1}$ [44], which is close to the value determined for polyamide D.

For the PMMA, between -100°C and 150°C , two relaxations processes can be determined. At around 115°C , the α -relaxation is visible. In the temperature range from -50°C to 100°C , a broad peak is visible and corresponds to the β -relaxation of the PMMA. The maximum of this peak at 1 Hz is around 10°C [165]. The activation energy determined for the β -relaxation is about $60 \text{ kJ}\cdot\text{mol}^{-1}$ [44], which is close to the values determined for polyamides A and B.

3.3 Proton Nuclear Magnetic Resonance

^1H NMR analysis was performed in order to confirm the composition of the different PPA (6I and 6T fractions), as well as to determine the number-average molecular weight, M_n of each polymer and the nature of the chain ends.

The 6I/6T ratio can be calculated by integrating the signals corresponding to the aromatic protons of each motif (6I or 6T). The chemical shift of the aromatic protons as well as their integral are shown in Table 12 with a 10% error bar.

Table 12 – Chemical shift of the aromatic protons and their corresponding integration.

Chemical shift (ppm)	Aromatic protons			
	a	b	d	c
	8.03	7.89	7.81	7.63
Polyamide A	71.3652	140.6451	118.669	74.6423
Polyamide B	50.6508	103.4588	196.975	54.5008
Polyamide C	34.487	67.1286	274.2085	36.2507
Polyamide D	69.1017	148.734	131.6334	74.3883

Using Equation 29 (2.3.2.3), the 6I/6T ratio of each polymer can be calculated with a 10% error bar. For each PPA, the 6I/6T ratio is displayed in Table 13.

Table 13 – 6I/6T ratio of each PPA obtained with ^1H NMR.

	6I/6T ratio (%)
Polyamide A	70.7/29.3
Polyamide B	51.4/48.6
Polyamide C	33.5/66.5
Polyamide D	69/31

Polyamides A and D are similar with a 6I/6T ratio of about 70/30. Polyamide B is a low semi-crystalline PPA with a 6I/6T ratio of 51/49. Polyamide C has a 6I/6T ratio of 33/66. The ^1H NMR analysis confirmed the composition of the different PPA.

The nature of the chain ends was determined by ^1H NMR. Chain ends were blocked during synthesis with a monofunctional acetic acid. The quantity of blockers (acetamide content) can be determined by ^1H NMR. The number of acid (CEG) and amine (AEG) end groups are expressed in mmol.kg^{-1} , as well as the quantity of acetamide. From the values determined for CEG, AEG and acetamide, it is possible to calculate a number-average molecular weight, M_n with Equation 28. All the values are presented in Table 14.

Table 14 – Number of acid (CEG) and amine (AEG) end groups, quantity of acetamide and number-average molecular weight M_n determined by Proton Nuclear Magnetic Resonance for each PPA.

	[CEG] (mmol.kg^{-1})	[AEG] (mmol.kg^{-1})	[Acetamide] (mmol.kg^{-1})	M_n (NMR) (g.mol^{-1})
Polyamide A	76	97	44	9217
Polyamide B	4	141	95	8333
Polyamide C	18	190	100	6493
Polyamide D	35	118	80	8584

The number-average molecular weight M_n determined by ^1H NMR are close to those determined by SEC (see paragraph 3.4 below).

3.4 Chemical structure

The chemical structure of the studied polymers was studied by Size Exclusion Chromatography (SEC) and by End Group Titration (EGT). These two techniques allowed us to characterize the molar mass, the polydispersity, and the chemical structure of our PPA. It is important to characterize well the chemical structure because this has an influence on the macroscopic properties. The quantity of branching created during the synthesis of the PPA was estimated using a dosage (BHT quantification).

SEC analysis allows accessing to both number and weight-average molecular weights, M_n and M_w . From M_n and M_w , the polydispersity index I_p can be calculated. Relative values obtained for M_n , M_w and I_p are presented in Table 15. Chromatograms of the four PPA are presented in Figure 64.

As seen in Table 15, the most semi-crystalline PPA, polyamide C, as a high polydispersity index ($I_p = 5.1$). The increase in the dispersity of the chain lengths could be explained by the increase of the terephthalic content in the copolyamide composition, which leads to higher reaction temperature and then more side reactions [55].

Table 15 – Number and weight-average molecular weights, M_n and M_w , and the polydispersity index I_p of each PPA (relative values).

		M_n (g/mol) ($\pm 5\%$)	M_w (g/mol) ($\pm 2.5\%$)	$I_p =$ M_w/M_n
Polyamide A	PA6I/6T 70/30	9356	27963	3.0
Polyamide B	PA6I/6T 50/50	10424	32917	3.2
Polyamide C	PA6I/6T 30/70	6450	32779	5.1
Polyamide D	PA6I/6T 70/30	11576 ($\pm 10\%$)	38337 ($\pm 5\%$)	3.3

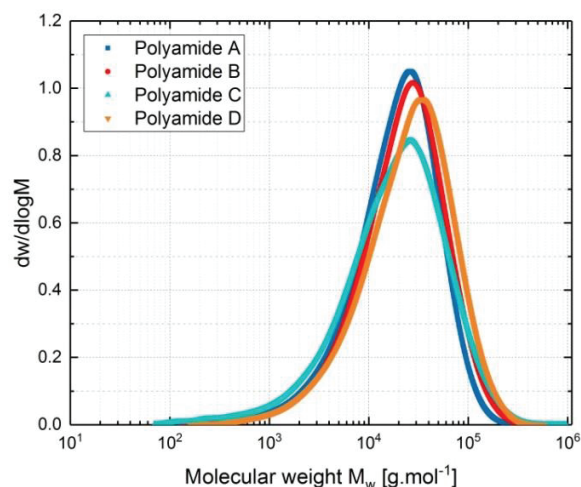


Figure 64 – Chromatograms of the four PPA: polyamide A, polyamide B, polyamide C and polyamide D.

As seen in Table 15, the number-average molecular weight M_n is around 10000 g.mol^{-1} for polyamide A, B and D, and around 6400 g.mol^{-1} for polyamide C whereas the weight-average molecular weight M_w is around 30000 g.mol^{-1} for polyamide A, B and C, and around 40000 g.mol^{-1} for polyamide D. M_n and M_w were used to calculate the polydispersity index I_p as $I_p = M_w/M_n$. The most semi-crystalline PPA, polyamide C, as a high polydispersity index ($I_p = 5.1$). The increase in the dispersity of the chain lengths could be explained by the increase of the terephthalic content in the copolyamide composition, which leads to higher reaction temperature and then more side reactions [55].

With the MALLS detector, we can have access to absolute measure of molecular weights (number and weight-average molecular weights) for three PPA. The results obtained are shown in Table 16.

Table 16 – Number and weight-average molecular weights, M_n and M_w , and the polydispersity index I_p of polyamide A, polyamide B and polyamide C (absolute values).

		M_n abs (g.mol^{-1})	M_w abs (g.mol^{-1})	$I_p =$ M_w/M_n
Polyamide A	PA6I/6T	12800	24550	1.9
	70/30	($\pm 3.5\%$)	($\pm 0.4\%$)	
Polyamide B	PA6I/6T	14270	30700	2.2
	50/50	($\pm 12.3\%$)	($\pm 1.0\%$)	
Polyamide C	PA6I/6T	15270	34740	2.3
	30/70	($\pm 3.5\%$)	($\pm 0.4\%$)	

In light scattering, small masses are not well detected. The value of absolute M_n is much higher than the relative M_n determined in PMMA equivalent because they are overestimated. M_w absolute does not take into account small masses. We can therefore recalculate absolute M_n using the following formula:

$$M_n^{abs} = \frac{M_w^{abs}}{I_p [PMMA]} \quad (54)$$

Recalculated absolute values of M_n are shown the table below (Table 17).

Table 17 – Absolute Number-average molecular weight, M_n of polyamide A, polyamide B and Polyamide C (recalculated values).

		M_n abs (g.mol^{-1}) ($\pm 5\%$)
Polyamide A	PA6I/6T 70/30	8214
Polyamide B	PA6I/6T 50/50	9721
Polyamide C	PA6I/6T 30/70	9835

Chain ends were blocked during synthesis step with a monofunctional acetic acid. The End Group Titration (EGT) was performed by dissolution of the polyamide sample in a solvent and by a potentiometric back titration of the amine $-\text{NH}_2$ and acid $-\text{COOH}$. The number of acid (CEG) and amine (AEG) end groups are expressed in mmol.kg^{-1} . From the values determined for CEG and AEG, and with a quantity of blockers determined previously by ^1H NMR (Acetamide content), it is possible to calculate an absolute number-average molecular weight, M_n with Equation 28 (see Chapter 2). Only the two amorphous PPA were soluble and so could be analyzed. The number of acid (CEG) and amine (AEG) end groups and the number-average molecular weight M_n are presented in Table 18.

Table 18 – Number of acid (CEG) and amine (AEG) end groups and number-average molecular weight M_n obtained by End Group Titration for polyamide A and polyamide D.

	[CEG] (mmol.kg^{-1})	[AEG] (mmol.kg^{-1})	M_n (EGT) (g.mol^{-1})	M_n (abs, SEC) (g.mol^{-1})
Polyamide A	121.1	37.4	9876	8214
Polyamide D	83.2	38	9940	N/A

The number-average molecular weight, M_n , calculated from EGT data is close to the absolute number-average molecular weight determined by SEC analysis.

As explained in the previous chapter, secondary reactions may occur during the polyamide synthesis. A monomer with three amine sites can react with the acid monomer to form a branched polymer. The presence of branched chains may explain the variations in the polydispersity index from 3.0 to 5.1 [124]. As observed in Table 4, the values of polydispersity are larger than 2, which is the value expected by Flory's theory for linear polycondensation [124], [125].

In PA6I, a single branching reaction was considered. It is the reaction between two diamines or two amide chain ends, as shown in Figure 41. Bis-(hexamethylene) triamine (BHT) can be formed during the reaction. The concentration of BHT is determined by dosage after hydrolyzation of polyamide for each PPA and is shown in Table 19. The BHT concentration is given in ppm (parts per million) referred to the initial polyamide weight.

Table 19 – Quantity of branching formed during reaction by formation of BHT for the four PPA. The polydispersity index I_p was determined by SEC.

	BHT (ppm)	I_p
Polyamide A	2291	3.0
Polyamide B	5908	3.2
Polyamide C	7929	5.1
Polyamide D	5333	3.3

The most semi-crystalline PPA, polyamide C, has the higher quantity of branching formed during reaction with 7929 ppm of BHT. Polyamide C has also the largest polydispersity index I_p ($I_p = 5.1$), as seen in Table 19.

The polymer with the lowest quantity of BHT also has the lowest polydispersity index. The polydispersity index reflects the presence of branched chains.

The advantage of SEC over the End Group Titration (EGT) is that it provides directly the number and weight-average molecular weights, M_n and M_w , and the polydispersity index I_p .

3.5 Conclusion

In this chapter, the thermal properties were determined by DSC for the PPA, polycarbonate and PMMA studied. The introduction of a fraction of terephthalic acid in the polymer mainly composed of isophthalic acid leads to a change in the glass transition T_g of the copolymer. When 6T fraction increases, the glass transition also increases. This increase can be related to the positions of the carboxylic acid functions on the aromatic ring on both terephthalic and isophthalic acids. The positions of the carboxylic acid functions on the aromatic ring lead to rigid and straight PA6T chains, with a reduced mobility and thereby a higher glass transition temperature T_g than PA6I is observed.

The thermomechanical properties of the PPA have been studied through DMTA experiments. All the studied PPA exhibit a characteristic dynamic mechanical response for a thermoplastic material. Three relaxations processes have been identified, denoted γ , β and α from the lower to the higher temperature.

The chemical structure of the studied PPA was studied by Size Exclusion Chromatography (SEC) and by End Group Titration (EGT). SEC analysis allows accessing to both number and weight-average molecular weights, M_n and M_w . The quantity of branching created during the synthesis of the PPA was estimated using a dosage (BHT quantification). ^1H NMR analysis was used in order to determine the composition of the different PPA (6I/6T ratio). This ratio was calculated by integrating the signals corresponding to the aromatic protons of each motif (6I/6T). The nature of the chain ends was also determined by ^1H NMR, as well as the quantity of blockers (acetamide content).

Chapter 4 – Macroscopic study of the mechanical properties

This chapter exposes the results obtained regarding the mechanical behavior of PPA, polycarbonate and PMMA. First, the brittle-to-ductile transition temperature is determined by Charpy impact strength at different temperatures. Then, we describe the tensile and compressive behaviors of the different polymers. From the true strain - true stress curves obtained in tensile test, the effect of the temperature on the Young modulus and the yield stress, the influence of the geometry used and the injection process, as well as the evolution of the volume variation and the Poisson's ratio are described. The strain hardening behavior observed at large strain in compression and the influence of the temperature are described. The surface tensions of polymers before and after deformation are presented.

4.1 Characterization of the brittle-ductile transition T_{bd}

4.1.1 Charpy impact strength

The brittle-ductile transition, T_{bd} , is an essential notion when dealing with ultimate mechanical properties of engineering plastics such as polyphthalamides. The T_{bd} may be defined in Charpy impact test or in uniaxial tensile experiments. Charpy impact test is a dynamic test at a frequency of 10^3 Hz. Charpy impact strength tests are conducted on all the studied samples as described in the experimental section. For polyamide A, polyamide B and polyamide C, specimens are obtained via the injection process A, whereas for polyamide D, specimens are obtained via the process B. For each polymer, measurements are performed at different temperatures, in order to determine the brittle-ductile transition temperature T_{bd} . Figure 65 shows the impact strength as a function of temperature (brittle-to-ductile transition curves) for all the studied samples.

All the curves show a well-defined transition from brittle failure at low temperature, where the impact strength is of the order 3 to 11 kJ/m², to ductile failure at high temperature where the resilience is of an order of 130-160 kJ/m². The brittle-ductile transition was determined for the four PPA (Figure 65). For the amorphous polymers, polyamide A and polyamide D, the T_{bd} is equal to 140°C and 137°C, respectively. For the low semi-crystalline PPA, polyamide B, the T_{bd} is close, 135°C. For these three polymers, we can see that this transition T_{bd} is very close to the glass transition T_g determined by DSC (see Table 4). For the semi-crystalline PPA, polyamide C, the T_{bd} is higher and is 192°C.

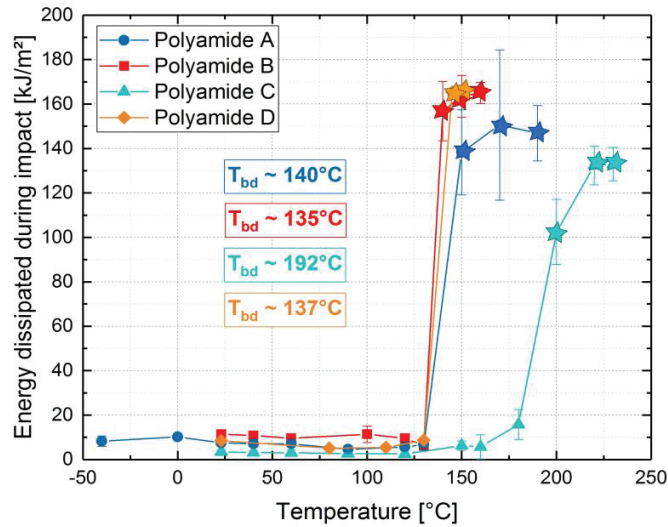


Figure 65 – Brittle-ductile transition curves of all the PPA samples obtained from Charpy impact measurements. Evolution of the energy dissipated by the material with the temperature and the brittle-ductile transition temperature T_{bd} . The stars represent the unbroken samples above the T_{bd} .

The same behavior is observed for different PA6,6 with a well-defined ductile-brittle transition with a resilience at low temperature of order 2 to 5 kJ/m² [75]. At high temperature, the resilience of the PA6,6 is of order 60 kJ/m², which is lower than for the studied PPA. The brittle-ductile transition temperature of RT-PMMA (rubber-toughened PMMA) is about 20°C, which is very low compared to the studied PPA [44]. The resilience in the ductile regime at 150°C is high (from 130 to 160 kJ/m²). The brittle-ductile transition temperature is also very high.

The impact performance is influenced by the crystallinity: the ductile-brittle transition temperature is higher for the most semi-crystalline PPA, polyamide C (192°C).

Table 20 – Brittle-ductile transition temperature T_{bd} determined by Charpy impact strength of each PPA with their associated crystallinity determined by DSC.

Copolyamide	Crystallinity (%)	T_{bd} (°C)
Polyamide A	0	140
Polyamide B	4.3	135
Polyamide C	16.4	192
Polyamide D	0	137

The fracture surfaces of polyamides A, B and C were observed in SEM (Figure 66 and Figure 67). Figure 66 shows SEM observations of the fracture surface after Charpy impact test at 23°C. The failure is brittle for the three polymers, as expected with an impact strength of around 3 to 11 kJ/m².

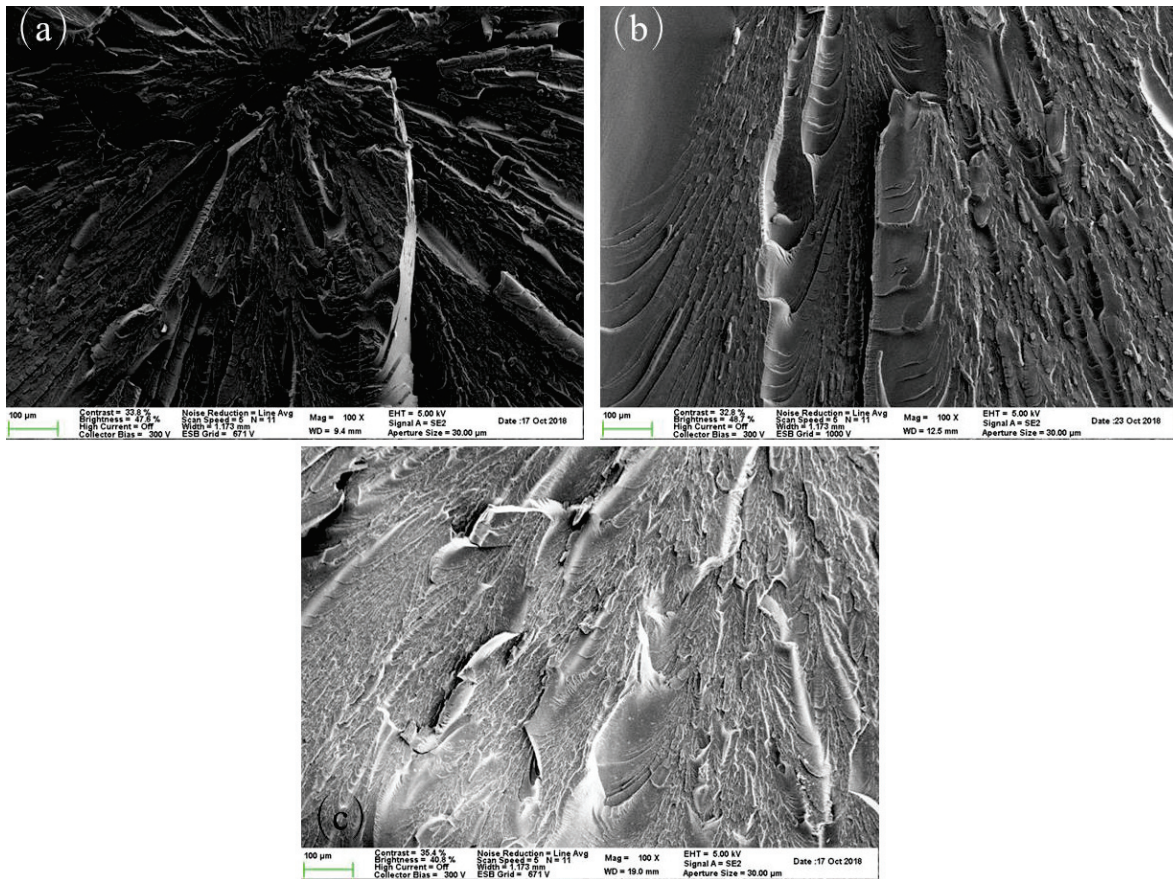


Figure 66 – SEM observations of the fracture surface after Charpy impact test at 23°C for (a) polyamide A, (b) polyamide B and (c) polyamide C.

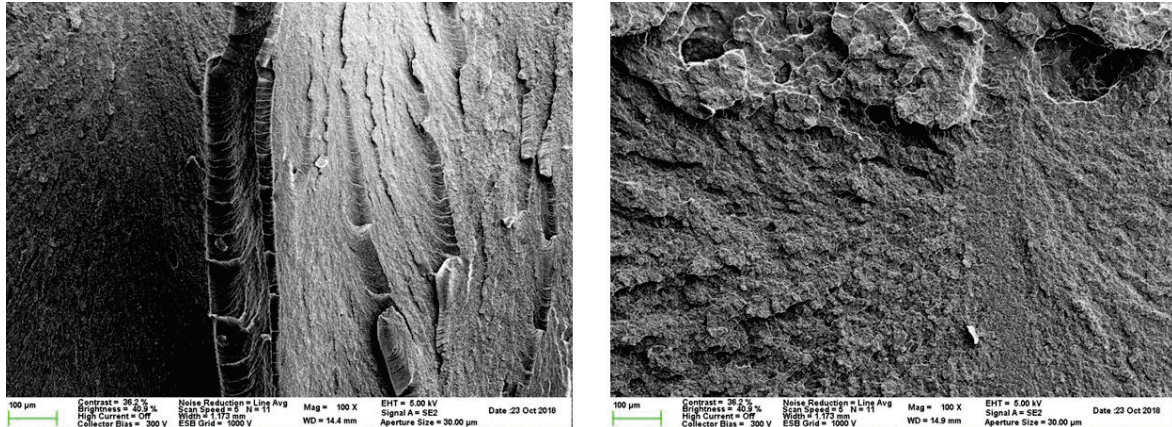


Figure 67 – SEM observations of the fracture surface after Charpy impact test at 160°C for polyamide C.

Figure 67 shows SEM observations of the fracture surface after Charpy impact test at 160°C for polyamide C. This temperature is at the beginning of the ductile-brittle transition. The SEM images show a semi-ductile failure, with a failure surface heterogeneous. During the crack initiation, a toughness mechanism is developed, but the propagation remains catastrophic and leads to failure (resilience of 18 kJ/m²). Domains with a ductile failure and domains with a brittle failure coexist on the same fracture surface and are randomly positioned over the fracture surface.

4.1.2 Influence of frequency on T_{bd}

The brittle-ductile transition temperature T_{bd} can be defined from uniaxial tensile experiments as the temperature at which failure occurs at the yield stress σ_y . The true stress-true strain curves obtained from tensile experiments at different temperatures and at a constant true strain rate $\dot{\epsilon} = 1.10^{-3} s^{-1}$ are presented in Figure 68 for the four polyamides. A decrease in temperature induces an increase of the rigidity of the polymer and a transition from a ductile to a brittle behavior, as shown in Figure 68. Below 110°C, polyamide C is considered brittle, the failure is reached before reaching the yield stress σ_y . When the temperature increases, the mobility of the chains is accelerated and the behavior becomes more ductile and a yield point can be determined, as observed for polyamide A and B, and above 110°C for polyamide C in Figure 68-c). The temperature T_{bd} is defined for polyamide A and polyamide B below -40°C. For polyamide C, T_{bd} is clearly visible and is determined at 110°C. Because of the limitation of the temperature of the temperature chamber, we cannot perform tensile tests below -40°C. Contrary to the Charpy impact strength described in the previous paragraph (§4.1.1), the tensile test is a quasi-static test at a frequency of 10⁻³ Hz. We can emphasize the influence of the frequency on this temperature: the

higher the frequency, the higher the temperature T_{bd} . As for the Charpy impact test, the ductile-brittle transition temperature is strongly influenced by the crystallinity and is higher for the most semi-crystalline PPA, polyamide C (192°C).

In the case of polyamide D, the brittle-ductile transition temperature T_{bd} in tensile test was not determined. According to Figure 68-d, this polymer is ductile at 23°C and $\theta = 0^\circ$. The brittle-ductile transition is below 23°C.

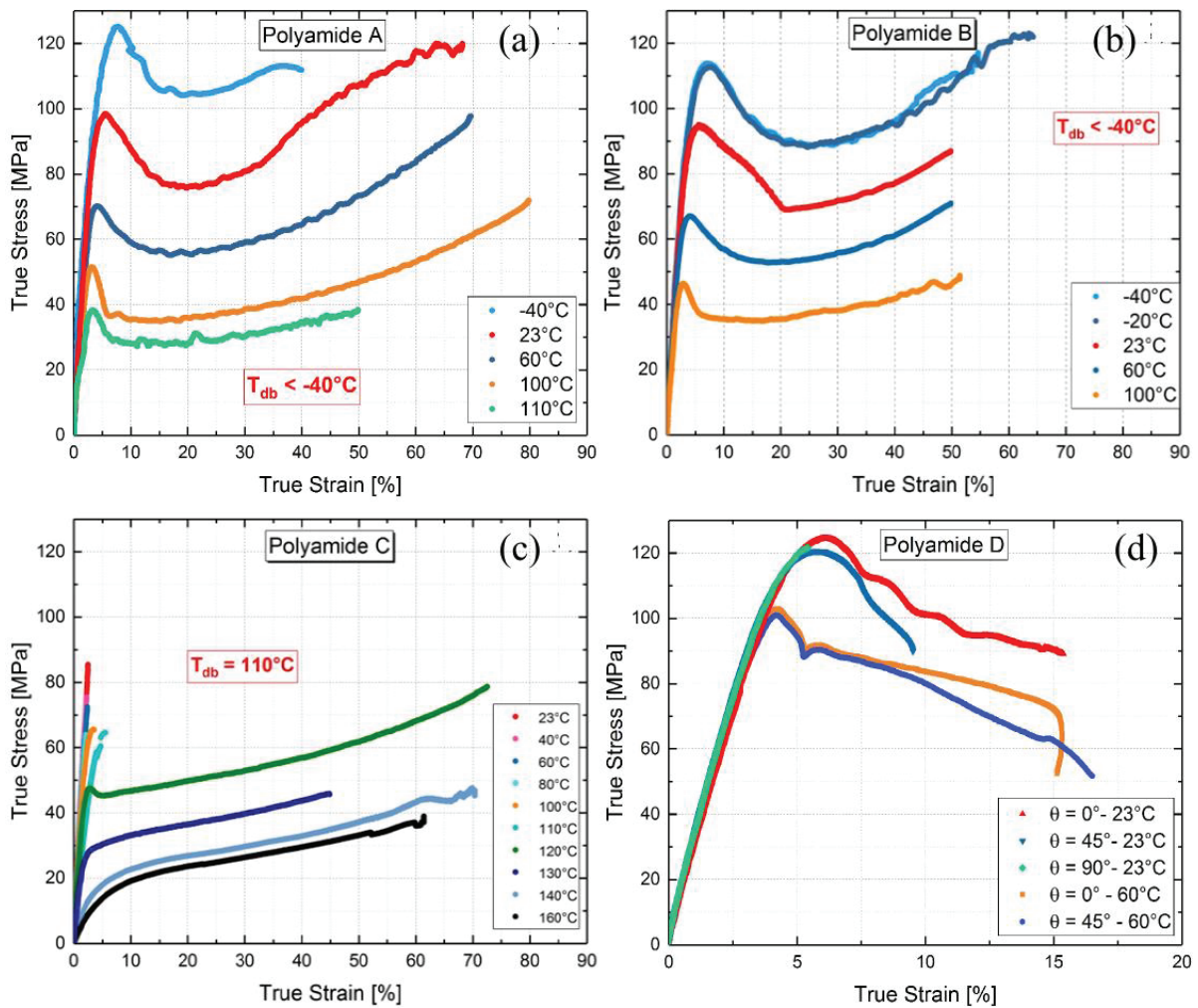


Figure 68 – Uniaxial tensile true stress-true strain curves determined for polyamide A (a), polyamide B (b), polyamide C (c) and polyamide D (d) at several temperatures and a strain rate of 1.10^{-3} s^{-1} .

4.2 Tensile behavior

Figure 68 represents the true stress-true strain curves obtained from tensile experiments for the four polyamides. The behavior of all samples is essentially the same for polyamide A, polyamide B and polyamide C. Beyond yield, a strain softening followed by a strain hardening behavior can be observed. The strain hardening behavior is also observed in others amorphous polymers such as cellulose acetate, PC, PMMA or PVC ([23]–[25], [166]). It can be defined as a stress increase at large strains with a characteristic slope (strain hardening modulus E_{SH}). These three PPA have a very ductile behavior. Beyond the brittle-ductile transition T_{bd} , the samples did not break but reached the limit displacements of the tensile machine, which is a limitation for the study of strain hardening. The study of strain hardening will be detailed in the case of the compression test (see paragraph 4.3). The strain softening amplitude is larger at low temperatures than at high temperatures, which is similar to the behavior observed for PMMA or PC [66], [165].

Polyamide D samples obtained with process B have a completely different behavior, as seen in Figure 68-d. For the process B, tensile specimens have been cut at three different angles θ between the direction of injection and the direction of the tensile test. Beyond yield, no strain hardening behavior is observed. At 23°C and $\theta = 0^\circ$ and 45° and at 60°C and $\theta = 0^\circ$ and 45° , the appearance of shear bands is observed directly after the yield. Moreover, polyamide D is less ductile than the other PPA studied. When the shear bands have spread on both sides of the sample, the rupture is observed. At 23°C and $\theta = 90^\circ$, the sample is brittle and the failure occurs at 5% of true strain. The influence of the injection process (process A vs process B) is detailed in paragraph 4.2.5 and compares the ISO-527 geometry and the hourglass geometry.

The true stress-true strain curves obtained from tensile experiments for polycarbonate and PMMA at different temperatures are presented in Figure 69.

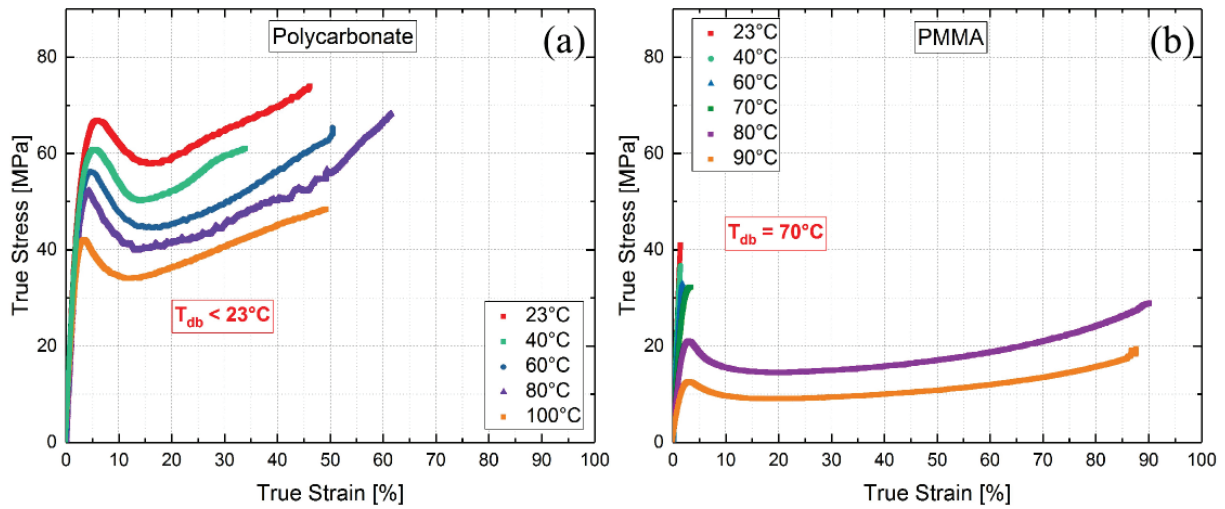


Figure 69 – Uniaxial tensile true stress-true strain curves determined for polycarbonate (a) and PMMA (b) at several temperatures and a strain rate of 1.10^{-3} s^{-1} .

The behavior of polycarbonate and PMMA is close to that observed for polyamide A, polyamide B and polyamide C. Polycarbonate is ductile over the range of temperatures tested, whereas PMMA is brittle up to 70°C. At 70°C, a brittle-ductile transition is observed. At 80°C and 90°C, PMMA is ductile and the failure appears at 90% of true strain. Beyond yield, a strain softening is observed for both polycarbonate and PMMA, followed by a strain hardening, as observed for the three PPA (polyamide A, polyamide B and polyamide C). The strain softening amplitude is larger at low temperatures than at high temperatures, which is similar to literature for other PMMA or PC [66], [165]. All polycarbonate and PMMA samples reach failure.

4.2.1 Temperature dependence of the Young modulus E and the yield stress σ_y

The Young modulus E is calculated from the tangent line in the elastic domain (between 0.05 and 0.25% of true strain) and the yield stress σ_y is defined as the observed maximum stress. Up to the yield, the tensile behavior is not influenced by the process. All samples exhibit the same behavior.

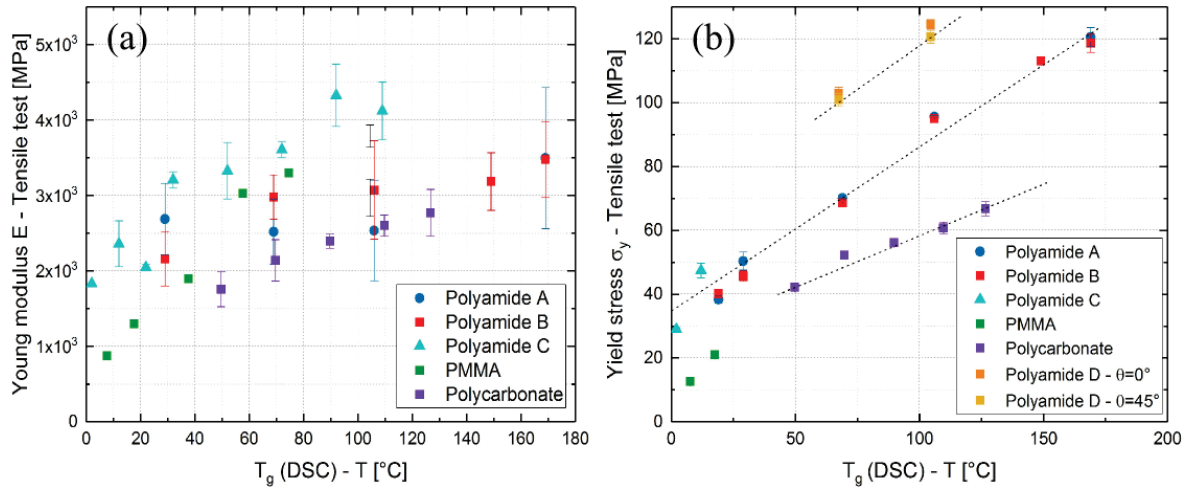


Figure 70 – Evolution of the Young modulus E (a) and the yield stress σ_y (b) as a function of $T_g - T$. Datas are obtained from tensile measurements at a constant strain rate of 1.10^{-3} s^{-1} .

The different samples are compared at a given state of molecular mobility, defined by the difference $T_g - T$, as shown in Figure 70. Young modulus E and yield stress σ_y values are reported for temperatures below the glass transition temperature T_g . When the distance to T_g increases, an increase of the Young modulus E is observed for all polymers tested. Indeed, when increasing the experimental temperature, the Young Modulus E decreases, as observed in Figure 70. This decrease is expected and can be attributed to the visco-elastic behavior of polymer. The yield stress σ_y is observed to decrease strongly when increasing the testing temperature, which is the expected trend for a visco-elastic polymer. The temperature influences the mobility of the polymer's chains. For PPA, no particular relation appears for the Young modulus when plotted as a function of $T_g - T$, whereas the yield stress fall on a linear master curve.

For polycarbonate and PMMA, the Young moduli values determine a linear master curve with a positive slope. The yield stress σ_y has the same behavior as for the PPA. When the distance to T_g increases, an increase of the yield stress σ_y is observed.

All the data concerning the Young modulus and the yield stress are presented in Table 21.

4.2.2 Evolution of the Poisson's ratio ν

Direct measurements of Poisson's ratio have been carried out on PPA, PMMA and polycarbonate during tensile experiments with the VidéoTraction system, under a constant strain rate $\dot{\epsilon} = 1.10^{-3} \text{ s}^{-1}$.

Figure 71 represents the evolution of the Poisson's ratio and the true stress of the different polymers, at different temperatures. For all polymers, the Poisson's ratio is not constant during the tensile deformation.

The initial part of the tensile curve of polyamide A at 60°C and 100°C, polyamide B at 110°C and PMMA at 80°C until the yield, can be characterized by a regular increase of the Poisson's ratio. After the yield, the Poisson's ratio has a tendency to converge to a value of 0.5 (polyamide A, or slightly above 0.5 for polyamide B and PMMA), representative value of incompressibility conditions. Poisson's ratio values higher than 0.5 can be interpreted as scattered around 0.5 and affected by inaccuracies related to the VidéoTraction measurement or by non-homogeneity on a microstructural scale already present in the material (such as crystalline regions, porosity) or developed during the deformation (cavitation [167]–[170]), as seen in literature [171]. For polyamide C, the Poisson's ratio increases until the yield and then no longer varies with deformation (equal to 0.4). For polycarbonate, the Poisson's ratio also increases until the yield but then oscillates between 0.4 and 0.5. As for polyamide B and PMMA, Poisson's ratio values higher than 0.5 can be interpreted as scattered around 0.5 and affected by inaccuracies related to the VidéoTraction measurement or by non-homogeneity on a microstructural scale already present in the material.

The evolution of the Poisson's ratio with the deformation will be discussed in our interpretation of the damage in our polymers (Chapter 5).

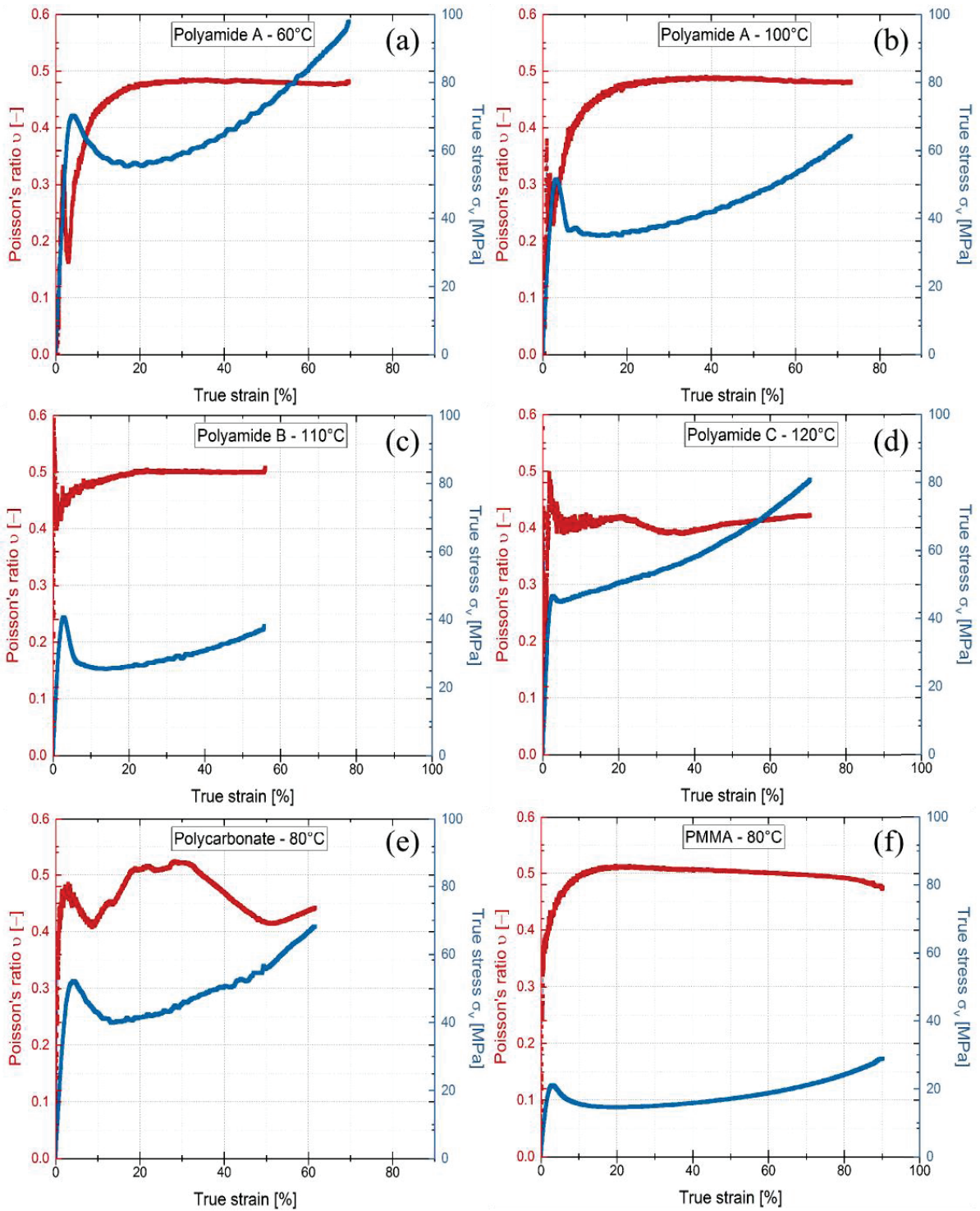


Figure 71 – Evolution of the Poisson's ratio and the true stress of the different polymers: (a) polyamide A at 60°C, (b) polyamide A at 100°C, (c) polyamide B at 110°C, (d) polyamide C at 120°C, (e) polycarbonate at 80°C and (f) PMMA at 80°C.

Table 21 – Mechanical properties of the different polymers studied. Data obtained from Figure 68 and Figure 69.

Polymer	Temperature (°C)	Young modulus E (MPa)	Yield stress σ_y (MPa)
Polyamide A	-40	3496 ± 933	120.5 ± 3
	23	2536 ± 667	95.6 ± 0.3
	60	2521 ± 434	70.1 ± 0.5
	100	2689 ± 475	50.4 ± 2.8
	110	2462 ± 319	38.3 ± 1.1
Polyamide B	-40	3478 ± 502	118.6 ± 2.9
	-20	3186 ± 382	113 ± 0.5
	23	3073 ± 653	95 ± 0.25
	60	2980 ± 293	68.6 ± 0.3
	100	2872 ± 358	45 ± 1.6
	110	2558 ± 165	40.1 ± 0.3
Polyamide C	23	4123 ± 383	N/A
	40	4328 ± 412	N/A
	60	3609 ± 107	N/A
	80	3328 ± 375	N/A
	100	3208 ± 107	N/A
	110	2045 ± 44	N/A
	120	2360 ± 303	47.4 ± 2.3
	130	1830 ± 354	29 ± 0.5
	140	656 ± 216	19.2 ± 1
	160	478 ± 205	15.2 ± 0.5
Polycarbonate	23	2771 ± 310	66.8 ± 2.2
	40	2602 ± 141	60.8 ± 1.8
	60	2394 ± 94	56.1 ± 1.1
	80	2141 ± 275	52.2 ± 0.6
	100	1756 ± 230	42.1 ± 0.5
PMMA	23	3299 ± 148	N/A
	40	3030 ± 246	N/A
	60	1897 ± 169	N/A
	80	1297 ± 203	21 ± 0.3
	90	874 ± 76	12.6 ± 0.5

4.2.3 Volume variation

The volume variation expressed by the term V/V_0 is calculated thanks to the longitudinal strain and the transverse strains (deformation of the sample in thickness and width) measured by VidéoTraction. Figure 72 shows the volume variation V/V_0 with the true strain for each polymer at different temperatures.

Polyamide C, PMMA and polycarbonate display the same tendency: the volume increases with the deformation. For polyamide A, at 60°C and 100°C, the volume increases up to 5% of deformation and then no longer varies with deformation. At 110°C, the volume increases up to 10% of deformation and then decreases. Polyamide B at 100°C and 110°C shows no or very little increase in volume (less than 1%). On the other hand, at 60°C, the volume increases from about 7% to 35% true strain, and then decreases.

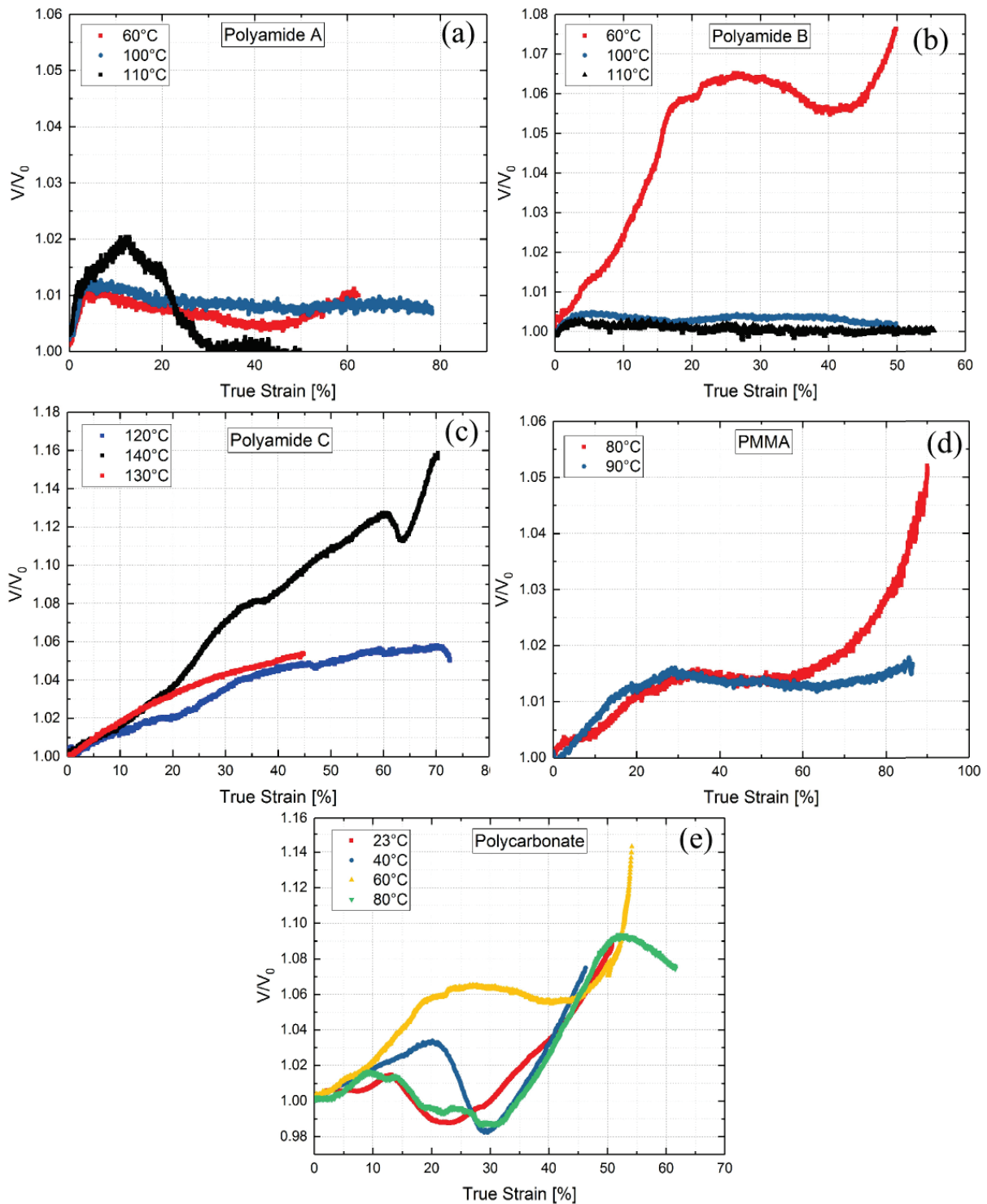


Figure 72 – Evolution of the volume variation V/V_0 with the true strain for each polymer at different temperatures: (a) polyamide A at 60, 100 and 110°C; (b) polyamide B at 60, 100 and 110°C; (c) polyamide C at 120, 130 and 140°C; (d) PMMA at 80 and 90°C and (e) polycarbonate at 23, 40, 60 and 80°C.

4.2.4 Necking: Considère's construction

The Considère's construction consists in plotting the true stress as a function of the extension ratio λ and in looking for the possible existence of tangent(s) starting from the point of abscissa $\lambda = 0$ [44].

The three PPA studied present a necking regime. Their Considère's constructions are shown in Figure 73. We can draw two tangents to the curve from the abscissa point $\lambda = 0$. The point of contact of the first tangent (it is a maximum of the curve) represents the initiation of the necking. The drop in the true stress after yield and after the initiation of necking corresponds to the strain softening. The second tangent (which is a minimum) represents the end of consolidation of the necking. The molecular orientation is sufficient to stiffen the material and strain hardening can occur. It is the case of a stable necking. In the case where a single tangent to the curve can be constructed, we would be in the case of an unstable necking, leading to the rupture of the sample.

We therefore have a stable necking, which confirms the reproducibility of our measurements in this zone with the VidéoTraction system.

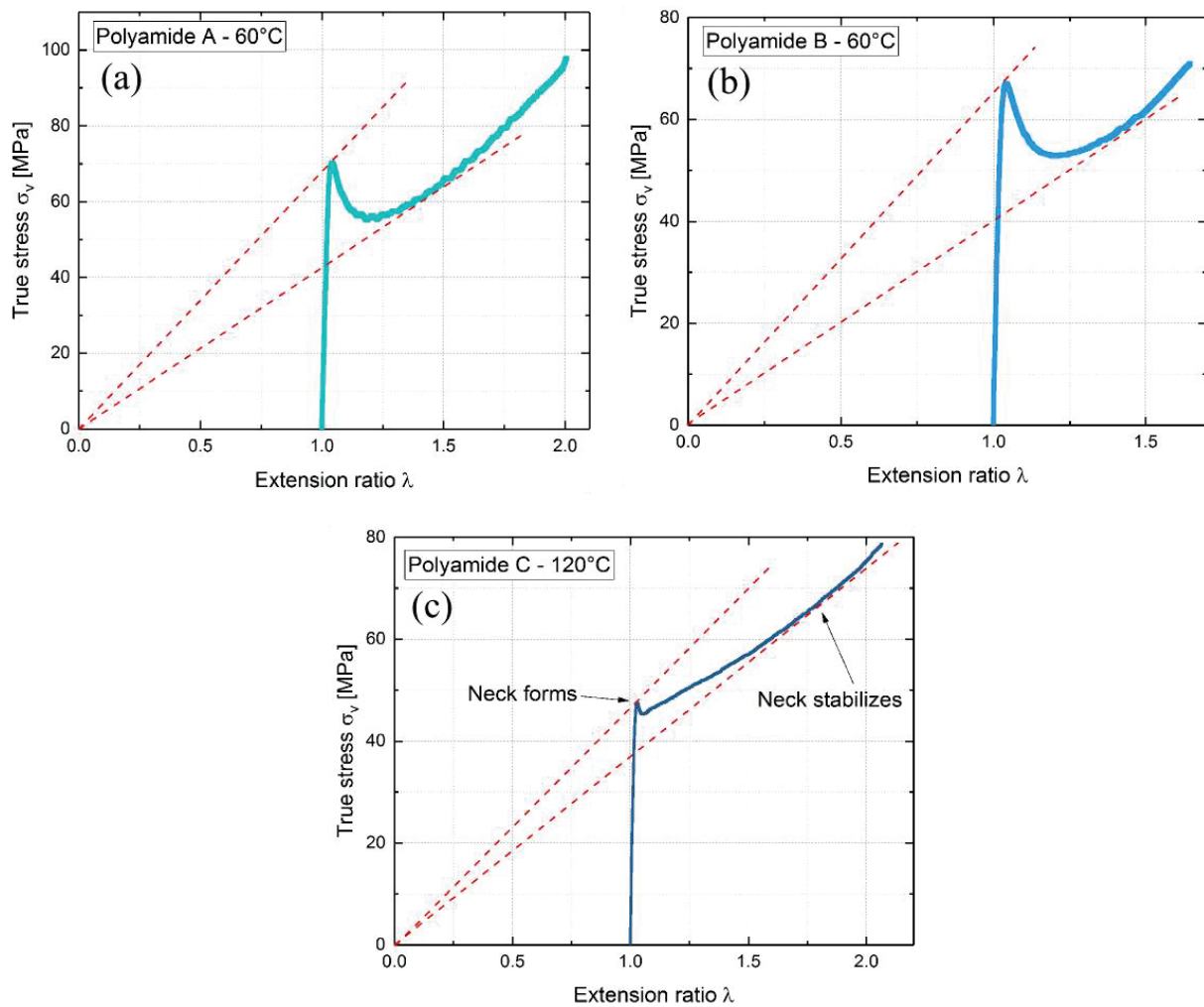


Figure 73 – Considère's construction for polyamide A (a), polyamide B (b) and polyamide C (c).

4.2.5 Influence of the injection process and the polymer chains orientation

During the injection process, the polymer chains are strongly oriented in the direction of injection [172]. It has been reported in literature that processing-induced orientation has an influence on several mechanical properties [166], [173].

The true stress-strain curves obtained for Polyamide C with the process A at different temperatures and at a true strain rate of 1.10^{-3} s^{-1} are plotted in Figure 68-c. The ISO-527 geometry is not adapted to investigate the strain hardening regime. Some tensile measurements have been done on polyamide C specimens processed with the process B. Polyamide D was injection-molded with the process A in order to obtain some tensile specimens with the ISO-527 geometry. During injection, we set the mold at two

different temperatures (30°C and 80°C). 30°C corresponds to the mold temperature used for processing polyamide A, polyamide B and polyamide C with the process A, and 80°C corresponds to the mold temperature of the process B for polyamide D. We study the influence of both the process and the tensile geometry on polyamide C and polyamide D.

For the process B, tensile specimens have been cut at three different angles θ between the direction of injection and the direction of the tensile test. The curvature of the hourglass geometry is larger than ISO-527 geometry ($\phi = 71$), which localizes the constraints at the minimum section during the tensile experiment and favors homogeneous deformation.

The influence of the process and the loading angle θ on the tensile measurements of polyamide C at 120°C and polyamide D at 23°C is shown in Figure 74. The tensile behaviors observed for both processes are different. There is a strong influence of the sample geometry and the injection process on the yield stress σ_y . Indeed, the yield stress is improved with specimens obtained from process B. The yield stress σ_y is higher with process B than with process A (from 48 to 65 MPa for polyamide C, and from 100 to 120 MPa for polyamide D).

With process B, no necking was observed, whether for polyamide C or polyamide D.

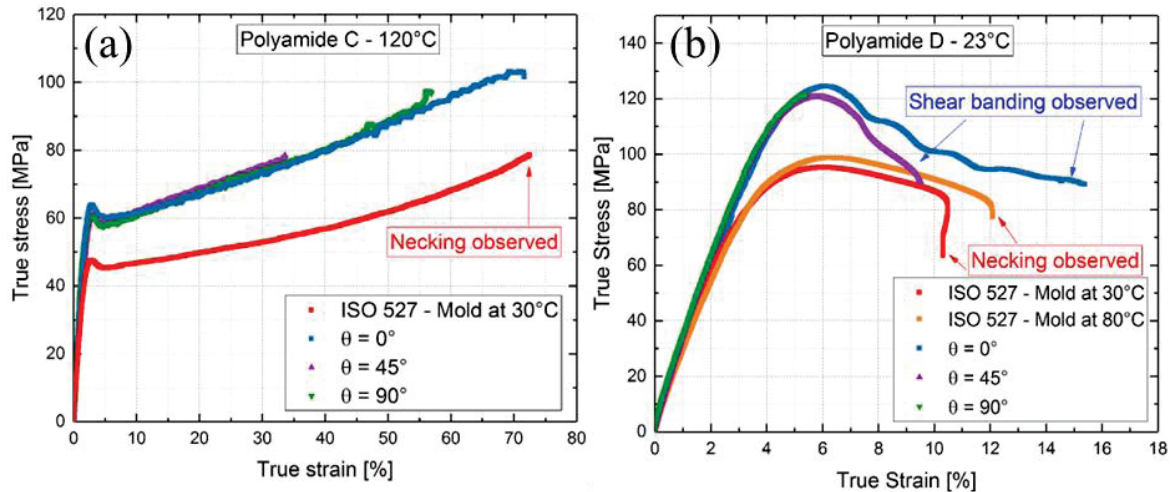


Figure 74 – Uniaxial tensile true stress-true strain curves determined for polyamide C at 120°C (a) and polyamide D at 23°C (b), at a strain rate of 1.10^{-3} s^{-1} for samples obtained from process A (ISO-527) and process B (θ varying from 0° to 90° with respect to the main flow direction).

The different geometry of each polymer tested, as well as their deformations observed are presented in Table 22. The necking and shear banding phenomenon appear just after the yield stress.

Figure 75 shows the necking observed on polyamide A during tensile deformation at 110°C and the apparition of shear band on polyamide D during the tensile deformation at 23°C.

Table 22 – Geometry of the different specimens and the deformation observed.

	Geometry of the specimen	Deformation observed
Polyamide A	ISO-527 (Process A)	Necking
Polyamide B	ISO-527 (Process A)	Necking
Polyamide C	ISO-527 (Process A)	Necking
	Hourglass (Process B)	Homogeneous
Polyamide D	ISO-527 (Process A)	Necking
	Hourglass (Process B)	Shear banding
Polycarbonate	Hourglass	Homogeneous
PMMA	Hourglass	Homogeneous

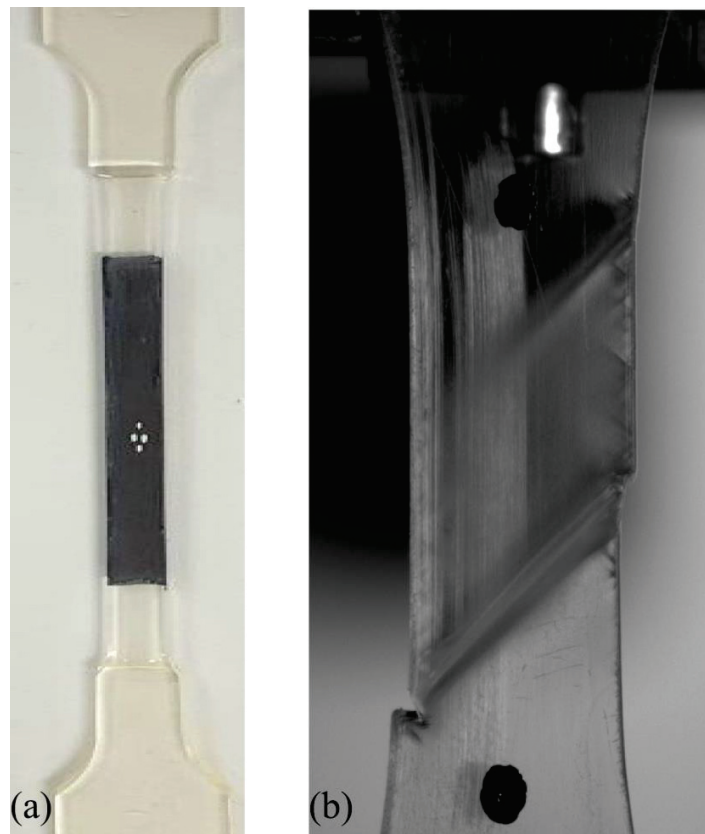


Figure 75 – Picture of the tensile specimens of (a) polyamide A at 110°C and (b) polyamide D at 23°C. (a) The specimen presents a necking phenomenon; (b) The tensile specimen shows the development of shear band.

4.3 Compression behavior

The true stress-true strain curves obtained in tensile tests present a necking phenomenon. We performed compression tests to avoid localization phenomena at large deformation. The behavior at large deformations can be analyzed using the Haward-Thackray ϵ_{HT} [27], [174] variable defined by:

$$\epsilon_{HT} = \lambda^2 - \lambda^{-1} \quad (55)$$

with λ , the relative elongation defined by: $\lambda = \exp(\epsilon_{11}) = \frac{l}{l_0}$.

It is a standard representation for the study of the strain hardening and often used in literature [7], [24].

Figure 76 and Figure 77 show the results plotted as true stress versus $(\lambda^2 - \lambda^{-1})$ for polycarbonate and the four polyamides at several temperatures. A moderate strain softening followed by a strain hardening results in a macroscopic ductile behavior [175].

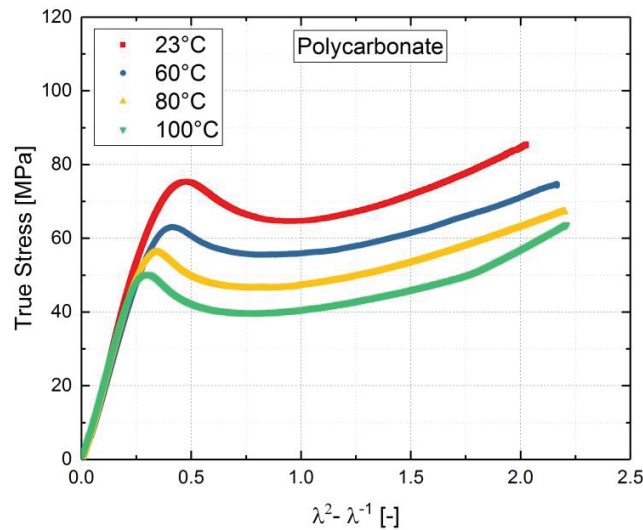


Figure 76 – Compressive behavior of polycarbonate at several temperatures at a strain rate of 10^{-3} s^{-1} .

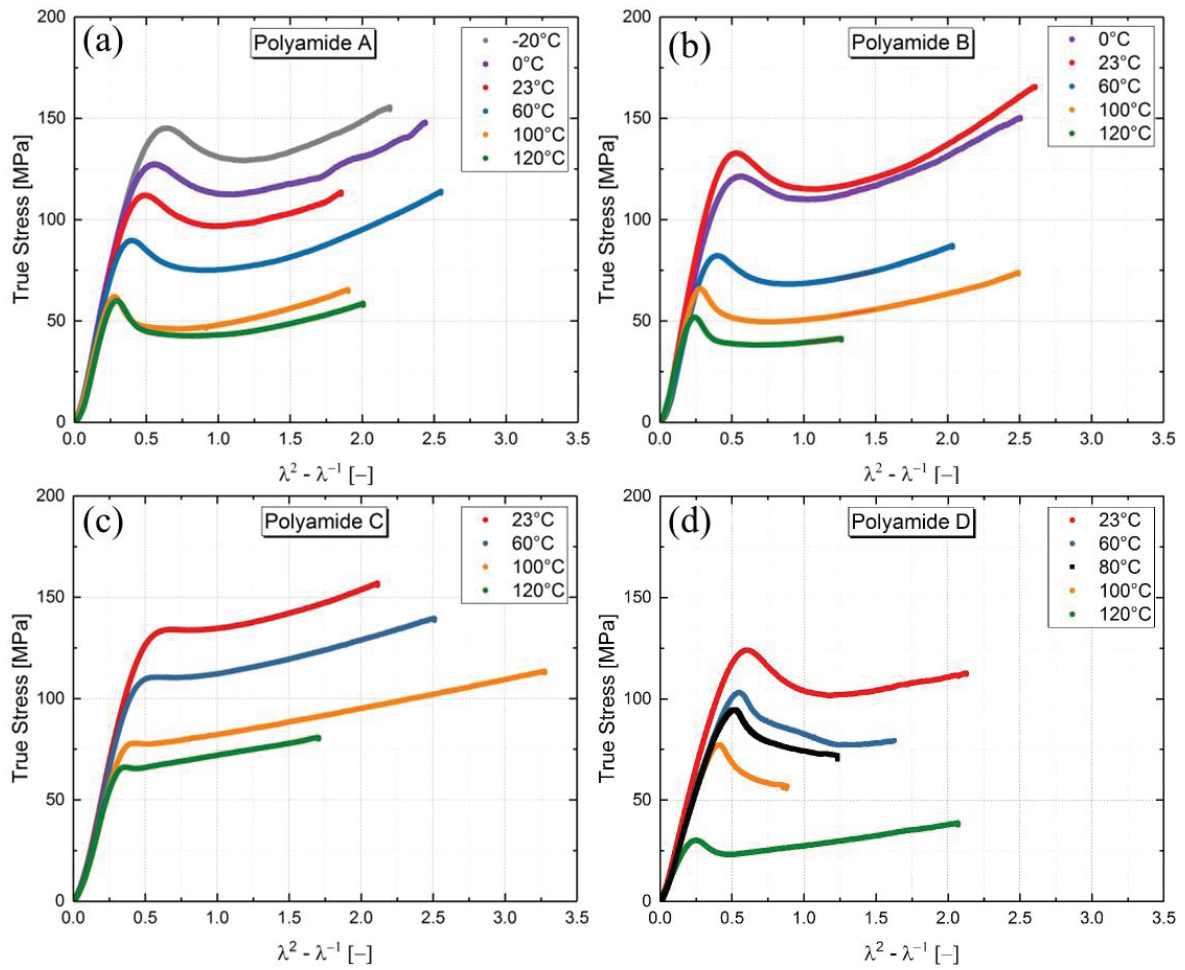


Figure 77 – Compressive behavior of PPA at several temperatures at a strain rate of 10^{-3} s^{-1} : (a) polyamide A, (b) polyamide B, (c) polyamide C and (d) polyamide D.

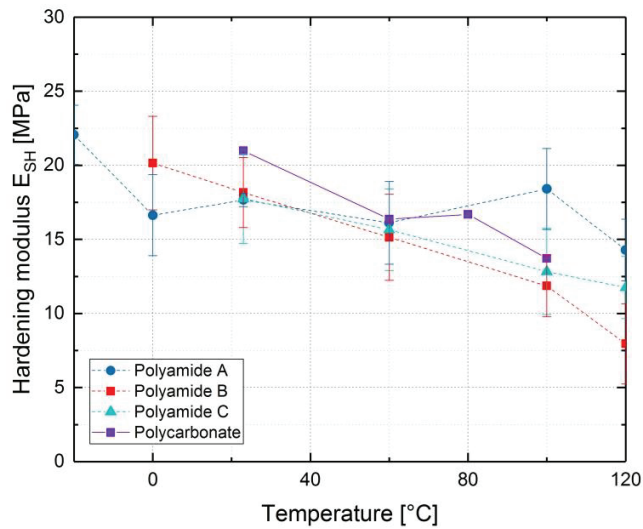


Figure 78 – Evolution of the hardening modulus E_{SH} with the temperature for PPA and polycarbonate. The modulus E_{SH} was determined from the slope of the curves in the strain range 1.25-1.75

From Figure 77-d, no hardening modulus can be determined for polyamide D.

Figure 78 shows the evolution of the strain hardening modulus E_{SH} determined from the true stress – ($\lambda^2 - \lambda^{-1}$) curves with the temperature for each polymer tested. The strain hardening response is the same for the three PPA considered (polyamide A, polyamide B and polyamide C) and for polycarbonate. Values of hardening modulus determined from Figure 76 and Figure 77 are shown in Table 23.

At room temperature, the strain hardening modulus E_{SH} for the three PPA is about 18 MPa. It is more than the strain hardening modulus of PS (13 MPa) [24] but less than other amorphous polymers (29 MPa for PC [24], 75 MPa for PPO [24], 25 MPa for PMMA[7], [63], [176]). The strain hardening modulus E_{SH} for the polycarbonate is about 21 MPa at 23°C, which is in good agreement with literature [24]. The strain hardening modulus of the semi-crystalline PPA is found to be equal to that of the amorphous PPA and is clearly not related to the degree of crystallinity. This was observed in literature by Schrauwen et al with different semi-crystalline polymers (polyethylene, polypropylene and poly(ethylene terephthalate)) [177]. The strain hardening modulus decreases linearly with the temperature for polyamide B, polyamide C and polycarbonate, which is observed in literature by Engels and Van Melick with other polymers such as polycarbonate [24], [175]. For polyamide A, the strain hardening modulus seems no affected by temperature: there is no dependence to temperature.

Table 23 – Hardening modulus E_{SH} in compression determined from the slope of the curves in the strain range 1.25-1.75 for polyamide A, polyamide B, polyamide C and polycarbonate.

Hardening modulus E_{SH} (MPa)	-20°C	0°C	23°C	60°C	80°C	100°C	120°C
Polyamide A	22.06	16.63	17.66	16.12	/	18.40	14.29
Polyamide B	/	20.15	18.17	15.14	/	11.86	7.95
Polyamide C	/	/	17.75	15.65	/	12.83	11.75
Polycarbonate	/	/	20.98	16.37	16.68	13.72	/

4.4 Surface tension

Contact angles were measured before and after deformation on the polymers to determine surface tensions, γ_s . To do this, water and diiodomethane were used. The measured contact angles for each polymer before and after tensile deformation are shown in Table 24. The polymers tested after deformation was:

polyamide A after tensile test at 60°C and 60% of deformation, polyamide B after tensile test at 60°C and 50% of deformation, polyamide C after tensile test at 160°C and 60% of deformation, polycarbonate after tensile test at 23°C and 45% of deformation and PMMA after tensile test at 80°C and 90% of deformation.

Table 24 – Contact angles measured with two liquids: water and diiodomethane, before and after tensile deformation.

	Before deformation		True strain (%)	After deformation	
	Water	Diiodomethane		Water	Diiodomethane
Polyamide A	59.4°	36.4°	60%	47.3°	19.4°
Polyamide B	61.2°	59.1°	50%	47.5°	45.3°
Polyamide C	62.5°	58.9°	60%	47.5°	46.4°
Polycarbonate	84.5°	54.5°	45%	68.9°	40.6°
PMMA	64.1°	56.2°	90%	55.2°	51.4°

The contact angles measured with water are higher than with diiodomethane. With the measured contact angles, and with Equations 23 and 24, the surface tension before and after deformation can be calculated for each polymer. Table 25 shows the calculated surface tensions.

Table 25 – Dispersive and non-dispersive components of the surface energy of each polymer (γ_s^d and γ_s^{nd}), and surface tension (γ_s) before and after tensile deformation.

	Before deformation			True strain (%)	After deformation		
	γ_s^d (mJ/m ²)	γ_s^{nd} (mJ/m ²)	γ_s (mJ/m ²)		γ_s^d (mJ/m ²)	γ_s^{nd} (mJ/m ²)	γ_s (mJ/m ²)
Polyamide A	43.3	11.5	54.8	60%	50.2	15.3	65.5
Polyamide B	30.5	15.5	46.0	50%	38.6	20.0	58.6
Polyamide C	30.6	14.7	45.3	60%	38.0	20.3	58.3
Polycarbonate	33.2	3.3	36.5	45%	41.1	7.5	48.6
PMMA	32.2	13.1	45.3	90%	35.1	17.1	52.2

Figure 79 shows a representation of the surface tension γ_s for each polymer before and after deformation.

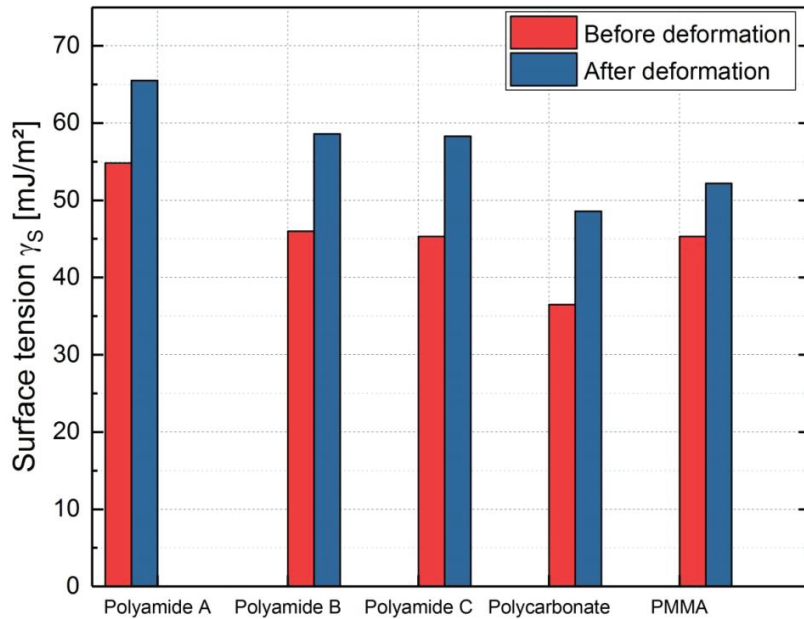


Figure 79 – Surface tension γ_s of each polymer before and after tensile deformation.

In literature, different surface energy values can be found, depending on the test conditions (temperature, humidity) and on the polymer studied (molecular weight). For polycarbonate, values of surface energy are found around 33 mJ/m² [178]. For PMMA, a value close to 45 mJ/m² was found with the same probe liquids (water and diiodomethane) [179]. For PPA, no data was found in the literature. For PA6, or PA66, the surface energy values are respectively 46.5 mJ/m² and 46 mJ/m² [180], [181].

The surface tension values measured on the polymers before deformation are consistent with values that can be found in the literature. The existing difference may be due to the temperature or mass of the polymer. Indeed the difference may be due to the temperature or molecular weight of the polymer. Indeed, the temperature will have some effect on the surface energy: the surface energy will decrease as the temperature increases [180]. Moreover, the molecular weight has also some effect on the surface energy. Indeed, the surface energy will increase as the molecular weight increases but will reach a value at high molecular weights. This was shown by Wu for polystyrene [145].

After deformation, the surface tension is higher for all the polymers studied, as observed in Figure 79. Polyamide A has a surface tension of 65.5 mJ/m² after deformation, which is more than the other two PPA (polyamide B and polyamide C) which have a surface tension of 58.6 and 58.3 mJ/m² respectively.

The polycarbonate studied has a surface tension of 48.6 mJ/m² after deformation, and the PMMA has a surface tension of 52.2 mJ/m² after deformation.

Strong molecular cohesion (surface tension) may block the cavitation. If the molecular cohesion decreases (for example presence of impurities), the molecules can move more easily, move away and create a cavity: there can be cavitation. On the other hand, if the molecular cohesion increases, the molecules will have difficulty moving and there will be no cavitation possible. This is observed in the case of polyamide A: the measured surface tension is much higher for the deformed sample than for the sample before deformation. Cavitation will be highly reduced or blocked. This will be discussed in Chapter 5.

4.5 Conclusion

In this chapter the mechanical and ultimate properties of PPA, polycarbonate and PMMA samples have been studied. The impact properties were studied on a broad temperature range, using an instrumented Charpy impact test. The three PPA samples exhibited a brittle-ductile transition from a low energy dissipated during impact to a high energy dissipated during impact of the order 130-160 kJ m⁻². At room temperature, the three PPA studied are brittle. The tensile and the compression behavior of the four PPA with different degree of crystallinity have been studied. In tensile test, the PPA with the largest crystallinity is brittle at room temperature (polyamide C), while the polyamide A and polyamide B are ductile. These three PPA under study show necking during tensile test. This is not the case of polyamide D, obtained with a different process (process B). Beyond yield, no strain hardening behavior was observed. The appearance of shear bands was observed for $\theta=0^\circ$ and 45° , leading to the failure of the samples. Polyamide D is less ductile than the other PPA studied. Polycarbonate and PMMA was studied. The PMMA is brittle up to 70°C and ductile after this temperature, whereas polycarbonate is ductile over the range of temperatures studied. A strain hardening behavior, following by the failure of these two polymers was observed.

Direct measurements of Poisson's ratio have been carried out during tensile experiments with the VidéoTraction system. The Poisson's ratio is not constant during the tensile deformation for all polymers. Until the yield a regular increase of the Poisson's ratio is observed. After the yield, the evolution of the Poisson's ratio is different for each polymer: ν converges to 0.5 for polyamide A, polyamide B and PMMA, ν converge to 0.4 for polyamide C just after the yield and no longer varies with deformation, and ν oscillates between 0.4 and 0.5 for polycarbonate. The volume variation was calculated. For polyamide C,

PMMA and polycarbonate, the volume increases with deformation. For polyamide A, the volume increases up to the yield and then no longer varies. For polyamide B at 100 and 110°C, there is less than 1% of increase in volume.

The influence of the process was studied on polyamide C and polyamide D. It is observed that the tensile behavior depends on the injection process, in particular on the geometry.

In both tensile and compression tests, a strain hardening behavior was observed, which is more pronounced in compression. The measured strain hardening moduli in compression are around 18 MPa for the three PPA at 23°C. The strain hardening modulus is shown not to depend on crystallinity. Indeed, the strain hardening modulus E_{SH} of the semi-crystalline PPA, polyamide C and polyamide B, is found to be equal to the hardening modulus of the amorphous. Only the temperature has an influence on the strain hardening modulus E_{SH} : the strain hardening modulus decreases with increasing temperature. Strain hardening is a key feature for resistance to damage [121], [182] but its origin is still debated [7], [9], [11]–[19], [27], [28].

The mechanical properties are strongly influenced by the response to large deformations of polymers. Meijer and Govaert [29] have studied the polycarbonate and have shown that polymers with high strain hardening have also ductile rather than brittle deformation. According to the authors, the strain hardening suppresses the strain localization and/or the shear banding. This behavior does not prevent the failure of the polymer, which can occur when the strain is increased.

Several questions can be asked. What are the damage mechanisms of the different polymers studied? Will strain hardening play a role in stabilizing damage? The next chapter concerns the study of damage mechanisms of the different polymers studied under tensile deformation by X-ray scattering.

Chapter 5 – Damage mechanisms under tensile deformation

The objective of this chapter is to focus on the damage mechanisms of different polymers, from amorphous to semi-crystalline: polyphthalamides (PPA), as well as polycarbonate (PC) and poly(methyl)methacrylate (PMMA). PC and PMMA are highly studied polymers known for their strain hardening regime, especially in compression. PC presents a strong strain hardening regime, while PMMA presents a weak strain hardening. We describe the initiation and growth of damage and the mechanisms of failure when the failure is reachable. Our approach is similar to the approach used by Stoclet et al [49], Mourglia-Seignobos et al [50] and Charvet et al [26], consisting in analyzing by USAXS different samples corresponding to different elongations during a uniaxial tensile test. Measurements performed by USAXS allow to determine the evolution of the number density, volume fraction and size of damages during the tensile deformation. All this information allows us to describe the damage mechanism in the polymers studied.

Microscopic observations will be presented. The scattered intensities obtained by USAXS measurements at different strain values will be modeled quantitatively and different parameters will be presented. Damage mechanisms observed in PPA, PC and PMMA will be discussed. The observations are performed on ISO-527 geometry (process A) for three PPA (polyamide A, polyamide B and polyamide C) and on hourglass specimen (process B) for polyamide D. Polycarbonate and PMMA were in the form of plate. Hourglass specimens (the same as in process B) were cut in the plates.

5.1 Microscopic study

Microscopic observations have been done by macroscope, optical microscopy (OM) and scanning transmission electron microscopy (STEM), in the useful area (schematized in Figure 52). PMMA has a high sensitivity to electron irradiation. It is very difficult to perform microscopic observation. The focus must be done quickly in order to prevent polymer degradation [26].

Figure 80 and Figure 81 show the STEM observations on polyamide A, polyamide B, polyamide C, polycarbonate and PMMA before tensile experiment. No cavities are observed on these samples before tensile experiment by macroscope, OM or STEM.

All the deformed samples were analyzed by STEM but no damage was observed on the micrographs. It is supposed that the size of damage is not compatible with the microscope resolution, or the contrast between structural damage (homogeneous crazes) and the polymer matrix is too small. USAXS measurements permit a quantitative study of the damages. Note that it was also the case in the study of Mourglia-Seignobos et al [50] for PA66 during fatigue solicitation. Damage could be characterized in USAXS experiments in the early stages but not by electron microscopy.

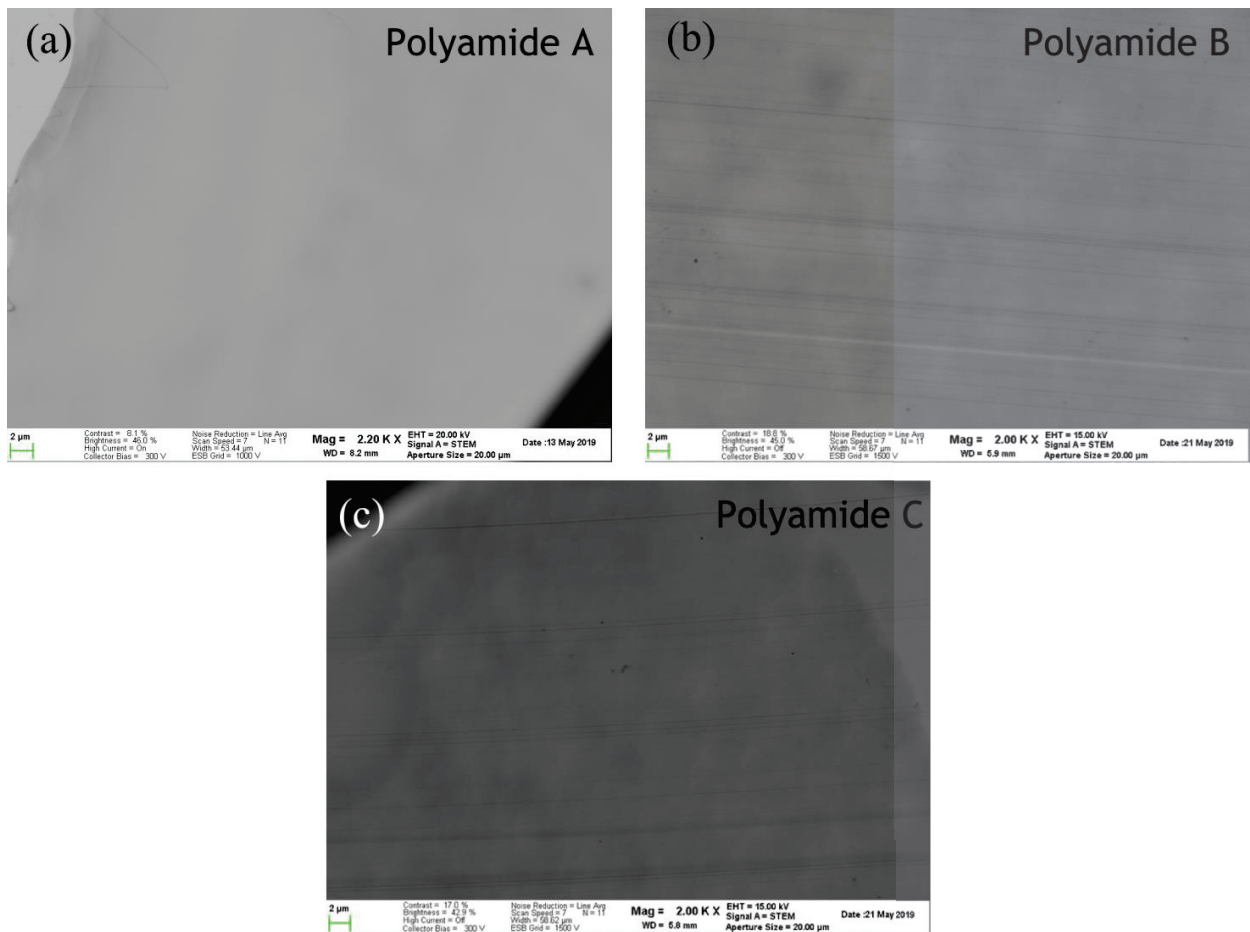


Figure 80 – STEM micrographs of PPA before tensile experiment: (a) polyamide A, (b) polyamide B, and (c) polyamide C.

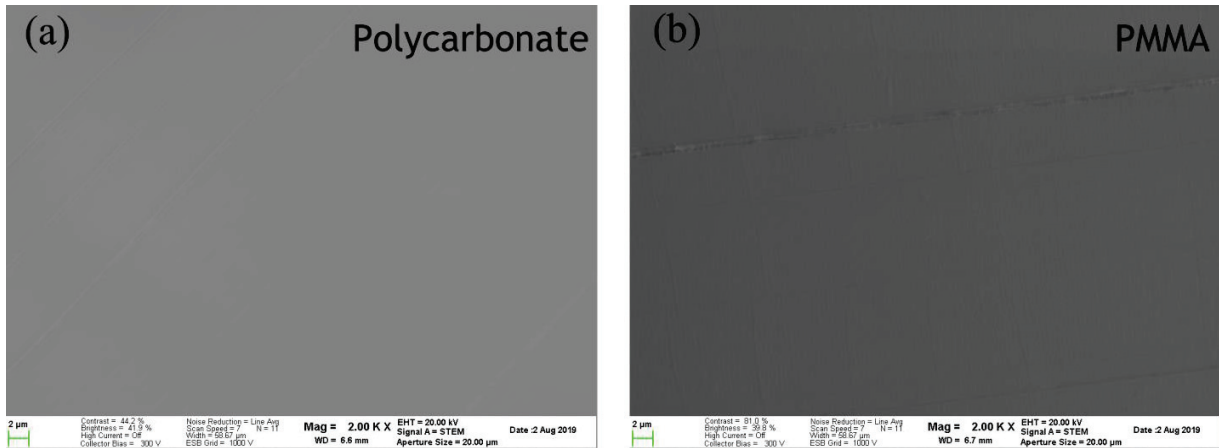


Figure 81 – STEM observations of polycarbonate (a) and PMMA (b) before tensile experiment.

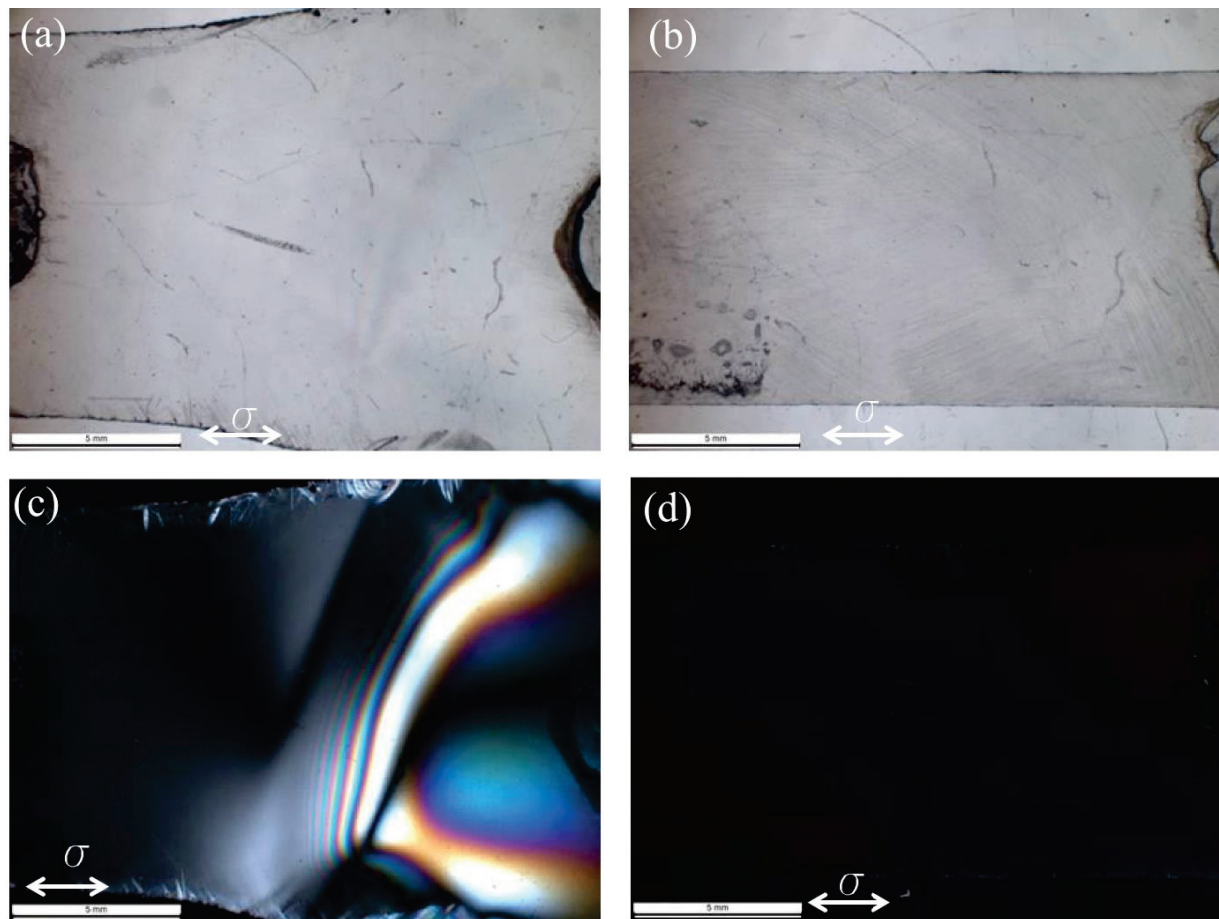


Figure 82 – Macroscopic observations in transmission of polycarbonate at 60°C and 59% of elongation (a-c) and PMMA at 80°C and 90% of deformation (b-d). (a) and (b): bright field; (c) and (d): crossed polarized light. The white rectangle corresponds to 5mm. On the sides of each micrograph, the glue points required for sample preparation for the USAXS analysis are visible.

Polycarbonate and PMMA were observed by macroscope after tensile deformation (Figure 82), in bright-field and in crossed-polarized light. In bright field, no deformation can be observed for both polymers. In crossed-polarized optical microscopy, polycarbonate appears birefringent and deformations can be seen. PMMA, unlike polycarbonate, has no birefringence (Figure 82-d). Indeed, PMMA remains dark.

Polyamide D (tensile measurement at 23°C, with $\theta = 0^\circ$) was observed by macroscope, optical microscope (OM) and STEM. Figure 83 and Figure 84 show the macroscope micrographs obtained in transmission in bright field (Figure 83) and in cross-polarized light (Figure 84) for different strain.

In Figure 83, a strong bleaching of the sample is observed from 7% elongation (Figure 83-e). The first signs are observed at the edges of the sample at 6% elongation (Figure 83-d). In Figure 84, the crossed polarization highlights the deformations of the specimen and makes it possible to observe objects present in the specimen at 6% of elongation, which is not visible in bright field.

The macroscope observation makes it possible to highlight the appearance of the shear bands, starting from 6% of elongation.

Polyamide D was observed in STEM (Figure 85). Shear bands can be observed from 6% of elongation, as well as parabolae. This makes us think of the sections of a cone: if we change the plane of observation (initially “XZ” plane, as in Figure 86), we should observe circles or ellipses, if the observed deformations are cones.

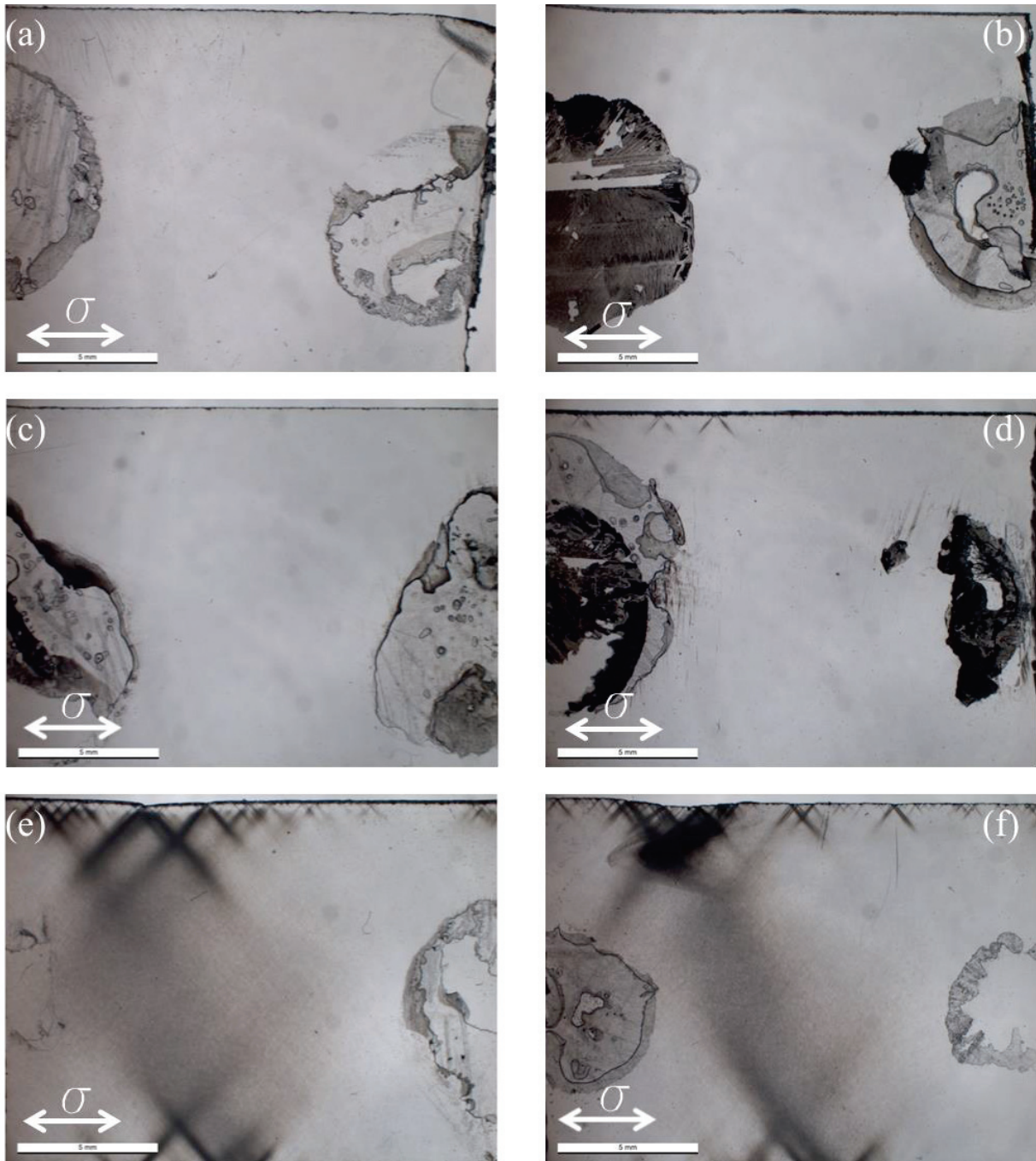


Figure 83 – Macrograph micrographs obtained in transmission (bright field) for polyamide D at 23°C: (a) before tensile experiment, (b) 4% elongation, (c) 5% elongation, (d) 6% elongation, (e) 7% elongation and (f) 15% elongation at failure. The white rectangle corresponds to 5mm. On the sides of each micrograph, the glue points required for sample preparation for the USAXS analysis are visible.

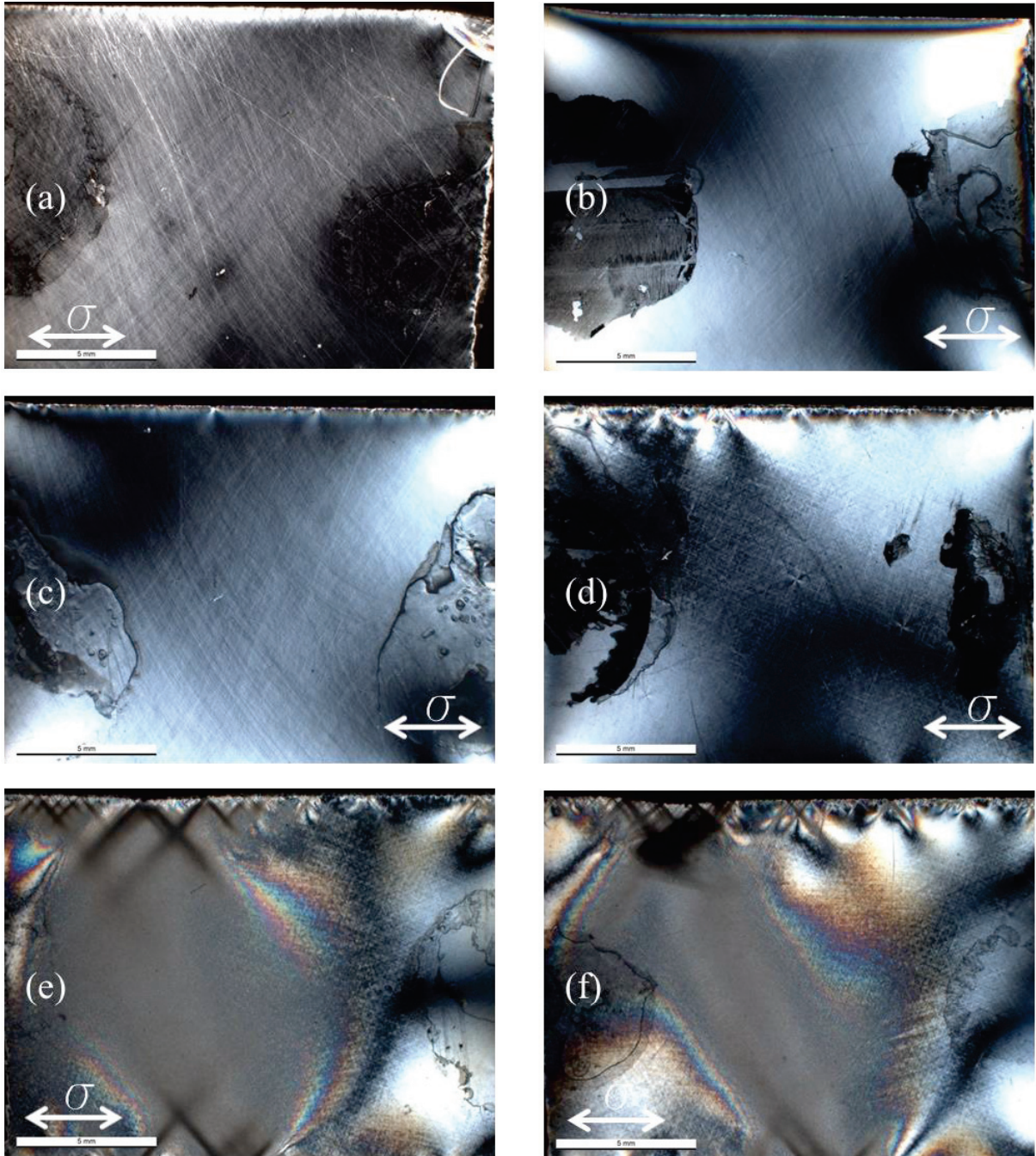


Figure 84 – Macro-micrographs obtained in transmission (cross-polarized light) for polyamide D at 23°C: (a) before tensile experiment, (b) 4% elongation, (c) 5% elongation, (d) 6% elongation, (e) 7% elongation and (f) 15% elongation at failure. The white rectangle corresponds to 5 mm. On the sides of each micrograph, the glue points required for sample preparation for the USAXS analysis are visible.

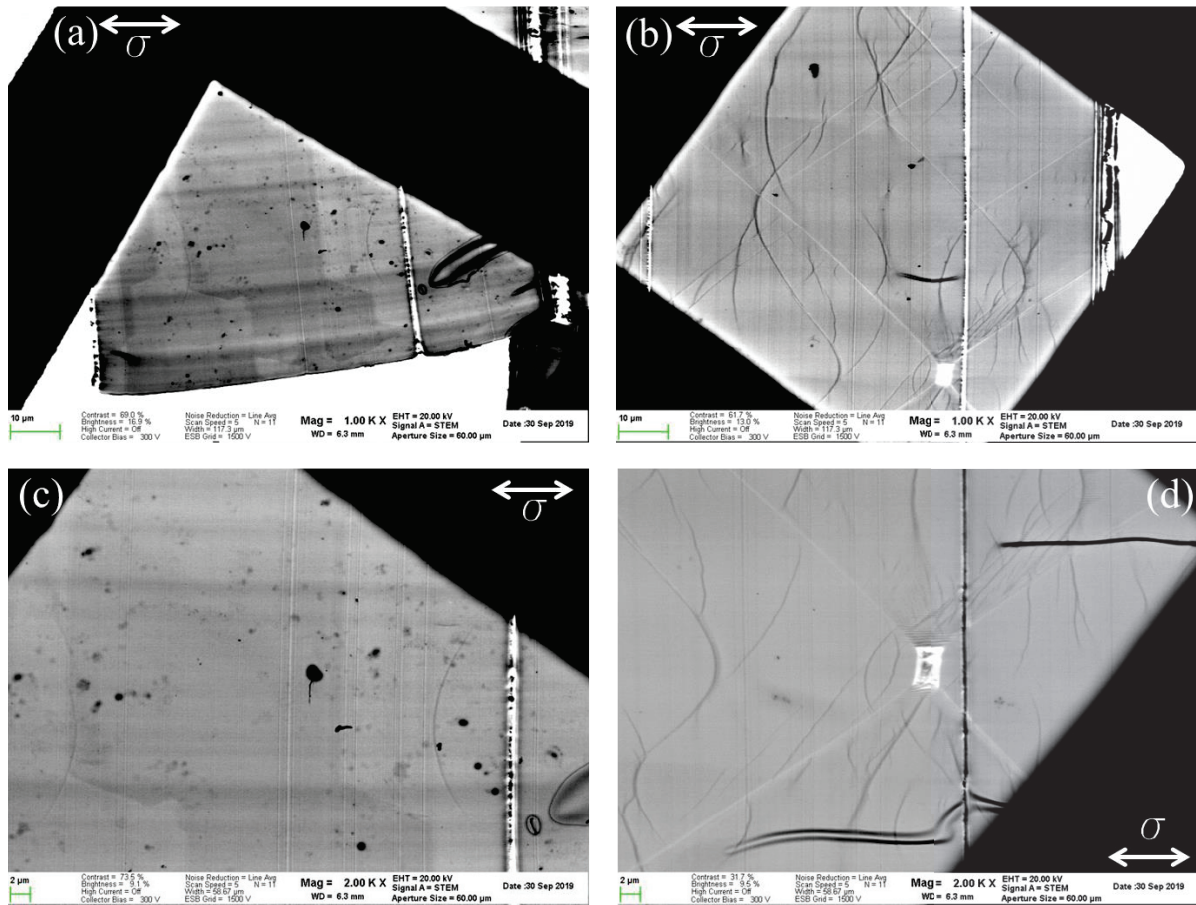


Figure 85 – STEM micrographs of polyamide D after tensile deformation at 23°C and $\theta=0^\circ$. (a) and (c) at 6% of elongation; (b) and (d) at 15% of elongation.

Polyamide D was analyzed by optical microscopy according to two observation plans: “XZ” plane and “YZ” plane (Figure 86). In the XZ plane, the same observations as STEM are expected, namely crosses and parabolas. In the “YZ” plane, if the observed deformations are indeed cones, we should observe circles or ellipses.

“XZ” Plane

Figure 87 represents the phase contrast microscopy observations of polyamide D in the “XZ” plane, at different strain levels (before tensile experiment, 6%, 7% and 15% of elongation). Before tensile experiment, no deformation is visible. At 6% of elongation, the appearance of a parabola can be observed. At 7% of deformation (Figure 87-c), many parabolas are observed, as well as shear bands, which join

forming crosses. At 15% of deformation and failure of the specimen (Figure 87-d), many parabolas are also observed. There is no evolution compared to 7% of elongation. More objects between the shear bands are visible.

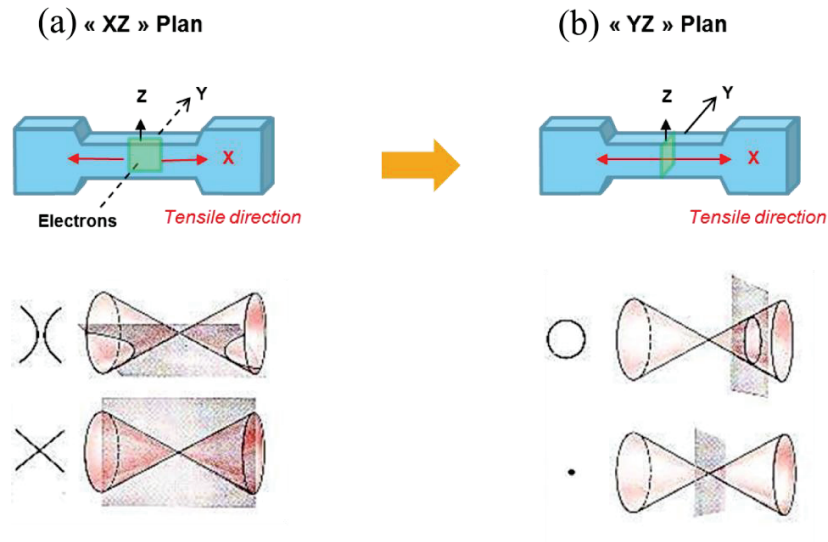


Figure 86 – Plan of observations and expected observed geometries.

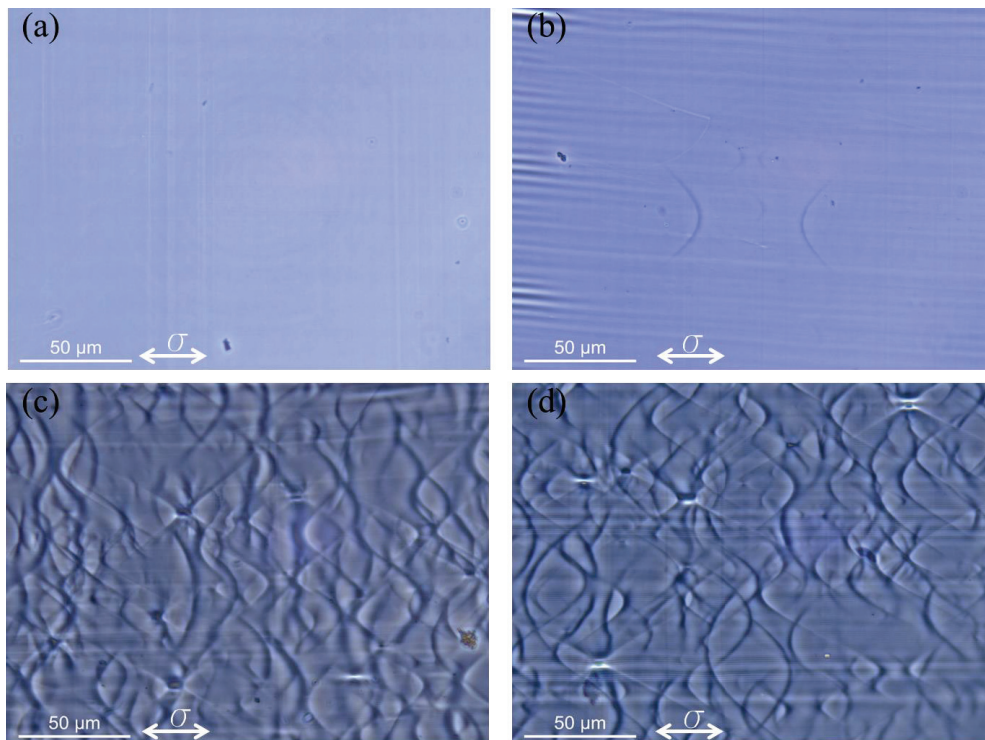


Figure 87 – Phase contrast Optical microscopy observations obtained in transmission for polyamide D at 23°C and $\theta=0^\circ$. Observation of the “XZ” plane: (a) before tensile experiment, (b) 6% of elongation, (c) 7% of elongation, and (d) 15% of elongation at failure.

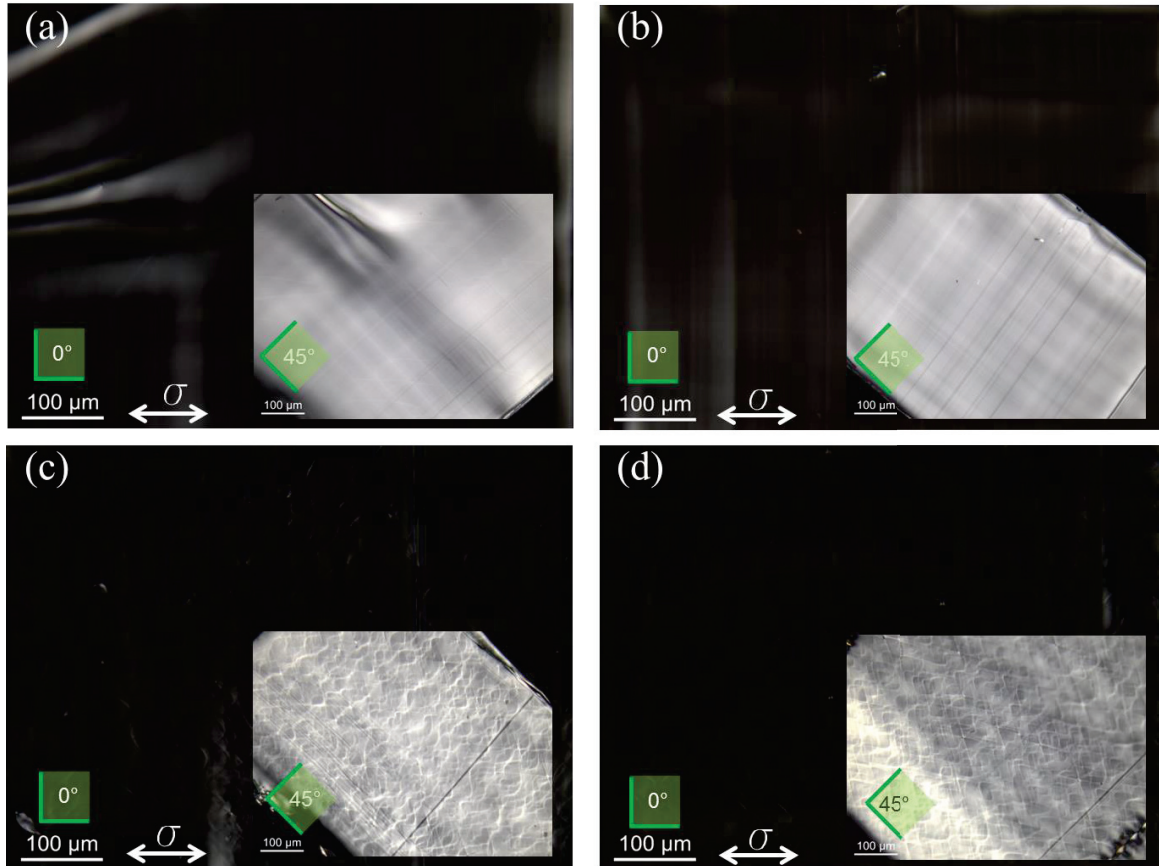
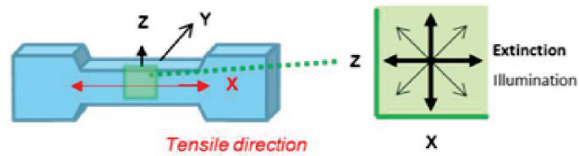


Figure 88 – Crossed-polarized Optical microscopy observations obtained in transmission for polyamide D at 23°C and $\theta=0^\circ$. Observation of the “XZ” plane: (a) before tensile experiment, (b) 6% of elongation, (c) 7% of elongation, and (d) 15% of elongation at failure.

In crossed-polarized optical microscopy, the angle of illumination between the analyzer and the polarizer can vary, from 0° to 90° . Isotropic materials remain permanently in extinction (they remain dark), whereas anisotropic materials appear illuminated. In the observation plane "XZ", polyamide D appears illuminated at 45° , but extinguished at 0° , as observed in Figure 88.

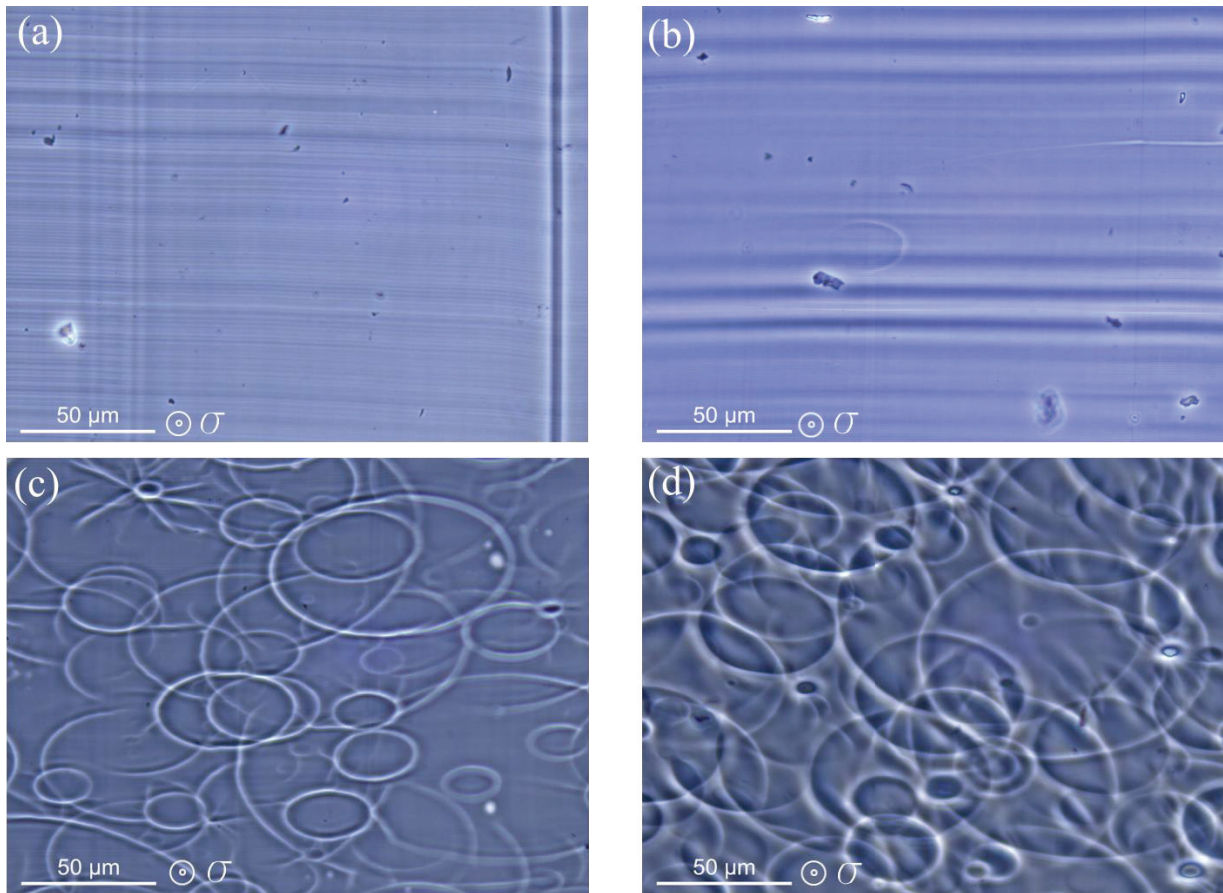
“YZ” Plane

Figure 89 – Phase contrast Optical microscopy observations obtained in transmission for polyamide D at 23°C and $\theta=0^\circ$. Observation of the “YZ” plane: (a) before tensile experiment, (b) 6% of elongation, (c) 7% of elongation, and (d) 15% of elongation at failure.

Figure 89 represents the phase contrast microscopy observations of polyamide D in the “YZ” plane, at different strain levels (before tensile experiment, 6%, 7% and 15% of elongation). Before tensile experiment, no deformation is visible. At 6% of elongation, the appearance of a circle can be observed. At 7% of deformation (Figure 89-c), many circles are observed, of several diameters. At 15% of deformation and failure of the specimen (Figure 87-d), many circles are also observed.

In crossed-polarized optical microscopy, the observation of the "YZ" plane gives the same response as the observation of the “XZ” plane: polyamide D appears illuminated at 45° , but extinguished at 0° , as observed in Figure 90.

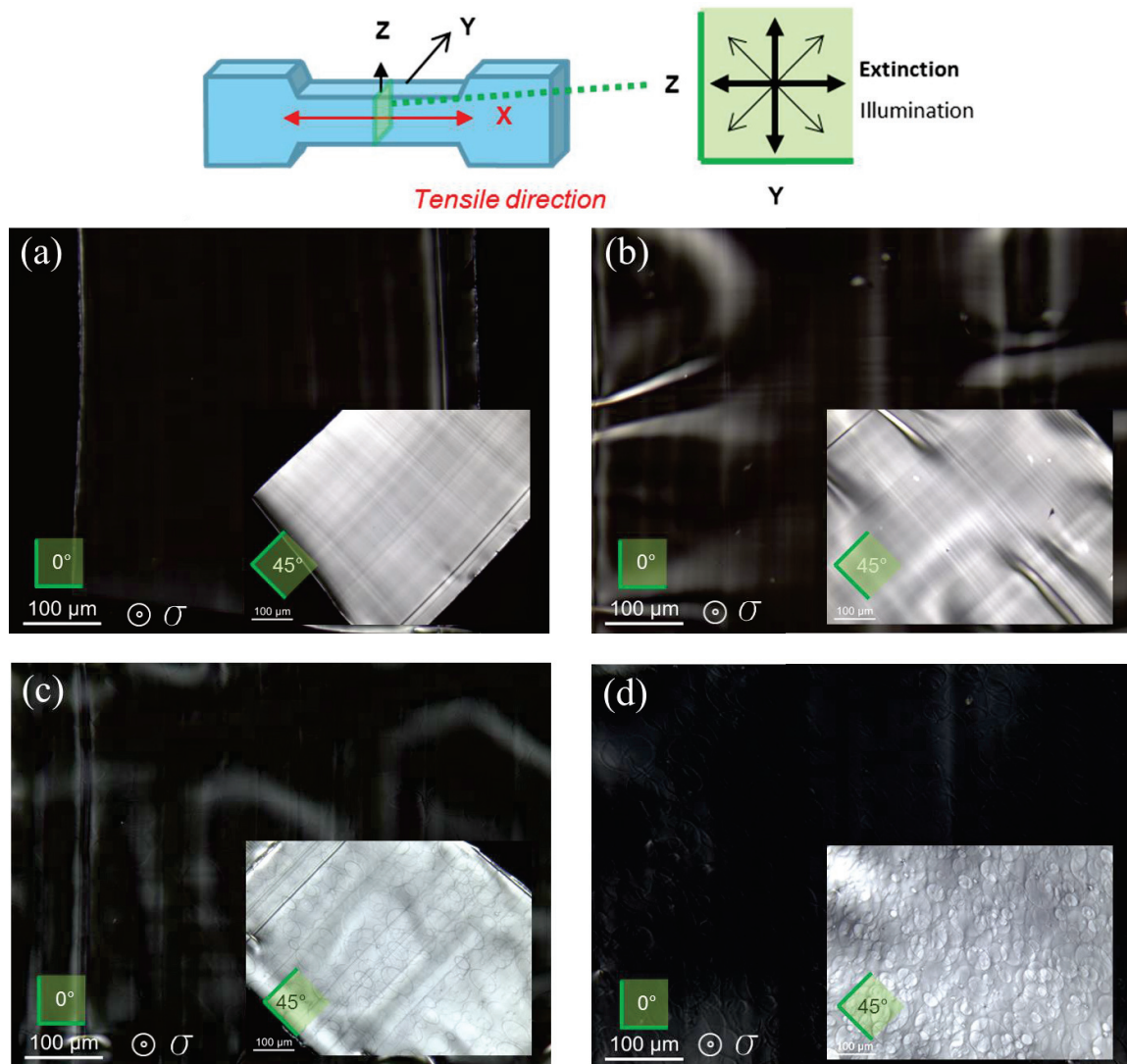


Figure 90 – Crossed-polarized Optical microscopy observations obtained in transmission for polyamide D at 23°C and $\theta=0^\circ$. Observation of the “YZ” plane: (a) before tensile experiment, (b) 6% of elongation, (c) 7% of elongation, and (d) 15% of elongation at failure.

A mechanism for deformation of polyamide D by the deformation of an object tangent to a family of shear bands is proposed (Figure 91).

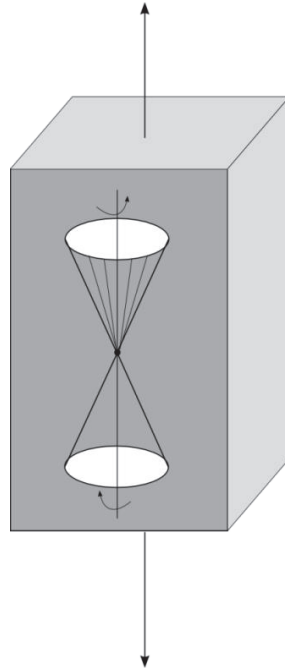


Figure 91 – Schematic representation of the deformation of polyamide D.

With all the polymers studied, we were not able to observe in microscopy the damage morphology. Based on literature (Kramer, Michler [31], [35], [37], [39]) and on the recent study by Charvet et al [26], the different types of damage expected in the polymers studied are shown schematically in Figure 92.

The scattered intensities measured by USAXS experiments are analyzed thanks to this diagram, according to the objects encountered. The first category of defects corresponds to small elongated cavities (interior structure of crazes). In this category, the long radius of the ellipsoids in the direction parallel to the tensile direction (X axis) is defined as d , and the short radius of the ellipsoids in the direction perpendicular to the tensile direction (Z axis) is defined as c . The second category corresponds to homogeneous and fibrillated crazes. Crazes are modeled in this category by uniaxial ellipsoids with radius (half thickness) L along the tensile direction and larger radius D in the perpendicular direction. The last category, 3, corresponds to large cavities induced by injection process, with dimension R . Figure 93 shows a schematic representation of a craze with the corresponding dimensions.

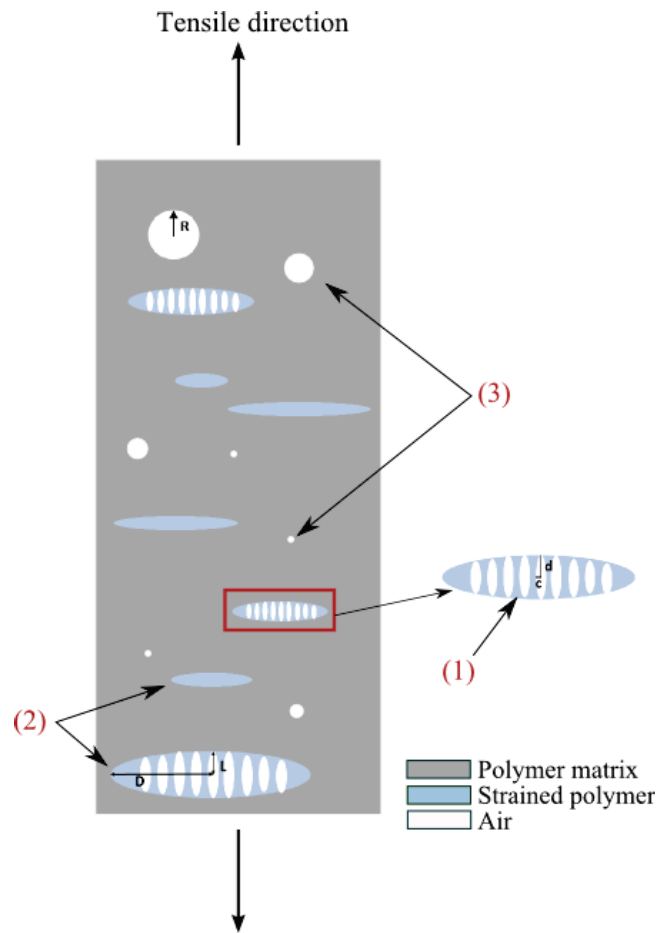


Figure 92 – Representation of the different damage morphologies expected in the polymers studied.

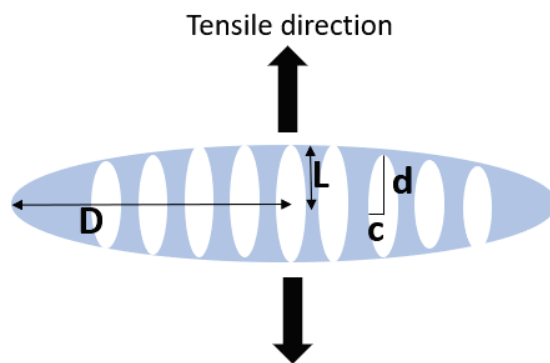


Figure 93 – Schematic representation of a craze, according to the tensile direction, with the characteristic dimensions: D , the large radius of the ellipsoid in the perpendicular direction; L , the short radius of the ellipsoid along the tensile direction; d , the long radius of the ellipsoid in the direction parallel to the tensile direction and c , the short radius of the ellipsoid in the direction perpendicular to the tensile direction.

5.2 Characterization of damage by Ultra-small Angle X-ray Scattering (USAXS)

All the studied polymers were analyzed by Ultra-small angle X-ray Scattering (USAXS) with a 2D detector, after tensile experiments at several temperatures. During the USAXS experiments, the scattered intensity is initially isotropic, as observed in Figure 94-a. The scattered intensity becomes anisotropic with the deformation: the observed diffusion is not homogeneous, as seen in Figure 94-b-c.

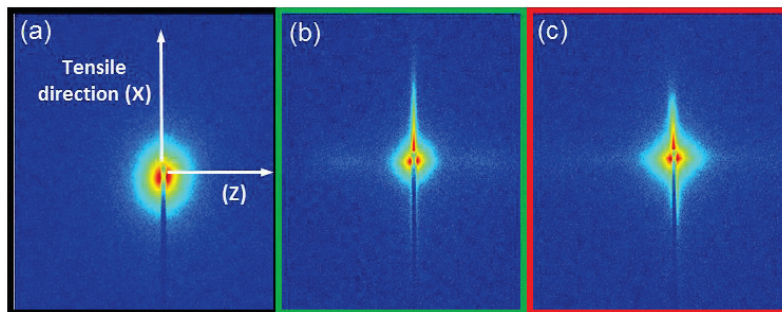


Figure 94 – 2D USAXS patterns for polyamide A before tensile deformation (a), and after tensile experiment at 60°C: (b) 25% of deformation and (c) 60% of deformation.

5.2.1 Fitting equations

From the 2D patterns obtained in USAXS experiments, the scattered intensities are integrated along the tensile direction (*parallel*), in an interval of azimuth angle $[-10, +10^\circ]$, and perpendicular to the tensile direction (*perpendicular*), in an interval of azimuth angle $[80, 100^\circ]$. Figure 95 gives a schematic representation of the general form of the global scattered intensities in both parallel direction (X axis, blue curve) and perpendicular direction (Z axis, green curve). We obtained the restricted scattered intensities in both directions.

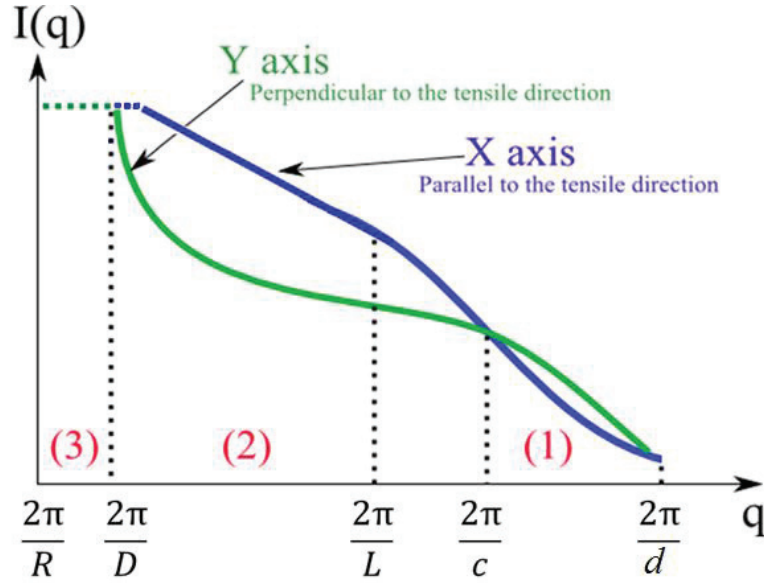


Figure 95 – Schematic representation of the general form of the global scattered intensities of a polymer with different damage morphologies. The contributions of different types of defects are shown: 1: small elongated cavities (interior structure of crazes), 2: homogeneous and fibrillated crazes and 3: large cavities induced by injection process. Adapted from [26].

As schematized in Figure 95, three regions can be determined in the scattered intensities of our polymer samples. At high q values, for $q > 2\pi/c$ (region 1 in Figure 95), the scattering is due to small elongated cavities inside the fibrillated crazes. The scattering pattern of these cavities is anisotropic. Uniaxial ellipsoids elongated along the tensile direction are used to model the cavities. The long radius of the ellipsoids in the direction parallel to the tensile direction (X axis) is defined as d , and the short radius of the ellipsoids in the direction perpendicular to the tensile direction (Z axis) is defined as c . The scattered intensities resulting in both directions (parallel and perpendicular to the tensile direction) can be expressed by Equations 56 and 57.

$$I_{parallel_1}(q) = \beta^2 \rho_{pol}^2 V_1^2 N_1 \left(\exp\left(\frac{-q^2 d^2}{5}\right) + 4.5 \frac{\text{erf}\left(\frac{qd}{\sqrt{10}}\right)^{12}}{(qd)^4} \right) \quad (56)$$

$$I_{perpendicular_1}(q) = \beta^2 \rho_{pol}^2 V_1^2 N_1 \left(\exp\left(\frac{-q^2 c^2}{5}\right) + 4.5 \frac{\text{erf}\left(\frac{qc}{\sqrt{10}}\right)^{12}}{(qc)^4} \right) \quad (57)$$

where $V_1 = 4\pi dc^2/3$ is the volume of small elongated cavities, and N_1 is the number density of these small elongated cavities. The volume fraction is expressed by $\phi_1 = N_1 V_1$.

In the region 2, q is in the range $2\pi/D < q < 2\pi/c$. In this region, small isotropic and elongated cavities described above are unresolved and the scattering reveal only the global craze structure. Crazes are filled with polymer with a volume fraction of air φ . The contrast factor can be written as $\rho_e^2 = \varphi^2 \rho_{pol}^2$ where ρ_{pol} is the average electron density of the polymer matrix. We consider the value $\varphi = 0.25$ which is coherent with the cavities polymer volume fraction used by Mourglia et al [50] in polyamide and with the volume fraction of air within a fibrillar craze found by Michler et al [35] in polystyrene. Crazes are modeled by uniaxial ellipsoids with radius (half thickness) L along the tensile direction and larger radius D in the perpendicular direction. According to the work of Charvet et al on CDA [26], the microscopic observations showed a broad distribution for the size of crazes. To describe the resulting scattered intensity, some hypotheses must be done. We assume that the larger radius D (respectively L) varies between extremum values D_{min} and D_{max} (respectively L_{min} and L_{max}) and that D is a linear function of L as given in Equations 58 to 60:

$$D(L) = \epsilon L + \beta \quad (58)$$

with:

$$\epsilon = \frac{D_{max} - D_{min}}{L_{max} - L_{min}} \quad (59)$$

and

$$\beta = \frac{L_{max} D_{min} - D_{max} L_{min}}{L_{max} - L_{min}} \quad (60)$$

We assume that the size distribution $P(L)$ (where $P(L)dL$ denotes the number of cavities per unit volume with a size comprised between L and $L + dL$) can be described by a power law:

$$P_2(L) = P_2 L^{-\alpha} \quad (61)$$

The distribution $P(L)$ is normalized so that the number density of crazes of type 2 is given by:

$$N_2 = \int_{L_{min}}^{L_{max}} P_2(L) dL \quad (62)$$

The corresponding volume fraction of crazes ϕ_2 is given by the following equation:

$$\phi_2 = \int_{L_{min}}^{L_{max}} V_2(L) P_2(L) dL \quad (63)$$

Where $V_2 = 4\pi LD^2/3$ is the ellipsoid volume.

In region 2, the scattered intensity in both parallel and perpendicular directions is expressed by the following equations:

$$I_{parallel_2}(q) = \beta^2 \rho_{pol}^2 \varphi^2 \int_{L_{min}}^{L_{max}} V_2^2 \left(\exp\left(\frac{-q^2 L^2}{5}\right) + 4.5 \frac{\text{erf}\left(\frac{qL}{\sqrt{10}}\right)^{12}}{(qL)^4} \right) P_2(L) dL \quad (64)$$

$$I_{perpendicular_2}(q) = \beta^2 \rho_{pol}^2 \varphi^2 \int_{L_{min}}^{L_{max}} V_2^2 \left(\exp\left(\frac{-q^2 D^2}{5}\right) + 4.5 \frac{\text{erf}\left(\frac{qD}{\sqrt{10}}\right)^{12}}{(qD)^4} \right) P_2(L) dL \quad (65)$$

In the region 3 (Figure 95), at low q values ($q < 2\pi/D$), the scattered intensity has always been isotropic in our experiments. The scattered intensity observed comes from the response of large spherical cavities formed during the injection process. The radius of these cavities is comprised between R_{min} and R_{max} . The size distribution is expressed by a power law as in Equation 66:

$$P_3(R) = P_3 R^{-\alpha_1} \quad (66)$$

The scattered intensity is expressed as:

$$I_3(q) = \beta^2 \rho_{pol}^2 \int_{R_{min}}^{R_{max}} V_3^2 \left(\exp\left(\frac{-q^2 R^2}{5}\right) + 4.5 \frac{\text{erf}\left(\frac{qR}{\sqrt{10}}\right)^{12}}{(qR)^4} \right) P_3(R) dR \quad (67)$$

With V_3 , the volume of spherical cavities of radius R . Note that in this region, we don't know if the large spherical cavities formed during injection are empty. If they are empty, the volume fraction of air φ must be used. This would change the volume fraction of the cavities. Note however that the types of cavities were observed to be empty for CDA [26].

The number density of large cavities N_3 is given by the following equation:

$$N_3 = \int_{R_{min}}^{R_{max}} P_4(R) dR \quad (68)$$

The corresponding volume fraction ϕ_3 is given by Equation 69:

$$\phi_3 = \int_{R_{min}}^{R_{max}} V_3(R) P_3(R) dR \quad (69)$$

In both directions, the global scattered intensity is the sum of all contributions [150]:

$$I_{parallel}(q) = I_0(q) + I_{parallel_1}(q) + I_{parallel_2}(q) + I_3(q) \quad (70)$$

$$I_{perpendicular}(q) = I_0(q) + I_{perpendicular_1}(q) + I_{perpendicular_2}(q) + I_3(q) \quad (71)$$

Where $I_0(q)$ is the incident beam intensity.

Figure 96 shows two examples of curves fitted thanks to Equations 70 and 71. Both parallel and perpendicular curves to the tensile direction were fitted together. All the results were fitted in the same way.

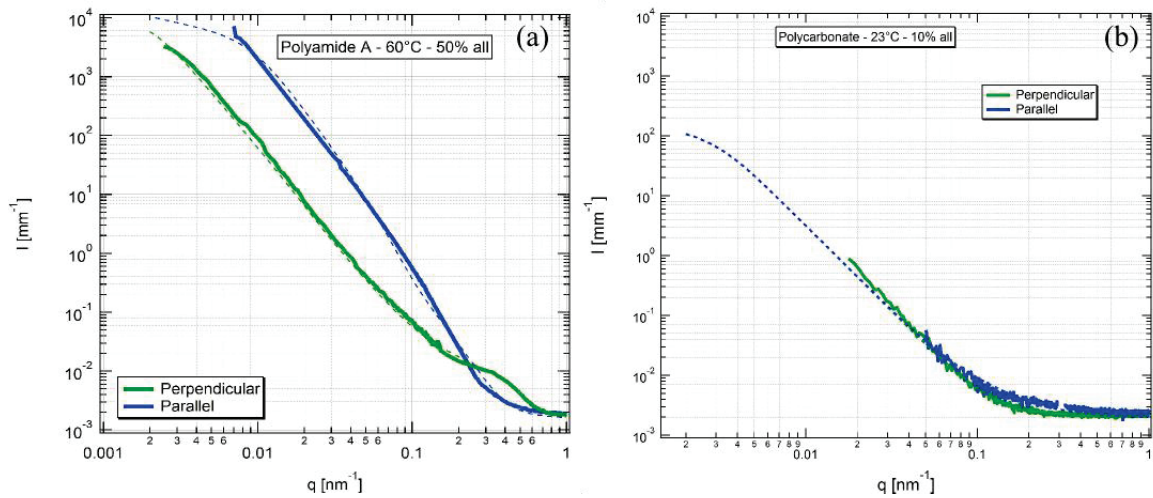


Figure 96 – USAXS scattered intensities in the directions parallel (blue) and perpendicular (green) to the tensile direction on polyamide A at 60°C and 50 % of strain (a) and on polycarbonate at 23°C and 10 % of strain (b). The solid curve represents the experimental data, and the dotted curve represents the fit.

5.2.2 Experimental results

5.2.2.1 Before tensile experiments

In Figure 97 and Figure 98, the restricted scattered intensities in the parallel (blue curve) and perpendicular (green curve) directions to the injection direction are plotted for the four PPA (Figure 97) and for polycarbonate and PMMA (Figure 98) before tensile experiment. The difference in scattering intensities between the parallel direction and the perpendicular direction is due to cavities which nucleate or impurities during the injection process as was assumed by Charvet et al [26]. Using Equation 67, both directions can be fitted. The distribution of the sizes of cavities is modelled with an exponent $\alpha=3.8$. Before tensile experiment for polyamide A, the signal is higher in the parallel direction to the perpendicular direction: we observe cavities oriented in the perpendicular direction. For polyamide B and polyamide C, a small bump in the q range 0.1 to 1 nm^{-1} is observable. This signal can be assimilate to cavities on the order of 10 nm oriented in the direction parallel to the injection. For the other polymers, the signal can be considered as almost isotropic. The volume fraction of initial damages φ_i , the number of initial damages per unit volume N_i , the size R_{\min} and R_{\max} of each polymer are given in Table 26.

Table 26 – Size and volume fractions of initial damages corresponding to fitting parameters used for each polymer before tensile deformation in Figure 97 and Figure 98, $\alpha=3.8$.

	R_{\min} (nm)	R_{\max} (nm)	Volume fraction ϕ_i	Number of initial damage N_i (mm^{-3})
Polyamide A	13	1500	9.0×10^{-6}	1.1×10^9
Polyamide B	1	1000	3.1×10^{-5}	2.0×10^{10}
Polyamide C	10	1200	4.0×10^{-5}	1.0×10^{11}
Polyamide D	1	1000	2.6×10^{-6}	4.8×10^7
Polycarbonate	1	1000	1.9×10^{-6}	3.9×10^5
PMMA	5	500	1.9×10^{-6}	4.2×10^7

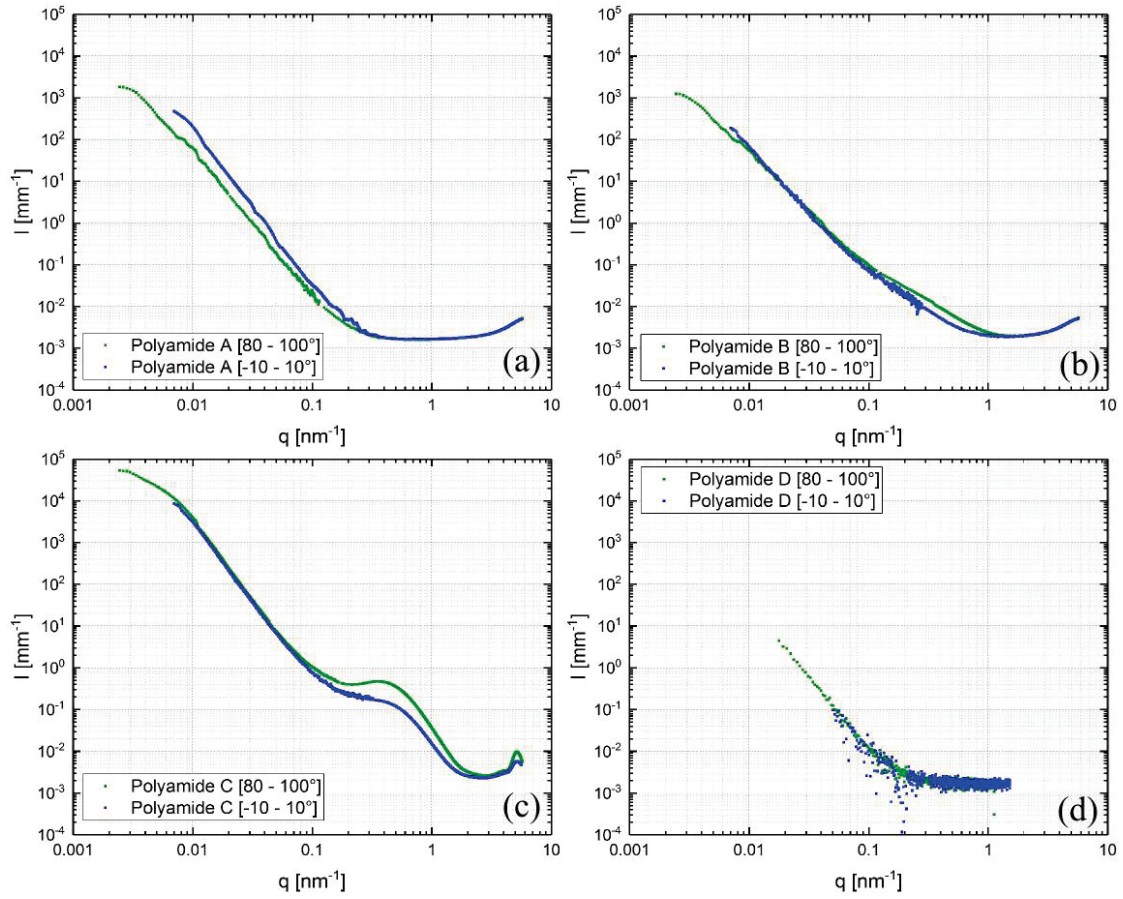


Figure 97 – Restricted scattered intensities in both parallel (blue curve) and perpendicular (green curve) directions to the injection direction obtained by USAXS experiments on (a) polyamide A; (b) polyamide B; (c) polyamide C and (d) polyamide D.

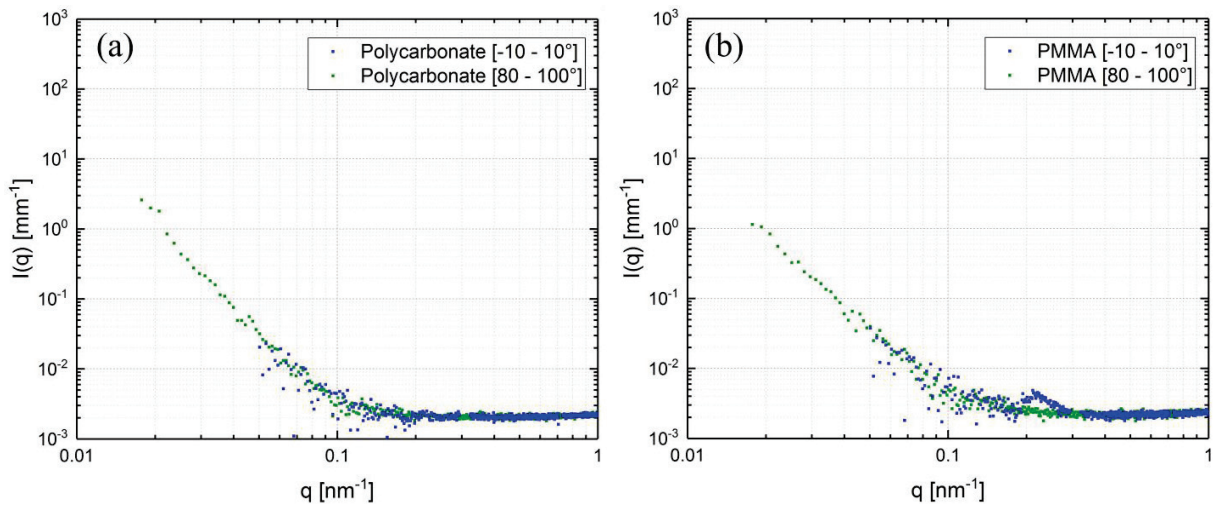


Figure 98 - Restricted scattered intensities in both parallel (blue curve) and perpendicular (green curve) directions to the injection direction obtained by USAXS experiments on (a) polycarbonate and (b) PMMA.

5.2.2.2 Evolution of damage under tensile deformation

The aim of the characterization of damage using USAXS experiments is to determine the mechanisms of initiation and propagation of damages, under uniaxial tensile deformation. In order to analyze a wide range of deformation, USAXS measurements were performed at different strain levels, as indicated by stars in Figure 99 and Figure 100.

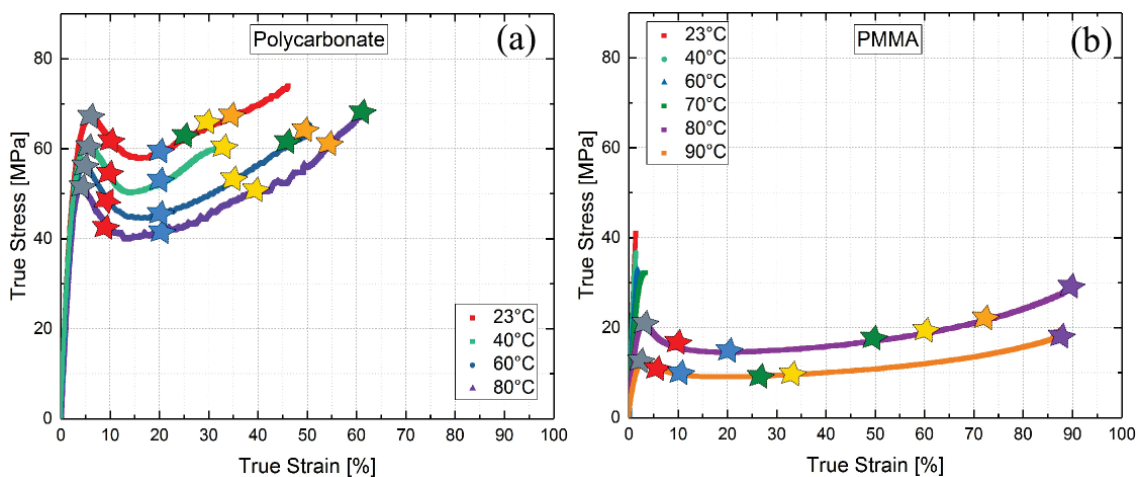


Figure 99 – Tensile true stress – true strain curves obtained at 0.001 s^{-1} for polycarbonate (a) and PMMA (b). Stars indicate the USAXS measurements.

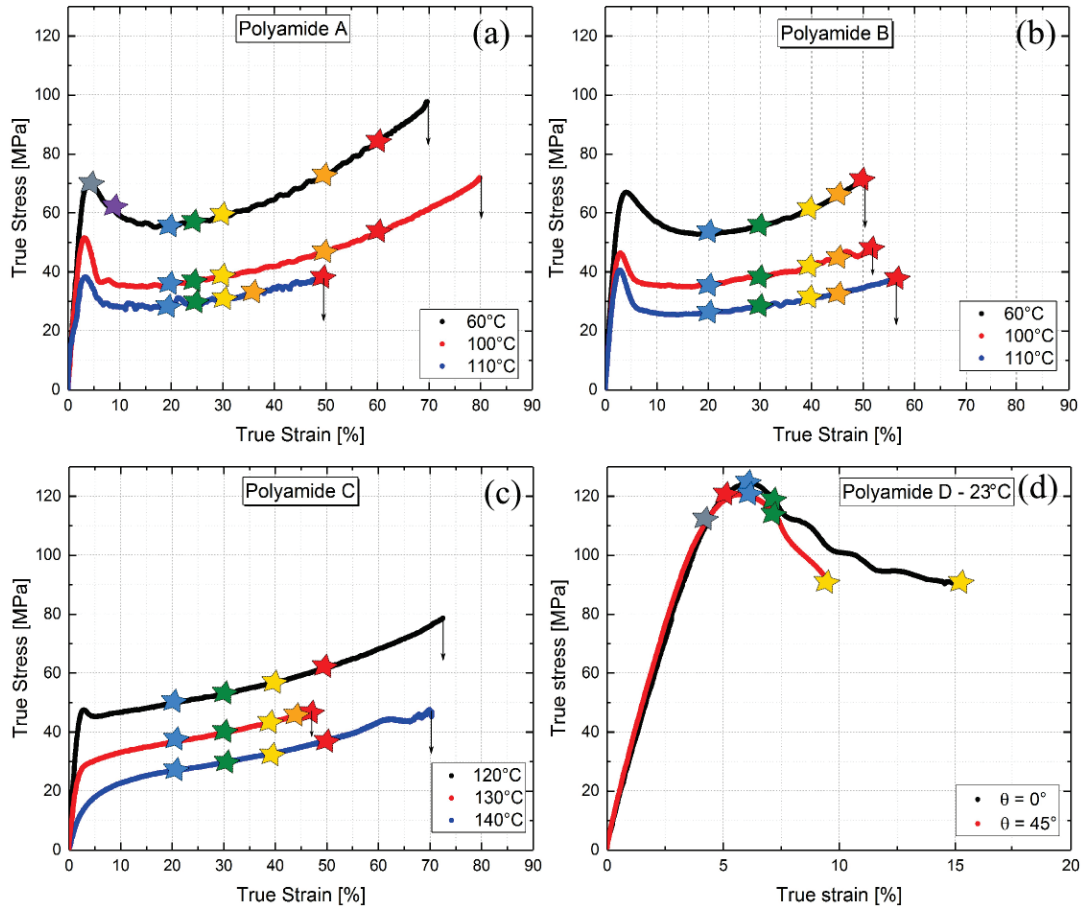


Figure 100 – Tensile true stress – true strain curves obtained at 0.001 s^{-1} for each PPA: (a) polyamide A, (b) polyamide B, (c) polyamide C and (d) polyamide D. Stars indicate the USAXS measurements, arrows indicate unbroken samples.

5.2.2.2.1 *Behavior under tensile deformation of polyamide A*

Figure 101 shows both parallel and perpendicular scattered intensities at different strain levels at 60°C (a-b), 100°C (c-d) and 110°C (e-f) for polyamide A. The experimental data are fitted by global scattered intensity given by Equations 70 and 71. Thanks to the analysis of the experimental data, the size and the volume fraction of each typology of damage can be determined. All the adjustable parameters are given in Table 27, Table 28 and Table 29.

For the three temperatures tested (60°C , 100°C and 110°C), the same evolution of intensities is observed, as shown in Figure 101. Indeed, at small q values, the scattered intensities parallel to the tensile direction increase with deformation but do not evolve after 9% of deformation. The scattered intensity in the direction parallel to the deformation is about one decade higher than that in the direction normal to the

deformation. On the contrary, the scattered intensities perpendicular to the tensile direction remain constant. This evolution corresponds to the growth of elongated cavities oriented in the direction normal to the direction of traction.

The damage mechanisms of polyamide A during tensile deformation at 60°C can be defined by two regimes. The first regime is visible at high q values. In this regime, damages are initiated by the nucleation of small crazes, occurring before 9% of true strain, as visible on Figure 101-a (bump at $q > 0.1 \text{ nm}^{-1}$). These nucleated crazes remain very small, with a maximal size of 100 nm in length (Table 27). The volume fraction of these crazes increases with deformation, from 2.0×10^{-6} to 1.4×10^{-5} .

The analysis of USAXS results permits to access to the number of the nucleated crazes per unit volume (N_2). Note that the non-monotonous evolution of N_2 may be attributed to the fact that the samples are different for each measurement made on different deformation. At 20% of true strain, 3.7×10^9 of small crazes per unit volume (mm^{-3}) have nucleated. The number of pre-existing defects N_1 is $1.1 \times 10^9 \text{ mm}^{-3}$ as given in Table 27. The number of the small nucleated crazes is of the same order of magnitude as the pre-existing defects. At 60% of true strain, this number is 1.8×10^{10} , which shows that this population of crazes increases slowly in the range of accessible deformation. The initial growth after nucleation of these small crazes is blocked at a size of 100 nm in length. Charvet et al attributed this behavior to the strain hardening which blocks the growth of cavities in this regime of deformation [26]. Between 9% and 60% of true strain, the size of crazes increases from 40 to 100 nm in length (D_{max}) and from 20 to 100 nm in thickness (L_{max}). Their volume fraction ϕ_2 increases with deformation, from 2.0×10^{-6} to 1.4×10^{-5} . All the values determined for polyamide A at 60°C are reported in Table 27.

Additionally to this first craze family, whose size is limited to 100 nm, we observe a second family of crazes which sizes are larger. This second family is visible at low q values and corresponds to large crazes with dimensions DD and LL (Table 27). A small fraction of the crazes formed by nucleation of cavities in the vicinity of pre-existing impurities during the first regime grow faster. As reported in Table 27, there are about 10^7 mm^{-3} (N_2') crazes of the second family, which represents a small fraction of the total number of crazes present in the sample (around 1.0×10^9). The maximum sizes of these crazes are 3000 nm in length (DD_{max}) and 800 nm in thickness (LL_{max}), with a volume fraction of 1.7×10^{-4} . Their growth is blocked at this size, by an effect to be discussed later.

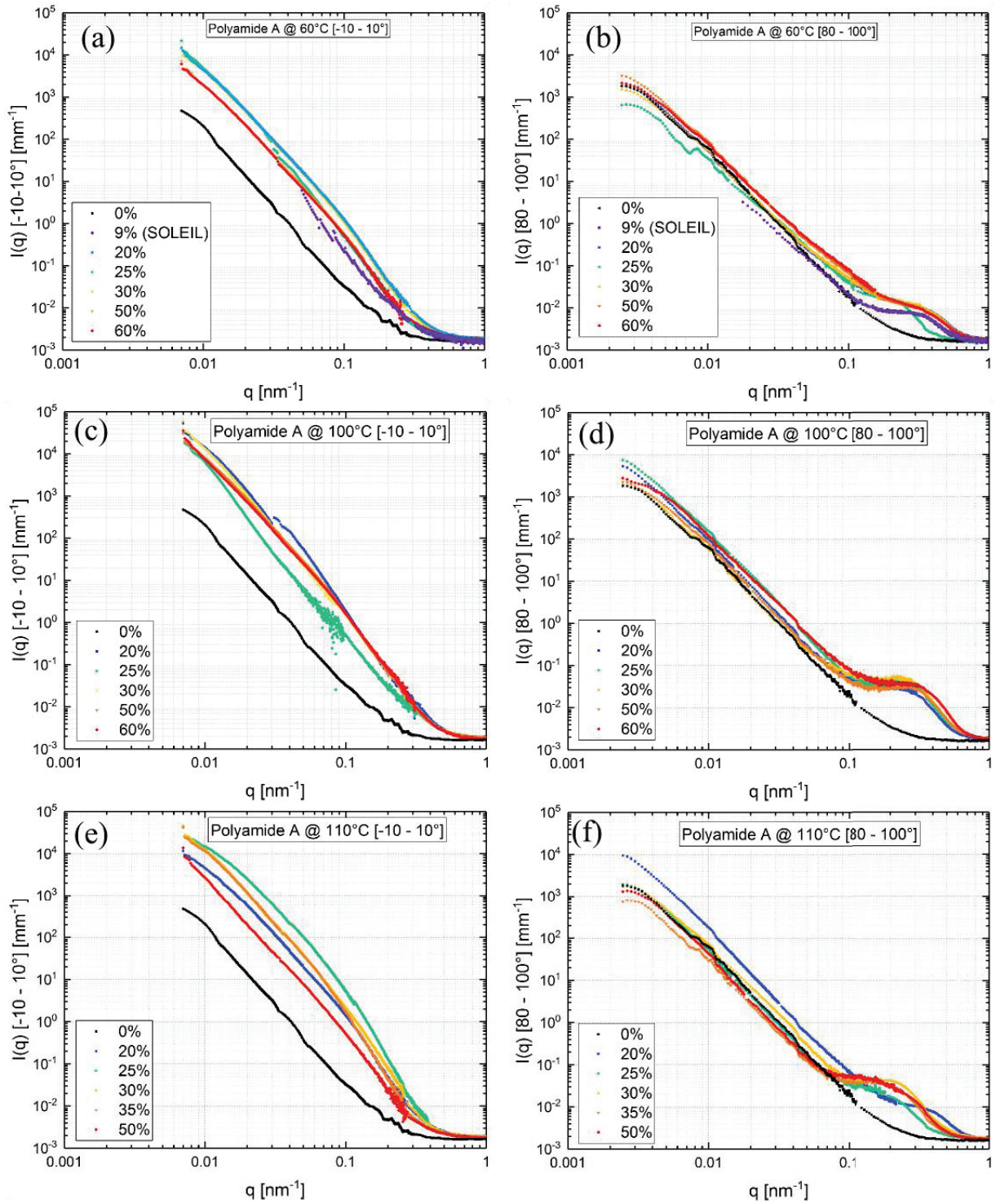


Figure 101 – Restricted scattered intensities in the parallel direction (a-c-e) and perpendicular direction (b-d-f) to the tensile direction obtained by USAXS experiments on polyamide A at different strain during tensile test and at different temperatures: (a-b) 60°C; (c-d) 100°C and (e-f) 110°C.

Table 27 – Sizes and volume fractions of damage corresponding to fitting parameters used at different strain for polyamide A at T=60°C in Figure 101(a-b). N_2 and Φ_2 are the number per unit volume and the volume fraction of the first family of crazes. N_2' and Φ_2' are the number per unit volume and the volume fraction of the second family of crazes.

Strain (%)	1 st craze family						2 nd craze family					
	D_{min}	D_{max}	L_{min}	L_{max}	Φ_2	N_2	DD _{min}	DD _{max}	LL _{min}	LL _{max}	Φ_2'	N_2'
	nm	nm	nm	nm		mm ⁻³	nm	nm	nm	nm		mm ⁻³
5%	5	10	1	10	2.0×10^{-6}	9.4×10^9	40	1000	10	140	2.0×10^{-4}	5.6×10^7
9%	5	20	1	10	3.0×10^{-6}	9.0×10^{10}	50	150	30	90	9.0×10^{-6}	4.5×10^6
20%	5	50	2	50	2.8×10^{-6}	3.7×10^9	100	1300	40	300	4.8×10^{-4}	3.7×10^7
25%	5	50	2	50	8.3×10^{-6}	1.1×10^{10}	100	1500	40	300	1.8×10^{-4}	2.1×10^7
30%	5	50	2	50	2.8×10^{-6}	3.7×10^9	120	1500	40	350	5.3×10^{-4}	6.3×10^7
50%	5	50	2	50	8.3×10^{-6}	1.1×10^{10}	120	1500	40	350	1.8×10^{-4}	2.1×10^7
60%	5	50	2	50	1.4×10^{-5}	1.8×10^{10}	120	1500	35	400	1.7×10^{-4}	2.6×10^7

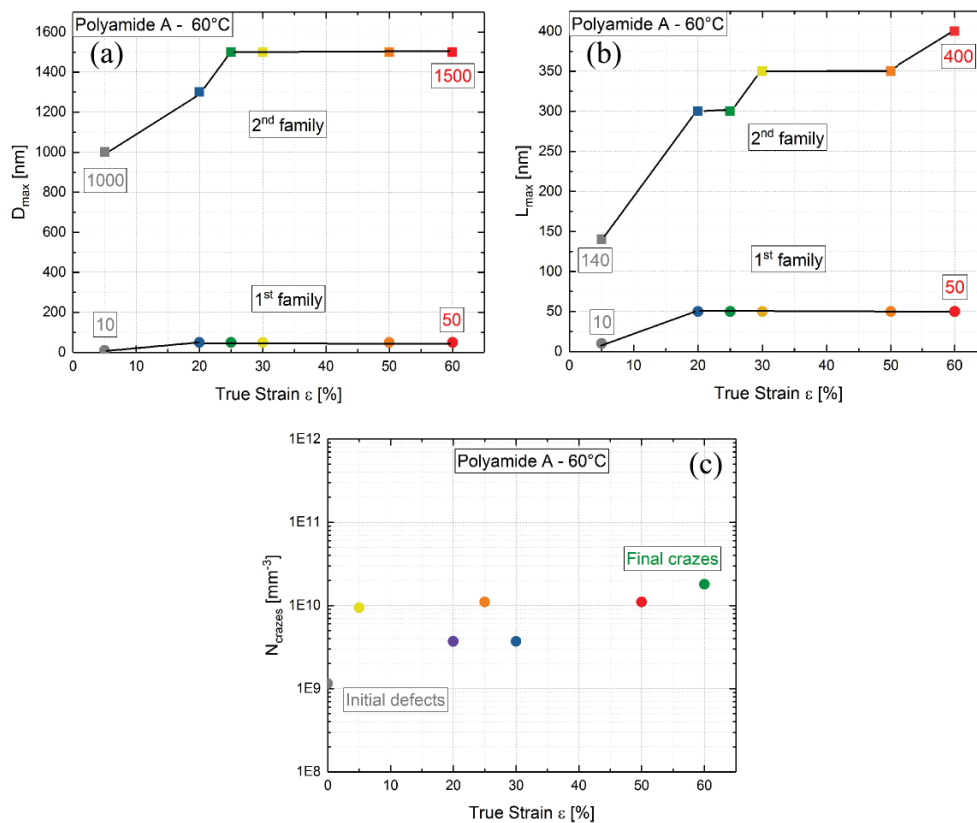


Figure 102 – Schematic representation of the evolution of the fitting parameters with the true strain: (a) D_{max} , (b) L_{max} and (c) N_{crazes} .

Table 28 – Sizes and volume fractions of damage corresponding to fitting parameters used at different strain for polyamide A at T=100°C in Figure 101(c-d). N_2 and Φ_2 are the number per unit volume and the volume fraction of the first family of crazes. N_2' and Φ_2' are the number per unit volume and the volume fraction of the second family of crazes.

Strain (%)	1 st craze family						2 nd craze family					
	D_{min} nm	D_{max} nm	L_{min} nm	L_{max} nm	Φ_2	N_2 mm^{-3}	DD_{min} nm	DD_{max} nm	LL_{min} nm	LL_{max} nm	Φ_2'	N_2' mm^{-3}
20%	1	10	1	30	1.8×10^{-6}	1.8×10^{10}	95	1300	40	300	1.6×10^{-4}	2.1×10^7
25%	1	10	1	30	2.7×10^{-6}	7.1×10^{10}	100	1300	40	350	2.6×10^{-4}	3.1×10^7
30%	1	10	1	30	2.7×10^{-6}	7.1×10^{10}	200	1300	40	350	5.0×10^{-4}	4.7×10^7
50%	1	10	1	40	2.4×10^{-6}	6.1×10^{10}	200	1320	40	350	1.3×10^{-4}	1.3×10^7
60%	1	10	1	40	2.5×10^{-6}	6.2×10^{10}	200	1320	40	350	1.3×10^{-4}	1.2×10^7

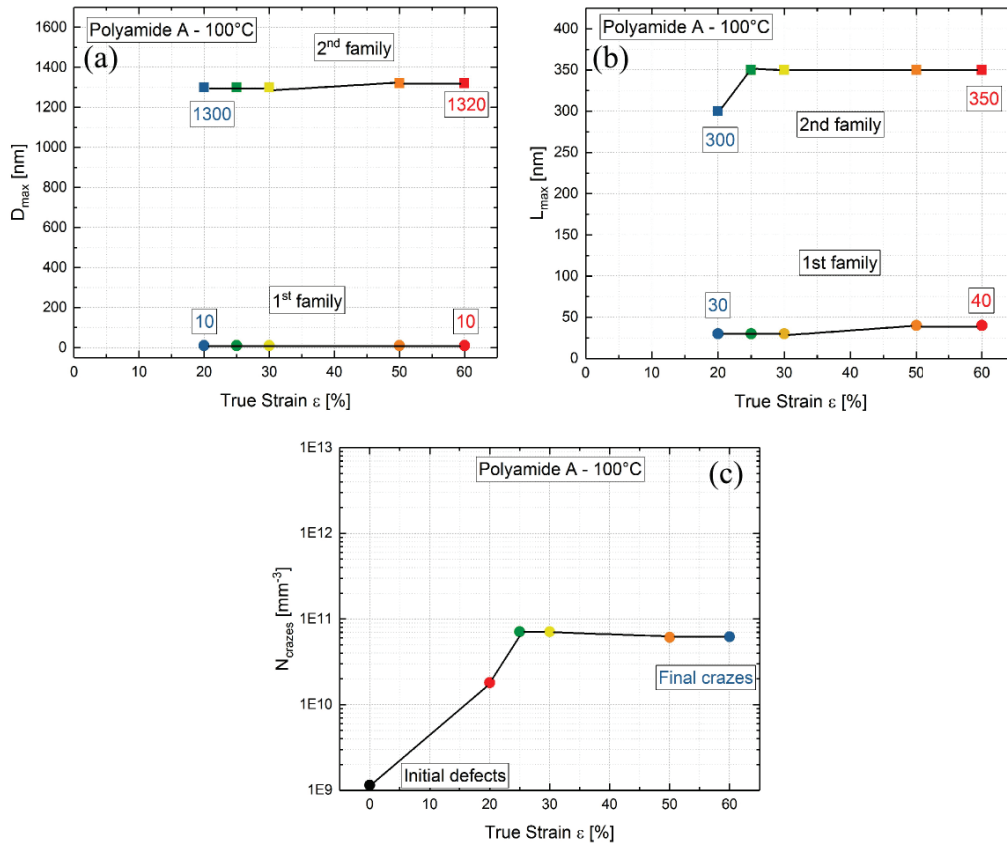


Figure 103 – Schematic representation of the evolution of the fitting parameters with the true strain: (a) D_{max} , (b) L_{max} and (c) N_{crazes} .

Table 29 – Sizes and volume fractions of damage corresponding to fitting parameters used at different strain for polyamide A at T=110°C in Figure 101(e-f). N_2 and Φ_2 are the number per unit volume and the volume fraction of the first family of crazes. N_2' and Φ_2' are the number per unit volume and the volume fraction of the second family of crazes.

Strain (%)	1 st craze family						2 nd craze family					
	D_{min} nm	D_{max} nm	L_{min} nm	L_{max} nm	Φ_2	N_2 mm^{-3}	DD_{min} nm	DD_{max} nm	LL_{min} nm	LL_{max} nm	Φ_2'	N_2' mm^{-3}
20%	1	10	1	20	3.2×10^{-6}	1.4×10^9	150	1200	40	300	8.2×10^{-5}	2.8×10^7
25%	5	10	2	40	3.5×10^{-6}	1.2×10^9	150	1200	45	300	8.2×10^{-5}	2.8×10^7
30%	5	10	2	40	7.1×10^{-6}	1.2×10^9	150	1200	45	300	8.2×10^{-5}	2.3×10^7
35%	5	10	2	50	7.3×10^{-6}	2×10^9	150	1300	45	300	8.5×10^{-5}	2.3×10^7
50%	5	10	2	50	1.1×10^{-6}	2.9×10^9	150	1300	45	300	2.4×10^{-4}	2.3×10^7

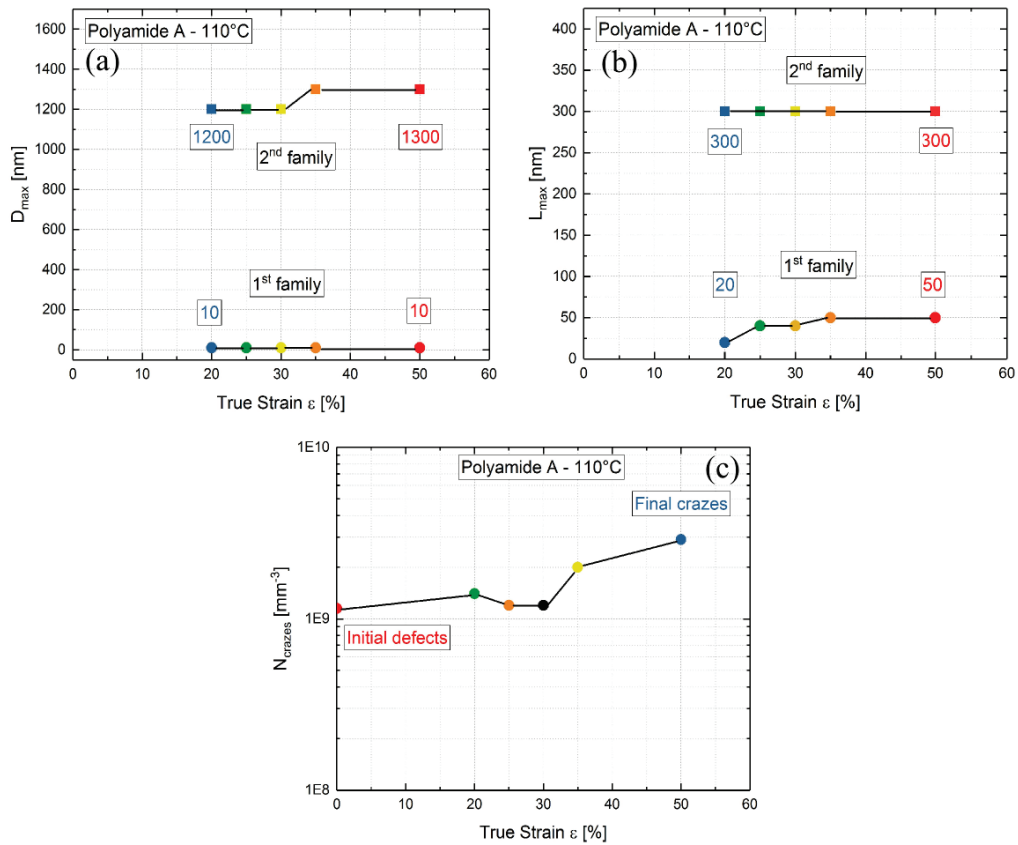


Figure 104 – Schematic representation of the evolution of the fitting parameters with the true strain: (a) D_{max} , (b) L_{max} and (c) N_{crazes} .

The damage mechanisms of polyamide A during tensile deformation at 100°C and 110°C can be also defined by the two regimes determined previously.

At 100°C, the nucleated crazes remain very small, with a maximal size of 20 nm in length (Table 28). The volume fraction of these crazes is also very low, 2.5×10^{-6} . The analysis of USAXS results permits to access to the number of the nucleated crazes per unit volume (N_2). At 20% of true strain, 1.8×10^{10} of small crazes per unit volume (mm^{-3}) have nucleated. At 60% of true strain, this number is 6.2×10^{10} . The initial growth after nucleation of these small crazes is blocked at a size of 20 nm in length, by an internal process within the polymer. Between 20% and 60% of true strain, the size of crazes does not evolve in length (D_{max}) and varies from 60 to 80 nm in thickness (L_{max}). Their volume fraction ϕ_2 increases from 1.8×10^{-6} to 2.5×10^{-6} . All the values determined for polyamide A at 100°C are reported in Table 28.

As reported in Table 28, around 10^7 mm^{-3} crazes per unit volume (N_2') are in the second craze family, which is less than the total number of crazes present in the sample (around 6.0×10^{10}). Compared to the first family of crazes, the second family of crazes has bigger sizes. The maximum sizes of these crazes are 2640 nm in length (DD_{max}) and 700 nm in thickness (LL_{max}), with a volume fraction of 1.3×10^{-4} . Their growth is blocked at this size, by another internal process within the polymer.

At 110°C, the nucleated crazes remain very small, with a maximal size of 20 nm in length (Table 29). The volume fraction of these crazes is also low, 1.1×10^{-6} . The analysis of USAXS results permits to access to the number of the nucleated crazes per unit volume (N_2). At 20% of true strain, 1.4×10^9 of small crazes per unit volume (mm^{-3}) have nucleated. At 50% of true strain, this number is 2.9×10^9 . The initial growth after nucleation of these small crazes is blocked at a size of 20 nm in length, by an internal process within the polymer. Between 20% and 50% of true strain, the size of crazes does not evolve in length (D_{max}) and varies from 40 to 100 nm in thickness (L_{max}). Their volume fraction ϕ_2 does not evolve with the deformation and is about 1×10^{-6} . All the values determined for polyamide A at 110°C are reported in Table 29.

As reported in Table 29, around 10^7 mm^{-3} crazes per unit volume (N_2') are in the second craze family, which is less than the total number of crazes present in the sample (around 2.0×10^9). Compared to the first family of crazes, the second family of crazes has bigger sizes. The maximum sizes of these crazes are 2600 nm in length (DD_{max}) and 600 nm in thickness (LL_{max}), with a volume fraction of 2.4×10^{-4} . Their growth is blocked at this size, by another internal process within the polymer.

5.2.2.2.2 ***Behavior under tensile deformation of polyamide B and polyamide C***

Figure 105 and Figure 106 show both parallel and perpendicular scattered intensities at different strain levels at 60°C (a-b), 100°C (c-d) and 110°C (e-f) for polyamide B and at 120°C (a-b), 130°C (c-d) and 140°C (e-f) for polyamide C, respectively. The study of the damage is done in the ductile regime.

For both polymers and for the three temperatures tested, no evolution of the scattered intensities is observed by USAXS experiments as observed in Figure 105 and Figure 106. At large q values, the curves in both parallel and perpendicular direction overlap (the signal is isotropic). At small q values, the curves do not overlap perfectly, they are not monotonous. This is due to reproducibility, and cavities related to the injection process (each time, a different sample is stretched). We deduce that these polymers do not get damaged up to 50 % of true strain for both polyamide B and polyamide C. We measured only the signal due to cavities related to the injection process.

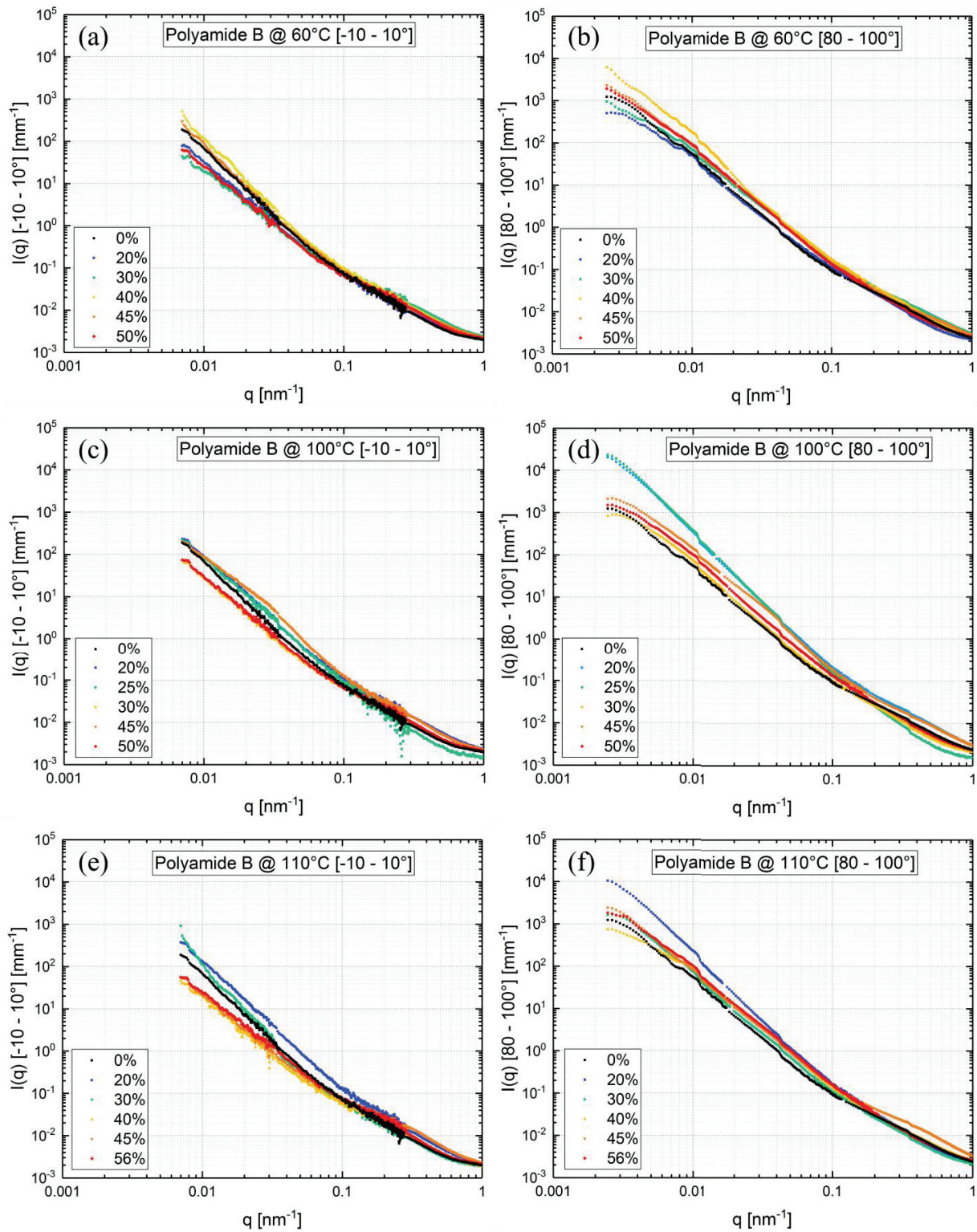


Figure 105 – Restricted scattered intensities in the parallel direction (a-c-e) and perpendicular direction (b-d-f) to the tensile direction obtained by USAXS experiments on polyamide B at different strain during tensile test and at different temperatures: (a-b) 60°C; (c-d) 100°C and (e-f) 110°C.

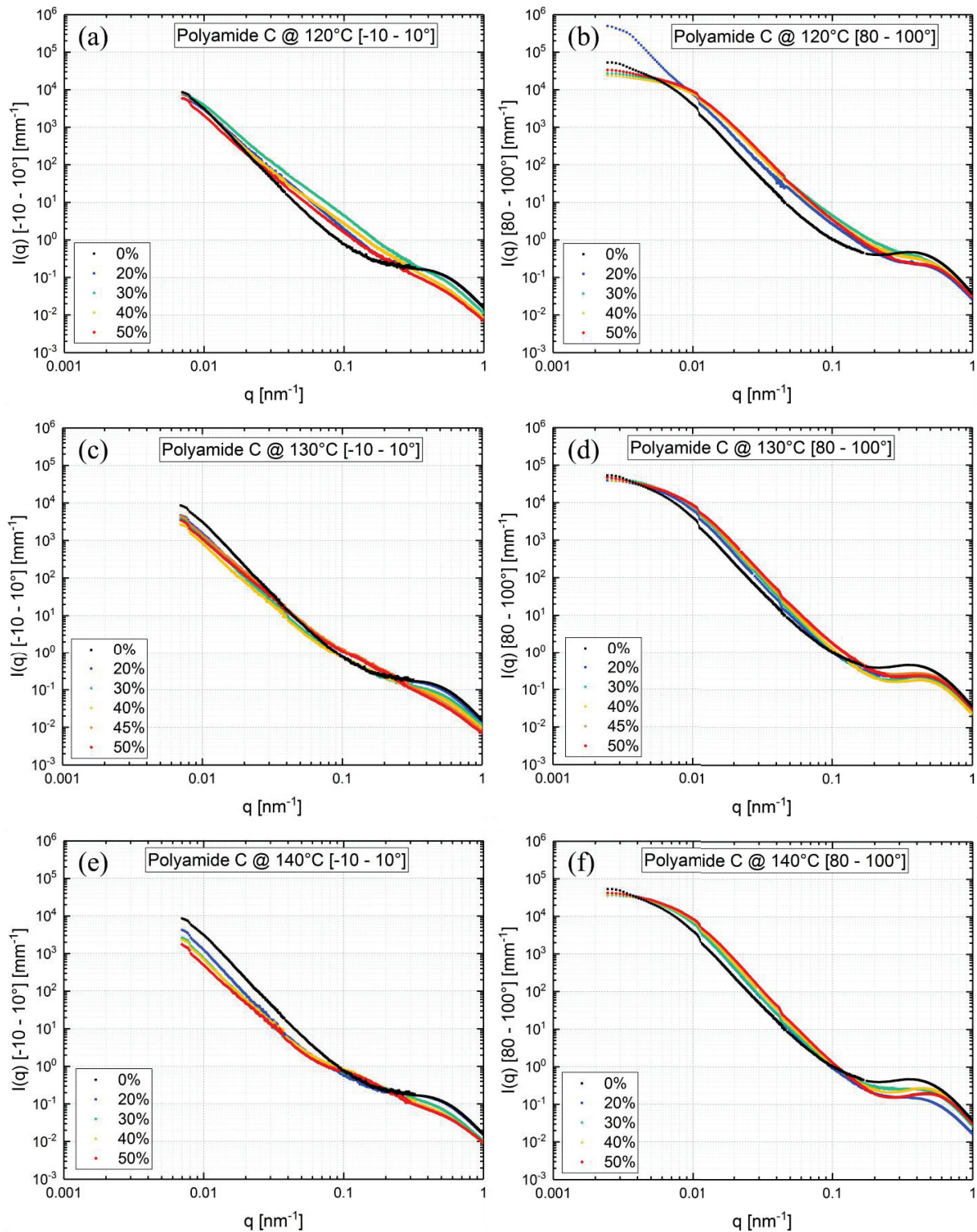


Figure 106 – Restricted scattered intensities in the parallel direction (a-c-e) and perpendicular direction (b-d-f) to the tensile direction obtained by USAXS experiments on polyamide C at different strain during tensile test and at different temperatures: (a-b) 120°C; (c-d) 130°C and (e-f) 140°C.

5.2.2.2.3 *Behavior under tensile deformation of polycarbonate*

Polycarbonate is a tough and ductile polymer at 23°C and for all the considered studied temperatures. Figure 107 shows the restricted scattered intensities in the parallel direction (a) and perpendicular direction (b) to the tensile direction obtained by USAXS experiments on polycarbonate at different strain during tensile test until failure and at 23°C. Experimental data are fitted by global scattered intensity given by Equations 70 and 71. Thanks to the analysis of the experimental data, the size and the volume fraction of each typology of damage can be determined. All the adjustable parameters are given in Table 30.

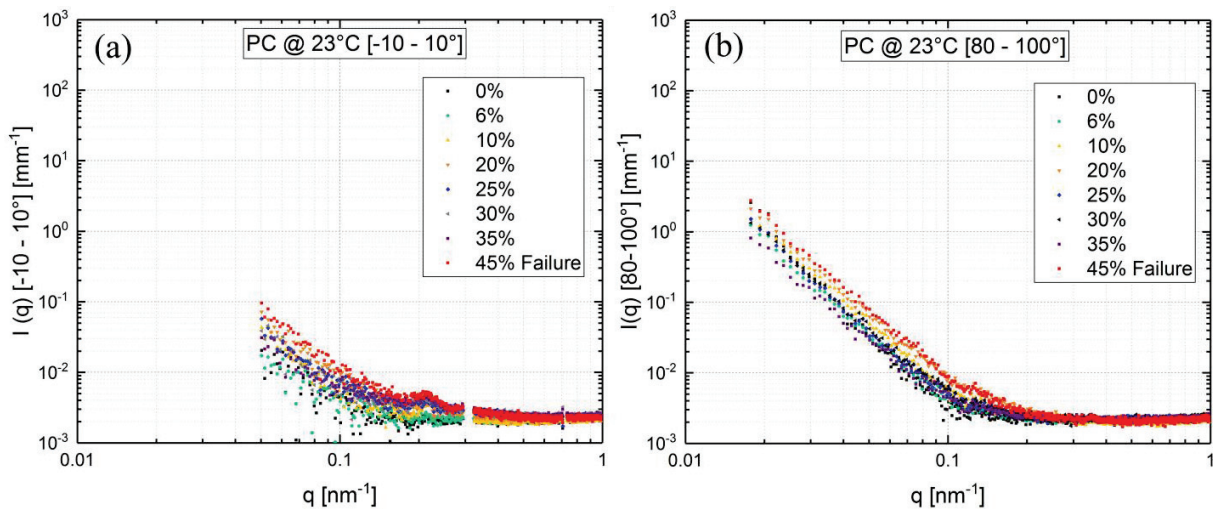


Figure 107 – Restricted scattered intensities in the parallel direction (a) and perpendicular direction (b) to the tensile direction obtained by USAXS experiments on polycarbonate at different strain during tensile test until failure at 23°C.

In Figure 107, we observe a monotonous evolution. The curves in both parallel and perpendicular directions do not overlap: there is more diffusion in the parallel direction.

Table 30 – Sizes and volume fractions of damage corresponding to fitting parameters used for polycarbonate at 23°C at different strain until failure in Figure 107. N_2 and Φ_2 are the number per unit volume and the volume fraction of the first family of crazes. N_2' and Φ_2' are the number per unit volume and the volume fraction of the second family of crazes.

Strain (%)	1 st craze family						2 nd craze family					
	D_{\min}	D_{\max}	L_{\min}	L_{\max}	Φ_2	N_2	DD_{\min}	DD_{\max}	LL_{\min}	LL_{\max}	Φ_2'	N_2'
	<i>nm</i>	<i>nm</i>	<i>nm</i>	<i>nm</i>		<i>mm⁻³</i>	<i>nm</i>	<i>nm</i>	<i>nm</i>	<i>nm</i>		<i>mm⁻³</i>
6%	1	10	1	15	2.6×10^{-6}	1.5×10^{10}						
10%	1	10	1	15	3.3×10^{-6}	1.8×10^{10}				N/A		
20%	1	10	1	15	8.9×10^{-6}	3.2×10^{10}						
25%	1	15	1	15	1.9×10^{-5}	8.8×10^{10}	50	200	80	150	1.3×10^{-6}	2.6×10^5
30%	1	15	1	15	2.0×10^{-5}	8.8×10^{10}	50	300	80	150	1.7×10^{-6}	2.6×10^5
35%	1	15	1	15	2.0×10^{-5}	8.5×10^{10}	50	400	80	150	2.2×10^{-6}	2.6×10^5
45%	1	15	1	20	2.0×10^{-5}	8.2×10^{10}	50	600	80	150	3.1×10^{-5}	2.6×10^5

Two size distributions are necessary to describe the contribution of crazes at deformations larger than 25%. At small q values, both the scattered intensities parallel and perpendicular to the tensile direction increase with deformation. This evolution corresponds to the growth of elongated cavities oriented in the direction perpendicular to the tensile direction.

The damage mechanisms of polycarbonate during tensile deformation at 23°C can be defined by two regimes. The first regime is observable at high q values. In this regime, damages are initiated by the nucleation of small crazes, which occurs before 6% of true strain, as visible on Figure 107. These nucleated crazes remain small, with a maximal size of 30 nm in length (Table 30). The volume fraction of these crazes increases with deformation, from 2.6×10^{-6} to 2.0×10^{-5} at 45% of deformation.

The number of the nucleated crazes per unit volume (N_2) can be determined. At 25% of true strain, 8.8×10^{10} of small crazes per unit volume (mm^{-3}) have nucleated. The number of pre-existing cavities N_i resulting from the injection process is $3.9 \times 10^5 \text{ mm}^{-3}$ (Table 26). The number of the small nucleated crazes is higher than the pre-existing ones. This number remains constant after 6% of deformation which indicates that these crazes nucleate on impurities. At 45% of true strain (failure of the specimen), this number is still 8.2×10^{10} . The initial growth after nucleation of these small crazes is blocked at a size of 30 nm in length, an effect attributed to strain hardening by Charvet et al [26]. Between 6% and 45% of true strain, the size of crazes increases from 20 to 30 nm in length (D_{\max}) and from 30 to 40 nm in thickness (L_{\max}). Their volume fraction ϕ_2 increases with deformation, from 2.6×10^{-6} to 2.0×10^{-5} . All the values

determined for polycarbonate at 23°C are reported in Table 30. Note that φ_2 is dominated by the lower bound of the integral (small size, D_{\min} and L_{\min}).

Increasing the strain beyond 25% leads to a new growth regime for a small fraction of the nucleated crazes. This second growth regime is observable at low q values and corresponds to large crazes with dimensions DD and LL (Table 30). A small fraction of the crazes formed by nucleation of cavities on impurities grow faster. As reported in Table 30, the number of these large crazes per unit volume is of order 10^5 mm^{-3} (N_2'), which is much less than the total number of crazes present in the sample (around 8.0×10^{10}). The crazes observed continue to grow until the failure of the specimen at 45% of true strain. At failure, the maximum sizes of these crazes are 1200 nm in length (DD_{\max}) and 300 nm in thickness (LL_{\max}), with a volume fraction of 3.1×10^{-5} .

In the discussion part, we propose to explain the moderate growth of the two crazes families by the presence of the strain hardening for the first family of crazes, in a similar mechanism as for cellulose acetate [26].

5.2.2.2.4 ***Behavior under tensile deformation of PMMA***

Below 80°C, PMMA is fragile. Above 80°C, PMMA is ductile. Figure 108 shows the restricted scattered intensities in the parallel direction (a) and perpendicular direction (b) to the tensile direction obtained by USAXS experiments on PMMA at different strain during tensile test until failure and at 80°C. All the adjustable parameters are given in Table 31. Two size distributions are necessary to describe the contribution of crazes. A bump is visible on the scattered intensity in the direction parallel to the tensile direction (Figure 108-a).

The damage mechanisms of PMMA during tensile deformation at 80°C can be defined by two regimes. The first regime is visible at high q values. In this regime, damages are initiated by the nucleation of small crazes, occurring before 3% of true strain, as visible on Figure 108. These nucleated crazes remain small, with a maximal size of 200 nm in length (Table 31). The volume fraction of these crazes increases with deformation, from 2.0×10^{-5} to 1.5×10^{-4} .

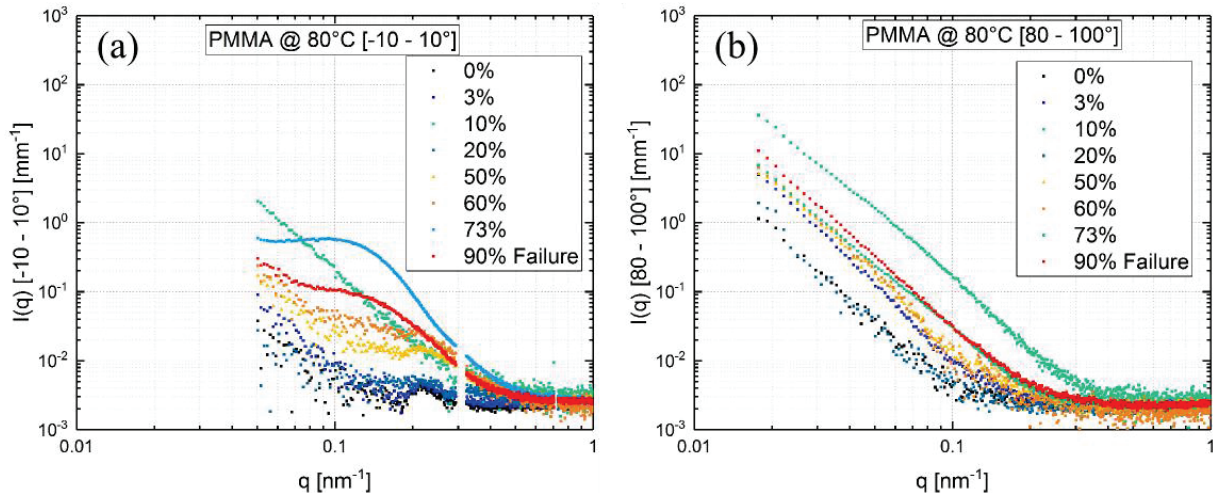


Figure 108 – Restricted scattered intensities in the parallel direction (a) and perpendicular direction (b) to the tensile direction obtained by USAXS experiments on PMMA at different strain during tensile test until failure at 80°C.

Table 31 – Sizes and volume fractions of damage corresponding to fitting parameters used at different strain for PMMA at 80°C in Figure 108. N_2 and Φ_2 are the number per unit volume and the volume fraction of the first family of crazes. N_2' and Φ_2' are the number per unit volume and the volume fraction of the second family of crazes.

Strain (%)	1 st craze family						2 nd craze family					
	D_{\min}	D_{\max}	L_{\min}	L_{\max}	Φ_2	N_2	DD_{\min}	DD_{\max}	LL_{\min}	LL_{\max}	Φ_2'	N_2'
	nm	nm	nm	nm			nm	nm	nm	nm		
3%	1	70	1	20	2.0×10^{-5}	2.7×10^8						
10%	1	70	1	20	4.3×10^{-5}	2.8×10^8				N/A		
20%	1	70	1	20	5.2×10^{-5}	2.8×10^8						
50%	1	70	1	20	2.0×10^{-5}	2.7×10^8	50	200	30	100	8.3×10^{-6}	2.4×10^4
60%	1	70	1	20	2.0×10^{-5}	2.7×10^8	50	250	30	100	2.1×10^{-5}	2.3×10^4
73%	1	80	1	30	1.5×10^{-4}	2.6×10^8	50	300	30	100	1.8×10^{-5}	2.4×10^4

The number of the nucleated crazes per unit volume (N_2) can be determined. At 3% of true strain, the number of small crazes per unit volume is of order $2.7 \times 10^8 \text{ mm}^{-3}$. This number remains constant almost up to failure. All the impurities present do not lead to nucleation on injection, but they can do so under deformation. When the number of cavities is constant, it is a sign of heterogeneous nucleation. It is also the case for polycarbonate. The number of pre-existing defects N_i is $4.2 \times 10^7 \text{ mm}^{-3}$ (Table 26). The number of the small nucleated crazes is higher than the pre-existing cavities. The initial growth after nucleation of these small crazes is blocked at a size of 160 nm in length, which we assume is due to strain

hardening [26]. The size of crazes slowly increases with the deformation until 73% of deformation, from 140 to 160 nm in length. Their volume fraction ϕ_2 increases with deformation, from 2.0×10^{-5} to 1.5×10^{-4} . All the values determined for PMMA at 90°C are reported in Table 31. The intensity measured at rupture (90% of true strain) is difficult to interpret. We therefore restrict our discussion at 73% of true strain.

Increasing the strain beyond 50% leads to a new growth regime for a small fraction of crazes. This second growth regime is visible at low q values and corresponds to large crazes with dimensions DD and LL (Table 31). A small fraction of the crazes formed by nucleation of cavities in the vicinity of pre-existing impurities during the first regime grow faster. As reported in Table 31, around 2.10^4 mm^{-3} crazes per unit volume (N_2') are in this second craze family, which is a very small number as compared to the total number of crazes present in the sample (around 1.0×10^{10} per mm^3). The crazes observed continue to grow until 73% of true strain. The maximum sizes of these crazes are 600 nm in length (DD_{\max}) and 200 nm in thickness (LL_{\max}), with a volume fraction of 1.8×10^{-5} .

In the discussion part, we propose to explain the moderate growth of the two crazes families by the presence of the strain hardening for the first family of crazes, in a similar mechanism as for cellulose acetate [26] and polycarbonate.

5.2.2.2.5 **Behavior under tensile deformation of polyamide D: effect of the orientation**

Figure 109 shows the normalized scattered intensities for the directions parallel and perpendicular to the tensile direction obtained after failure at 23°C for different angle θ (0°, 45° and 90°) for polyamide D. The fitting parameters are given in Table 32.

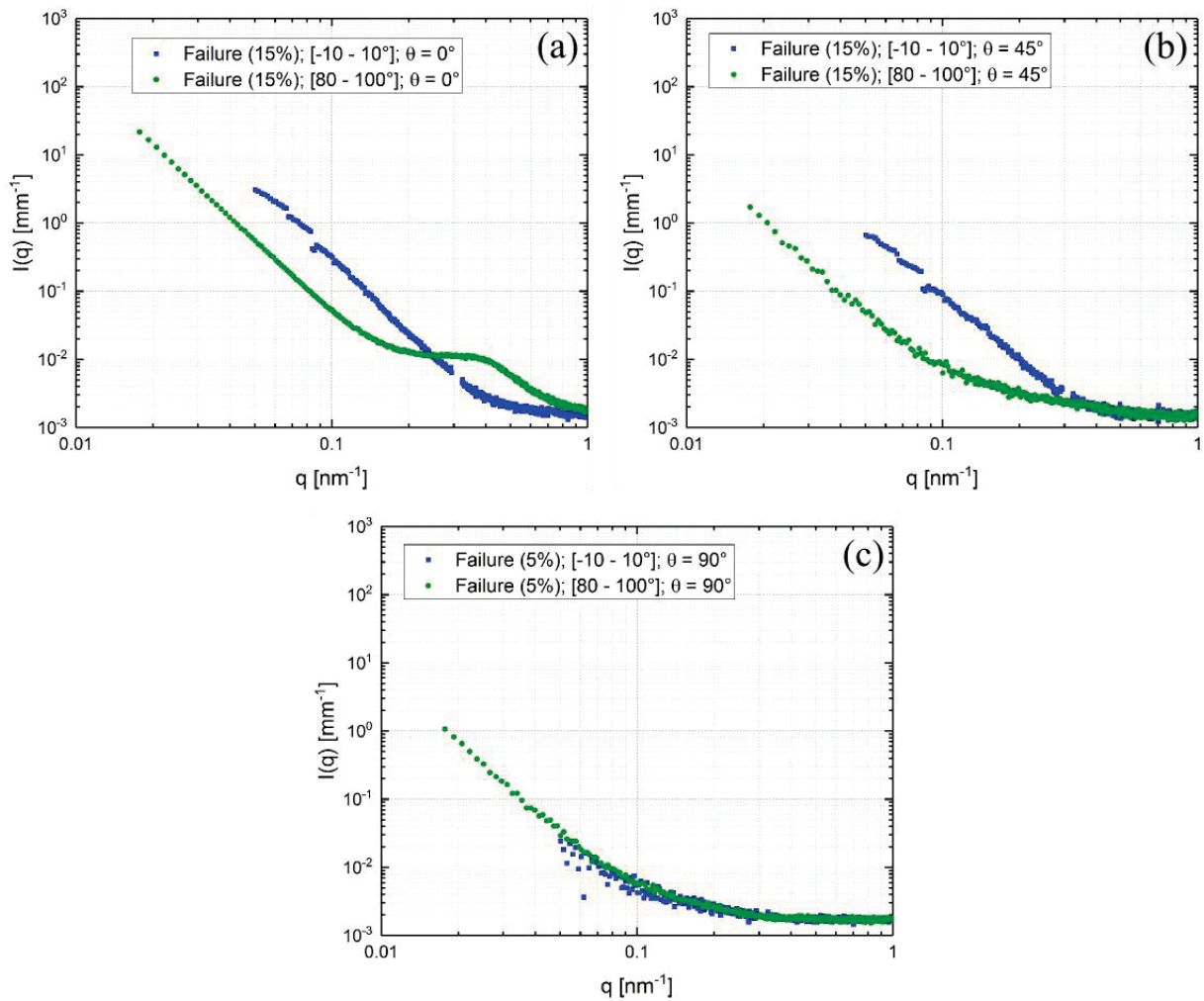


Figure 109 – USAXS scattered intensities in the parallel direction (blue curves) and perpendicular direction (green curves) to the tensile direction obtained after failure at 23°C for polyamide D for different angles θ : (a) $\theta = 0^\circ$, (b) $\theta = 45^\circ$ and (c) $\theta = 90^\circ$.

We can see different evolutions of the scattered intensities parallel to the tensile direction for each angle θ . For $\theta = 0^\circ$ and 45° , two size distributions of crazes are needed to describe the scattered intensities whereas for $\theta = 90^\circ$ only one size distribution of crazes is necessary.

The volume fraction of craze φ_2 of the first craze family is almost the same (around 2.1×10^{-5}). With $\theta = 0^\circ$, the volume fraction and the size of the crazes is higher.

Table 32 – Sizes and volume fractions of damage corresponding to fitting parameters used at different strain for polyamide D at 23°C in Figure 109 for different angles θ . N_2 and Φ_2 are the number per unit volume and the volume fraction of the first family of crazes. N_2' and Φ_2' are the number per unit volume and the volume fraction of the second family of crazes.

θ (°)	1 st craze family						2 nd craze family					
	D_{\min}	D_{\max}	L_{\min}	L_{\max}	Φ_2	N_2	DD_{\min}	DD_{\max}	LL_{\min}	LL_{\max}	Φ_2'	N_2'
	<i>nm</i>	<i>nm</i>	<i>nm</i>	<i>nm</i>		<i>mm⁻³</i>	<i>nm</i>	<i>nm</i>	<i>nm</i>	<i>nm</i>		<i>mm⁻³</i>
0°	1	20	5	10	2.1×10^{-5}	3.3×10^7	160	1200	50	300	2.4×10^{-5}	4.4×10^6
45°	1	30	3	10	5.6×10^{-5}	1.5×10^8	60	500	30	110	1.3×10^{-5}	1.77×10^7
90°	1	20	5	10	2.1×10^{-5}	3.3×10^7				N/A		

5.2.2.3 Absence of strain induced crystallization

In the case of polyamide A, the appearance of a peak at large q with the deformation is observed (see Figure 101). This peak is close to $q_{\max} = 0.6 \text{ nm}^{-1}$. In order to verify the absence of strain induced crystallization of this polymer, we performed WAXS experiments on deformed samples of polyamide A, and on some samples of polyamide C, which is semi-crystalline in order to compare the signals obtained. Figure 110 shows the WAXS patterns obtained for the polyamide A (tensile tests at 60°C and 110°C), as well as for the polyamide C (tensile tests at 120°C and 140°C).

For polyamide C, a peak close to $q_{\max} = 0.6 \text{ nm}^{-1}$ is already observed on the sample before deformation, which is not the case for polyamide A. The pattern obtained in WAXS clearly shows that polyamide A remains amorphous (Figure 110-a and Figure 110-b), unlike polyamide C which shows a semi-crystalline character before and after tensile deformation (Figure 110-c and Figure 110-d). The amorphous polymer polyamide A do not exhibit any crystalline structures in WAXS experiments.

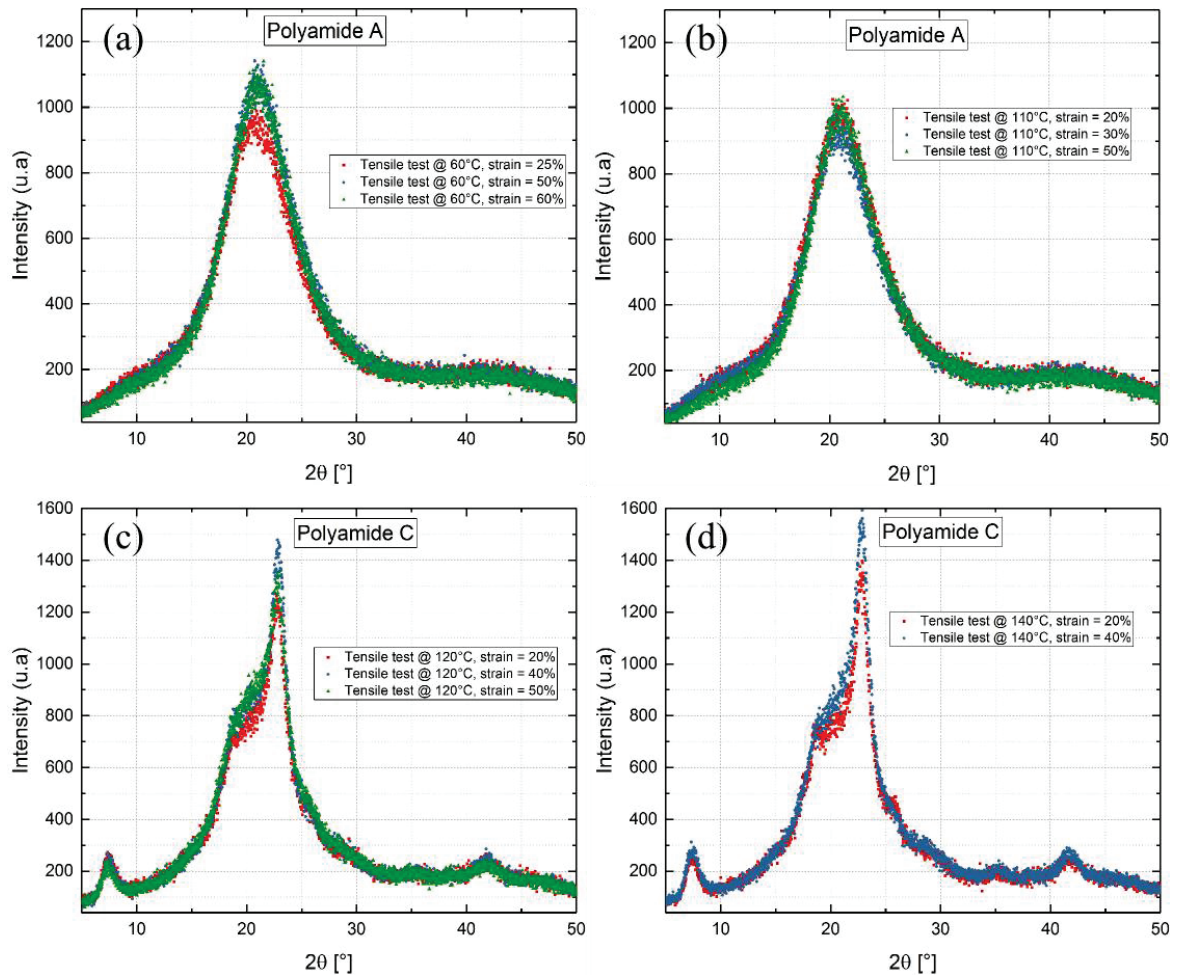


Figure 110 – WAXS patterns of polyamide A (a-b) and polyamide C (c-d) after tensile deformation.

The USAXS curves obtained for polycarbonate or PMMA do not show a peak towards $q_{\max} = 0.6 \text{ nm}^{-1}$ as is the case for polyamide A. We have nevertheless verified by DSC the absence of crystallinity for both polycarbonate and PMMA. The thermograms obtained for PC and PMMA are shown in Figure 111.

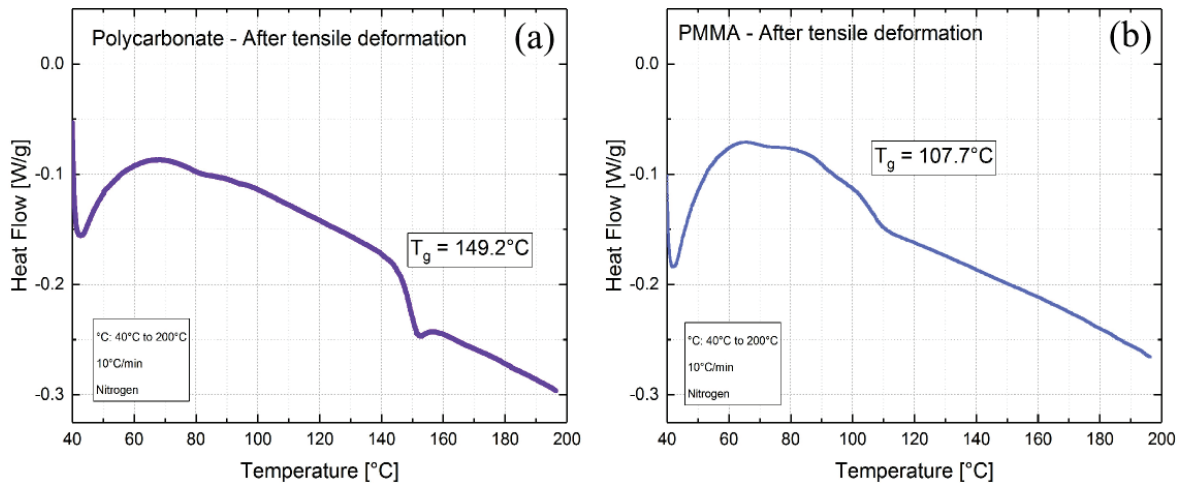


Figure 111 – Thermograms obtained by DSC for (a) polycarbonate and (b) PMMA, after tensile deformation. Polycarbonate was tested at 60°C and 52% of true strain, PMMA was tested at 90°C and 86% of true strain.

The glass transition temperature T_g of the polycarbonate after tensile deformation (at 60°C and 52% of true strain) is equivalent to that determined before tensile deformation ($T_g = 149.7^\circ\text{C}$). The thermogram observed after deformation is comparable to an expected thermogram for an amorphous polycarbonate without deformation. DSC analysis shows no peak of crystallinity. The polymer is still amorphous after deformation.

The thermogram observed after tensile deformation of PMMA at 90°C and 86% of true strain is comparable to an expected thermogram for an amorphous PMMA without deformation

5.2.3 Interpretation and discussion

5.2.3.1 Introduction

After having described the damaging mechanisms observed by USAXS experiments for the five polymers, we propose to classify these different mechanisms. Charvet et al [26] have shown in plasticized cellulose acetate polymers that damage mechanisms under tensile deformation take place in two main stages. Damages are initiated by cavitation. Charvet et al have observed the nucleation of cavities within the time resolution of the experiment around impurities due to the injection process. These cavities are observed when their sizes have reached a size of order $\xi \approx 50$ or 100 nm. Then, a slow growth regime is observed

upon increasing the stress further with a diameter which grows linearly with the stress. The authors propose to explain this moderate growth by the presence of strain hardening. Indeed, tensile experiments on plasticized cellulose acetate polymers display an important strain hardening regime above 8% of true strain [166]. Once the cavity nucleates, the tensile stress around it relaxes. Under the effect of the macroscopic stress the cavity starts to grow and tangential stress increases. At some point, the stress in the vicinity of the cavities becomes sufficiently high to equilibrate the stress on larger scale and the growth is blocked. This effect is the consequence of the strain hardening. Note that without this effect the nucleation of a single cavity in amorphous polymers would lead to rapid breaking of the sample. The same effect is observed with polyamide A, PMMA and polycarbonate.

Cavitation occurs when the isotropic component of the stress in the material (the negative pressure, Π) exceeds a critical value. The critical diameter a_c for cavitation is given by [26]:

$$a_c = \frac{4\gamma_s}{\Pi} \quad (72)$$

where γ_s the surface tension of the material. Beyond this value a_c , a cavity is unstable and grows rapidly [183]–[186] until its growth is blocked by the strain hardening which develops in its vicinity. a_c is of order 1 nm [183], [185], [186].

The corresponding free energy barrier for homogeneous nucleation is given by the following equation:

$$\zeta_{hom}^*(p) = \frac{16\pi\gamma_s^3}{3\Pi^2} \quad (73)$$

Note that in the case of heterogeneous nucleation, the value of the free energy barrier can be reduced by several orders of magnitude. This is the case of CDA [26] and also with the polymers considered in this manuscript.

Figure 112 gives a schematic representation of the first regime of craze growth, where Π is the macroscopic imposed stress, σ_{tan} is the local stress in the equator position of the cavity, $a(0)$ is the initial cavity diameter and R is the final diameter that the cavity can reach. When the cavity grows, the tangential stress increases.

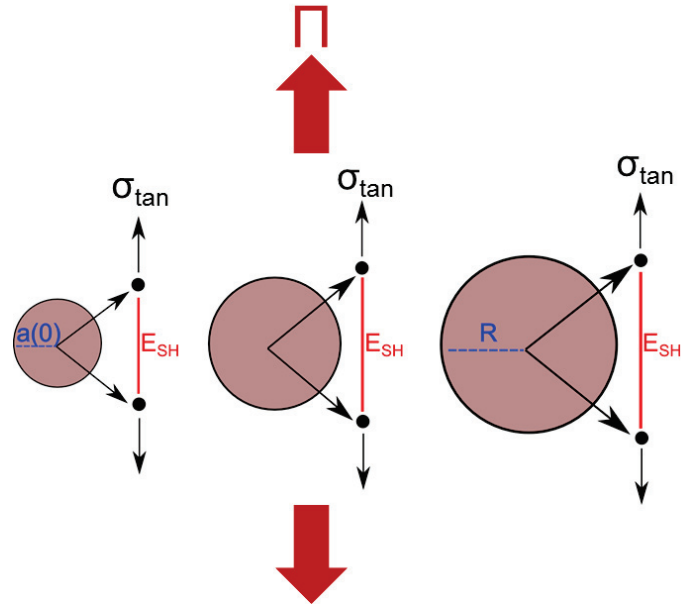


Figure 112 – Representation of the first regime of craze growth, blocked by the strain hardening regime.

The size R at which the strain hardening blocks the growth of the cavity is given by:

$$R = \kappa \frac{\Pi}{E_{SH}} a(0) + a(0) \quad (74)$$

Where κ is a number of order 1, $a(0)$ is an initial effective cavity diameter corresponding to the distance from a free interface beyond which the polymer recovers its bulk properties [26], [187]–[189]. E_{SH} is the strain hardening modulus. From Equation (74), one can deduce indeed that the growth of the cavities in this regime is linear with the applied stress and that this growth does not stem from new damages but is purely elastic and plastic in nature.

Once the applied stress becomes sufficiently high, the growth of the cavities enters a new regime. A small fraction of these crazes starts to grow faster until the failure of the sample. Charvet et al propose that this growth is governed by a mechanism of successive homogeneous nucleations of new cavities in the vicinity of the existing cavities, just ahead of them where the stress is the largest. Indeed, when a craze reaches a sufficiently large size, or when the local stress level is sufficiently high, this craze becomes

unstable and propagates as a crack resulting in the failure of the sample. Figure 113 gives a schematic representation of this mechanism.

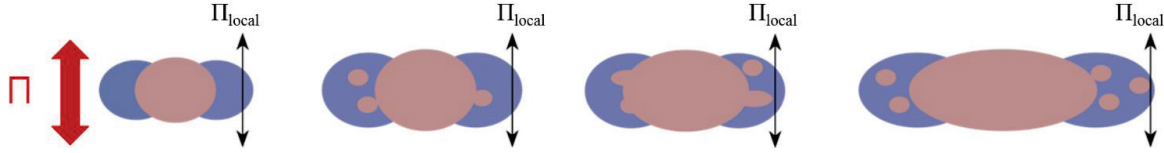


Figure 113 – Schematic representation of the growth crazes by nucleation of cavities followed by a coalescence mechanism.

The breaking time t_{∞} starting from a craze of size of $D(0)$ is found to be [26]:

$$t_{\infty} \approx \frac{a_c^3}{\xi D^2(0)} \tau \quad (75)$$

If we consider the nucleation time τ is of order $\tau_r = 10^8$ s, $a_c \sim 1$ nm; $\xi \sim 100$ nm and $D(0) \sim 100$ nm, the sample breaks in a time $t_{\infty} \approx 100$ s which corresponds to the order of magnitude of the experimental time scale.

This regime is unstable. The nucleation time τ decreases sharply when the stress increases. The evolution of the nucleation time as a function of the applied stress is given by equation:

$$\ln\left(\frac{\tau}{\tau_r}\right) \approx \ln\left(\frac{\tau_r}{\tau_0}\right) \left[\frac{\Pi_r^2}{\Pi^2} - 1\right] \approx 46 \left[\frac{\Pi_r^2}{\Pi^2} - 1\right] \quad (76)$$

With Π the local stress, $\tau_r = 10^8$ s, Π_r is the local stress at breaking.

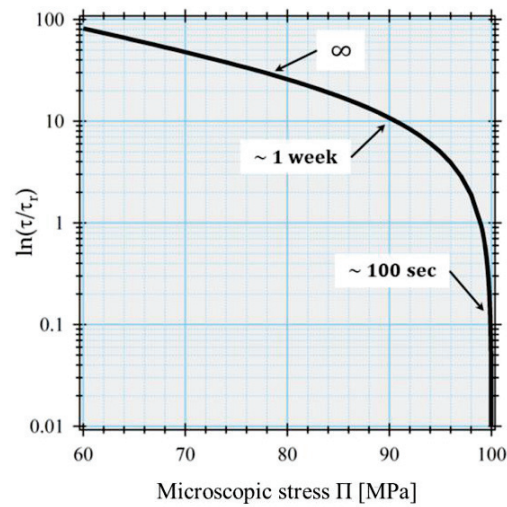


Figure 114 – Evolution of $\ln(\tau/\tau_r)$ as a function of the microscopic stress applied Π . From Charvet et al.[26]

Figure 114 shows the instability of this regime. Indeed, the rupture time is highly sensitive to the stress. If we assume as in Charvet et al study [26] that the local stress corresponding to rupture of the material in the experimental time scale is 100 MPa (for the sake of being specific), the nucleation time is $\tau_r = 10^8$ s and the corresponding macroscopic breaking time is $t_\infty \sim 100$ s. If the local stress is decreased to 85 MPa, the macroscopic breaking time is $t_\infty \sim 10^{10}$ s, which can be considered infinite for all practical purposes. The breaking time is thus strongly non-linear as a function of the applied macroscopic stress.

Our study focuses on five polymers, three of which do not break (the three PPA) and among them two of which are not damaged at all during deformation (polyamide B and C). The analysis of these different polymers by USAXS highlights different modes of ultimate behavior and damaging which we discuss now. The three PPA display a stabilized necking in the strain hardening regime and do not break, while the polycarbonate and PMMA do not show necking and deform homogeneously. The latter break at some point in the strain hardening regime. It can be observed that polyamide A has a stabilized damage and do not break, which is not the case for polycarbonate and PMMA, which have unstabilized damage and break in a way similar to that of cellulose acetate [26].

5.2.3.2 Damage mechanisms of polycarbonate and PMMA

The studied polycarbonate and PMMA have a behavior similar to another amorphous ductile polymer, the plasticized cellulose acetate studied by Charvet et al [26]. Unlike the studied PPA, these two polymers deform homogeneously without necking as it is the case of the CDA studied by Charvet et al. The damage mechanism can be described by a two-steps mechanism for both polycarbonate and PMMA, and is the same as the mechanism described by Charvet et al for plasticized cellulose acetate [166].

For PMMA at 80°C, during the first step, USAXS analysis show that small crazes with a size comprised between 2 and 160 nm nucleate simultaneously within the time resolution of our experiment, before 3 % of true strain. The number of these nucleated crazes per unit volume is found to be of order $N_2 = 2.7 \times 10^8 \text{ mm}^{-3}$, which is the same order of magnitude as but larger than that of the number of cavities initially present in the sample (which result from the injection process) with $N_i = 4.2 \times 10^7 \text{ mm}^{-3}$, measured on samples before tensile testing, as reported in Table 26. After this initial stage, it is observed that the number of nucleated crazes no longer varies with the deformation until 73% of deformation. The small increase of the volume fraction φ_2 and the size of these crazes with the deformation indicate that these initial crazes nucleation is followed by a slow craze growth without new nucleation, with a size which increases linearly with the stress according to Equation 74, as reported in Table 31. At 3% of true strain, PMMA displays a volume fraction of crazes $\varphi_2 = 2.0 \times 10^{-5}$ with a maximum length of 140 nm. With polyamide 6,6 which is a semi-crystalline polymer, Mourglia-Seignobos et al have shown that the craze growth is blocked by the crystalline phase [50]. PMMA is amorphous. In absence of a crystalline phase, the crazes growth should lead to a rapid brittle failure soon after the appearance of a single cavity after 3% of deformation. This is not what is observed. According to Charvet et al's work, we interpret the ductility observed in PMMA as a consequence of the strain hardening which blocks the propagation of crazes, as it is the case of cellulose acetate.

A 2nd family of crazes is observed at 50% of true strain for PMMA, which corresponds to a macroscopic stress of about 18 MPa. The number of crazes per unit volume is of order $N_2' = 2.4 \times 10^4 \text{ mm}^{-3}$, as shown in Table 31. The small volume fraction of observed crazes, even after failure indicates that this second craze family cannot result from a mechanism of crazes coalescence. This second family of larger crazes corresponds to a very small proportion of crazes initially nucleated (1st regime) which grow faster than the rest of the initial crazes population as a consequence of the strong instability discussed in section 5.2.3.1, Figure 114. Upon increasing the deformation, and when the applied stress becomes sufficiently high, the sample breaks due to crack propagation.

In the case of polycarbonate at 23°C, SAXS analysis shows that small crazes with a size comprised between 2 and 20 nm nucleate simultaneously within the time resolution of our experiment, before 6% of true strain. The number of these nucleated crazes per unit volume is found to be of order $N_2 = 1.5 \times 10^{10} \text{ mm}^{-3}$, which is higher than the number of cavities initially present in the sample with $N_i = 3.9 \times 10^5 \text{ mm}^{-3}$, (as reported in Table 26) and which result from the injection process. It is observed that the number of nucleated crazes increases until 25% of deformation, but no longer varies afterwards until failure at 45% and reaches a value $N_2 = 8.2 \times 10^{10} \text{ mm}^{-3}$. The small increase of the volume fraction ϕ_2 and of the size of these crazes with the deformation indicates that this initial crazes nucleation is followed by a slow craze growth without new nucleation, as reported in Table 30. At 6% of true strain, polycarbonate has a volume fraction of crazes $\phi_2 = 2.6 \times 10^{-6}$ with a maximum length of 20 nm. As in PMMA, there is no crystalline phase in polycarbonate, which is amorphous. In absence of this crystalline phase which blocks the propagation of crazes in PA66 for instance, the crazes growth would lead to a rapid brittle failure soon after the appearance of a single cavity after 6% of deformation. This is not what is observed. Here also, we interpret this fact as a consequence of the strain hardening which blocks the propagation of crazes.

When the applied stress is sufficiently high, the sample breaks due to a crack propagation. A 2nd family of large crazes is observed after 25% of true strain, which corresponds to a macroscopic stress of about 45 MPa. The number of these large crazes per unit volume is of order $N_2' = 2.6 \times 10^5 \text{ mm}^{-3}$, as shown in Table 30. The small volume fraction of observed crazes after failure indicates that this second craze family cannot result from a mechanism of crazes coalescence. This second family of larger crazes which reach a size of 600 nm at 45% of deformation from a very small proportion of crazes initially nucleated (1st regime) which grow faster than the rest of the initial craze population as a consequence of the instability mechanisms discussed in section 5.2.3.1.

As we shall see in the case of polyamide A, two mechanisms can prevent nucleation from occurring: the reduction of the volume variation under applied strain, and the increase of the surface tension of the polymer γ_s in the strain hardening regime. We do observe an increase of surface tension by 15% and 33% for PMMA and polycarbonate, respectively. This effect appears to be insufficient to prevent cavitation. Note that the volume increases by 5% and 10% at break for PMMA and polycarbonate respectively. This increase may be thought as favoring cavitation.

As it is the case for PMMA, the damaging behavior until breaking of polycarbonate is the same as that of cellulose acetate [26].

5.2.3.3 Damage mechanisms of polyphthalamides

Let us consider the case of the three PPA. None of them break, contrarily to the case of the plasticized cellulose acetate studied by Charvet et al or that of polycarbonate and PMMA studied here. Two of these PPA do not display damaging at all (polyamides B and C). Polyamide A gets damaged but do not break.

5.2.3.3.1 *Polyamide A*

In the case of polyamide A, necking appears at 5% of true strain. We observe two families of crazes at 9% of deformation. The number of crazes does not evolve with the deformation and their size is about 20 nm. They represent a volume fraction of 3.0×10^{-6} . The second family of crazes which represents a volume fraction of 9.0×10^{-6} at 9% of deformation has a size of 150 nm. Craze nucleation occurs thus before 9% of deformation. Upon increasing the stress further, we observe that the size of the first family grows roughly linearly with the stress from 20 nm to 50 nm. The size of the crazes of the second family increases from 150 nm to 1500 nm. However, at odds with the case of CDA, these large crazes do not lead to breaking at least within the accessible deformation range of our apparatus. The growth of these large crazes is stopped at a few microns, just after yield. This effect is not observed with the CDA studied by Charvet et al [26].

Our interpretation is that cavitation is suppressed after yield for polyamide A. Therefore, no new cavities can appear and the already existing cavities cannot grow further. Two mechanisms can prevent nucleation from occurring: the reduction of the volume variation and the increase of the surface tension of the polymer γ_s . Indeed, the necking process is accompanied by a decrease in volume variation, which may contribute to the suppression of cavitation. In the case of polyamide A, the volume increases until yield, and then remains constant as observed in Figure 72-a. We have calculated the Poisson's ratio ν of polyamide A, and we find a Poisson's ratio less than 0.5 before necking, and equal to 0.5 just after the beginning of necking, in the strain softening regime and which keeps this value afterwards. In addition, strong molecular cohesion contributes to suppress cavitation. Surface tension is higher in the strain hardening regime for all polymers. For polyamide A after deformation, in the necking zone, the surface tension γ_s increases from 54.8 mJ/m² to 65.5 mJ/m², an increase of almost 20%.

Our interpretation for the observed stabilized damages in polyamide A is that this may be the consequence of two effects: the reduction of the volume variation, which is the consequence of the increase of the Poisson's ratio, and of the surface tension of the polymer in the strain hardening regime.

One can see in Figure 72-a that the volume increase under applied strain is suppressed at about 5% of deformation in the case of polyamide A. To the best of our knowledge, no complete model for cavitation exist in solid polymers taking into account the volume variation under uniaxial deformation. However, one may assume that a Poisson ratio close to 0.5 inhibits cavitation in these circumstances, as compared to triaxial applied stress [185], [186], as cavitation is considered in liquids. In addition, the increase of surface tension by about 20% in the strain hardening regime (see Table 25) leads to an increase of the free energy barriers by a factor close to 2 according to Equation 73. Both effects tend to suppress cavitation. The growth of the large crazes (and also that of the smaller ones which are blocked at about 50 nm in diameter) is no longer possible. Strain hardening blocks the size of crazes at a few micrometers in the absence of new nucleations ahead of the crazes.

5.2.3.3.2 *Polyamide B and polyamide C*

The third category concerns the two low semi-crystalline PPA, polyamide B and polyamide C. These two semi-crystalline PPA deform by necking, which appears just after the yield stress. In the case of these polymers, no damaging takes place at all. No crazes are observed before yield, at yield and in the strain hardening regime. The absence of cavitation in the case of polyamide B and polyamide C can be interpreted macroscopically by the fact that the critical stress required for cavitation, $\sigma_{\text{cavitation}}$, is larger than the yield stress σ_y and remains larger afterwards than the stress in the strain hardening regime.

Cavitation depends on several parameters. It depends on the surface tension γ_s , and on the volume variation during applied strain. Essentially, a polymer is fragile if the second growth regime, during which a fraction of the crazes starts to grow by homogeneous nucleation in their immediate vicinity, takes place before yield stress, whereas a polymer may be ductile when this is the reverse and if the strain hardening is strong enough. In our interpretation, it means that a polymer is fragile when the free energy barriers for homogeneous cavitation are reached at smaller deformations than yield stress. It may be the case for polymers with low surface tension, small Poisson's ratio (large increase of volume) and/or for high yield stress. We assume that that polyamides B and C do not get damaged because the stress for cavitation even in the presence of impurities satisfies to the relation $\sigma_{\text{cavitation}} > \sigma_y$, an effect which may be enhanced by large surface tensions, high Poisson's ratio (close to 0.5), and/or low yield stress. Note that the volume variations for both polymers (Figure 72-b-c) do not allow to conclude unambiguously at this regard. However, the large increase of the surface tension (both increase by 28% in the strain hardening regime) and possibly a relatively low yield stress may lead to this behavior where damage does not take place.

5.2.3.4 Summary of damage mechanisms observed

The different damage mechanisms observed are schematized in Figure 115 and Figure 116. Damage is initiated by the simultaneous nucleation of cavities (sizes of order 50 to 100 nm) around pre-existing impurities. This process is observed for polyamide A, polycarbonate and PMMA. The growth of these cavities just after nucleation is blocked by the strain hardening of the polymer in the immediate vicinity of these cavities. During this regime where the cavities are stabilized by the strain hardening, these cavities grow linearly with the macroscopic stress, without new damages (Figure 115-a-b-c and Figure 116-a-b-c). For polyamide A, the appearance before yield of a second family of large crazes of a few micrometers in length is also observed, but their growth after yield in the stress softening regime is blocked and does not resume in the strain hardening regime.

As a consequence, polyamide A does not break within the accessible range of strain of our tensile machine. In the case of polycarbonate and PMMA (Figure 116), when the applied stress becomes sufficiently high, a small fraction of these cracks become unstable and grow faster by nucleation of new cavities just ahead of them and cause the rupture of the sample. Note that these polymers don't exhibit necking.

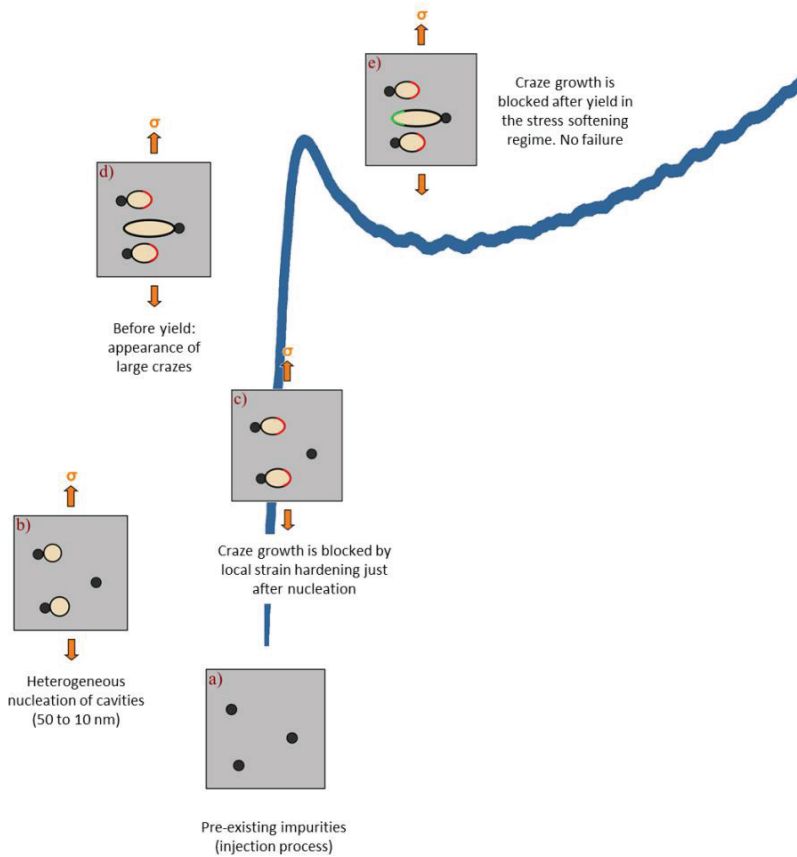


Figure 115 – Damage mechanisms of polyamide A under tensile deformation: a) Pre-existing impurities due to the injection process (before tensile experiment), b) Heterogeneous nucleation of cavities, or order 50 to 100 nm, c) The craze growth is blocked by the local strain hardening of the polymer, just after nucleation, in the vicinity of these cavities, d) Appearance before yield of a 2nd family of large crazes and e) Craze growth after yield is blocked in the stress softening regime.

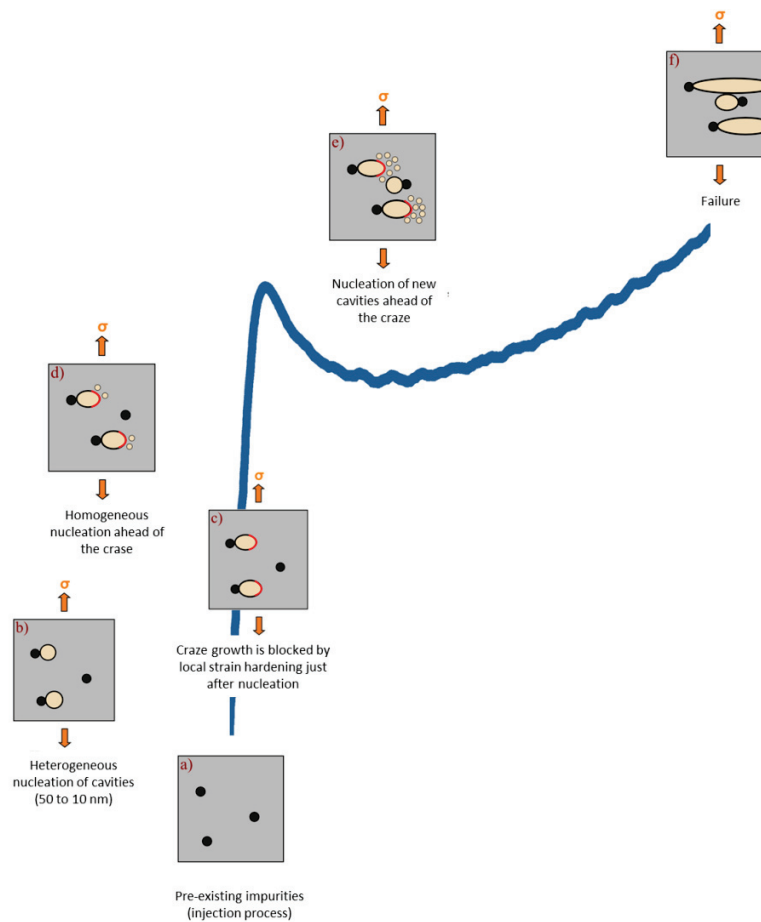


Figure 116 – Damage mechanisms of polycarbonate and PMMA under tensile deformation: a) Pre-existing impurities due to the injection process (before tensile experiment), b) Heterogeneous nucleation of cavities, or order 50 to 100 nm, c) The craze growth is blocked by the local strain hardening of the polymer, just after nucleation, in the vicinity of these cavities, d-e) Homogeneous nucleation in the immediate vicinity of the craze, f) Failure of the specimen when a craze reaches a critical growth rate.

5.2.4 Conclusion

The analysis of the damaging mechanisms for different polymers (amorphous and semi-crystalline PPA, PC, PMMA) by USAXS highlights different modes of damage for amorphous and low semi-crystalline polymers.

Damage, when it occurs, is initiated by the simultaneous nucleation of cavities which grow rapidly in this stage to reach a size of order 50 to 100 nm around pre-existing impurities due to the injection process. This process is observed for polyamide A, polycarbonate and PMMA, in a mechanism similar to that observed in the case of cellulose acetate [26]. The growth of these cavities at the end of this rapid growth

is blocked by the local strain hardening of the polymer in the immediate vicinity of these cavities, where the strain and the stress are the largest, when this local stress is able to equilibrate the macroscopic stress due to the applied deformation. During this regime where the cavities are stabilized by the strain hardening, these cavities grow linearly with the macroscopic stress, without new damages. In the case of polycarbonate and PMMA, when the applied stress becomes sufficiently high, a small fraction of these cracks become unstable and grow faster by homogeneous nucleation of new cavities just ahead of them which causes the rupture of the sample in a similar way as that observed for cellulose acetate [26]. This process is identified by the USAXS measurements which show the existence of a small number of large crazes in this regime. In the case of polyamide A we also observe the appearance before yield of a second family of large crazes of a few micrometers in length, but their growth after yield in the stress softening regime is suppressed and does not resume in the strain hardening regime. As a consequence, polyamide A does not break within the accessible range of strain of our apparatus. This polymer undergoes a stable necking regime, without further damage. This behavior may be the consequence of an increase of the Poisson's ratio after yield and an increase of the surface tension at large deformations. Both effects contribute to a suppression of cavitation. Note that this polymer is ductile above -40°C . Below this temperature, in the fragile regime, the strain hardening regime cannot be reached, and it is expected that the least cavitation may propagate and a brutal rupture may be observed. There will therefore be no intermediate stage where the strain hardening will block the propagation of damage. Indeed, it is difficult to quantify the intermediate stages in the brittle regime, as we observed for PMMA in our experiments. The two semi-crystalline PPA, polyamide B and polyamide C deform by stable necking at large deformation without any damage and do not break. The critical stress for cavitation remains larger than the current stress at every step of the applied deformation for these two amorphous and low semi-crystalline polymers. Unlike the semi-crystalline polymer studied by Mourglia-Seignobos et al in fatigue [50], there is no damage seen in the case of Polyamide C. No specific role of crystallinity was observed as regard to damage in our samples.

Damaging in polymers under strain has been the subject of research for many years [31]–[39]. The crazing process takes place in three stages: initiation step, growth and rupture, and is an active research field [37], [39], [40]. Recently, Michler [35] supposed that the initiation of a craze is preceded by the formation of a localized plastic deformation zone. As this plastic deformation zone develops, the hydrostatic stress increases until it becomes higher than a critical stress level which leads to the local development of microvoids. According to Michler [35], this localized plastic deformation zone is related to the entanglement network. To describe the craze initiation, the common approach used is the stress

concentration effect in the vicinity of the pre-existing impurities in the polymer [39] but nucleation as an activated process is usually not considered explicitly.

Argon [190] proposed long ago that crazes growth takes place by nucleation ahead of the craze tip but finally considered that this process is not relevant [118], [191]. According to Argon and Hannoosh, this mechanism is incompatible with the formation of fibrils. Moreover, the nucleation would not be possible at the observed stress levels. Based on the work done recently by Charvet et al [26] it appears that nucleation is possible on impurities (heterogeneous nucleation) in the initiation stage, and that at higher stress levels homogeneous nucleation is possible indeed just ahead of crazes where stress concentration is the highest. This latter process leads to the growth of a small fraction of crazes and to failure in cellulose acetate, polycarbonate and PMMA. This nucleation process of new cavities just ahead of craze tips is consistent with the apparition of fibrils. Indeed, between neighboring and growing cavities, thin polymer films are formed. Once they reach a thickness of order 10 nm, they become unstable due to disjoining pressure effects and they are expected to rupture [192]. This mechanism should lead to a fibril-like structure. In our experiments, we observed that damage, when it occurs, is initiated by the simultaneous nucleation of cavities (heterogeneous nucleation) which reach rapidly sizes of order 50 to 100 nm, in a similar way as what was observed in the work of Charvet et al [26]. The number of cavities does not evolve afterwards until breaking. We can assume that the same impurities which allow for the creation of cavities during injection lead also to the cavitation of crazes under applied stress. Their number has been found to be of order 10^{10} mm^{-3} for polyamide A and polycarbonate, and of order 10^8 mm^{-3} for PMMA.

Another mechanism used to describe the nucleation is the so-called meniscus instability [41], [193], proposed by Taylor [43]. Taylor [43] has described a hydrodynamic instability for a liquid film between two almost parallel hard sheets when they are pulled apart. This concept has been used for polymers by Argon and Salama [41]. This mechanism may be applied for a polymer in the molten state. However, all of our studied polymers exhibit strain hardening which does not seem compatible with this picture and should prevent this instability to take place. Indeed, we observed that crazes do not grow once they have reached a size of order 50 to 100 nm, until the local stress level is sufficiently high for homogeneous nucleation to take place in the vicinity of crazes. The nucleation models discussed in this manuscript and by Charvet et al [26] explain the strong dependences of the growth rate as a function of the macroscopic applied stress. Indeed, the nonlinear growth kinetics as a function of both the macroscopic applied stress and the size of cavities can explain why only a small fraction of cavities undergo a second growth step process. In literature, strongly nonlinear constitutive relations are used for describing this nonlinear

growth kinetics of the type $\frac{d}{dt}\gamma \propto \sigma^m$, where the exponent m can be equal to or larger than 20 [37], [194]. These constitutive relations derive from an Eyring picture [195]. The growth kinetics can be explained by a nucleation mechanism which involves the polymer surface energy and lead naturally to a strongly non-linear behavior. Note that there is a need to extend the current model for cavitation to deal explicitly with the uniaxial nature of the applied strain, in the presence of solid impurities, or in the vicinity of strain-hardened cavities beyond the current standard cavitation model [26], [185], [186].

Our qualitative interpretation of these effects lead us to propose that the no-damaging mechanism is favored by a high surface tension of the polymer and a relatively low yield stress which prevents cavitation before yield. It is also favored by an increase of the Poisson's ratio after the stress softening regime and an increase of the surface tension of the polymer in this regime. These mechanisms should be the subject of further scientific studies in order to demonstrate them more precisely, beyond the qualitative discussion proposed in this manuscript. In perspective, it would be interesting to modify the chemical structure of polymers, in order to increase molecular cohesion (and therefore increase γ_s) [196], [197], as well as an enhancement of the strain hardening behavior. As a conclusion, we observe that at least three different damaging behaviors can be observed in the ductile regime of polymers exhibiting strain hardening.

General conclusion

The main objective of this PhD thesis was to characterize and understand the damage mechanisms of different amorphous and low semi-crystalline polymers under tensile deformation. In this work, different polymers were considered: amorphous and low semi-crystalline polyphthalamides, polycarbonate and PMMA.

Thermal properties

The thermal properties were determined by DSC for the PPA, polycarbonate and PMMA studied. The introduction of a fraction of terephthalic acid in the polymer mainly composed of isophthalic acid leads to a change in the glass transition T_g of the copolymer. When 6T fraction increases, the glass transition also increases. This increase can be related to the positions of the carboxylic acid functions on the aromatic ring on both terephthalic and isophthalic acids. The positions of the carboxylic acid functions on the aromatic ring lead to rigid and straight PA6T chains, with a reduced mobility and thereby a higher glass transition temperature T_g than PA6I is observed.

The thermomechanical properties of the PPA have been studied through DMTA experiments. Three relaxations processes have been identified, denoted γ , β and α from the lower to the higher temperature.

Mechanical properties

The mechanical and ultimate properties of PPA, polycarbonate and PMMA samples have been studied. The impact properties were studied on a broad temperature range, using an instrumented Charpy impact test. The three PPA samples exhibited a brittle-ductile transition from a low energy dissipated during impact to a high energy dissipated during impact of the order 130-160 kJ m⁻². At room temperature, the three PPA studied are brittle. The tensile and the compression behavior of the four PPA with different degree of crystallinity have been studied. In tensile test, the PPA with the largest crystallinity is brittle at room temperature (polyamide C), while the polyamide A and polyamide B are ductile. These three PPA under study show necking during tensile test. This is not the case of polyamide D, obtained with a different process (process B). Beyond yield, no strain hardening behavior was observed. The appearance of shear bands was observed for $\theta=0^\circ$ and 45° , leading to the failure of the samples. Polyamide D is less ductile than the other PPA studied. Polycarbonate and PMMA was also studied. The PMMA is brittle up

to 70°C and ductile after this temperature, whereas polycarbonate is ductile over the range of temperatures studied. A strain hardening behavior, following by the failure of these two polymers was observed.

In both tensile and compression tests, a strain hardening behavior was observed, which is more pronounced in compression. The measured strain hardening moduli in compression are around 18 MPa for the three PPA at 23°C. The strain hardening modulus is shown not to depend on crystallinity. Indeed, the strain hardening modulus E_{SH} of the semi-crystalline PPA, polyamide C and polyamide B, is found to be equal to the hardening modulus of the amorphous. Only the temperature has an influence on the strain hardening modulus E_{SH} : the strain hardening modulus decreases with increasing temperature. Strain hardening is a key feature for resistance to damage [121], [182] but its origin is still debated [7], [9], [11]–[19], [27], [28].

The mechanical properties are strongly influenced by the response to large deformations of polymers. Meijer and Govaert [29] have studied the polycarbonate and have shown that polymers with high strain hardening have also ductile rather than brittle deformation. According to the authors, the strain hardening suppresses the strain localization and/or the shear banding. This behavior does not prevent the failure of the polymer, which can occur when the strain is increased.

Damage mechanisms

The analysis of the damaging mechanisms for different polymers (amorphous and semi-crystalline PPA, PC, PMMA) by USAXS highlights different modes of damage for amorphous and low semi-crystalline polymers. Damage, when it occurs, is initiated by the simultaneous nucleation of cavities of sizes of order 50 to 100 nm around pre-existing impurities (impurities due to the injection process). This process is observed for polyamide A, polycarbonate and PMMA, in a mechanism similar to that observed in the case of cellulose acetate [26]. The growth of these cavities just after nucleation is blocked by the strain hardening of the polymer in the immediate vicinity of these cavities, where the strain and the stress are the largest, when this local stress is able to equilibrate the macroscopic stress due to the applied deformation. During this regime where the cavities are stabilized by the strain hardening, these cavities grow linearly with the macroscopic stress, without new damages. In the case of polycarbonate and PMMA, when the applied stress becomes sufficiently high, a small fraction of these cracks become unstable and grow faster by nucleation of new cavities just ahead of them and cause the rupture of the sample in a similar way as that observed for cellulose acetate [26]. This process is identified by the

USAXS measurements which show the existence of a small number of large crazes in this regime. In the case of polyamide A we also observe the appearance before yield of a second family of large crazes of a few micrometers in length, but their growth after yield in the stress softening regime is suppressed and does not resume in the strain hardening regime. As a consequence, polyamide A does not break within the accessible range of strain of our apparatus. This polymer undergoes a stable necking regime, without further damage. We interpret qualitatively this behavior as the consequence of an increase of the Poisson's ratio after yield and an increase of the surface tension at large deformations. The two semi-crystalline PPA, polyamide B and polyamide C deform by stable necking at large deformation without any damage and do not break. The critical stress for cavitation remains larger than the current stress at every step of the applied deformation for amorphous and low semi-crystalline polymers.

As a conclusion, we observe that at least three different damaging behaviors can be observed in the ductile regime of these polymers.

Perspectives

The qualitative interpretation of these effects lead us to propose that the no-damaging mechanism is favored by a high surface tension of the polymer and a relatively low yield stress which prevent cavitation before yield. It is also favored by an increase of the Poisson's ratio after the stress softening regime and an increase of the surface tension of the polymer in this regime. These mechanisms should be the subject of further scientific studies in order to demonstrate them more precisely, beyond the qualitative discussion proposed in this manuscript.

It would also be interesting to do the same analysis of damage in other amorphous polymers (such as PMMA) with less strain hardening and try to improve this regime, in order to evaluate the influence on the damage mechanisms.

Bibliography

- [1] M. I. Kohan, *Nylon Plastics Handbook*. Hanser Publishers, 1995.
- [2] C. Duval, “Plastiques et automobile - D’hier à aujourd’hui,” *Techniques de l’Ingénieur*, vol. AM 3590-1, 2007.
- [3] C. Duval, “Plastiques et automobile - D’aujourd’hui à demain,” *Techniques de l’Ingénieur*, vol. AM 3591-1, 2007.
- [4] A. J. Uddin, Y. Ohkoshi, Y. Gotoh, M. Nagura, R. Endo, and T. Hara, “Melt Spinning and Laser-Heated Drawing of a New Semiaromatic Polyamide, PA9-T Fiber,” *Journal of Polymer Science Part B: Polymer Physics*, vol. 42, pp. 433–444, 2004, doi: 10.1002/polb.10710.
- [5] C. Leboeuf and D. A. Harbourne, “Synthesis of semi-crystalline polyphthalamides through reactive extrusion of hexamethylene terephthalamide oligomer with lower melting, semi-crystalline or amorphous polyamides,” WO1999061509A1, 1999.
- [6] J. Brandrup, E. H. Immergut, and E. A. Grulke, *Polymer Handbook, 4th Edition*, 2 vols. Wiley, 2003.
- [7] L. E. Govaert, T. A. P. Engels, M. Wendlandt, T. A. Tervoort, and U. W. Suter, “Does the strain hardening modulus of glassy polymers scale with the flow stress?,” *Journal of Polymer Science Part B: Polymer Physics*, vol. 46, no. 22, pp. 2475–2481, 2008, doi: 10.1002/polb.21579.
- [8] R. N. Haward, “Strain hardening of thermoplastics,” *Macromolecules*, vol. 26, no. 22, pp. 5860–5869, Oct. 1993, doi: 10.1021/ma00074a006.
- [9] E. J. Kramer, “Open questions in the physics of deformation of polymer glasses,” *Journal of Polymer Science Part B: Polymer Physics*, vol. 43, no. 23, pp. 3369–3371, 2005, doi: 10.1002/polb.20639.
- [10] E. M. Arruda and M. C. Boyce, “Evolution of plastic anisotropy in amorphous polymers during finite straining,” *International Journal of Plasticity*, vol. 9, no. 6, pp. 697–720, 1993, doi: [https://doi.org/10.1016/0749-6419\(93\)90034-N](https://doi.org/10.1016/0749-6419(93)90034-N).
- [11] D. J. A. Senden, J. A. W. van Dommelen, and L. E. Govaert, “Strain hardening and its relation to Bauschinger effects in oriented polymers,” *Journal of Polymer Science Part B: Polymer Physics*, vol. 48, no. 13, pp. 1483–1494, May 2010, doi: 10.1002/polb.22056.
- [12] Jatin, V. Sudarkodi, and S. Basu, “Investigations into the origins of plastic flow and strain hardening in amorphous glassy polymers,” *International Journal of Plasticity*, vol. 56, pp. 139–155, May 2014, doi: 10.1016/j.ijplas.2013.11.007.
- [13] D. J. A. Senden, S. Krop, J. A. W. van Dommelen, and L. E. Govaert, “Rate- and temperature-dependent strain hardening of polycarbonate,” *Journal of Polymer Science Part B: Polymer Physics*, vol. 50, no. 24, pp. 1680–1693, Dec. 2012, doi: 10.1002/polb.23165.
- [14] D. D. Senden, “Strain hardening and anisotropy in solid polymers.” Technische Universiteit Eindhoven, 2013, doi: 10.6100/ir747901.
- [15] R. Hoy and M. Robbins, “Strain hardening of polymer glasses: Effect of entanglement density, temperature, and rate,” *Journal of Polymer Science Part B: Polymer Physics*, vol. 44, pp. 3487–3500, 2006, doi: 10.1002/polb.21012.
- [16] R. Hoy and M. Robbins, “Strain Hardening in Polymer Glasses: Limitations of Network Models,” *Physical review letters*, vol. 99, p. 117801, 2007, doi: 10.1103/PhysRevLett.99.117801.

- [17] R. Hoy and M. Robbins, “Strain Hardening of Polymer Glasses: Entanglements, Energetics, and Plasticity,” *Physical review. E, Statistical, nonlinear, and soft matter physics*, vol. 77, p. 031801, 2008, doi: 10.1103/PhysRevE.77.031801.
- [18] M. O. Robbins and R. S. Hoy, “Scaling of the strain hardening modulus of glassy polymers with the flow stress,” *Journal of Polymer Science Part B: Polymer Physics*, vol. 47, no. 14, pp. 1406–1411, 2009, doi: 10.1002/polb.21734.
- [19] M. Wendlandt, T. A. Tervoort, and U. W. Suter, “Strain-hardening modulus of cross-linked glassy poly(methyl methacrylate),” *Journal of Polymer Science Part B: Polymer Physics*, vol. 48, no. 13, pp. 1464–1472, 2010, doi: 10.1002/polb.21979.
- [20] C. Millot, “Multi-scale characterization of deformation mechanisms of bulk polyamide 6 under tensile stretching below and above the glass transition,” PhD Thesis, INSA de Lyon, 2015.
- [21] C. G’sell, J. M. Hiver, and A. Dahoun, “Experimental characterization of deformation damage in solid polymers under tension, and its interrelation with necking,” *International Journal of solids and structures*, vol. 39, no. 13–14, pp. 3857–3872, 2002.
- [22] M. Ponçot, F. Addiego, and A. Dahoun, “True intrinsic mechanical behaviour of semi-crystalline and amorphous polymers: Influences of volume deformation and cavities shape,” *International Journal of Plasticity*, vol. 40, pp. 126–139, 2013, doi: 10.1016/j.ijplas.2012.07.007.
- [23] Kierkels, JTA (Jules), “Tailoring the mechanical properties of amorphous polymers.” Technische Universiteit Eindhoven, 2006, doi: 10.6100/ir613293.
- [24] H. G. H. van Melick, L. E. Govaert, and H. E. H. Meijer, “On the origin of strain hardening in glassy polymers,” *Polymer*, vol. 44, no. 8, pp. 2493–2502, 2003, doi: [https://doi.org/10.1016/S0032-3861\(03\)00112-5](https://doi.org/10.1016/S0032-3861(03)00112-5).
- [25] J. Richeton, S. Ahzi, L. Daridon, and Y. Rémond, “A formulation of the cooperative model for the yield stress of amorphous polymers for a wide range of strain rates and temperatures,” *Polymer*, vol. 46, no. 16, pp. 6035–6043, Jul. 2005, doi: 10.1016/j.polymer.2005.05.079.
- [26] A. Charvet, C. Vergelati, P. Sotta, and D. R. Long, “Damage Mechanisms of Plasticized Cellulose Acetate under Tensile Deformation Studied by Ultrasmall-Angle X-ray Scattering,” *Macromolecules*, vol. 52, no. 17, pp. 6613–6632, Sep. 2019, doi: 10.1021/acs.macromol.9b00858.
- [27] R. N. Haward, “Strain hardening of thermoplastics,” *Macromolecules*, vol. 26, no. 22, pp. 5860–5869, Oct. 1993, doi: 10.1021/ma00074a006.
- [28] E. M. Arruda and M. C. Boyce, “Evolution of plastic anisotropy in amorphous polymers during finite straining,” *International Journal of Plasticity*, vol. 9, no. 6, pp. 697–720, 1993, doi: [https://doi.org/10.1016/0749-6419\(93\)90034-N](https://doi.org/10.1016/0749-6419(93)90034-N).
- [29] H. E. H. Meijer and L. E. Govaert, “Mechanical performance of polymer systems: the relation between structure and properties. Prog. Polym. Sci. 30, 915-938,” *Progress in Polymer Science*, vol. 30, pp. 915–938, 2005, doi: 10.1016/j.progpolymsci.2005.06.009.
- [30] L. E. Govaert and T. A. Tervoort, “Strain hardening of polycarbonate in the glassy state: Influence of temperature and molecular weight,” *Journal of Polymer Science Part B: Polymer Physics*, vol. 42, no. 11, pp. 2041–2049, 2004, doi: 10.1002/polb.20095.
- [31] G. H. Michler, “Electron microscopic investigations of the structure of crazes in polystyrene,” *Colloid & Polymer Science*, vol. 263, no. 6, pp. 462–474, Jun. 1985, doi: 10.1007/BF01458336.

- [32] G. H. Michler, "Crazes in amorphous polymers I. Variety of the structure of crazes and classification of different types of crazes," *Colloid & Polymer Science*, vol. 267, no. 5, pp. 377–388, May 1989, doi: 10.1007/BF01410182.
- [33] G. H. Michler, "Correlation between craze formation and mechanical behaviour of amorphous polymers," *Journal of Materials Science*, vol. 25, no. 5, pp. 2321–2334, May 1990, doi: 10.1007/BF00638022.
- [34] M. C. García Gutiérrez, G. H. Michler, S. Henning, and C. Schade, "Micromechanical behavior of branched polystyrene as revealed by in situ transmission electron microscopy and microhardness," *Journal of Macromolecular Science, Part B*, vol. 40, no. 5, pp. 797–812, Nov. 2001, doi: 10.1081/MB-100107562.
- [35] G. H. Michler, *Electron Microscopy of Polymers*. Springer Berlin Heidelberg, 2008.
- [36] A. M. Donald, E. J. Kramer, and R. A. Bubeck, "The entanglement network and craze micromechanics in glassy polymers," *Journal of Polymer Science: Polymer Physics Edition*, vol. 20, no. 7, pp. 1129–1141, Jul. 1982, doi: 10.1002/pol.1982.180200703.
- [37] E. J. Kramer, "Microscopic and molecular fundamentals of crazing," in *Crazing in Polymers*, 1983, pp. 1–56.
- [38] C. S. Henkee and E. J. Kramer, "Crazing and shear deformation in crosslinked polystyrene," *Journal of Polymer Science: Polymer Physics Edition*, vol. 22, no. 4, pp. 721–737, Apr. 1984, doi: 10.1002/pol.1984.180220414.
- [39] E. J. Kramer and L. L. Berger, "Fundamental processes of craze growth and fracture," in *Crazing in Polymers Vol. 2*, vol. 91/92, H.-H. Kausch, Ed. Berlin, Heidelberg: Springer Berlin Heidelberg, 1990, pp. 1–68.
- [40] K. Friedrich, "Crazes and shear bands in semi-crystalline thermoplastics," in *Crazing in Polymers*, vol. 52–53, H. H. Kausch, Ed. Berlin/Heidelberg: Springer-Verlag, 1983, pp. 225–274.
- [41] A. S. Argon and M. M. Salama, "Growth of crazes in glassy polymers," *The Philosophical Magazine: A Journal of Theoretical Experimental and Applied Physics*, vol. 36, no. 5, pp. 1217–1234, 1977, doi: 10.1080/14786437708239790.
- [42] R. P. Kambour, "A review of crazing and fracture in thermoplastics," *Journal of Polymer Science: Macromolecular Reviews*, vol. 7, no. 1, pp. 1–154, 1973, doi: 10.1002/pol.1973.230070101.
- [43] G. I. Taylor, "The instability of liquid surfaces when accelerated in a direction perpendicular to their planes. I," *Proceedings of the Royal Society of London. Series A. Mathematical and Physical Sciences*, vol. 201, no. 1065, pp. 192–196, 1950, doi: 10.1098/rspa.1950.0052.
- [44] J. L. Halary, F. Laupretre, and L. Monnerie, *Polymer Materials: Macroscopic Properties and Molecular Interpretations*. Wiley, 2011.
- [45] P. J. Mills, E. J. Kramer, and H. R. Brown, "Real time small-angle X-ray scattering from polystyrene crazes during fatigue," *Journal of Materials Science*, vol. 20, no. 12, pp. 4413–4420, Dec. 1985, doi: 10.1007/BF00559330.
- [46] G. J. Salomons, M. A. Singh, T. Bardouille, W. A. Foran, and M. S. Capel, "Small-angle X-ray scattering analysis of craze-fibril structures," *Journal of Applied Crystallography*, vol. 32, no. 1, pp. 71–81, Feb. 1999, doi: 10.1107/S0021889898010486.
- [47] U. Lode *et al.*, "Development of crazes in polycarbonate, investigated by ultra small angle X-ray scattering of synchrotron radiation," *Macromolecular Rapid Communications*, vol. 19,

- no. 1, pp. 35–39, Jan. 1998, doi: 10.1002/(SICI)1521-3927(19980101)19:1<35::AID-MARC35>3.0.CO;2-3.
- [48] H. R. Brown, Y. Sindoni, E. J. Kramer, and P. J. Mills, “Diffraction studies of craze structure,” *Polymer Engineering and Science*, vol. 24, no. 10, pp. 825–832, Jul. 1984, doi: 10.1002/pen.760241013.
- [49] G. Stoclet, J. M. Lefebvre, R. Séguéla, and C. Vanmansart, “In-situ SAXS study of the plastic deformation behavior of polylactide upon cold-drawing,” *Polymer*, vol. 55, no. 7, pp. 1817–1828, Apr. 2014, doi: 10.1016/j.polymer.2014.02.010.
- [50] E. Mourglia-Seignobos, D. R. Long, L. Odoni, L. Vanel, P. Sotta, and C. Rochas, “Physical Mechanisms of Fatigue in Neat Polyamide 6,6,” *Macromolecules*, vol. 47, no. 12, pp. 3880–3894, Jun. 2014, doi: 10.1021/ma500256x.
- [51] “ASTM D5336 - 15a Standard Classification System and Basis for Specification for Polyphthalamide (PPA) Injection Molding Material.” ASTM International, West Conshohocken, PA, 2015.
- [52] B. GUÉRIN, “Polyamides PA,” *Techniques de l'ingénieur Matières thermoplastiques : monographies*, vol. base documentaire : TIB147DUO., no. ref. article : a3360, 1994.
- [53] C. Duval, “Plastiques et automobile - D'aujourd'hui à demain,” *Techniques de l'Ingénieur*, vol. AM 3591-1, 2007.
- [54] Novitsky TF, Lange CA, Mathias LJ, Osborn S, Ayotte R, and Manning S, “Eutectic melting behavior of polyamide 10,T-co-6,T and 12,T-co-6,T copolyterephthalamides,” *Polymer*, vol. 51, no. 11, pp. 2417–2425, 2010, doi: 10.1016/j.polymer.2010.03.045.
- [55] T. Cousin, “Synthesis and molecular modelling of bio-based polyamides,” PhD Thesis, 2013.
- [56] S. Vouyiouka, E. Karakatsani, and C. Papaspyrides, “Solid State Polymerization,” *Progress in Polymer Science*, vol. 36, pp. 10–37, 2005, doi: 10.1016/j.progpolymsci.2004.11.001.
- [57] M. Li, J. Bijleveld, and T. Dingemans, “Synthesis and Properties of Semi-crystalline Poly(decamethylene terephthalamide) Thermosets from Reactive Side-group Copolyamides,” *European Polymer Journal*, vol. 98, 2017, doi: 10.1016/j.eurpolymj.2017.11.019.
- [58] H. K. Reimschuessel and G. J. Dege, “Polyamides: Decarboxylation and desamination in nylon 6 equilibrium polymer,” *Journal of Polymer Science Part A-1: Polymer Chemistry*, vol. 8, no. 11, pp. 3265–3283, 1970, doi: 10.1002/pol.1970.150081120.
- [59] J.-P. Trotignon, *Précis matières plastiques : structures-propriétés, mise en oeuvre, normalisation*. Saint-Denis La Plaine; Paris: AFNOR ; Nathan, 2006.
- [60] “ISO 16396-2 Plastics – Polyamide (PA) moulding and extrusion materials.” ISO International Organization for Standardization, Geneva (CH) Std. ISO 16396-2:2017(E), 2017.
- [61] K. Chen and K. S. Schweizer, “Theory of Yielding, Strain Softening, and Steady Plastic Flow in Polymer Glasses under Constant Strain Rate Deformation,” *Macromolecules*, vol. 44, no. 10, pp. 3988–4000, May 2011, doi: 10.1021/ma200436w.
- [62] L. C. A. van Breemen, T. A. P. Engels, E. T. J. Klompen, D. J. A. Senden, and L. E. Govaert, “Rate- and temperature-dependent strain softening in solid polymers,” *Journal of Polymer Science Part B: Polymer Physics*, vol. 50, no. 24, pp. 1757–1771, Dec. 2012, doi: 10.1002/polb.23199.

- [63] M. Wendlandt, T. A. Tervoort, and U. W. Suter, “Non-linear, rate-dependent strain-hardening behavior of polymer glasses,” *Polymer*, vol. 46, no. 25, pp. 11786–11797, 2005, doi: <https://doi.org/10.1016/j.polymer.2005.08.079>.
- [64] T. A. Tervoort and L. E. Govaert, “Craze-initiation kinetics in polystyrene,” *Journal of Polymer Science Part B: Polymer Physics*, vol. 42, no. 11, pp. 2066–2073, 2004, doi: [10.1002/polb.20093](https://doi.org/10.1002/polb.20093).
- [65] Y. Xu, T. Gao, J. Wang, and W. Zhang, “Experimentation and Modeling of the Tension Behavior of Polycarbonate at High Strain Rates,” *Polymers (Basel)*, vol. 8, no. 3, p. 63, Feb. 2016, doi: [10.3390/polym8030063](https://doi.org/10.3390/polym8030063).
- [66] C. G’Sell, J. M. Hiver, A. Dahoun, and A. Souahi, “Video-controlled tensile testing of polymers and metals beyond the necking point,” *Journal of Materials Science*, vol. 27, no. 18, pp. 5031–5039, Sep. 1992, doi: [10.1007/BF01105270](https://doi.org/10.1007/BF01105270).
- [67] J. Sweeney, P. Caton-Rose, R. Spares, and P. D. Coates, “Unified model of necking and shear banding in amorphous and semicrystalline polymers,” *Journal of Applied Polymer Science*, vol. 106, no. 2, pp. 1095–1105, 2007, doi: [10.1002/app.26546](https://doi.org/10.1002/app.26546).
- [68] J. Ye, S. André, and L. Farge, “Kinematic study of necking in a semi-crystalline polymer through 3D Digital Image Correlation,” *International Journal of Solids and Structures*, vol. 59, pp. 58–72, 2015, doi: [10.1016/j.ijssolstr.2015.01.009](https://doi.org/10.1016/j.ijssolstr.2015.01.009).
- [69] J. L. Halary, F. Lauprêtre, and L. Monnerie, *Mécanique des matériaux polymères*. Belin, 2008.
- [70] S. D. Poisson, “Note sur l’extension des fils et des plaques élastiques,” in *Annales de Chimie et de Physique*, 1827, vol. 36, pp. 384–387.
- [71] G. N. Greaves, A. L. Greer, R. S. Lakes, and T. Rouxel, “Poisson’s ratio and modern materials,” *Nature Materials*, vol. 10, p. 823, Oct. 2011.
- [72] S. Jazouli, W. Luo, F. Brémand, and T. Vu-Khanh, “Nonlinear creep behavior of viscoelastic polycarbonate,” *Journal of Materials Science*, vol. 41, no. 2, pp. 531–536, Jan. 2006, doi: [10.1007/s10853-005-2276-1](https://doi.org/10.1007/s10853-005-2276-1).
- [73] A. Bocahut, J.-Y. Delannoy, D. R. Long, and P. Sotta, “Modeling Molecular Relaxation Mechanisms in Amorphous Polymers: Application to Polyamides,” *Macromolecules*, vol. 49, no. 5, pp. 1918–1932, Mar. 2016, doi: [10.1021/acs.macromol.5b01963](https://doi.org/10.1021/acs.macromol.5b01963).
- [74] L. P. Chen, A. F. Yee, and E. J. Moskala, “The Molecular Basis for the Relationship between the Secondary Relaxation and Mechanical Properties of a Series of Polyester Copolymer Glasses,” *Macromolecules*, vol. 32, no. 18, pp. 5944–5955, Sep. 1999, doi: [10.1021/ma981363a](https://doi.org/10.1021/ma981363a).
- [75] A. Rios de Anda, “Influence of the solvent sorption, additivation, and chemical modification on the molecular mobility dynamics of Polyamide 6,6 amorphous phase and its consequences on the tensile and impact strength properties of this polymer,” PhD Thesis, Université Lyon 1, 2012.
- [76] K. J. Laidler, “A glossary of terms used in chemical kinetics, including reaction dynamics (IUPAC Recommendations 1996),” *Pure and applied chemistry*, vol. 68, no. 1, pp. 149–192, 1996.
- [77] M. L. Williams, R. F. Landel, and J. D. Ferry, “The Temperature Dependence of Relaxation Mechanisms in Amorphous Polymers and Other Glass-forming Liquids,” *J. Am. Chem. Soc.*, vol. 77, no. 14, pp. 3701–3707, Jul. 1955, doi: [10.1021/ja01619a008](https://doi.org/10.1021/ja01619a008).

- [78] F. Beaume, B. Brulé, J.-L. Halary, F. Lauprêtre, and L. Monnerie, “Secondary transitions of aryl-aliphatic polyamides IV. Dynamic mechanical analysis,” *Polymer*, vol. 41, no. 14, pp. 5451–5459, 2000, doi: [https://doi.org/10.1016/S0032-3861\(99\)00752-1](https://doi.org/10.1016/S0032-3861(99)00752-1).
- [79] E. Laredo and M. Hernández, “Moisture effect on the low- and high-temperature dielectric relaxations in nylon-6,” *Journal of Polymer Science Part B-polymer Physics - J POLYM SCI B-POLYM PHYS*, vol. 35, pp. 2879–2888, 1997, doi: [10.1002/\(SICI\)1099-0488\(199712\)35:173.0.CO;2-4](https://doi.org/10.1002/(SICI)1099-0488(199712)35:173.0.CO;2-4).
- [80] E. Laredo, M. Grimau, F. Sánchez, and A. Bello, “Water Absorption Effect on the Dynamic Properties of Nylon-6 by Dielectric Spectroscopy,” *Macromolecules*, vol. 36, no. 26, pp. 9840–9850, 2003, doi: [10.1021/ma034954w](https://doi.org/10.1021/ma034954w).
- [81] M. Laurati *et al.*, “Dynamics of Water Absorbed in Polyamides,” *Macromolecules*, vol. 45, no. 3, pp. 1676–1687, 2012, doi: [10.1021/ma202368x](https://doi.org/10.1021/ma202368x).
- [82] F. Beaume, F. Lauprêtre, L. Monnerie, A. Maxwell, and G. R. Davies, “Secondary transitions of aryl-aliphatic polyamides. I. Broadband dielectric investigation,” *Polymer*, vol. 41, no. 7, pp. 2677–2690, 2000, doi: [https://doi.org/10.1016/S0032-3861\(99\)00437-1](https://doi.org/10.1016/S0032-3861(99)00437-1).
- [83] F. Kremer and A. Schönhals, *Broadband Dielectric Spectroscopy*. 2003.
- [84] J. Varlet, J. Y. Cavallé, J. Perez, and G. P. Johari, “Dynamic mechanical spectrometry of nylon-12,” *Journal of Polymer Science Part B: Polymer Physics*, vol. 28, no. 13, pp. 2691–2705, 1990, doi: [10.1002/polb.1990.090281315](https://doi.org/10.1002/polb.1990.090281315).
- [85] F. M. Preda, “Dynamics of polyamide in the solid state in presence of solvents and in the molten state,” PhD Thesis, Université Lyon 1, 2016.
- [86] P. B. Bowden and R. J. Young, “Deformation mechanisms in crystalline polymers,” *Journal of Materials Science*, vol. 9, no. 12, pp. 2034–2051, 1974.
- [87] J. M. Haudin and C. G’Sell, “Mécanismes microscopiques de déformation des polymères semi-cristallins,” *Introduction à la mécanique des polymères, Institut National polytechnique de Lorraine, Nancy*, pp. 251–273, 1995.
- [88] J. Petermann and J. M. Schultz, “Lamellar separation during the deformation of high-density polyethylene,” *Journal of Materials Science*, vol. 13, no. 1, pp. 50–54, Jan. 1978, doi: [10.1007/BF00739272](https://doi.org/10.1007/BF00739272).
- [89] S. Castagnet, J.-L. Gacougnolle, and P. Dang, “Correlation between macroscopical viscoelastic behaviour and micromechanisms in strained α polyvinylidene fluoride (PVDF),” *Materials Science and Engineering: A*, vol. 276, no. 1, pp. 152–159, Jan. 2000, doi: [10.1016/S0921-5093\(99\)00320-2](https://doi.org/10.1016/S0921-5093(99)00320-2).
- [90] A. Galeski, “Strength and toughness of crystalline polymer systems,” *Progress in Polymer Science*, vol. 28, no. 12, pp. 1643–1699, 2003, doi: <https://doi.org/10.1016/j.progpolymsci.2003.09.003>.
- [91] S. Castagnet, S. Girault, J. L. Gacougnolle, and P. Dang, “Cavitation in strained polyvinylidene fluoride: mechanical and X-ray experimental studies,” *Polymer*, vol. 41, no. 20, pp. 7523–7530, 2000.
- [92] M. Lafarge, “Modélisation couplée comportement-endommagement et critères de rupture dans le domaine de la transition du PVDF,” 2004.
- [93] A. Pawlak and A. Galeski, “Plastic Deformation of Crystalline Polymers: The Role of Cavitation and Crystal Plasticity,” *Macromolecules*, vol. 38, no. 23, pp. 9688–9697, Nov. 2005, doi: [10.1021/ma050842o](https://doi.org/10.1021/ma050842o).
- [94] V. S. Kuksenko and V. P. Tamusz, *Fracture Micromechanics of Polymer Materials*. Springer, 1981.

- [95] A. Galeski, A. S. Argon, and R. E. Cohen, "Changes in the morphology of bulk spherulitic nylon 6 due to plastic deformation," *Macromolecules*, vol. 21, no. 9, pp. 2761–2770, 1988.
- [96] A. Pawlak and E. Piorkowska, "Effect of negative pressure on melting behavior of spherulites in thin films of several crystalline polymers," *Journal of Applied Polymer Science*, vol. 74, no. 6, pp. 1380–1385, 1999, doi: 10.1002/(SICI)1097-4628(19991107)74:6<1380::AID-APP9>3.0.CO;2-M.
- [97] S. Castagnet, "Comportement mécanique du PVDF : compétition entre cavitation et écoulement visqueux," PhD Thesis, 1998.
- [98] W. Wu and A. P. L. Turner, "Shear bands in polycarbonate," *Journal of Polymer Science: Polymer Physics Edition*, vol. 11, no. 11, pp. 2199–2208, 1973, doi: 10.1002/pol.1973.180111110.
- [99] L. C. Sawyer, D. Grubb, and G. Meyers, "Polymer microscopy: Third edition," *Polymer Microscopy: Third Edition*, pp. 1–540, 2008, doi: 10.1007/978-0-387-72628-1.
- [100] S. Raha and P. B. Bowden, "Birefringence of plastically deformed poly(methyl methacrylate)," *Polymer*, vol. 13, no. 4, pp. 174–183, 1972, doi: [https://doi.org/10.1016/0032-3861\(72\)90042-0](https://doi.org/10.1016/0032-3861(72)90042-0).
- [101] P. D. Wu and E. van der Giessen, "Analysis of shear band propagation in amorphous glassy polymers," *International Journal of Solids and Structures*, vol. 31, no. 11, pp. 1493–1517, 1994, doi: [https://doi.org/10.1016/0020-7683\(94\)90011-6](https://doi.org/10.1016/0020-7683(94)90011-6).
- [102] R. QUINSON, J. PEREZ, M. RINK, and A. PAVAN, "Yield criteria for amorphous glassy polymers," *Journal of Materials Science*, vol. 32, no. 5, pp. 1371–1379, Mar. 1997, doi: 10.1023/A:1018525127466.
- [103] C. C. Chau and J. C. M. Li, "Intersections of coarse shear bands in polystyrene," *Journal of Materials Science*, vol. 14, no. 9, pp. 2172–2182, Sep. 1979, doi: 10.1007/BF00688423.
- [104] L. Jossierand, R. Schirrer, and P. Davies, "Influence of water on crack propagation in poly methyl methacrylate: craze stress and craze fibril lifetime," *Journal of Materials Science*, vol. 30, no. 7, pp. 1772–1780, Jan. 1995, doi: 10.1007/BF00351609.
- [105] L. L. Berger, D. J. Buckley, E. J. Kramer, H. R. Brown, and R. A. Bubeck, "Low-angle electron diffraction from high temperature polystyrene crazes," *Journal of Polymer Science Part B: Polymer Physics*, vol. 25, no. 8, pp. 1679–1697, 1987, doi: 10.1002/polb.1987.090250810.
- [106] M. G. A. Tijssens, E. Van der Giessen, and L. J. Sluys, "Modeling of crazing using a cohesive surface methodology," *Mechanics of Materials*, vol. 32, pp. 19–35, 2000, doi: 10.1016/S0167-6636(99)00044-7.
- [107] H. Yang, S. R. S, H. C. C, B. B. J, and E. J. Kramer, *Polym. Commun.*, vol. 27, p. 132, 1986.
- [108] G. H. Michler, "In-situ Deformation of Polymers in the HVEM," *Kristall und Technik*, vol. 14, no. 11, pp. 1357–1363, 1979, doi: 10.1002/crat.19790141113.
- [109] H. R. Brown and E. J. Kramer, "Effect of surface tension on the stress in environmental crazes," *Polymer*, vol. 22, no. 5, pp. 687–690, May 1981, doi: 10.1016/0032-3861(81)90362-1.
- [110] B. J. P. Jansen, S. Rastogi, H. E. H. Meijer, and P. J. Lemstra, "Rubber-Modified Glassy Amorphous Polymers Prepared via Chemically Induced Phase Separation. 2. Mode of Microscopic Deformation Studied by in-Situ Small-Angle X-ray Scattering during Tensile Deformation," *Macromolecules*, vol. 34, no. 12, pp. 4007–4018, Jun. 2001, doi: 10.1021/ma001810y.

- [111] S. Polizzi and F. Spinozzi, “Small Angle X-Ray Scattering (SAXS) with Synchrotron Radiation Sources,” in *Synchrotron Radiation: Basics, Methods and Applications*, S. Mobilio, F. Boscherini, and C. Meneghini, Eds. Berlin, Heidelberg: Springer Berlin Heidelberg, 2015, pp. 337–359.
- [112] E. Donth and G. H. Michler, “Discussion of craze formation and growth in amorphous polymers in terms of the multiplicity of glass transition at low temperatures,” *Colloid & Polymer Science*, vol. 267, no. 7, pp. 557–567, Jul. 1989, doi: 10.1007/BF01410431.
- [113] C. B. Bucknall, “Rubber toughening,” in *The Physics of Glassy Polymers*, R. N. Haward and R. J. Young, Eds. Dordrecht: Springer Netherlands, 1997, pp. 363–412.
- [114] D. Dompas, G. Groeninckx, M. Isogawa, T. Hasegawa, and M. Kadokura, “Toughening behaviour of rubber-modified thermoplastic polymers involving very small rubber particles: 3. Impact mechanical behaviour of poly(rmvinyl chloride)/methyl methacrylate-butadiene-styrene graft copolymer blends,” *Polymer*, vol. 35, no. 22, pp. 4760–4765, 1994, doi: [https://doi.org/10.1016/0032-3861\(94\)90729-3](https://doi.org/10.1016/0032-3861(94)90729-3).
- [115] C. J. G. Plummer and A. M. Donald, “Craze fibril breakdown in glassy polymers,” *Polymer*, vol. 32, no. 3, pp. 409–418, 1991, doi: [https://doi.org/10.1016/0032-3861\(91\)90443-M](https://doi.org/10.1016/0032-3861(91)90443-M).
- [116] H. H. Kausch, *Polymer fracture*. Springer-Verlag, 1978.
- [117] C. Fond, A. Lobbrecht, and R. Schirrer, “Polymers toughened with rubber microspheres: an analytical solution for stresses and strains in the rubber particles at equilibrium and rupture,” *International Journal of Fracture*, vol. 77, no. 2, pp. 141–159, Jun. 1996, doi: 10.1007/BF00037234.
- [118] A. S. Argon and J. G. Hannoosh, “Initiation of crazes in polystyrene,” *The Philosophical Magazine: A Journal of Theoretical Experimental and Applied Physics*, vol. 36, no. 5, pp. 1195–1216, 1977, doi: 10.1080/14786437708239789.
- [119] F. Addiego, “Caractérisation de la variation volumique du polyéthylène au cours de la déformation plastique en traction et en fluage,” 2006.
- [120] M. Poncot, “Comportement thermomecaniques de polymeres charges selon differents chemins de deformation et traitements thermiques,” PhD Thesis, Institut National Polytechnique de Lorraine, Nancy, France, 2009.
- [121] A. Charvet, “Study of mechanical properties and damage mechanisms in plasticized cellulose acetate polymers,” PhD Thesis, Université de Lyon, 2019.
- [122] C. Fusco, L. Vanel, and D. R. Long, “Long-time damage under creep experiments in disordered materials: Transition from exponential to logarithmic fracture dynamics,” *The European Physical Journal E*, vol. 36, no. 4, Apr. 2013, doi: 10.1140/epje/i2013-13034-y.
- [123] J. G. Dolden, “Structure-property relationships in amorphous polyamides,” *Polymer*, vol. 17, no. 10, pp. 875–892, 1976, doi: [https://doi.org/10.1016/0032-3861\(76\)90254-8](https://doi.org/10.1016/0032-3861(76)90254-8).
- [124] A. R. Martins, A. Bocahut, M.-L. Michon, and P. Sotta, “Effect of intermolecular interactions on the viscoelastic behavior of unentangled polyamide melts,” *Journal of Rheology*, vol. 63, no. 3, pp. 377–389, 2019, doi: 10.1122/1.5060713.
- [125] P. J. Flory, *Principles of Polymer Chemistry*. Cornell University Press, 1953.
- [126] H. Rolland, N. Saintier, P. Wilson, J. Merzeau, and G. Robert, “In situ X-ray tomography investigation on damage mechanisms in short glass fibre reinforced thermoplastics: Effects of fibre orientation and relative humidity,” *Composites Part B: Engineering*, vol. 109, pp. 170–186, 2017, doi: <https://doi.org/10.1016/j.compositesb.2016.10.043>.

- [127] T. B. van Erp, L. E. Govaert, and G. W. M. Peters, “Mechanical Performance of Injection-Molded Poly(propylene): Characterization and Modeling,” *Macromolecular Materials and Engineering*, vol. 298, no. 3, pp. 348–358, 2013, doi: 10.1002/mame.201200116.
- [128] E. Mourglia-Seignobos, “Compréhension des mécanismes physiques de fatigue dans le polyamide vierge et renforcé de fibres de verre,” PhD Thesis, INSA de Lyon, 2009.
- [129] M. R. Kantz, H. D. Newman Jr., and F. H. Stigale, “The skin-core morphology and structure–property relationships in injection-molded polypropylene,” *Journal of Applied Polymer Science*, vol. 16, no. 5, pp. 1249–1260, 1972, doi: 10.1002/app.1972.070160516.
- [130] D. P. Russell and P. W. R. Beaumont, “Structure and properties of injection-moulded nylon-6,” *Journal of Materials Science*, vol. 15, no. 1, pp. 216–221, Jan. 1980, doi: 10.1007/BF00552447.
- [131] S. Apichartpattanasiri, J. N. Hay, and S. N. Kukureka, “A study of the tribological behaviour of polyamide 66 with varying injection-moulding parameters,” *Wear*, vol. 251, no. 1, pp. 1557–1566, 2001, doi: [https://doi.org/10.1016/S0043-1648\(01\)00794-3](https://doi.org/10.1016/S0043-1648(01)00794-3).
- [132] A. Maurel-Pantel, E. Baquet, J. Bikard, J. L. Bouvard, and N. Billon, “A thermo-mechanical large deformation constitutive model for polymers based on material network description: Application to a semi-crystalline polyamide 66,” *International Journal of Plasticity*, vol. 67, pp. 102–126, 2015, doi: <https://doi.org/10.1016/j.ijplas.2014.10.004>.
- [133] N. Hussein, “Enhancement of the mechanical performance of semi-crystalline polyamides by tailoring the intermolecular interaction in the amorphous phase,” PhD Thesis, 2013.
- [134] J. H. Hubbell and S. M. Seltzer, *NIST: X-Ray Mass Attenuation Coefficients*. Radiation Physics Division, PML, NIST, 2004.
- [135] A. R. Martins, “Effect of intermolecular interactions on the viscoelastic behavior of polyamides,” PhD Thesis, 2019.
- [136] D. E. Packham, “Surface energy, surface topography and adhesion,” *International Journal of Adhesion and Adhesives*, vol. 23, no. 6, pp. 437–448, 2003, doi: [https://doi.org/10.1016/S0143-7496\(03\)00068-X](https://doi.org/10.1016/S0143-7496(03)00068-X).
- [137] T. Young, “III. An essay on the cohesion of fluids,” *Philosophical Transactions of the Royal Society of London*, vol. 95, pp. 65–87, 1805, doi: 10.1098/rstl.1805.0005.
- [138] M. E. Schrader, “Contact Angle and Vapor Adsorption,” *Langmuir*, vol. 12, no. 15, pp. 3728–3732, Jan. 1996, doi: 10.1021/la940962h.
- [139] J.-D. Muller, “Etude des changements de phase de polymère dans le procédé de rotomoulage : coalescence et cristallisation couplées à la thermique du procédé,” PhD Thesis, 2008.
- [140] N. T. Correia, J. J. M. Ramos, B. J. V. Saramago, and J. C. G. Calado, “Estimation of the Surface Tension of a Solid: Application to a Liquid Crystalline Polymer,” *Journal of Colloid and Interface Science*, vol. 189, no. 2, pp. 361–369, 1997, doi: <https://doi.org/10.1006/jcis.1997.4857>.
- [141] F. M. Fowkes, “ATTRACTIVE FORCES AT INTERFACES,” *Ind. Eng. Chem.*, vol. 56, no. 12, pp. 40–52, Dec. 1964, doi: 10.1021/ie50660a008.
- [142] D. K. Owens and R. C. Wendt, “Estimation of the surface free energy of polymers,” *Journal of Applied Polymer Science*, vol. 13, no. 8, pp. 1741–1747, Aug. 1969, doi: 10.1002/app.1969.070130815.
- [143] J. H. Clint, “Adhesion and components of solid surface energies,” *Current Opinion in Colloid & Interface Science*, vol. 6, no. 1, pp. 28–33, 2001, doi: [https://doi.org/10.1016/S1359-0294\(00\)00084-4](https://doi.org/10.1016/S1359-0294(00)00084-4).

- [144] J. Clint and A. Wicks, "Adhesion under water: Surface energy considerations," *International Journal of Adhesion and Adhesives*, vol. 21, pp. 267–273, 2001, doi: 10.1016/S0143-7496(00)00029-4.
- [145] S. Wu, *Polymer interface and adhesion*, vol. 188. M. Dekker New York, 1982.
- [146] B. Jańczuk, W. Wójcik, and A. Zdziennicka, "Determination of the Components of the Surface Tension of Some Liquids from Interfacial Liquid-Liquid Tension Measurements," *Journal of Colloid and Interface Science*, vol. 157, no. 2, pp. 384–393, 1993, doi: <https://doi.org/10.1006/jcis.1993.1200>.
- [147] TA Instruments, "RSA-G2 solids analyzer." 2014.
- [148] J. D. Ferry, *Viscoelastic Properties of Polymers*. Wiley, 1980.
- [149] Nikon, "MicroscopyU. Introduction to Polarized Light Microscopy. Polarized Light Microscopy Configuration." 2015.
- [150] C. M. Sorensen, C. Oh, P. W. Schmidt, and T. P. Rieker, "Scaling description of the structure factor of fractal soot composites," *Phys. Rev. E*, vol. 58, no. 4, pp. 4666–4672, Oct. 1998, doi: 10.1103/PhysRevE.58.4666.
- [151] A. Guinier and G. Fournet, *Small Angle Scattering of X-Rays*, John Wiley and Son, New York. 1955.
- [152] G. Beaucage, H. K. Kammler, and S. E. Pratsinis, "Particle size distributions from small-angle scattering using global scattering functions," *Journal of Applied Crystallography*, vol. 37, no. 4, pp. 523–535, Aug. 2004, doi: 10.1107/S0021889804008969.
- [153] M. Abramowitz, I. A. Stegun, and R. H. Romer, "Handbook of Mathematical Functions with Formulas, Graphs, and Mathematical Tables," *American Journal of Physics*, vol. 56, no. 10, pp. 958–958, 1988, doi: 10.1119/1.15378.
- [154] M. Sztucki and T. Narayanan, "Development of an ultra-small-angle X-ray scattering instrument for probing the microstructure and the dynamics of soft matter," *Journal of Applied Crystallography - J APPL CRYST*, vol. 40, 2006, doi: 10.1107/S0021889806045833.
- [155] A. Siciliano, D. Severgnini, A. Seves, T. Pedrelli, and L. Vicini, "Thermal and mechanical behavior of polyamide 6/polyamide 6I/6T blends," *Journal of Applied Polymer Science*, vol. 60, no. 10, pp. 1757–1764, 1996, doi: 10.1002/(SICI)1097-4628(19960606)60:10<1757::AID-APP29>3.0.CO;2-#.
- [156] T. Cousin, J. Galy, and J. Dupuy, "Molecular modelling of polyphthalamides thermal properties: Comparison between modelling and experimental results," *Polymer*, vol. 53, pp. 3203–3210, 2012, doi: 10.1016/j.polymer.2012.05.051.
- [157] J. E. Mark, *Polymer Data Handbook*. Oxford University Press, 1999.
- [158] Y. Park, J. Ko, T.-K. Ahn, and S. Choe, "Moisture effects on the glass transition and the low temperature relaxations in semiaromatic polyamides," *Journal of Polymer Science Part B: Polymer Physics*, vol. 35, no. 5, pp. 807–815, 1997, doi: 10.1002/(SICI)1099-0488(19970415)35:5<807::AID-POLB9>3.0.CO;2-I.
- [159] Y. Shangguan, F. Chen, E. Jia, Y. Lin, J. Hu, and Q. Zheng, "New Insight into Time-Temperature Correlation for Polymer Relaxations Ranging from Secondary Relaxation to Terminal Flow: Application of a Universal and Developed WLF Equation," *Polymers (Basel)*, vol. 9, no. 11, p. 567, Nov. 2017, doi: 10.3390/polym9110567.
- [160] H. W. Starkweather and J. R. Barkley, "The effect of water on the secondary dielectric relaxations in nylon 66," *Journal of Polymer Science: Polymer Physics Edition*, vol. 19, pp. 1211–1220, 1981, doi: 10.1002/pol.1981.180190804.

- [161] A. Beneduci, “Which is the effective time scale of the fast Debye relaxation process in water?,” *Journal of Molecular Liquids*, vol. 138, no. 1, pp. 55–60, 2008, doi: <https://doi.org/10.1016/j.molliq.2007.07.003>.
- [162] G. D. Smith and R. L. Jaffe, “Quantum Chemistry Study of Conformational Energies and Rotational Energy Barriers in n-Alkanes,” *J. Phys. Chem.*, vol. 100, no. 48, pp. 18718–18724, Jan. 1996, doi: 10.1021/jp960413f.
- [163] K. B. Wiberg and M. A. Murcko, “Rotational barriers. 2. Energies of alkane rotamers. An examination of gauche interactions,” *J. Am. Chem. Soc.*, vol. 110, no. 24, pp. 8029–8038, Nov. 1988, doi: 10.1021/ja00232a012.
- [164] B. Brûlé, “PhD Thesis,” Université Pierre et Marie Curie, Paris, 1999.
- [165] L. Monnerie, J. Halary, and H. Kausch, “Deformation, Yield and Fracture of Amorphous Polymers: Relation to the Secondary Transitions,” in *Advances in Polymer Science*, vol. 187, 2005, pp. 215–372.
- [166] A. Charvet, C. Vergelati, and D. R. Long, “Mechanical and ultimate properties of injection molded cellulose acetate/plasticizer materials,” *Carbohydrate Polymers*, vol. 204, pp. 182–189, 2019, doi: <https://doi.org/10.1016/j.carbpol.2018.10.013>.
- [167] A. Pawlak and A. Galeski, “Cavitation during Tensile Deformation of Polypropylene,” *Macromolecules*, vol. 41, no. 8, pp. 2839–2851, Apr. 2008, doi: 10.1021/ma0715122.
- [168] T. Quatruvaux, S. Elkoun, C. G’Sell, L. Cangemi, and Y. Meimon, “Experimental characterization of the volume strain of poly(vinylidene fluoride) in the region of homogeneous plastic deformation,” *Journal of Polymer Science Part B: Polymer Physics*, vol. 40, no. 22, pp. 2516–2522, 2002, doi: 10.1002/polb.10318.
- [169] Addiego, F., Dahoun, A., G’Sell, C., and Hiver, J. M., “Volume Variation Process of High-Density Polyethylene During Tensile and Creep Tests,” *Oil & Gas Science and Technology - Rev. IFP*, vol. 61, no. 6, pp. 715–724, 2006, doi: 10.2516/ogst:2006009.
- [170] F. Addiego, A. Dahoun, C. G’Sell, and J.-M. Hiver, “Characterization of volume strain at large deformation under uniaxial tension in high-density polyethylene,” *Polymer*, vol. 47, no. 12, pp. 4387–4399, 2006, doi: <https://doi.org/10.1016/j.polymer.2006.03.093>.
- [171] S. Pandini and A. Pegoretti, “Time and temperature effects on Poisson’s ratio of poly(butylene terephthalate),” *Express Polymer Letters*, vol. 5, pp. 685–697, 2011, doi: 10.3144/expresspolymlett.2011.67.
- [172] B. S. Thakkar and L. J. Broutman, “The influence of residual stresses and orientation on the properties of amorphous polymers,” *Polymer Engineering & Science*, vol. 20, no. 18, pp. 1214–1219, 1980, doi: 10.1002/pen.760201807.
- [173] F. F. Rawson and J. G. Rider, “A correlation of Young’s modulus with yield stress in oriented poly(vinyl chloride),” *Polymer*, vol. 15, no. 2, pp. 107–110, Feb. 1974, doi: 10.1016/0032-3861(74)90009-3.
- [174] R. N. Haward, “Strain hardening of high density polyethylene,” *Journal of Polymer Science Part B: Polymer Physics*, vol. 45, no. 9, pp. 1090–1099, 2007, doi: 10.1002/polb.21123.
- [175] T. A. P. Engels, L. E. Govaert, and H. E. H. Meijer, “The Influence of Molecular Orientation on the Yield and Post-Yield Response of Injection-Molded Polycarbonate,” *Macromolecular Materials and Engineering*, vol. 294, pp. 821–828, 2009, doi: 10.1002/mame.200900050.
- [176] J. Richeton, S. Ahzi, K. S. Vecchio, F. C. Jiang, and A. Makradi, “Modeling and validation of the large deformation inelastic response of amorphous polymers over a wide range of

- temperatures and strain rates,” *International Journal of Solids and Structures*, vol. 44, no. 24, pp. 7938–7954, Dec. 2007, doi: 10.1016/j.ijsolstr.2007.05.018.
- [177] B. A. G. Schrauwen, R. P. M. Janssen, L. E. Govaert, and H. E. H. Meijer, “Intrinsic Deformation Behavior of Semicrystalline Polymers,” *Macromolecules*, vol. 37, no. 16, pp. 6069–6078, Aug. 2004, doi: 10.1021/ma035279t.
- [178] K. A. Vijayalakshmi, C. P. Yoganand, and K. Pandiyaraj, “Studies on Modification of Surface Properties in Polycarbonate (PC) Film Induced by DC Glow Discharge Plasma,” *International Journal of Polymer Science*, vol. 2011, 2011, doi: 10.1155/2011/426057.
- [179] C. Ozcan and N. Hasirci, “Evaluation of surface free energy for PMMA films,” *Journal of Applied Polymer Science*, vol. 108, no. 1, pp. 438–446, 2008, doi: 10.1002/app.27687.
- [180] J. C. Arnold, “6.06 - Environmental Effects on Crack Growth in Polymers,” in *Comprehensive Structural Integrity*, I. Milne, R. O. Ritchie, and B. Karahaloo, Eds. Oxford: Pergamon, 2003, pp. 281–319.
- [181] W. A. ZISMAN, “Relation of the Equilibrium Contact Angle to Liquid and Solid Constitution,” in *Contact Angle, Wettability, and Adhesion*, vol. 43, 0 vols., AMERICAN CHEMICAL SOCIETY, 1964, pp. 1–51.
- [182] L. E. Govaert, T. A. P. Engels, E. T. J. Klompen, G. W. M. Peters, and H. E. H. Meijer, “Processing-induced Properties in Glassy Polymers,” *IPP*, vol. 20, no. 2, pp. 170–177, May 2005, doi: 10.3139/217.1870.
- [183] N. E. Zafeiropoulos, R. J. Davies, K. Schneider, M. Burghammer, C. Riekel, and M. Stamm, “The Relationship between Craze Structure and Molecular Weight in Polystyrene as Revealed by μ SAXS Experiments,” *Macromolecular Rapid Communications*, vol. 27, no. 19, pp. 1689–1694, Oct. 2006, doi: 10.1002/marc.200600453.
- [184] C. Bridle, A. Buckley, and J. Scanlan, “Mechanical anisotropy of oriented polymers,” *Journal of Materials Science*, vol. 3, no. 6, pp. 622–628, Nov. 1968, doi: 10.1007/BF00757909.
- [185] L. D. LANDAU and E. M. LIFSHITZ, “CHAPTER XV - SURFACES,” in *Statistical Physics (Third Edition)*, Third Edition., L. D. LANDAU and E. M. LIFSHITZ, Eds. Oxford: Butterworth-Heinemann, 1980, pp. 517–537.
- [186] J. C. Fisher, “The Fracture of Liquids,” *Journal of Applied Physics*, vol. 19, no. 11, pp. 1062–1067, 1948, doi: 10.1063/1.1698012.
- [187] C. Roth, J. Pye, and R. Baglay, “Correlating glass transition and physical aging in thin polymer films,” 2016, pp. 181–204.
- [188] R. R. Baglay and C. B. Roth, “Communication: Experimentally determined profile of local glass transition temperature across a glassy-rubbery polymer interface with a T_g difference of 80 K,” *The Journal of Chemical Physics*, vol. 143, no. 11, p. 111101, 2015, doi: 10.1063/1.4931403.
- [189] R. R. Baglay and C. B. Roth, “Local glass transition temperature T_g(z) of polystyrene next to different polymers: Hard vs. soft confinement,” *The Journal of Chemical Physics*, vol. 146, no. 20, p. 203307, 2017, doi: 10.1063/1.4975168.
- [190] A. Argon, “A Theory for the Low-Temperature Plastic Deformation of Glassy Polymers,” *Philosophical Magazine A-physics of Condensed Matter Structure Defects and Mechanical Properties - PHIL MAG A*, vol. 28, pp. 839–865, 1973, doi: 10.1080/14786437308220987.
- [191] A. Argon, “Craze initiation in glassy polymers – Revisited,” *Polymer*, vol. 52, pp. 2319–2327, 2011, doi: 10.1016/j.polymer.2011.03.019.

- [192] P. G. de Gennes, "Wetting: statics and dynamics," *Rev. Mod. Phys.*, vol. 57, no. 3, pp. 827–863, Jul. 1985, doi: 10.1103/RevModPhys.57.827.
- [193] R. J. Fields and M. F. Ashby, "Finger-like crack growth in solids and liquids," *Philosophical Magazine*, vol. 33, no. 1, pp. 33–48, 1976.
- [194] A. M. Donald, "Crazing," in *The Physics of Glassy Polymers*, R. N. Haward and R. J. Young, Eds. Dordrecht: Springer Netherlands, 1997, pp. 295–341.
- [195] A. S. Argon and M. I. Bessonov, "Plastic flow in glassy polymers," *Polymer Engineering & Science*, vol. 17, no. 3, pp. 174–182, Mar. 1977, doi: 10.1002/pen.760170306.
- [196] N. Hussein, D. Long, L.-A. Fillot, and L. Trouillet-Fonti, "Aliphatic/semi-aromatic block copolyamide," US9688823B2, 27-Jun-2017.
- [197] L.-A. Fillot, S. Jeol, D. Long, and N. Hussein, "Method for increasing fatigue resistance of polyamides," WO2014076139A1, 22-May-2014.